Investigating the Roles of *NFATC2* in Acute Myeloid Leukaemia

Shaun David Patterson, MSc, BSc (Hons)

Submitted in fulfilment of the requirements for the Degree of Doctor of Philosophy

Institute of Cancer Sciences

College of Medical, Veterinary and Life Sciences

University of Glasgow

28th May 2022

Abstract

Acute myeloid leukaemia (AML) is a malignancy affecting the myeloid lineage of haemopoietic cells and has poor patient outcomes. Chemotherapy is poorly tolerated in a high proportion of patients and targeted therapies have limited impact at present. Additionally, relapse and/or resistance to existing therapy are common. High (cyto)genetic heterogeneity within and between AML patients make the development of effective, long-term targeted therapies highly challenging. As such, there is an unmet clinical need for the identification of novel oncogenic mechanisms and pathways which can be targeted therapeutically, in order to improve the clinical outcomes for larger groups of AML patients.

Previously, the histone lysine demethylase *KDM4A* was identified as a putative 'master regulator' of leukaemogenic signalling in models of AML, which was not essential for healthy haemopoietic cell survival. One of the key targets of KDM4A identified in AML was the nuclear factor of activated T cells (cytoplasmic) 2 (*NFATC2*). The wider NFAT family of transcription factors (TFs) has been attributed roles in normal myelopoiesis, in which it is thought to regulate elements of the cell cycle and differentiation, which are key processes that become deregulated in AML. NFATs are also characterised as contributing to oncogenesis and drug resistance in myeloid leukaemias, however much of the evidence focuses on *NFATC1*. In light of the identification of the *KDM4A*-*NFATC2* axis in AML, it was hypothesised that *NFATC2* is essential for the oncogenic function and survival of AML cells.

Prior to testing this hypothesis, *NFATC2* was first characterised in cell line models of AML. Using established compounds, it was found that the MLL-AF9 *TP53*^{mut} THP-1 AML cell line was sensitive to depletion/inhibition of calcium and calcineurin, which are both upstream regulators of NFATs in T cells. Next, shRNA knockdown (KD) of *NFATC2* led to the loss of colony-forming capacity in a number of AML cell lines, highlighting that numerous subtypes of AML cells are dependent on *NFATC2*. In addition, increased apoptosis and cell cycle arrest were individually observed in some of these AML models, but not others, indicating that the mechanisms affected by *NFATC2* depletion are dependent on the (cyto)genetic landscape.

Global transcriptome profiling of THP-1 cells with *NFATC2* KD identified a list of deregulated genes, of which a subset was validated in several other cell lines with

NFATC2 KD. These included genes involved in intracellular transport and membrane protein function. Enrichment analyses also highlighted targets of oncogene *MYC* and serine/threonine kinase 33 (*STK33*) as enriched in the genes perturbed by *NFATC2* depletion. Chromatin immunoprecipitation sequencing (ChIP-Seq) found NFATc2 gene binding targets to be enriched with a c-Myc DNA consensus binding sequence. Additionally, a number of novel NFATc2 DNA binding motifs were identified.

The expression of *NFATC2* was found to stratify patient outcomes in the TARGET-AML dataset, from paediatric AML patients. Of the genes identified by sequencing analyses as putative *NFATC2*/NFATc2 targets, the expression levels of 13 genes were found to be prognostic for patients in the TARGET-AML dataset, also.

Together these data have shown that *NFATC2* is essential for the survival of multiple AML cell lines and that it likely regulates elements of the cell cycle and/or apoptosis, depending on the cellular context. Newly-identified transcriptional and binding targets suggest that the oncogene *MYC* cooperates with *NFATC2* and it could be hypothesised that they maintain an oncogenic transcriptional program together in THP-1 cells. These findings require translation into patient cells, which is challenging given the lack of NFATc2-specific inhibitors available. However, findings from open-source patient datasets indicate that *NFATC2* and its targets have a significant role to play in clinical outcome and so warrant further investigation to elucidate some of the cellular mechanisms involved.

List of Contents

List of tables

List of figures

Additional publications

Papers

Patterson, S. D., Huang, X., Jørgensen, H. G. & Michie, A. M. 2021. Transcriptional Regulation by the NFAT Family in Acute Myeloid Leukaemia. *Hemato*, 2, 556-571.

Massett, M. E., Monaghan, L., **Patterson, S.**, Mannion, N., Bunschoten, R. P., Hoose, A., Marmiroli, S., Liskamp, R. M. J., Jørgensen, H. G., Vetrie, D., Michie, A. M. & Huang, X. 2021. A KDM4A-PAF1-mediated epigenomic network is essential for acute myeloid leukemia cell self-renewal and survival. *Cell Death & Disease*, 12, 573.

Conference Abstracts

Patterson, S. D., Massett, M. E., Wheadon, H., Huang, X., Jørgensen, H. G. & Michie, A. M. 2021. NFATC2 regulates Targets of *MYC* Signaling in MLL-AF9 AML. *Blood*, 138, 3301-3301.

Patterson, S. D., Monaghan, L., Hsieh, Y., Hay, J., Michie, A. M., Huang, X. 2019. Identification of signalling pathways regulated by *KDM4A* in MLL-AF9 AML via a novel kinase activity screen. *BJH*, 185, 38-39.

Acknowledgements

This PhD has been simultaneously challenging and enjoyable from day one. I have gained a huge amount out of this process and none of this would have been possible without the contribution of many others. Firstly, my thanks go to my supervisors Drs. Alison Michie, Heather Jørgensen and Xu Huang. Their extensive support, wisdom and guidance have not only made this PhD project a stimulating academic journey, but they have also helped shaped me into a (hopefully!) proficient researcher. I am very grateful that they supported me as a new student in 2018 and inducted me into the exciting fields of leukaemia research.

I also owe a great deal of thanks to everyone at POG-LRC and the Institute of Cancer Sciences throughout the last ~3½ years, but I can't name absolutely everyone here! In summary, thanks to everyone in the Huang lab for creating a supportive environment in which we were able to cross-fertilise knowledge between our differing projects. Thanks to the Michie lab also for taking me in at a later stage, where I also received much sage advice. For all my *in vivo* work, though it may not be written into this thesis, I received a huge amount of help from Ms. Karen Dunn and the BSU/BRU staff, without which it would not have been possible. Additionally, thanks go to Dr. Alan Hair and Ms. Jennifer Cassels for their technical support throughout. Finally, thanks to Drs. Karen Keeshan, Kevin Rattigan and Heather Jørgensen (in a different role!) for helping me to improve year on year, by reviewing my ongoing work.

Beyond POG-LRC I have to thank the Carnegie Trust for the Universities of Scotland and everyone working there, not just for their financial support but also for providing opportunities to engage and learn from other researchers in varied subject disciplines. Finally, all my thanks go to my family and friends around me, who have been a support through my academic journey before, during and hopefully(!) after this PhD. There are too many people to name here, aside from my parents, Michele, Chris and Charlie (🐾), but anyone else who has endured my complaints after a hard day in the lab or listened to any other scientific ramblings will know who they are!

Author's declaration

I declare that, except where explicit reference is made to the contribution of others, that this thesis is the result of my own work and has not been submitted for any other degree at the University of Glasgow or any other institution.

Signature (electronic):

Date: 25/02/2022

Abbreviations

(*GENE*)^{mut}	Mutated (*GENE*)
(*GENE*)^{wt}	Wild-type (*GENE*)
AML	Acute myeloid leukaemia
ANOVA	Analysis of variance
AP-1	Activator protein 1
APC	Allophycocyanin
APL	Acute promyelocytic leukaemia
ARCH	Age-related clonal haemopoiesis
BCL-2	B-cell lymphoma 2
BM(T)	Bone marrow (transplant)
BrdU	5-bromo-2'-deoxyuridine
BSA	Bovine serum albumin
CAMK	Calmodulin kinase
CAR	Chimeric antigen receptor
CCN(*A*/*B*/*C*/*D*/*E*)	Cyclin(A/B/C/D/E) (gene)
CDK	Cyclin-dependent kinase
CEBPA / CEBP/α	CCAAT Enhancer Binding Protein Alpha
CFC	Colony-forming cell
CFSE	Carboxyfluorescein N-succinimidyl ester
CFU-GM	Granulocyte-macrophage colony-forming unit
CHIP	Clonal haemopoiesis of indeterminate potential
ChIP-Seq	Chromatin immunoprecipitation sequencing
CLB	Cell lysis buffer
CLP	Common lymphoid progenitor
CMP	Common myeloid progenitor
CN	Cytogenetically normal
CNBR	Calcineurin-binding region
CRAC	Calcium release activated channel
CsA	Cyclosporine A

C_t	Cycle threshold
dNTP	Deoxynucleoside triphosphate
DAPI	4′,6-diamidino-2-phenylindole
DBD	DNA-binding domain
DC	Dendritic cell
DIFP	Diisopropyl fluorophosphate
DMEM	Dulbecco's Modified Eagle Medium
DMF	Dimethylformamide
DMSO	Dimethyl sulphoxide
DNMT3A	DNA methyltransferase 3A
DOT1L	DOT1-like histone H3K79 methyltransferase
DTT	Dithiothreitol
EDTA	Ethylenediaminetetraacetic acid
EFS	Event-free survival
EGTA	Ethylene glycol tetraacetic acid
ELN	European LeukemiaNet
EMA	European Medicines Agency
ER	Endoplasmic reticulum
ERK	Extracellular signal-related kinase
FAB	French-American-British (Classification)
FACS	Fluorescence-activated cell sorting
FBS	Foetal bovine serum
FDA	(US) Food and Drug Administration
FDR	False discovery rate
FITC	Fluorescein isothiocyanate
FLT3(-L)	Fms-like tyrosine kinase 3 (ligand)
FLT3^{ITD}	Fms-like tyrosine kinase 3 internal tandem duplication
FPKM	Fragments per kilobase of transcript per million mapped reads
FSC(-A/-H/-W)	Forward scatter (-area / -height / -width)
FWER	Family-wise error rate

GATA	GATA (nucleotide sequence)-binding transcription factor(s)
gDNA	Genomic DNA
G-CSF	Granulocyte colony-stimulating factor
GEO	Gene Expression Omnibus
GFP	Green fluorescent protein
GMP	Granulocyte-macrophage progenitor
GSEA	Gene Set Enrichment Analysis
h*NFATC2*	Human *NFATC2*
H2AX	H2A histone family member X
H3	Histone 3
H3K27	Histone 3 lysine 27
H3K79	Histone 3 lysine 79
H3K9	Histone 3 lysine 9
HBSS	Hanks' Balance Saline Solution
HF	High fidelity
HOX	Homeobox
HRAS	Harvey rat sarcoma viral oncogene homologue
HSC	Haemopoietic stem cell
IF	Immunofluorescence
IL	Interleukin
IMDM	Iscove's Modified Dulbecco's Medium
IP	Immunoprecipitate/immunoprecipitation
IRES-eGFP	Internal ribosome entry site - enhanced green fluorescent protein
ITG	Integrin
IT-HSC	Intermediate-term haemopoietic stem cell
kDa	Kilodalton(s)
KDM/JMJD	Lysine demethylase/Jumonji C domain-containing
KDM4A	Lysine demethylase 4
KRAS	Kirsten rat sarcoma viral oncogene homologue

LB	Luria-Bertani (Medium)
LMO2	LIM domain only 2
LMPP	Lymphoid-primed multipotent progenitor
LIC	Leukaemia-initiating cell
LSC	Leukaemia stem cell
LT-HSC	Long-term haemopoietic stem cell
m*Nfatc2*	Mouse *Nfatc2*
mAb	Monoclonal antibody
MAPK	Mitogen-activated protein kinase
M-CSF	Macrophage colony-stimulating factor
MDM2	Mouse double minute 2 homologue
MEP	Megakaryocyte-erythrocyte progenitor
MPP	Multipotent progenitor
MLL(r)	Mixed lineage leukaemia (rearranged/rearrangement)
MRD	Minimal residual disease
MW	Molecular weight
MYC	Myelocytomatosis (gene)
N.D.	No data
NFAT(*C*)(*1-5*)	Nuclear factor of activated T cells (cytoplasmic) (1-5)
NHD	Nuclear homology domain
NLB	Nuclear lysis buffer
NOS	Not otherwise specified
NPM1	Nucleophosmin 1
NRAS	Neuroblastoma rat sarcoma viral oncogene homologue (gene)
ns	Not significant
NSG	NOD.Cg-Prkdcscid Il2rgtm1Wjl/SzJ (mouse strain)
o/e	Overexpression/overexpressed
OS	Overall survival
OXPHOS	Oxidative phosphorylation
pAb	Polyclonal antibody

PAF1	RNA polymerase II-associated factor
PARP1	Poly(ADP-Ribose) Polymerase 1
PBS(T)	Phosphate-buffered saline (with 0.1% TWEEN®20)
PCA	Principal component analysis
PCR	Polymerase chain reaction
PE	Phycoerythrin
PEI	Polyethylenimine
Pgp	P-glycoprotein
PI	Propidium iodide
PI3K	Phosphoinositide 3-kinase
PIC	Protease inhibitor cocktail
PLC	Phospholipase C
PLL	Poly-L-lysine
PMA	phorbol 12-myristate 13-acetate
PPL	Procedure project license
PRR	Pattern recognition receptor
qRT-PCR	Quantitative real-time polymerase chain reaction
QC	Quality control
Rb	Retinoblastoma protein
RIPA	Radioimmunoprecipitation assay (buffer)
RNA-Seq	Ribonucleic acid sequencing
ROS	Reactive oxygen species
RPKM	Reads per kilobase of transcript per million mapped reads
RPMI	Roswell Park Memorial Institute (1640 Medium)
RSEM	Ribonucleic acid sequencing by Expectation Maximisation
RT	Room temperature
SCL	Stem cell leukaemia
SD	Standard deviation
SDS	Sodium dodecyl sulphate
SEM	Standard error of the mean

shRNA	Short hairpin ribonucleic acid
SOCE	Store-operated calcium entry
SPIA	Signaling Pathway Impact Analysis
SSC(-A/-H/-W)	Side scatter (-area / -height / -width)
ST-HSC	Short-term haemopoietic stem cell
STK33	Serine/threonine kinase 33
TAD	Transactivation domain
TAE	Tris-acetate-EDTA (buffer)
TBS(T)	Tris-buffered saline (with 0.1% TWEEN®20)
TCGA	The Cancer Genome Atlas
TF	Transcription factor
TFS	Thermo Fisher Scientific
TKI	Tyrosine kinase inhibitor
TLR	Toll-like receptor
TMM	Trimmed Mean of M-values
TP53	Tumour protein 53
TSS	Transcription start site
UCSC	University of California, Santa Cruz
WCL	Whole cell lysate
WHO	World Health Organization
WT	Wild-type

1 Introduction

1.1 Acute myeloid leukaemia: background

AML is a haemopoietic malignancy of clonal origin with dismal outcomes; 5-year survival is as low as 15% (Haematological Malignancy Research Network, 2016). Improvements to patient outcomes have been made over the last 50 years through the implementation of specific chemotherapy regimens and, in the cases of disease subtypes including acute promyelocytic leukaemia (APL), the development of non-chemotherapeutic treatments. Most of these improvements have been observed in patients under 60 years old, while outcomes for older patients remain extremely poor, partly due to the challenges in administering chemotherapy to patients in this cohort (Kantarjian *et al.*, 2021). This is significant as the majority of AML patients tend to fall into the >60 age group, although there is incidence of AML in all age groups from infancy (Sasaki *et al.*, 2021).

AML results from an accumulation of mutations within cells of the myeloid lineage, leading to the expansion of immature and dysfunctional blasts, rapid clinical sequelae and often rapid death. Many of the genetic and epigenetic lesions responsible for driving AML pathogenesis are well-characterised, enabling sophisticated patient stratification into molecular subgroups and a shift towards the development of targeted therapies for smaller strata of patients (De Kouchkovsky and Abdul-Hay, 2016).

Targeted therapies in clinical use include inhibitors of the Fms related tyrosine kinase receptor 3 (FLT3), which carries a gain-of-function mutation in a proportion of AML (Chan, 2011, Lagunas-Rangel and Chávez-Valencia, 2017). However, the continuous mutational evolution of AML means that resistance to FLT3-targeted therapy is not uncommon (Tyner *et al.*, 2018, Morita *et al.*, 2020), which is a general concern in the development of novel AML therapies. Newer therapies include B-cell lymphoma protein (BCL-2)-targeting venetoclax (Juárez-Salcedo *et al.*, 2019) and CD33-targeting gemtuzumab ozogamicin (Juliette *et al.*, 2019).

1.2 Haemopoiesis: normal and malignant

1.2.1 Physiological haemopoiesis

A rare population of multipotent haemopoietic stem cells (HSCs) possess a high or near-unlimited capacity for self-renewal and give rise to all types of mature blood cells. HSCs divide 'asymmetrically', meaning that one of the progeny cells becomes more lineage-committed, while the other retains its multipotent capacity. At steady state, HSCs and progenitors differentiate sequentially into more lineage-committed cells, while losing self-renewal capacity, until eventual terminal differentiation into effector cells (Reya *et al.*, 2001), as illustrated in Figure 1-1.

In this classic paradigm a clear distinction is made between populations of HSCs, progenitor cells and mature cells in the haemopoietic hierarchy. More sophisticated approaches, including single-cell transcriptomics, have revealed that differentiation and lineage commitment is a continuous process, and that haemopoietic cells are considerably more heterogeneous than traditionally illustrated (Laurenti and Göttgens, 2018, Zhang *et al.*, 2018).

HSCs can be sub-classified by their ability to maintain self-renewal over time. While long-term (LT)-HSCs retain their multipotency, intermediate-term (IT)- and short-term (ST)-HSCs differentiate more readily, and a continuum exists between these subtypes. Definitions of these cells have been made based on their ability to reconstitute the blood cells of recipient immunodeficient mice over set periods of time. Downstream of HSCs a number of multipotent progenitor (MPP) subtypes have also been defined. Typically, differentiating MPPs 'bifurcate' early, in that they commit towards the lymphoid or myeloid lineages, although it is thought that some more primitive HSCs are already biased towards a particular lineage despite retaining apparent multipotency (Ema *et al.*, 2014).

Alternatively, some models have proposed a downstream lymphoid-primed MPP (LMPP) which can give rise to progenitors of the myeloid or lymphoid lineages, demonstrating the complexity of this hierarchy (Laurenti and Göttgens, 2018). In the classical model myeloid cells differentiate from progenitors towards either the monocyte/granulocyte phenotype, megakaryocytes or erythroid cells, gradually acquiring functional properties of these effector cells. However, the

concept of common oligopotent progenitor subtypes has been challenged by Notta *et al.*, who have shown that differentiated cell populations are derived directly from heterogeneous populations of multipotent cells, without the involvement of a lineage-restricted progenitor intermediate (Notta *et al.*, 2016). Types of blood cell are usually identified by surface antigen expression profiles, which for HSCs includes $CD34^{+}CD38^{-}CD90^{+}CD45RA^{-}$ (Seita and Weissman, 2010), though more specific markers have been identified for some subtypes (Laurenti and Göttgens, 2018). However, due to the heterogeneity and often rarity of some cell types, defining cell types by their immunophenotype alone is challenging.

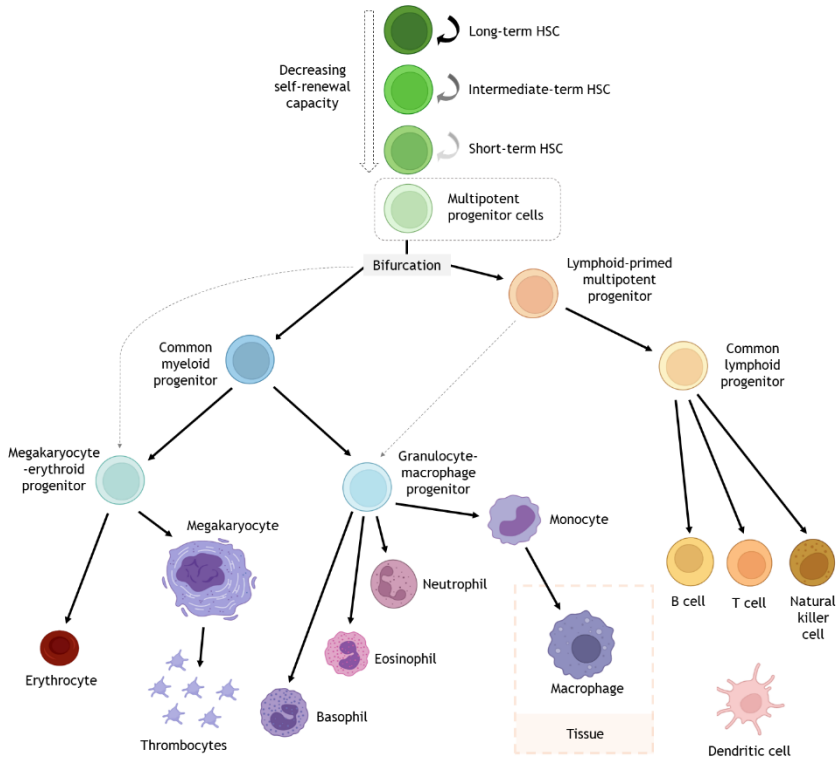

Figure 1-1. Schematic diagram representing the haemopoietic hierarchy.
This diagram represents the classical depiction of the haemopoietic hierarchy. This is simplified and omits several layers of progenitor development. At the top is shown the 'tiers' of HSCs, by which each gives rise to HSCs with gradually reducing self-renewal capacity. A bifurcation occurs, whereby HSCs give rise MPPs, LMPPs and later common myeloid or lymphoid progenitor cells (CMP or CLP). The CMP can give rise to a megakaryocyte-erythroid progenitor (MEP) and a granulocyte-macrophage progenitor (GMP) which then give rise to mature blood cells as shown. Megakaryocytes further develop into mature thrombocytes (platelets) by fragmentation. Monocytes differentiate further into macrophages within tissues. The CLP gives rise to 3 primary lymphocyte types as shown. Dendritic cell (DC) development is highly complex, with subtypes arising from myeloid and lymphocyte backgrounds, so it is not attached to any specific progenitor population here. The diagram was produced using images from biorender.com.

More sophisticated single-cell approaches have suggested that the haemopoietic hierarchy exists as a continuum of branching cellular differentiation states, as opposed to discrete cell types shown here. These differentiation states are driven by oscillations of TF expression and activity, and characterised by their surface immunophenotype and transcriptional profile (Pellin *et al.*, 2019). The expression patterns of some TFs have been identified previously as key markers of specific lineages, including TFs of the GATA family and C/EBPα (Akashi *et al.*, 2000). In fact, the specific order of expression and interplay of these TFs are important in defining lineage commitment. For example, GATA-2 expression in GMPs was shown to drive eosinophil-committed progenitor differentiation, while in CLPs it favoured bipotent basophil/mast cell progenitor development (Iwasaki *et al.*, 2006). During development, in the yolk sac and/or foetal liver, TFs such as SCL, GATA-2 and LMO2 are essential for haemopoiesis. In adults, differentiation of haemopoietic cells and control of self-renewal are heavily regulated by the homeobox (HOX) gene family, isoforms of Ikaros and NOTCH1, amongst others (Zhu and Emerson, 2002).

Epigenetic remodelling is also known to be important in HSC differentiation in haemopoiesis. Methylation of DNA and of histone residues, such as histone 3 lysine 27 (H3K27), are key features in determining cell fate and are often regulated by TF activity (Brown and Ceredig, 2019).

1.2.2 Clonal evolution of AML

The AML cells within a patient harbour 13 gene mutations on average, which is a low mutational burden compared to some other cancers, although thousands of individual somatic mutations have been identified by AML cell profiling (Ley *et al.*, 2013, Tyner *et al.*, 2018). Single-cell analyses have also shown that several distinct clones can exist within the same patient, with divergent patterns of evolution. A number of the mutations in these clones were found to be functionally redundant (Morita *et al.*, 2020), suggesting that common aberrant signalling pathways drive AML transformation.

The accumulation of mutations in AML likely originates in HSCs, or progenitors which acquire self-renewal capacity through the mutation(s) themselves. Analyses of HSCs and leukaemia cells from selected AML patients showed that some HSCs exist in a pre-leukaemic state, whereby they possess some of the mutations found

in the AML clone but do not exhibit a fully leukaemic phenotype or clonal advantage (Jan *et al.*, 2012). It is suggested that subsequent clones acquire mutations which confer a phenotypic advantage, such as a differentiation block, until eventual transformation to AML. This process fits with the classic description of malignant evolution from an early single cell (Nowell Peter, 1976). A number of mutations in AML cells are also likely to be passenger mutations, meaning that they do not confer a cellular advantage and have arisen in the pre-leukaemic clone over time and by chance (Welch *et al.*, 2012).

The concept of 'clonal haemopoiesis of indeterminate potential' (CHIP) describes the presence of somatic mutations in cells of the blood or bone marrow (BM), without other malignant features or cytopenia (Heuser *et al.*, 2016). The prevalence in the population is considerably higher with age and increases the risk of neoplastic transformation in these older patients (Jaiswal *et al.*, 2014). The skewing of haemopoietic cells towards mutation-carrying clones, which have a clonal advantage, has been described as age-related clonal haemopoiesis (ARCH) (Shlush, 2018). Such mutations are most commonly found in *DNMT3A* and *TET2*, encoding epigenetic regulators, in addition to *ASXL1*, *JAK2* and *TP53*.

However, some of these mutations are unable to transform cells into overt AML, indicating that these alone are 'weak drivers' of leukaemogenesis (Steensma, 2018). Various passenger mutations are found in the general ageing population and may have no contribution to AML development, since they are often not associated with known driver mutations. Suggestions for such mutations arising include inherited epigenetic features of the DNA and 'neutral drift', which describes the stochastic expansion of stem cell clones where no existing mutation confers a clonal advantage at the stem cell level. (Klein and Simons, 2011, Zink *et al.*, 2017). It should also be noted that the development of paediatric AML is driven by a distinct set of transcriptional, epigenetic and cytogenetic factors to adult AML (Chaudhury *et al.*, 2018), and so the ARCH model is less relevant.

Studies in pre-leukaemic cells have revealed that the earliest mutational events tend to be in genes encoding epigenetic modifiers, which can change chromatin structure, modify DNA methylation and alter histone residues. Subsequent events tend to occur in 'proliferative' genes such as *NPM1, NRAS* or *FLT3*, in order for AML transformation to occur (Corces-Zimmerman *et al.*, 2014). Kelly *et al.*

demonstrated that expressing internal tandem duplication of *FLT3* (*FLT3*^{ITD}) in an *in vivo* model initiated a myeloproliferative disease, but not penetrant AML (Kelly *et al.*, 2002), supporting the idea that such proliferative oncogenes are insufficient for leukaemogenesis on their own.

The two-hit model of leukaemic transformation separates mutations into class I, which lead to enhanced cell proliferation, and class II, which limit cell differentiation capacity and/or ability to undergo apoptosis. Mutations in both classes are required for full oncogenic transformation, under this model (Gilliland and Griffin, 2002, Kelly *et al.*, 2002). Lesions within epigenetic regulator genes are often reported as an additional 'class' of mutations which is involved in the multi-hit model (Shih *et al.*, 2015). DNA methylation at specific loci is also thought to be important in the ongoing evolution of AML but is not well characterised in this context (Li *et al.*, 2016).

Mutations in AML can be classified by broad function, including TF fusions (most often caused by chromosomal translocation), signalling genes and spliceosome complex genes. Some gene mutations are also known to co-occur frequently – such as *FLT3*^{ITD} and *NPM1*, but the heterogeneity of other gene mutations between patients makes targeting specific pathways challenging (Ley *et al.*, 2013). Additionally, some mutations, such as in *TP53* and *ASXL1*, can make AML cells more resistant to a broad range of existing inhibitors (Tyner *et al.*, 2018).

In addition, the mutational profile of AML cells can change from the clone found at diagnosis and that found at relapse. There is evidence to suggest that pre-leukaemic HSCs may persist following induction chemotherapy and, while these may not be overtly leukaemic, they could acquire (an)other distinct mutation(s) and undergo subsequent leukaemic transformation (Corces-Zimmerman et al., 2014). Alternatively, an originating leukaemic clone may be resistant to chemotherapy and expand following withdrawal of therapy. It has also been suggested that the chemotherapy itself could induce mutagenesis through its effects on DNA replication and so is a contributing factor in the development of relapsed AML (Ding *et al.*, 2012).

1.2.3 The leukaemia stem cell (LSC)

Persistence of minimal residual disease (MRD) after chemotherapy is a major driver of AML relapse and is often attributed to treatment-resistant leukaemia stem cells (LSCs), which exhibit distinct phenotypic and genomic properties to the bulk of AML blasts. The LSC is the mutated HSC clone which is capable of reconstituting the pool of immature AML blasts, which then carry these mutations. LSCs are often thought to be quiescent, so they are less susceptible to cell cycle-targeting chemotherapeutic agents. As such, therapeutics research and development is driven towards finding novel LSC vulnerabilities (Jordan, 2007).

LSCs reside within the $CD34^{+}CD38^{-}CD123^{+}$ cell population, although identification of novel surface markers which differentiate LSCs from normal HSCs is an ongoing challenge. Other antigens regarded as LSC markers include CD96 (Hosen *et al.*, 2007) and TIM3 (Kikushige *et al.*, 2010). Often the presence of LSCs is identified by their ability to fully reconstitute AML within a recipient immunocompromised murine host, and can be quantified using limiting dilution analyses. For this reason, they may also be termed leukaemia-initiating cells (LICs) (Lapidot *et al.*, 1994, Bonnet and Dick, 1997, Pollyea and Jordan, 2017, Haubner *et al.*, 2019). They localise to a BM niche, which can protect them further from chemotherapy, but were also found to home to spleen tissue in a model of MLL-AF9 AML (Somervaille and Cleary, 2006).

Proposed therapeutic modalities to target LSCs include targeting of LSC-specific metabolic pathways, LSC surface antigens, features of the BM microenvironment and unique epigenetic features (Ishikawa *et al.*, 2007, Pollyea and Jordan, 2017). For example, BCL-2 inhibitor ABT-199 was shown to block engraftment after serial transplantation of *IDH1*^{mut} AML cells *in vivo*, suggesting that it impacts upon LIC activity specifically. The mechanism driving BCL-2 dependence in these cells may secondary to the rewired metabolic landscape downstream of *IDH1*^{mut} (Chan *et al.*, 2015). In another study, blockade of hedgehog signalling with SMO inhibitor glasdegib led to quiescent LSCs entering the cell cycle, which might facilitate their elimination them using cell cycle-targeting agents (Kent *et al.*, 2020).

However, few definitive LSC-targeting modalities have emerged in a clinical setting to date, although venetoclax has been postulated to have enhanced LSC-targeting activity. Additionally, AML patients often present with LSC clonal

diversification at relapse as a result of selection pressure and/or enhanced DNA damage, presenting an even further challenge in developing effective therapy in these patients (Vetrie *et al.*, 2020).

1.3 Classification of AML

1.3.1 The French-American-British (FAB) Classification

AML can be classified using the FAB Classification, which groups patient disease based on the overall morphology of BM blasts. Broadly speaking, classes M0-M5 define blasts of increasing differentiation status from 'minimally differentiated' AML in M0 towards a monocytic morphology in M5. Blasts in M6 and M7 resemble the more differentiated cells of the erythroid and megakaryocytic lineages, respectively. Mixed lineage (myeloid and lymphoid) morphologies have also been described. The description of each FAB classification category is shown in Table 1-1 (Schiffer, 2003).

FAB Classification	Description
M0	Minimally differentiated AML
M1	Myeloid leukaemia (without maturation)
M2	Myeloid leukaemia (with maturation)
M3	Acute progranulocytic leukaemia
M4	Myelomonocytic leukaemia
M5	Monocytic leukaemia
M6	Erythroid leukaemia
M7	Megakaryocytic leukaemia

Table 1-1. Description of the categories in the FAB Classification system. These headings are as described by Schiffer *et al.*

However, some studies have shown that the FAB classification is not prognostic, highlighting that patients within the same classification are heterogenous regarding cytogenetics and immunophenotypes (Keating *et al.*, 1996, Tallman *et al.*, 2004), which may be more prognostically significant than morphology alone. In contrast, the M6 and M7 classes can provide prognostic information for post-bone marrow transplant (BMT) patients if combined with *NPM1* and/or *FLT3*^{ITD} status (Canaani *et al.*, 2017).

1.3.2 The World Health Organization (WHO) classification

A model of AML classification was developed by the WHO, which aims to link (cyto)genetic features more closely with clinical features and potential therapeutic modalities. This system classifies AML using 'recurrent genetic abnormalities', which includes chromosomal translocations and gene mutations.

It also introduces a category of AML 'not otherwise specified' (NOS) which uses morphological features, primarily derived from the FAB classification, to group patient disease (Arber *et al.*, 2016). However, Walter *et al*. have shown that morphology is not useful for prognosis in the NOS group when information on *NPM1* and *CEBPA* mutational status is available (Walter *et al.*, 2013). Further adaptations to the system are likely as more is understood about the AML genomic landscape and clinical correlates. Additionally, the threshold for a diagnosis of AML under the WHO classification is ≥20% blasts in the blood or BM, with exceptions, which is lower than the ≥30% threshold defined under the FAB classification (Vardiman *et al.*, 2002). Selected WHO classification groups for AML are shown in Table 1-2.

Group	Sub-group	Additional Notes (Summarised in (Hwang, 2020))
AML with recurrent genetic abnormalities	AML with t(8;21)(q22;q22.1);RUNX1-RUNX1T1	
	AML with inv(16)(p13.1q22) or t(16;16)(p13.1;q22);CBFB-MYH11	No blast threshold for AML diagnosis if t(8;21) present
	APL with PML-RARA	No blast threshold for AML diagnosis if t(8;21) present
	AML with t(9;11)(p21.3;q23.3);MLLT3-KMT2A	
	AML with t(6;9)(p23;q34.1);DEK-NUP214	
	AML with inv(3)(q21.3q26.2) or t(3;3)(q21.3;q26.2); GATA2, MECOM	
	AML (megakaryoblastic) with t(1;22)(p13.3;q13.3);RBM15-MKL1	
	Provisional entity: AML with BCR-ABL1	Distinct to blast phase chronic myeloid leukaemia (BP-CML)
	AML with mutated *NPM1*	Good prognosis, depending on FLT3 mutational status
	AML with biallelic mutations of *CEBPA*	Good prognosis, does not reply to monoallelic
	Provisional entity: AML with mutated *RUNX1*	Diagnosis secondary to other diagnosis categories
AML with myelodysplasia-related changes	-	Blast count in blood or BM should be ≥20% Poorer prognosis than other subtypes
Therapy-related myeloid neoplasms	-	Occurs secondary to cytotoxic therapy or radiation therapy
AML, NOS	AML with minimal differentiation	Morphology and immunophenotype, as highlighted in the FAB classification, serves as a basis for sub-group classification.
	AML without maturation	
	AML with maturation	
	Acute myelomonocytic leukaemia	
	Acute monoblastic/monocytic leukaemia	
	Pure erythroid leukaemia	
	Acute megakaryoblastic leukaemia	
	Acute basophilic leukaemia	
	Acute panmyelosis with myelofibrosis	

Table 1-2. WHO Classification of Myeloid Neoplasms: AML.

1.4 Therapeutic intervention

Often the mainstay of treatment in AML is chemotherapy ± BMT. The European LeukemiaNet (ELN) expert panel guidance recommends that patients should be selected for first-line intensive chemotherapy based on a balance of age (<65-year-olds have generally better outcomes), patient fitness and co-morbidities. This regimen usually includes anthracycline for 3 days and cytarabine for 7 days (known as a '7+3' regimen) followed by consolidation therapy, which is guided by cytogenetics and age. Patients with a more adverse cytogenetic profile are more likely to be recommended for haemopoietic cell transplantation after intensive chemotherapy.

Non-chemotherapeutic regimens include inhibitors of FLT3 and gemtuzumab ozogamicin, usually combined with chemotherapy (Döhner *et al.*, 2017). A number of therapies have also been approved in various regions for clinical use since the ELN guidelines were last updated. These include venetoclax, tyrosine kinase inhibitor (TKI) midostaurin, hedgehog pathway-targeting glasdegib and IDH1-targeting ivosidenib, though fewer of the novel medicines are approved by the European Medicines Agency (EMA), compared with the US Food and Drug Administration (FDA). Further clinical trials are required to identify and refine the strata of patients who can optimally benefit from these treatments, and guidelines should be updated accordingly (Estey *et al.*, 2020). However, recent clinical trials show promising results for novel therapies in AML, such as improved outcomes with venetoclax/azacitidine combination therapy (DiNardo *et al.*, 2020) and FLT3 inhibitor gilteritinib (Perl *et al.*, 2019).

A number of other strategies are being investigated for the treatment of AML. These include inhibition of DNA damage molecule Poly[ADP-ribose] polymerase 1 (PARP1), which has been shown to have synergy with FLT3 inhibition. Other modalities include blocking reactive oxygen species (ROS) formation by targeting NADPH oxidases (NOX) or the induction of differentiation. Strategies to overcome drug resistance, which is a major driver of relapse, are also key to improving outcomes (Nair *et al.*, 2021). Chimeric antigen receptor (CAR) T cells are a novel therapeutic modality by which the patient's T cells can be engineered to target malignant cells and re-infused to the patient. A number of target antigens for the

use of CAR-T cells in AML have been proposed, including CD33 and CD123 (Marofi *et al.*, 2021).

While there is a promise of novel targeted therapies for AML, the ongoing issues of resistance to therapy and inter-patient heterogeneity remain as barriers to effective treatments. Clearly there is an unmet clinical need for AML therapeutics which have long-term efficacy and/or can be combined with existing treatments.

1.5 Key mutations and aberrant signalling in AML

1.5.1 Mixed lineage leukaemia 1 (MLL)-rearranged (MLLr) AML

Chromosomal translocations are common in AML and only around 40-50% of *de novo* cases have been reported as being cytogenetically normal (CN). Fusions of the *MLL1* gene have been reported in 2.5-10% of all AML cases (Schoch *et al.*, 2003, Krivtsov and Armstrong, 2007), but are considerably more common in paediatric cases at 15-20% (Balgobind *et al.*, 2011). The normal MLL protein regulates TFs including the *HOX* gene family, which they positively regulate during normal development. MLL also regulates acetylation and methylation of histone residues, such as histone 3 lysine 4 (H3K4) and histone 3 lysine 9 (H3K9) in the regulation of gene transcription, partly through its methyltransferase SET domain. Translocation resulting in the fusion of MLL to another gene at the MLL N-terminal results in MLL truncation, loss of its SET domain and usually a gain of function. The MLL fusion protein can dimerise, giving it enhanced affinity for *HOX* gene promoter binding and activation of the *HOX* co-factor *MEIS1*, amongst several other known mechanisms (Hess, 2004).

Over 50 MLL fusion partners have been identified, though transcriptional regulators account for the majority, including *AF4*, *AF9*, *AF10*, *ENL* and *ELL*. The most common MLL fusion in childhood and adult leukaemia is with *AF9* (also known as *MLLT3*), comprising around 1 in 3 cases of MLL fusion. A number of these fusions have been shown to regulate transcription by chromatin remodelling. In particular, MLL fusion proteins can recruit the histone methyltransferase DOT1L to transcriptional complexes, which can activate gene transcription by methylating lysine 79 of histone 3 (H3K79). This is one proposed mechanism by which MLL fusions can aid leukaemogenic transformation of haemopoietic cells (Krivtsov and Armstrong, 2007).

In addition, *MLL* fusions have roles in LSCs. Expression of *MLL-AF9* in lineage-committed granulocyte-macrophage progenitor (GMP) cells was shown to confer a self-renewal transcriptional signature akin to that found in HSCs, and recapitulate an AML phenotype *in vivo* which was transplantable to secondary recipients with low cell input (Krivtsov *et al.*, 2006). Further work by Krivtsov *et al*. demonstrated that the leukaemic cell of origin, whether HSCs or downstream progenitors, is significant to prognosis. HSC-derived leukaemia had a similar immunophenotype to GMP-derived leukaemia but had a stronger stem cell-like transcriptomic signature, altered methylation status, caused faster leukaemia development *in vivo* and reduced sensitivity to chemotherapy *in vitro* (Krivtsov *et al.*, 2013).

Another model of *MLL-AF9* expression in murine cells generated AML LSCs which, despite sharing the self-renewal properties of HSCs, actually expressed an immunophenotype more similar to lineage committed cells (Somervaille and Cleary, 2006). *MLL-ENL* expression can also confer self-renewal properties to committed progenitor cells (Cozzio *et al.*, 2003). In summary, MLL fusion oncoproteins have the capacity to transform haemopoietic cells at multiple levels of the hierarchy *in vitro*, by upregulating a self-renewal expression programme including genes such as *HOX*.

While clinical outcomes for paediatric *MLL-AF9* AML have been reported as favourable, outcomes vary dramatically for other fusion partners. A variety of therapeutic strategies are under investigation for *MLL*-rearranged (*MLL*r) AML, including inhibition of histone deacetylases, proteasome inhibition, and hypomethylating agents (Winters and Bernt, 2017). Pinometostat, an inhibitor of the histone lysine methyltransferase DOT1L, is under clinical investigation as a treatment for adult MLLr AML (Stein *et al.*, 2018).

1.5.2 Fms-like tyrosine kinase 3-internal tandem duplication (*FLT3*^{ITD})

FLT3^{ITD} is one of the most common mutations in AML, occurring in 25-30% of all cases and it is often associated with a particularly poor outcome (Haematological Malignancy ResearchNetwork, 2016, Lagunas-Rangel and Chávez-Valencia, 2017). *FLT3*^{ITD} can arise at the level of the LSC or it may be found in subclones, which can be eliminated by chemotherapy; its contribution to clonal evolution is not clear (Levis *et al.*, 2005). It is a gain-of-function mutation which leads to

constitutively active downstream signalling, independent of the FLT3 ligand (FLT3-L) and can activate signalling pathways driven by phosphoinositide 3-kinase (PI3K), signal transducer and activator of transcription 5 (STAT5) and extracellular signal-related kinase (ERK) (Choudhary *et al.*, 2007, Chan, 2011). There are a number of effective TKIs against FLT3, such as sorafenib, quizartinib and the novel gilteritinib, however patients often develop resistance to these and so long-term benefit is limited (Fathi and Chabner, 2011, Daver *et al.*, 2021).

1.5.3 Nucleophosmin 1 (*NPM1*)

Mutation of the *NPM1* gene is one of the most common perturbations found in AML occurring in 25-30% of cases (Thiede *et al.*, 2006). The normal NPM1 protein functions in the nucleolus where it regulates ribosome synthesis, in addition to other functions in DNA repair regulation and modulation of the centrosome. When mutated it resides exclusively in the cytoplasm, which leads to a number of aberrant functions, including dysregulated p53 activity, genomic instability and upregulation of *HOX* genes. Vassiliou *et al.* reported that *Npm1*^{mut} did not efficiently initiate AML on its own *in vivo*, though did lead to upregulation of the self-renewal *Hox* gene program (Vassiliou *et al.*, 2011). A more recent study had a similar finding, in addition to suggesting that *Npm1*^{mut} could be an earlier pre-leukaemic event than *Dnmt3a*^{mut} in the sequential initiation of AML (Uckelmann *et al.*, 2020).

NPM1^{mut} is actually associated with improved outcomes in AML. Additionally, 40% of *NPM1*^{mut} AML also have co-occurring *FLT3*^{ITD}, which has a poorer survival than *NPM1*^{mut} alone but better than *FLT3*^{ITD} alone (Thiede *et al.*, 2006). Interestingly, the genesis of both *NPM1*^{mut} and *FLT3*^{ITD} may result from aberrant activity of the enzyme terminal deoxynucleotidyl transferase (TdT) (Borrow *et al.*, 2019). While *NPM1*^{mut} AML is generally responsive to chemotherapy, the specific clinical course may be determined by co-occurring (cyto)genetic abnormalities which sometimes override the good prognosis conferred by *NPM1*^{mut} alone (Zarka *et al.*, 2020, Falini *et al.*, 2021).

1.5.4 DNA methyltransferase 3α (*DNMT3A*)

As highlighted previously, *DNMT3A*^{mut} is one of the earliest mutations to arise in AML and occurs in over 20% of AML patients, though it is considerably more

common in CN AML (40-50%). Known mutations can increase or decrease its methyltransferase activity at some known promoter regions; for example, hypermethylation of the *CDKN2B* promoter, leading to a reduction in *CDKN2B* tumour suppressive activity. *DNMT3A*^{mut} AML has poorer outcomes compared to wild type (WT) *DNMT3A* (Sandoval *et al.*, 2019, Park *et al.*, 2020). Some hypomethylating agents which inhibit DNMT3A, such as azacitidine, are in ongoing clinical investigation for AML (Wong *et al.*, 2019).

1.5.5 TP53

The 'guardian of the genome' *TP53* is very frequently mutated in cancers of various tissues, however it occurs in just 8% of adult *de novo* AML, making it one of the less prevalent (but still recurrent) gene mutations. However, these mutations are associated with a significantly poorer outcome. The role of *TP53* in HSCs is to constrain self-renewal and mediate responses to DNA damage. Somatic mutations of *TP53* in AML are often dominant negative and loss-of-function, resulting in clonal expansion of transformed haemopoietic cells, although some gain-of-function mutations are possible. Clinical investigation into some small molecule inhibitors targeting mutated *TP53* have been initiated (Barbosa *et al.*, 2019, Dutta *et al.*, 2020).

However, dysregulation of the *TP53* pathway has been reported in the presence of *TP53*^{WT} in AML. For example, p53 (protein) negative regulator *MDM2* was found to be overexpressed in one-third of AML. As such, inhibition of the MDM2/p53 interaction is a promising therapeutic target. Other p53-interacting proteins are being reviewed as targets in a similar manner (Quintás-Cardama *et al.*, 2017, Barbosa *et al.*, 2019).

1.5.6 *NRAS* and *KRAS*

The *RAS* gene family code for membrane-associated GTPase proteins which are responsive to ligand activation and activate various downstream pathways. Mutations in 2 of these genes, *NRAS* and *KRAS*, are found in approximately 11% and 5% of AML cases, respectively, while *HRAS* mutations are uncommon in AML. *RAS* mutations can lead to activation of signalling pathways such as PI3K and MAPK and the impact of these mutations on patient outcomes is unclear, if not insignificant (Bowen *et al.*, 2005, Bacher *et al.*, 2006, Ball *et al.*, 2021).

1.5.7 The transcriptome

It is not solely mutations or cytogenetic lesions which offer clues about AML prognosis: transcriptional profiling can be used to risk stratify AML patients and identify potential novel therapeutic strategies (Docking *et al.*, 2021). Interestingly, the Cancer Genome Atlas (TCGA) analysis found that 200 primary AML samples could be clustered by global expression data into groups similar to the FAB classes, concluding that the transcriptome is closely linked to AML cell differentiation status (Ley *et al.*, 2013). Disordered transcription might be expected in AML, since recurrent mutations are often in transcriptional regulators including *CEBPA*, *RUNX1* and *ASXL1*.

In normal myelopoiesis, RUNX1 regulates C/EBPα and its substrates/interaction partners, including AP-1, in maintaining the balance of monocyte and granulocyte development. In AML, *RUNX1* point mutations or fusions (e.g. RUNX1-ETO) can result in downregulated *CEBPA*, while *CEBPA* mutations (in up to 15% of AML) lead to dysfunctional C/EBPα proteins. The result(s) of these events include reduced myeloid differentiation, increased proliferation and/or suppression of apoptosis (Paz-Priel and Friedman, 2011). Somatic mutations of *RUNX1* occur in ~15% of adult AML and are associated with a characteristic expression profile (Sood *et al.*, 2017). Mutations of *ASXL1* are found in an estimated 6.5% of AML and associated with significantly poorer outcomes. A frameshift mutation is the most common, which leads to a dysfunctional truncated protein (Gelsi-Boyer *et al.*, 2012).

A number of TFs with known roles in leukaemia are under investigation as putative drug targets for AML, including RUNX1 and c-Myc (Takei and Kobayashi, 2019).

1.5.8 The *KDM4A-PAF1-NFATC2* axis

More recently the *KDM* (also known as *JMJD*) families have become more significant in the pathogenesis of AML. One member, *KDM4A*, is known to regulate histone methylation at residues including H3K9 and H3K36, which are generally markers of inhibited or activated transcription at specific loci, respectively. In addition, KDM4A can also impair DNA repair and contribute to genome instability in some cancers (Berry and Janknecht, 2013). More recently, it was shown that KDM4A may regulate H3K27 methylation directly, in AML cells (Massett *et al.*, 2021). In AML, small molecule inhibition of KDM4 and KDM6 was detrimental to

cell survival, and H3K27 was also identified as a key target of these demethylases (Boila *et al.*, 2018). Activity of the related KDM1A was shown to be essential for the survival of MLL-AF9 AML cells, in which it maintained a pro-oncogenic transcriptional signature (Harris *et al.*, 2012).

Knockdown (KD) of *KDM4A* and inhibition with a pan-KDM4 inhibitor both resulted in impaired AML cell survival, while sparing HSCs. In addition, the RNA polymerase II associated factor (*PAF1*) was identified as a key co-factor of KDM4A activity in various models of MLLr AML, which together maintain the expression of MLL-fusion gene targets (Massett *et al.*, 2021). Subsequently *NFATC2* was identified as a transcriptional target of *KDM4A* and *PAF1*, whereby an axis of *KDM4A-PAF1-NFATC2* was established (unpublished data).

The Nuclear Factor of Activated T Cells (*NFAT*) family of TFs has been demonstrated to have roles in the pathology of myeloid leukaemias (Gregory *et al.*, 2010, Metzelder *et al.*, 2015). *NFAT* signalling has been well-characterised in various solid and lymphoid cancers, in addition to the mechanics of the innate immune system. Their role in pathology is often dependent on regulation of cell type-specific cytokine signalling networks, cell cycle progression and apoptosis (Mancini and Toker, 2009, Fric *et al.*, 2012b, Qin *et al.*, 2014, Mognol *et al.*, 2016). However, there is currently no published primary evidence outlining the contribution or role(s) of *NFATC2* in AML.

1.6 The NFAT family in AML

1.6.1 The NFAT family: background

The general structure and function of the *NFAT* family have been reviewed extensively (Rao *et al.*, 1997b, Macián *et al.*, 2001, Macian, 2005, Qin *et al.*, 2014). To summarise, the *NFAT* family consists of five members, in which NFATc1-4 function downstream of calcium signalling – denoted as '*NFATc*', although other nomenclature is often used - while *NFAT5* is responsive to osmotic stress. NFATc1-4 are referred to here as '*NFAT*' collectively. Additionally, each *NFAT* gene can undergo alternative splicing, giving rise to a number of transcript and protein variants per family member; these protein variants vary structurally at their N- and C-terminals. Differential expression of *NFAT* splice variants has been described in neurological tissues but the functional significance of these is not well understood (Vihma *et al.*, 2008). Here, each of *NFATC1-4* is referred to as an *NFAT* 'family member', while each protein arising from alternative splicing is a 'protein variant'.

NFAT proteins have high sequence homology in a conserved DNA-binding Rel homology domain, which is shared with the Rel superfamily of TFs (including NFκB) (Graef *et al.*, 2001). At the N-terminus is the NFAT homology domain (NHD), which contains phosphorylation sites that are targeted by upstream regulatory kinases. Critically this region possesses docking sites for regulatory phosphatase calcineurin, which dephosphorylates most of these phospho-sites. The N- and C-termini are flanked by transactivation domains (TADs) which are non-homologous between family members and are a key interaction point with transcriptional partner proteins (Hogan *et al.*, 2003, Vihma *et al.*, 2008). Figure 1-2 shows some of the nomenclature (Fig 1-2A), protein regions with sequence alignment between differing NFAT family members (Fig 1-2B) and alignment amongst protein variants of NFATc2 (Fig 1-2C). Regions of high sequence homology and functional regions of the protein are derived from the literature (Rao *et al.*, 1997b, Macián *et al.*, 2001, Macian, 2005, Qin *et al.*, 2014, Mognol *et al.*, 2016, Kitamura and Kaminuma, 2021).

A

Name	Alternative Name(s)	Number of Known Protein Variants	Protein Length (Amino Acids)
NFATc1	NFAT2, NFATc	10	353-943
NFATc2	NFAT1, NFATp	6	688-917
NFATc3	NFAT4, NFATx	3	1065-1075
NFATc4	NFAT3	9	782-965

B

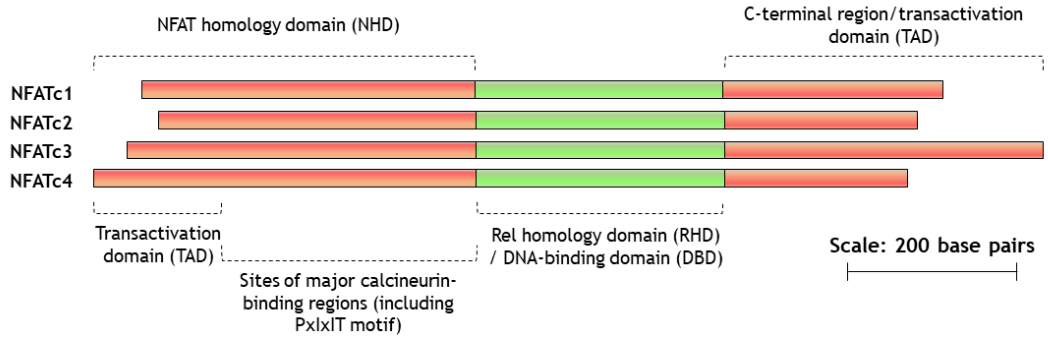

C

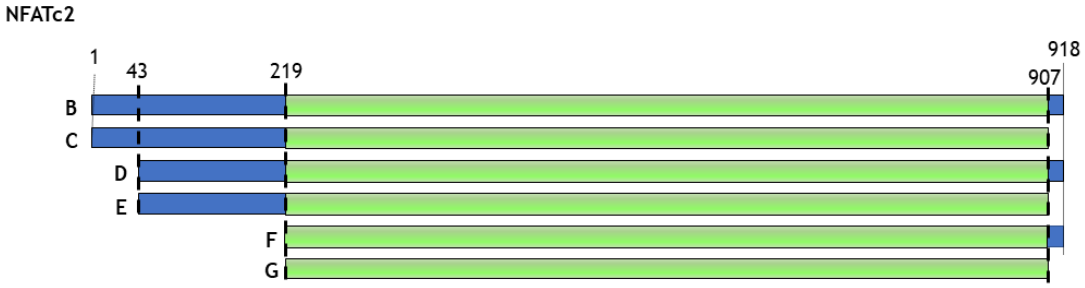

Figure 1-2. Nomenclature of *NFAT* and schematic diagrams of NFAT protein alignment. **A:** Table highlighting alternative nomenclature for *NFATC1-4*. The number of protein variants (as arises from alternative splicing) is highlighted per *NFAT* family member. The protein length, given in amino acids, is shown as a range from the shortest to longest protein variant, per NFAT family member. These data were extracted from the NCBI database, based on the GRCh38 genome. **B:** Protein alignment diagram for NFATc1-4. Protein sequences for each of NFATc1-4, for the longest protein variant per family member, were aligned and scored for strength of alignment using the online PRALINE multiple sequence alignment tool (via Centre for Integrative Bioinformatics VU, University of Amsterdam). Sequences were obtained as in **A**. A central region of high sequence homology was defined at a similar position as in the literature (amino acid position 400-698, relative to NFATc1 in this case, shown in green) and showed a higher mean alignment score amongst all NFATc1-4 than other regions (7.84 for the central homologous region; 3.58 for the N-terminal; 2.64 for the C-terminal; maximum possible score is 10). Highlighted are approximate locations for key functional regions as described in the literature. **C:** Schematic diagram showing the protein sequence alignment between protein variants of NFATc2. Sequences were obtained and aligned as in **B**. Shown are all 6 variants 'B'-'G' with the amino acid position given (relative to variant 'B'). Regions of 100% sequence homology are shown in green.

Inactive NFAT proteins reside in the cytoplasm in a heavily phosphorylated state. Activation of calcium-coupled surface receptors (e.g. receptor tyrosine kinases) triggers a signalling cascade via phospholipase C (PLC), which promotes calcium influx in a process known as store operated calcium entry (SOCE). In response to elevated calcium the messenger calmodulin activates multiple target enzymes, which include calcineurin and calmodulin kinase (CAMK) isoforms. Activated calcineurin docks on NFAT at conserved PxIxIT peptide motifs and subsequently dephosphorylate at up to 14 known serine-rich motifs on the NHD (Macian, 2005, Gwack *et al.*, 2007).

The conformational change which follows NFAT dephosphorylation exposes a 'nuclear localization signal' enabling its nuclear import. The subcellular location of NFAT is carefully balanced by opposing calcineurin phosphatase activity and that of numerous kinases, which mask these localization signals to facilitate nuclear export in the absence of raised intracellular calcium. Examples of these kinases include GSK3, CK1 and JNK. Additionally, p38 MAPK has been found to regulate NFAT transactivation in the nucleus through phosphorylation at a motif separate to those regulated by calcineurin (Hogan *et al.*, 2003, Villar *et al.*, 2006, Leung-Theung-Long *et al.*, 2009).

Once inside the nucleus NFAT binds DNA as a monomer, unlike other Rel superfamily members. The core NFAT DNA consensus binding sequence has been defined as 5'-GGAA(A)-3' in T cells, but variations have been described with differing binding affinities (Rao *et al.*, 1997b, Badran *et al.*, 2002, Hogan *et al.*, 2003). Lone NFAT DNA binding is often weak and it must bind in tandem with other factors at composite sequences to regulate transcription, as has been shown with AP-1 proteins Fos and Jun (Chen *et al.*, 1998). In the case of NFκB proteins, NFAT could either compete with them or bind cooperatively, depending on the DNA motifs (Badran *et al.*, 2002). One proteomics study described hundreds of putative NFAT interaction partners in T cells (Gabriel *et al.*, 2016), raising the notion that NFAT proteins function as part of large transcriptional complexes and so are master integrators of upstream signalling pathways. A schematic diagram of NFAT function in the cell is shown in Figure 1-3.

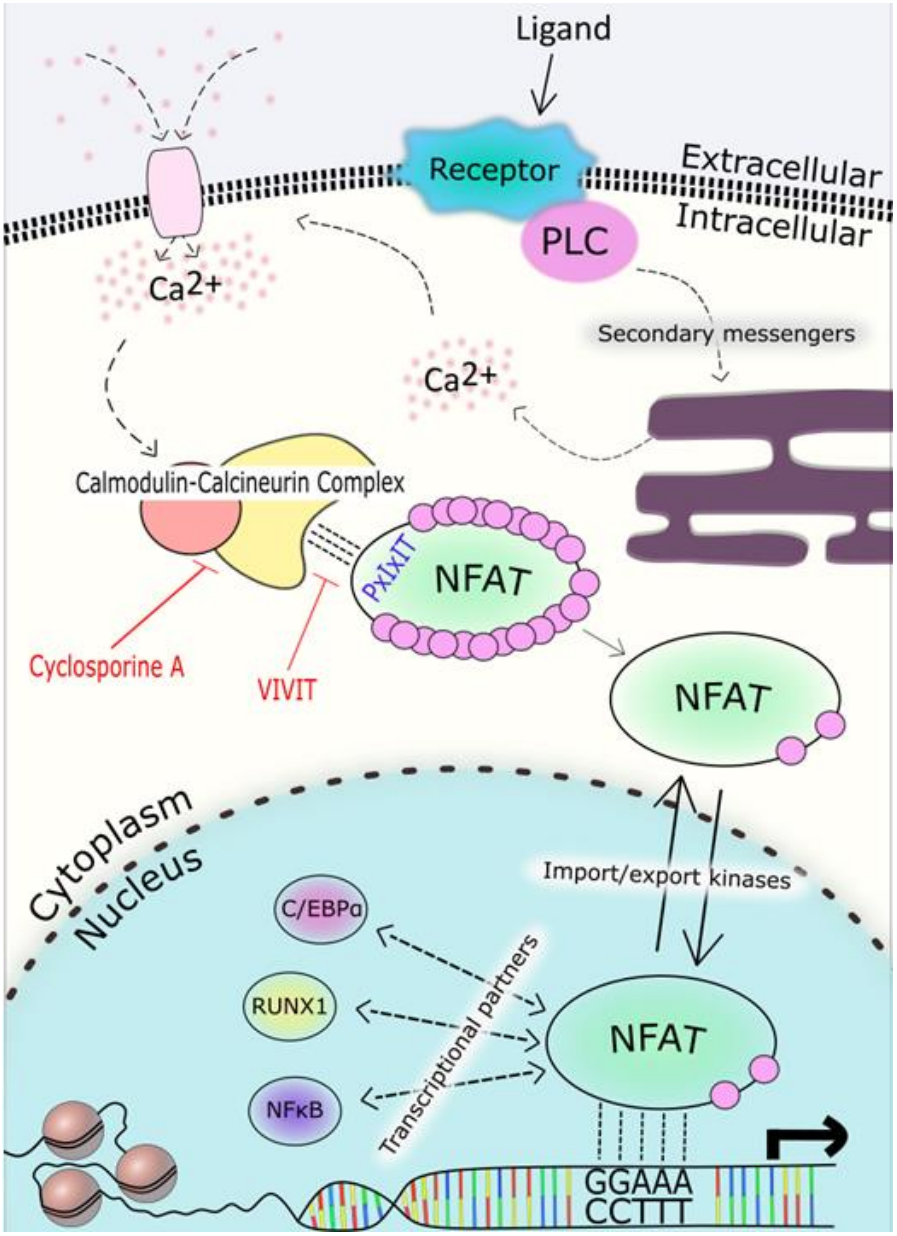

Figure 1-3. Schematic diagram of calcium-NFAT signalling.
1. Engagement of a calcium-coupled surface receptor by its ligand leads to activation of PLC. 2. A cascade of signalling events is initiated by PLC which leads to the movement of calcium from the endoplasmic reticulum (ER) into the cytoplasm. 3. Following depletion of ER calcium stores surface calcium release-activated calcium (CRAC) channels are opened, enabling influx of calcium to the cell. 4. Raised calcium levels triggers activation of calmodulin, which binds calcineurin. 5. A conformational change in calcineurin allows it to bind to NFAT at the PxIxIT docking motif and dephosphorylate NFAT at ~14 phospho-sites. 6. Dephosphorylation of NFAT – with the exception of some residues not targeted by calcineurin – exposes a nuclear localization signal and enables its import to the nucleus. 7. Once in the nucleus NFAT can bind to consensus DNA sequences – including 5'-GGAAA-3' – and activate (or inhibit) transcription. It may do so in cooperation with various transcriptional partners, which can include C/EBPα, RUNX1 and/or NFκB. NFAT's position in the nucleus is balanced by the activity of import and export kinases. Note that inhibitors cyclosporine A (CsA) and VIVIT peptide can inhibit activation of the calmodulin-calcineurin complex or binding of calcineurin to NFAT, respectively.

Inhibition of NFAT activation can be achieved by targeting calcineurin, using either of the small molecule inhibitors cyclosporine A (CsA) or tacrolimus. These are both used clinically to prevent graft rejection after organ transplantation, primarily due to the immunosuppressive effects on T and B cell activation secondary to inhibited NFAT-dependent cytokine transcription. While different in structure and target, they both form complexes with cellular immunophilins which can inhibit calcineurin phosphatase activity (Bierer *et al.*, 1993). Calcineurin has numerous targets in addition to NFAT (Li *et al.*, 2011a), making this a relatively non-specific means of inhibiting NFAT activity. Subsequently a more selective peptide inhibitor 'VIVIT peptide' was developed, which directly binds the calcineurin docking motif PxIxIT on NFAT, thus more selectively inhibiting NFAT activity (Aramburu *et al.*, 1999). These inhibitors are useful tool compounds to study NFAT function.

1.6.2 NFATs in the myeloid lineage

NFAT expression in differentiated myeloid cells is generally lower than in T cells and $CD34^+$ HSCs. Kiani *et al*. demonstrated that *NFATC1-3*, but not *NFATC4*, are well expressed in $CD34^+$ blood cells and altered within myeloid lineages. *NFATC2* is downregulated in most differentiated myeloid cells, while *NFATC1* is upregulated during the course of erythroid and megakaryocyte differentiation. *NFATC3* is upregulated during erythroid but not megakaryocyte or eosinophil differentiation. Furthermore, inhibition of calcineurin-NFAT signalling with CsA was found to be permissive of $CD34^+$ HSC differentiation into neutrophils (Kiani *et al.*, 2004, Kiani *et al.*, 2007). These data suggest that *NFAT*s are responsible for regulating differentiation in healthy cells and that the *NFAT* family members are non-redundant in determining cell fate. This also suggests that specific *NFAT* members could be more important in the development of some morphological subtypes of AML.

AML cells are characteristically poorly differentiated (Olsson *et al.*, 1996) and it is worth considering whether *NFAT* could have a role in maintaining the stem cell-like properties of blasts, given the observed gene expression profiles in healthy myeloid tissue.

NFAT proteins regulate genes which determine proliferation and lineage commitment in the myeloid lineage. In murine GMP cells Nfat was found to negatively regulate genes which determine cell cycle entry such as *Cdk4* and *Cdk6*.

This activity was dependent on Flt3-L signalling and PLCγ1-dependent calcium influx (Fric *et al.*, 2014). Another study found that CsA inhibition of Flt3-L stimulated murine DCs led to upregulation of genes which progress the cell cycle, suggesting that targets of calcineurin block Flt3 receptor-mediated cycling. Additionally, blockade of the calcineurin-Nfat interaction with VIVIT also led to the expansion of the myeloid compartment *in vivo* (Fric *et al.*, 2012a). These studies suggest that the NFAT/Nfat proteins inhibit proliferative signalling in myeloid development and interact with FLT3 receptor signalling.

In normal physiology the growth factors macrophage- and granulocyte- colony stimulating factor (M-CSF and G-CSF) trigger HSCs to differentiate into either macrophages/monocytes or granulocytes, respectively. *Nfatc1* expression was found to increase in murine BM cultures stimulated with M-CSF, but not G-CSF. Differentiation triggered by M-CSF was partially blocked by VIVIT, suggesting that it is dependent on calcineurin-NFAT interaction. Furthermore, distinct from the Flt3-L-stimulated GMPs described above, stimulation with either M-CSF or G-CSF was found to induce PLCγ2 (but not PLCγ1) activity (Barbosa *et al.*, 2014). Therefore it appears that the regulatory function of *NFAT* in myelopoiesis, in the balance of proliferation and differentiation, is dependent on specific upstream signalling networks.

NFAT proteins are well characterised in T cell effector function and also play a role in the myeloid cell response to pathogens. Pattern recognition receptors (PRRs), such as TLR4, respond to structural elements of invading microbes to trigger an immune response. Engagement of PRRs in a number of differentiated myeloid cell types can stimulate the calcineurin-NFAT interaction via calcium influx initiated by Syk and PLCγ (Bendickova *et al.*, 2017). NFAT can also bind the canonical 5'-GGAAA-3' DNA motif and regulate the expression of various cytokines in DCs and macrophages, including IL-2, IL-10 and IL-12, which influence immune responses (Elloumi *et al.*, 2012, Yu *et al.*, 2014). There is limited evidence suggesting that systemic CsA treatment in transplant patients could worsen outcomes due to a greater risk of fungal infection, secondary to inhibition of myeloid effector cell function specifically (Bendickova *et al.*, 2017). Some of these roles of *NFAT*s are shown schematically in Figure 1-4.

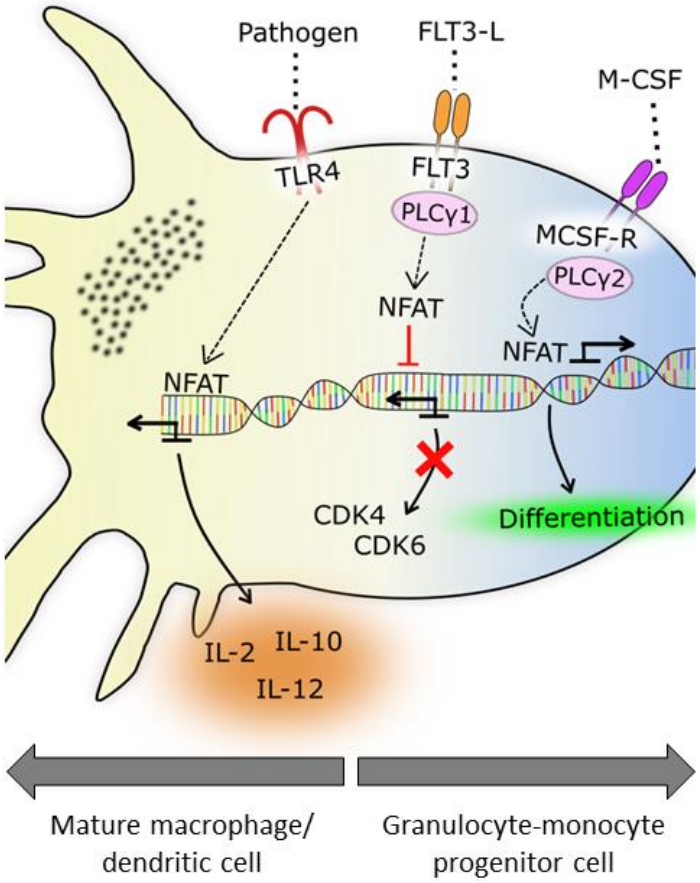

Figure 1-4. Schematic diagram of putative roles for NFAT in myeloid lineage cells. Roles for NFAT inferred from aforementioned studies are shown as putative roles in human myeloid cells, schematically as a myeloid cell in different 'stages' of differentiation. Left: in mature dendritic cells pathogens trigger pattern recognition receptors (PRRs) such as TLR4, which is thought to be upstream of NFAT-driven cytokine transcription. Middle: in progenitor cells NFAT is downstream of a FLT3-PLCγ1 axis, whereby it inhibits regulators of the cell cycle. NFAT may also act downstream of FLT3 in dendritic cells. Right: in GMPs NFAT activates myeloid differentiation in response to M-CSF receptor engagement, which also signals via PLCγ2.

The evidence discussed highlights that *NFAT* activity can direct myeloid progenitors towards quiescence by inhibiting the cell cycle or favour differentiation, depending on the specific upstream pathways activated. Leukaemic transformation to AML is dependent on deregulation of these processes in steady state myelopoiesis and these changes are often promoted through TFs (Olsson *et al.*, 1996). As such, NFAT proteins could influence AML initiation or maintenance downstream of mutated signalling proteins. For example, the FLT3 receptor is commonly mutated in AML, leading to enhanced proliferation.

Understanding the relationship between FLT3-L and *NFAT* activity in healthy myeloid cells could therefore provide insight into this relationship in leukaemia. In parallel, TLR4 participates in HSC regulation and is overexpressed in some types of AML (Rybka *et al.*, 2015, Monlish *et al.*, 2016) and so it is worth considering whether a TLR-NFAT axis is as important in oncogenesis as in mature myeloid cell function.

Broadly speaking, NFAT proteins have a greater role in less differentiated myeloid cells (see Figure 1-4) and might also be important in the differentiation status of AML. It could also be inferred that each family member is non-redundant and so further investigation into individual roles is warranted. Ultimately, given the distorted nature of the haemopoietic hierarchy in AML (Pollyea and Jordan, 2017) these are only inferences from healthy cells and should be examined more closely in leukaemia tissue.

1.6.3 *NFAT*s in AML

There is growing evidence that NFAT signalling cooperates with mutations of the FLT3 receptor in AML. *FLT3*^{ITD} is present in around 25% of AML cases and confers particularly poor outcomes for patients compared to other AML subtypes (Lagunas-Rangel and Chávez-Valencia, 2017). This is a gain-of-function mutation which causes ligand-independent proliferative signalling (Chan, 2011).

Exogenous expression of *Flt3*^{ITD}/*FLT3*^{ITD} in haemopoietic cells has been shown to induce a myeloproliferative disease and it is understood to require other driver mutations to induce overt AML (Kelly *et al.*, 2002, Solovey *et al.*, 2019). In one of these models co-expression of *Flt3*^{ITD} with a constitutively active form of human *NFATC1* led to the rapid development of myeloid leukaemia and expansion of immature blasts *in vivo*. Interestingly the expression of constitutive *NFATC1* alone inhibited the colony forming capacity of sorted Lin-Sca1+c-kit+ (LSK) BM cells, but *Flt3*^{ITD} co-expression increased colony formation dramatically, more than *Flt3*^{ITD} alone (Solovey *et al.*, 2019).

The observed phenotypes imply that NFATc1 has an inhibitory effect on expansion of primitive LSK cells, in parallel to the studies conducted in GMPs (Fric *et al.*, 2012a, Fric *et al.*, 2014). Constitutively active FLT3 signalling appears to supersede this and the cooperativity with NFAT induces a distinct transcriptional

program permissive of AML development (Solovey *et al.*, 2019). Signalling downstream of *FLT3*^{ITD} is different from that of the normal FLT3 receptor, as has been demonstrated in murine haemopoietic cells with aberrant activation of STAT5 (Rocnik *et al.*, 2006). One possibility is that engagement of pathological signalling by *FLT3*^{ITD} may influence the recruitment of other factors to transcriptional complexes containing NFATc1. However, this model is an artificial representation of AML and does not reflect on the true ontogeny of leukaemia. Evidence from relapsed AML patients suggests that *FLT3*^{ITD} often arises as a later event and is not consistently found in the founding LSC clone (Levis and Small, 2003), which should be borne in mind when considering NFAT as an effective therapeutic target.

NFATc1 activity can also mediate resistance to TKI. *FLT3*^{ITD} AML can be treated with TKIs such as sorafenib and quizartinib but point mutations and/or 'escape' signalling pathways often lead to resistance and relapse (Fathi and Chen, 2011). Metzelder *et al*. demonstrated that depletion of *NFATC1* by shRNA or NFATc1 functional inhibition with CsA or VIVIT treatment could increase sensitivity of *FLT3*^{ITD} AML cells to sorafenib. Expression of a constitutively nuclear NFATc1 with *FLT3*^{ITD} in myeloid progenitor cells increased resistance to sorafenib and also induced morphological signs of de-differentiation (Metzelder *et al.*, 2015). It is not clear whether NFATc1 and *FLT3*^{ITD} cooperativity activate a specific resistance mechanism, which permit *FLT3*^{ITD} blasts to escape sorafenib-mediated cell death. The reversal of cell maturation may also highlight a pathogenic role of NFATc1 in maintaining stem cell-like properties, akin to the high expression of NFATc1-3 observed in in normal HSCs (Kiani *et al.*, 2004, Kiani *et al.*, 2007).

Resistance to TKIs in CML was also found to be linked to NFAT activity. CML is characterised by the *BCR-ABL1* fusion oncogene, which is effectively targeted by the TKI imatinib. As with FLT3 inhibitors, resistance to imatinib can arise through a number of mechanisms, including BCR-ABL mutations and receptor-independent means (Valent, 2007). Gregory *et al*. identified NFAT-stimulated autocrine IL-4 signalling as a mechanism of imatinib resistance and the effect was modulated primarily by NFATc1 (Gregory *et al.*, 2010). IL-4 is an established regulatory target of NFAT in the function of various immune cells (Fric *et al.*, 2012b). Sung et al. found that AML cells can increase resistance to FLT3^{ITD} inhibition by autocrine stimulation with various cytokines, including IL-6 and GM-CSF, which are also

targets of NFAT in some myeloid lineage cells (Fric *et al.*, 2012b, Sung *et al.*, 2019). Based on the evidence available investigation into the role of NFAT in autocrine cytokine signalling in AML may yield further insight into the mechanism(s) of resistance to FLT3 inhibitors.

Resistance to therapy, be it FLT3 inhibitors or otherwise, is a common cause of relapse in AML (Yeung and Radich, 2017), with evidence so far focusing on TKIs and *FLT3*^{ITD} AML.

Chemotherapy primarily targets cycling cells and so is often evaded in AML by subclones that are more quiescent and/or plastic in their state of differentiation, like the LSC population. However, the ability of the LSCs to persist through treatment and regenerate AML blasts is highly multi-dimensional, depending on the interaction of epigenetic and transcriptional regulators, evasion of the immune response and interaction with BM microenvironment (Yeung and Radich, 2017, van Gils *et al.*, 2021). The evidence discussed shows that NFAT can regulate cycle genes and stem cell properties in myeloid physiology and pathology, and so could plausibly have roles in mediating chemotherapy resistance or LSC development, but its precise role in this complex interplay is not yet clear.

The role of NFAT transcriptional partners may aid the generation of a more complete picture of the active regulatory networks in AML. For example, RUNX1 may cooperate with *FLT3*^{ITD} in the development of AML (Behrens *et al.*, 2017) and is also known to regulate key oncogenes, such as p53 (Takei and Kobayashi, 2019). RUNX1 somatic mutations and chromosomal translocations are well characterised in AML (Sood *et al.*, 2017). Masuda *et al.* demonstrated that RUNX proteins regulate *NFATC2* transcription and this was inhibited by the RUNX inhibitor Chb-M' in their models of AML, particularly in APL (Masuda *et al.*, 2020), suggesting that *NFATC2* could play a role in the mechanism of RUNX-driven oncogenesis here. NFAT was also found to interact with promyelocytic leukaemia (PML) protein - a tumour suppressor frequently disrupted in APL – in fibroblasts (Mu *et al.*, 1994, Lo *et al.*, 2008). Further investigation of these transcriptional partners may also highlight a novel role for NFAT in APL pathogenesis. Various other transcriptional partners of NFAT are known to be deregulated in AML, such as AP-1 proteins (Takahashi, 2006, Ptasinska *et al.*, 2019) and C/EBPα (Paz-Priel and Friedman, 2011), although their intrinsic involvement with NFAT has not been demonstrated

in this context. A focused investigation into their relationship with NFAT in AML may yield novel mechanisms of action and/or means of targeting NFAT activity.

At present there is a lack of evidence around whether NFAT proteins mediate leukaemia initiation or participate in maintenance in tandem with other mutational drivers. Existing models focus on *FLT3*^{ITD}-driven signalling and are based primarily on synthetic models of AML, which do not necessarily reflect the complex clonal architecture or molecular heterogeneity of *de novo* leukaemogenesis. Additionally, most studies present evidence for NFATc1 activity or are based on inhibition of all NFAT or calcineurin activity, in the absence of more specific compounds. Evidence from solid tumours suggests that individual members of the *NFAT* family have distinct and sometimes opposing roles in regulation of the cell cycle (Mognol *et al.*, 2016). It is reasonable to postulate that each NFAT family member may contribute differentially to AML pathogenesis, and should be investigated as such. It should also be noted that functional variants of *NFAT* genes are not commonly found, although not absent, as shown by mutational profiling of large AML patient datasets (Ley *et al.*, 2013, Tyner *et al.*, 2018). In light of the evidence available, there are some considerations for future therapeutic strategies to target NFAT signalling in AML.

1.6.4 Therapeutic targeting of NFATs

CsA, tacrolimus and VIVIT peptide have served as key inhibitors for experimental research into *NFAT* but their clinical application is quite limited. Calcineurin, the target of CsA, has a number of targets other than NFAT which are less well characterised (Li *et al.*, 2011a). Clinical use of CsA in organ transplant patients is associated with significant nephrotoxicity and neurotoxicity, due to some of these other targets and the role of NFAT proteins in the nervous and cardiovascular systems (Tedesco and Haragsim, 2012). Tacrolimus has even higher toxicity but some evidence suggests that lower doses could be well-tolerated by patients (Klintmalm, 1994, Spiekerkoetter *et al.*, 2017), although this would still carry the issue of non-specificity towards NFAT. CsA is also known to inhibit P-glycoprotein (Pgp), which can increase cellular efflux of some chemotherapeutics and reduce their efficacy. One randomised controlled trial of patients with poor risk AML (n=226) found that intravenous CsA treatment improved overall survival, although this was linked with inhibition of Pgp and so potentially not connected to NFAT

activity (List *et al.*, 2001). However, highly toxic chemotherapy regimens are not well tolerated by cohorts of older AML patients and so more targeted drugs would be advantageous.

VIVIT has the advantage of targeting the calcineurin-NFAT interaction specifically. It has been developed to be cell permeable, stable in the circulation (half-life = 30 hr) and is capable of inhibiting T cell function in mice (Noguchi *et al.*, 2004). There is currently no clinical data regarding VIVIT, however some *in vivo* data in cardiovascular disease models suggest that its pharmacological properties are undesirable for application to patients (Yu *et al.*, 2007). There are various experimental compounds which target other elements of NFAT function. The salicylic acid derivative UR-1505 specifically blocks NFAT binding to DNA and was found to be an effective immunosuppressant (Román *et al.*, 2007), but its efficacy translated poorly to the clinic as a dermatitis therapy, particularly when compared with tacrolimus (Vives *et al.*, 2015). Based on extremely limited clinical information there is clearly a need to develop NFAT-targeted therapy further in order to progress research into its viability.

Recent research has identified novel means of targeting specific *NFAT* family members. A novel calcineurin-binding region (CNBR) is present in the N-terminus of some NFATs, while other binding regions have variable binding affinities for calcineurin between NFATc1-4, meaning that it could be possible to preferentially target some of the *NFAT* family members therapeutically. For example, it may be possible to specifically inhibit the interaction of calcineurin with either NFATc1 and NFATc4 by targeting CNBR3, but no such inhibitor exists presently (Kitamura and Kaminuma, 2021). More broadly, therapeutic targeting of TFs has been shown to be challenging, although inhibitors of the related Rel protein NF-κB are in early clinical trials for the treatment of AML and other cancers (Ramadass *et al.*, 2020). Some of these inhibitors target nuclear shuttling, DNA binding and downstream targets of NF-κB, which could be applied similarly for inhibition of NFAT in a clinical setting. It may therefore be possible to target nuclear import/export kinases, targets of NFAT and/or transcriptional partners of NFAT, but further evidence is needed.

Given that NFAT has roles in a number of immune cells the effect(s) of NFAT inhibition on the wider AML microenvironment must also be considered. T cell-

driven immune surveillance is a major defence against the development of cancers, including leukaemias. Often the interface between AML blasts and T cells within the BM microenvironment is distorted in such a way that allows the AML cells to escape immune recognition (Vago and Gojo, 2020). *In vitro* studies have demonstrated either AML cell supernatant or direct AML cell contact suppresses T cell activation, via NFAT signalling specifically (Buggins *et al.*, 2001, van Galen *et al.*, 2019). If suppressed NFAT signalling in T cells is permissive of AML immune evasion, then significant caution should be taken when developing global NFAT inhibition as a means of therapy. This further stresses the need to elucidate the contribution of differing *NFAT* family members to each of the biological processes relevant in AML development, to allow more targeted therapies to be developed.

1.6.5 Hypothesis

At present there is intriguing evidence to implicate NFAT proteins in AML. By looking at their roles in normal myeloid physiology and in other types of cancer it is conceivable that NFAT regulates the transcription of key cell cycle and/or differentiation programs in leukaemogenesis. Furthermore, NFAT has been observed to play a role in resistance to TKIs in myeloid leukaemias and may mediate patient relapse. However, it is still to be ascertained whether *NFAT* is important in the context of some mutational profiles – as with *FLT3*^{ITD} – or if its oncogenic properties are applicable across numerous AML subtypes.

Recent evidence identified *NFATC2* as a key target of *KDM4A*, which is known to be essential for AML cells, in a model of MLL-AF9 AML. Together with the available data it seems plausible that *NFATC2* could be essential for the survival and oncogenic function of AML cells of this subtype and other subtypes. This study was designed to test this hypothesis.

1.6.6 Study aims

1. Identify suitable *in vitro* models to investigate the relationship of *NFATC2* and AML cell pathobiology by characterising *NFATC2*/NFATc2 expression and basic function in selected AML cell lines.
2. Determine the phenotype of AML cells after overexpression of *NFATC2* as a method of elucidating its function in these cells.
3. Assess the dependence of AML cells on calcineurin-NFAT signalling by treating cell lines with established inhibitors of this pathway.
4. Measure the dependence of AML cells on *NFATC2* specifically by shRNA KD of *NFATC2* in AML cell lines. Determine the function(s) of *NFATC2* in these cells by measuring the cell phenotype after *NFATC2* KD.
5. Characterise the global transcriptional consequences of *NFATC2* KD in AML cells using RNA sequencing (RNA-Seq).
6. Identify DNA binding targets of NFATc2 in AML cells using ChIP sequencing (ChIP-Seq). Combine with RNA-Seq data to ascertain functional targets of *NFATC2*.
7. Determine the relationship of *NFATC2* expression with AML patients' clinical outcome and disease subtype using open-source datasets. Additionally, investigate these relationships for the putative *NFATC2* targets identified in aims 5&6.

2 Materials and Methods

2.1 Materials

Detailed lists of suppliers and external sequencing providers are given in the digital appendix. A list of general plasticware and glassware used is also given.

2.1.1 Equipment

Equipment	Supplier
SpectraMax® M5 Plate Reader	Molecular Devices
Eppendorf® Thermomixer Compact	Merck
NanoDrop™ 1000 Spectrophotometer	LabTech
Mini-Sub Cell Gel Tank Systems	Bio-Rad
PowerPac™ Basic/HC Power Supply	Bio-Rad
Mini Gel Tank	TFS
Odyssey Imaging System	LI-COR®
Zeiss Axioimager M1 Epifluorescence and Brightfield Microscope	Zeiss
MidiMACS™ Separator	Miltenyi Biotec
MACS® magnetic stand	Miltenyi Biotec
FACSCanto™ II	BD Biosciences
FACSAria™ III	BD Biosciences
ProFlex™ Thermal Cycler	TFS
QuantStudio™ 7 Pro	TFS
Biomark™ HD	Fluidigm®
Biomark™ IFC Controller MX	Fluidigm®
2100 Bioanalyzer Instrument	Agilent
EpiShearTM Probe Sonicator	ActiveMotif®

2.1.2 Web tools and software platforms

Tool/software name	Version	Function	Additional information
Microsoft Office	2110	Word processing (Word), image design (PowerPoint), data processing (Excel)	-
GraphPad Prism	8.0.2	Data analysis, graphic design	-
SnapGene® Viewer	5.0.6	Chromatogram visualisation	-
EMBOSS Needle	-	Global alignment of paired DNA sequences	(Needleman and Wunsch, 1970) https://www.ebi.ac.uk/Tools/psa/emboss_needle/
ImageJ	1.53k	Measure object area in images	-
FACSDiva™	-	Acquire and analyse flow cytometry data	-
SoftMax® Pro Software	-	Acquire plate spectrophotometer data	-
FlowJo	10.5.3	Analysing flow cytometry data	-
ImageStudio Lite	5.2	Analyse imaging data from LI-COR Odyssey Imaging System	-
RStudio	1.1.456	Various functions: see 2.1.4	-
Galaxy	-	Various functions: see 2.1.4	http://heighliner.cvr.gla.ac.uk/
Protein Molecular Weight (MW)	-	Estimate protein MW from sequence	https://www.bioinformatics.org/sms/prot_mw.html
ENSEMBL Gene ID to Gene Symbol Converter	-	Convert ENSEMBL gene IDs to gene symbols	https://www.biotools.fr/human/ensembl_symbol_converter
STRING Database	11.5	Predicts protein-protein interactions through known associations	https://string-db.org/ (Szklarczyk *et al.*, 2021)
DAVID Bioinformatics Resources	6.8	Multiple, including functional annotation and conversion of gene IDs between nomenclatures	https://david.ncifcrf.gov/
Gene Set Enrichment Analysis (GSEA)	4.1.0	Identify pathways containing genes which are enriched in a set of data	(Subramanian *et al.*, 2005)
KEGG	-	Repository of known molecular pathways	https://www.genome.jp/kegg/pathway.html

PANTHER Classification System	-	Identifies enrichment of a gene list in known PANTHER, gene ontology (GO) or Reactome pathways	http://www.pantherdb.org/
Reactome	-	Identifies enrichment of a gene list in known pathways, which some visual interactive features	https://reactome.org/
MEME-ChIP	5.4.1 (MEME Suite)	Identification of novel DNA motifs in a set of provided sequences	https://meme-suite.org/meme/tools/meme-chip (Machanick and Bailey, 2011)
TOMTOM	5.4.1 (MEME Suite)	Aligns a set of motifs to known motifs	https://meme-suite.org/meme/tools/tomtom
Axiovision Rel 4.8	-	Acquisition and imaging from Zeiss Axioimager microscope	-
Fluidigm® Real-Time PCR Analysis Software	3.0.2	Analysis of multiplex qRT-PCR data from Fluidigm® BioMark™	-
BioMark HD Data Collection Software	3.1.2	Acquisition of multiplex qRT-PCR data from Fluidigm® BioMark™	-
NCBI Primer-BLAST	-	Designs primers to specifications against a specified sequence	https://www.ncbi.nlm.nih.gov/tools/primer-blast/
NCBI BLAST® (BLASTn)	-	Matches query nucleotide sequences to known sequences	https://blast.ncbi.nlm.nih.gov/Blast.cgi
2100 Expert	B.02.10.SI764	Analysis of data from 2100 Bioanalyzer platform	-
Biorender	-	Provision of cartoons/icons for diagrams	https://biorender.com/
Inkscape	1.0.2	Open-source graphics editor	-

2.1.3 R and Galaxy Packages

Package name	R/Galaxy access	Version (Galaxy or R)
dplyr	R	1.0.7
stats	R	4.0.3
VennDiagram	R	1.7.1
ggplot2	R	3.3.5
SPIA	R	2.42.0
edgeR	R	3.32.1
SummarizedExperiment	R	1.20.0
Readxl	R	1.3.1
stringr	R	1.4.0
gplots	R	3.1.1
RColorBrewer	R	1.1-2
Trimmomatic	Galaxy	(G) 0.36.5
BWA-MEM	Galaxy	(G) 0.7.17.1
samtools	Galaxy	1.3.1
SortSam	Galaxy	(G) 2.18.2.0
MACS	Galaxy	(G) 2.1.1.20160309.3
ChIPseeker	Galaxy R	(G) 1.18.0+galaxy1 (R) 1.26.0
GenomicRanges	R	1.42.0
ChIPQC	R	1.26.0
DiffBind	R	3.0.15
metagene2	R	1.6.1
GenomicFeatures	R	1.42.3
Biostrings	R	2.58.0
corrplot	R	0.92

2.1.4 Databases

Database source(s)	**Dataset**	**Means of access**
GDC Database (https://portal.gdc.cancer.gov/), (Ley *et al.*, 2013)	TCGA-LAML	*TCGABiolinks* R package and publication supplementary information
(Tyner *et al.*, 2018)	BEAT-AML	Publication supplementary information
GDC Database (https://portal.gdc.cancer.gov/)	TARGET-AML	*TCGABiolinks* R package and GDC portal directly
Gene expression omnibus (GEO) https://www.ncbi.nlm.nih.gov/geo/	GSE83533	Downloaded from GEO directly

2.1.5 Cells, reagents and other consumables

2.1.5.1 Cell culture

Reagent	Supplier	Catalogue #
Roswell Park Memorial Institute (RPMI) 1640 Medium, no glutamine	TFS	31870025
Dulbecco's Modified Eagle Medium (DMEM), high glucose, pyruvate, no glutamine	TFS	21969035
Iscove's Modified Dulbecco's Medium (IMDM)	TFS	12440053
Trypsin-EDTA (0.25%), phenol red	TFS	25200072
Fetal Bovine Serum, qualified, heat inactivated, Brazil	TFS	10500064
L-glutamine (200 mM)	TFS	25030024
Penicillin-Streptomycin (10,000 U/mL)	TFS	15140122
Hygromycin B (50 mg/mL)	TFS	10687010
Diphtheria Toxin from *Corynebacterium diphtheriae*	Merck	D0564
MycoAlert™ Mycoplasma Detection Kit	Lonza	LT07-418
MethoCult™ H4230 Methylcellulose-Based Medium	StemCell™ Technologies	04230
MethoCult™ M3231 Methylcellulose-Based Medium	StemCell™ Technologies	03231
Recombinant Murine (m)IL-3	PeproTech	213-13
Recombinant mIL-6	PeproTech	216-16
Recombinant mGM-CSF	PeproTech	315-03
Recombinant mSCF	PeproTech	250-03

2.1.5.2 Chemical reagents

Reagent/material	Supplier	Catalogue #
Ethanol (Absolute)	VWR	20821.330
2-Propanol (Absolute)	Fisher Scientific	24137
Methanol (Absolute)	Fisher Scientific	24229
Dimethyl sulphoxide (DMSO)	Merck	D8418
N,N-Dimethylformamide (DMF)	Merck	D-4551
Phosphate-buffered saline tablets (PBS)	TFS	BR0014G
Hanks-buffered saline solution (HBSS) 10X	TFS	14065-049
Potassium acetate (CH_3CO_2K)	Merck	P1190
Calcium chloride ($CaCl_2$) dihydrate	Merck	C8106
Manganese(II) chloride ($MnCl_2$) tetrahydrate	Merck	M3634
Rubidium chloride (RbCl)	Merck	R2252
Glycerol ($C_3H_8O_3$)	Merck	G5516
MOPS ($C_7H_{15}NO_4S$)	Merck	M1254
Glacial Acetic acid (CH_2O)	VWR	20104.334

Potassium hydroxide (KOH)	Merck	221473
Magnesium sulfate ($MgSO_4$) heptahydrate	Merck	230391
Potassium chloride (KCl)	Merck	P9541
D-(+)-Glucose	Merck	G7528
Sodium hydroxide (NaOH)	Merck	S5881
Agarose ($C_{24}H_{38}O_{19}$)	Merck	A9539
Sigma 7-9® ($C_4H_{11}NO_3$)	Merck	T1378
EDTA ($C_{10}H_{16}N_2O_8$), anhydrous	Merck	EDS
Polyethylinimine (PEI)	Fisher Scientific	23966
Polybrene Infection / Transfection Reagent (hexadimethrine bromide)	Merck	TR-1003-vG
Trypan Blue	Merck	T6146
Bovine serum albumin (BSA) Fraction V	Merck	10735086001
May-Grünwald stain	Merck	MG500
Giemsa stain	Merck	48900
Pertex® Mounting Medium	Histolab	00801
ß-mercaptoethanol	Merck	M6250
Diisopropyl fluorophosphate (DIFP)	Merck	D0879
HEPES 1M	TFS	15630-080
Magnesium chloride ($MgCl_2$) Hexahydrate	Merck	M2393
Triton X-100	Merck	93443
IGEPAL CA-630 (NP-40)	Merck	I8896
Sodium deoxycholate	Merck	D6750
Sodium dodecyl sulphate (SDS)	Merck	L5750
Sodium chloride (NaCl)	Merck	1.06404.1000
Sodium fluoride (NaF)	Merck	S7920
cOmplete™ ULTRA Tablets, EDTA-free, glass vials Protease Inhibitor Cocktail (PIC)	Merck	5892953001
PhosSTOP™	Merck	4906837001
TWEEN® 20	Merck	P2287
Ovalbumin	Merck	A5503
Lithium chloride (LiCl)	Merck	L9650
Agar	Merck	A1296
Formaldehyde solution	Merck	47608
Puromycin dihydrochloride	Merck	P9620
Ampicillin sodium salt	Merck	A0166
Rely+On™ Virkon Powder	VWR	148-0202
Dithiothreitol (DTT)	Merck	10708984001
Resazurin salt	Merck	R7017
Ponceau S	Merck	141194
Monopotassium phosphate (KH_2PO_4)	Merck	60229
Disodium phosphate (Na_2HPO_4)	Merck	1.06585
Dipotassium phosphate (K_2HPO_4)	Merck	P3786
DNase I, Bovine Pancreas	Merck	260913
Saponin	Merck	558255

2.1.5.3 Restriction enzymes

Enzyme	Cut site	Supplier	Catalogue #
BamHI-HF®	5'-GGATCC-3' 3'-CCTAGG-5'	NEB	R3136
EcoRI-HF®	5'-GAATTC-3' 3'-CTTAAG-5'	NEB	R3101
NdeI	5'-CATATG-3' 3'-GTATAC-5'	NEB	R0111
NotI-HF®	5'-GCGGCCGC-3' 3'-CGCCGGCG-5'	NEB	R3189

2.1.5.4 Molecular biology and virus production

Reagent/material	Supplier	Catalogue #
SYBR™ Safe DNA Gel Stain	TFS	S33102
1 kb Plus DNA ladder	NEB	N3200
Gel Loading Dye, Purple (6X)	NEB	B7024
Polybrene Infection/Transfection Reagent	Merck	TR-1003
Plasmid Mini Kit	QIAGEN	12123
Plasmid Maxi Kit	QIAGEN	12162
QIAquick PCR Purification Kit	QIAGEN	28104
RNeasy Plus Mini Kit	QIAGEN	74104
RNeasy Plus Micro Kit	QIAGEN	74034
QIAshredder	QIAGEN	79656
SuperScript™ IV Reverse Transcriptase	TFS	18090010
Random Hexamers (50 µM)	TFS	N8080127
deoxynucleoside triphosphate (dNTP) Mix (10 Mm)	TFS	R0191
DTT (dithioethreitol) (0.1 M)	TFS	Y00147
RNaseOUT™ Recombinant Ribonuclease Inhibitor (40 U/µL)	TFS	10777019
Proteinase K, recombinant, PCR grade	TFS	EO0492
PowerUp SYBR™ Green Master Mix	TFS	A25743

2.1.5.5 Multiplexed qRT-PCR

Reagent/material	Supplier	Catalogue #
96.96 Dynamic Array™ IFC for Gene Expression	Fluidigm®	BMK-M-96.96
GE 96.96 Dynamic Array DNA Binding Dye Reagent Kit with Control Line Fluid	Fluidigm®	100-3415
2X SsoFast EvaGreen Supermix with Low ROX	Bio-Rad	172-5211
20X DNA Binding Dye Sample Loading Reagent	Fluidigm®	100-0388
QIAGEN Multiplex PCR Plus Kit	QIAGEN	206152
T7 Exonuclease	NEB	M0263

2.1.5.6 Agilent kits

Reagent/material	Supplier	Catalogue #
RNA 6000 Nano Kit	Agilent	5067-1511
DNA 1000 Kit	Agilent	5067-1504

2.1.5.7 ChIP-Seq

Reagent/material	Supplier	Catalogue #
IPure kit V2	Diagenode	C03010015
AMPure XP for PCR Purification	Beckman Coulter	A63880
MicroPlex Library Preparation Kit v2 (12 indexes)	Diagenode	C05010012
Dynabeads® Protein G	TFS	10003D
Qubit® dsDNA HS Assay Kit	TFS	Q32851
NFAT1 (D43B1) XP® Rabbit mAb	CST	5861
Rabbit IgG antibody	Diagenode	C15410206
Anti-Histone H3 antibody (Rabbit pAb)	Abcam	ab1791

2.1.5.8 Compounds and inhibitors

Inhibitor	Solvent required	Supplier	Catalogue #
cyclosporine A (CsA)	DMSO	Merck	30024
NFAT Inhibitor, Cell Permeable (VIVIT-11R)	H_2O	Tocris	592517-80-1
INCA-6	DMSO	Tocris	3519-82-2
U73122	DMF*	Tocris	112648-68-7
ionomycin calcium salt	DMSO	Merck	I3909
phorbol 12-myristate 13-acetate (PMA)	DMSO	Fisher Scientific	BMLPE1350005
cytarabine (U-19920A)	DMSO	SelleckChem	S1648

*U73122 was dissolved in DMF in a water bath at 50°C.

2.1.5.9 Flow cytometry antibodies and reagents

Reagent/material	Supplier	Catalogue #
BD Pharmingen™ FITC Annexin V	BD Biosciences	556420
BD Pharmingen™ APC Annexin V	BD Biosciences	550474
BD Pharmingen™ 4',6-diamidino-2-phenylindole (DAPI) Solution	BD Biosciences	564907
Annexin binding buffer (10X)	BD Biosciences	51-6612EBD
Propidium iodide (PI)	TFS	P1304MP
Ribonuclease (RNase) A from bovine pancreas	Merck	R6513
UltraComp eBeads™ Plus Compensation Beads	TFS	01-3333-41
CellTrace™ CFSE (carboxyfluorescein succinimidyl ester) Cell Proliferation Kit	TFS	C34554
PerCP-Cy™5.5 Rat Anti-Mouse CD117, Clone 2B8 (RUO)	BD Biosciences	560557
5-Bromo-2'-Deoxyuridine (BrdU)	TFS	B23151
BrdU Monoclonal Antibody (BU20A), APC, eBioscience™	TFS	17507141

2.1.5.10 Primary antibodies for Western blot or IF

Reagent/material	Supplier	Catalogue #
NFAT1 (D43B1) XP® Rabbit monoclonal antibody (mAb)**	CST	5861
NFATc1 mAb (7A6), Mouse	TFS	MA3-024
Phospho- (p-)NFATC2 (Ser54) polyclonal antibody (pAb), rabbit	TFS	44-944G
B-actin (8H10D10) Mouse mAb	CST	3700
B-actin (D6A8) Rabbit mAb	CST	4970
B-tubulin Antibody, Rabbit	CST	2146
Lamin A/C Antibody, Rabbi	CST	2032
Tri-Methyl-Histone H3 (Lys9) (D4W1U) Rabbit mAb	CST	13969
Tri-Methyl-Histone H3 (Lys27) (C36B11) Rabbit mAb	CST	9733
Histone H3 (1B1B2) Mouse mAb	CST	14269
PARP (46D11) Rabbit mAb	CST	9532
Cleaved PARP (Asp214) (D64E10) XP® Rabbit mAb	CST	5625
Histone H2AX (D17A3) XP® Rabbit mAb	CST	7631
Phospho- (p-)H2AX^{ser139} Rabbit mAb	CST	2577
STK33 (D3S4R) Rabbit mAb	CST	95343
c-Myc (N-262), Rabbit pAb	Santa Cruz	sc-764

**Already described for ChIP-Seq

2.1.5.11 Secondary antibodies for Western blotting

Reagent/material	Supplier	Catalogue #
IRDye® 680RD Goat anti-Rabbit IgG (H+L)	LI-COR Biosciences	926-68071
IRDye® 800RD Donkey anti-Mouse IgG (H+L)	LI-COR Biosciences	926-32212

2.1.5.12 Secondary antibodies for IF

Reagent/material	Supplier	Catalogue #
Goat anti-Mouse IgG (H+L), Cross-Adsorbed Secondary Antibody, Alexa Fluor® 488	TFS	A-11001
Goat anti-Rabbit IgG (H+L) Cross-Adsorbed Secondary Antibody, Alexa Fluor® 488	TFS	A-11008

2.1.5.13 Other materials for protein-based work

Reagent/material	Supplier	Catalogue #
NuPAGE™ 4 to 12%, Bis-Tris, 1.0 mm, Mini Protein Gel, 10-well	TFS	NP0321BOX
NuPAGE™ 4 to 12%, Bis-Tris, 1.0 mm, Mini Protein Gel, 12-well	TFS	NP0322PK2
NuPAGE™ 4 to 12%, Bis-Tris, 1.5 mm, Mini Protein Gel, 15-well	TFS	NP0336BOX
Nitrocellulose Membrane, 0.45 µm, 30 cm x 3.5 m	TFS	88018
Western Blotting Filter Paper	TFS	84784
NuPAGE™ LDS Sample Buffer (4X)	TFS	NP0007
NuPAGE™ Sample Reducing Agent (10X)	TFS	NP0009
NuPAGE™ MOPS SDS Running Buffer (20X)	TFS	NP0001
ReBlot Plus Strong Antibody Stripping Solution, 10x	Merck	2504
ProLong™ Diamond Antifade Mountant with DAPI	TFS	P36962
Carl Zeiss™ Immersol™ Immersion Oil 518F	Zeiss	10690586
CD117 MicroBeads, mouse	Miltenyi Biotec	130-091-224
Pierce™ Coomassie (Bradford) Protein Assay Kit	TFS	23200
Pierce™ BCA Protein Assay Kit	TFS	23225
Poly-L-lysine	Merck	P4832

2.1.6 Buffer and solution preparations

2.1.6.1 General and miscellaneous buffers/solutions

Tris-acetate-EDTA (TAE) buffer (10X)	
Reagent	**Concentration for 10X**
Sigma 7-9®	400 mM
Acetic acid	1.14% (v/v)
EDTA (solution at pH 8.0)	10 mM

'MACS' buffer	
Reagent	**Final concentration**
BSA	0.5% (w/v)
EDTA	2 mM

These were dissolved in PBS (pH 7.2).

Sorensen's phosphate buffer (CSH, 2010)	
Reagent	**Buffer concentration (each)**
Monopotassium phosphate (KH_2PO_4)	0.133 M
Disodium phosphate (Na_2HPO_4)	0.133 M

These were dissolved in H_2O and mixed in a 3:7 volumetric ratio to achieve pH 7.2.

2.1.6.2 Bacterial growth (buffers and cells)

Reagent/material	Supplier	Catalogue #
One Shot™ Stbl3™ Chemically Competent *E. coli*	TFS	C737303

LB growth medium	
Reagent	**Final concentration**
Tryptone	1% (w/v)
Sodium chloride (NaCl)	0.5% (w/v)
Yeast extract	0.5% (w/v)

Growth medium was then autoclaved to 121°C for 20 min.

Stbl3™ buffer 1	
Reagent	**Final concentration**
Potassium acetate (CH_3CO_2K)	30 mM
Calcium chloride ($CaCl_2$)	10 mM
Manganese(II) chloride ($MnCl_2$)	50 mM
Rubidium chloride (RbCl)	100 mM
Glycerol	15% (v/v)

Final buffer was adjusted to pH 5.8 using acetic acid (CH_3COOH) and filter sterilised using a 0.45 µM Filtropur vacuum filtration unit (Sarstedt).

Stbl3™ buffer 2	
Reagent	**Final concentration**
MOPS	10 mM
Calcium chloride ($CaCl_2$)	75 mM
Rubidium chloride (RbCl)	10 mM
Glycerol	15% (v/v)

Final buffer was adjusted to pH 6.5 using potassium hydroxide (KOH) and filter sterilised using a 0.45 µM Filtropur vacuum filtration unit (Sarstedt).

SOC medium	
Reagent	**Final concentration**
Tryptone	2% (w/v)
Yeast extract	0.5% (w/v)
Sodium chloride (NaCl)	0.05% (w/v)
Potassium chloride (KCl)	2.5 mM
Magnesium chloride ($MgCl_2$)	10 mM
Glucose	20 mM

This medium was made in the following order:

1. Tryptone, yeast extract and sodium chloride were dissolved in 80% final volume of H_2O.
2. KCl solution was added and adjusted to pH 7.0 using 5N NaOH.
3. Solution autoclaved at 121°C for 20 min.
4. $MgCl_2$ solution, which had been autoclaved to 121°C for 20 min, was added to the solution.
5. Glucose solution, which had been filter sterilised using a 0.22 µM syringe filter (Fisher Scientific™), was added.
6. H_2O added to final volume.

LB agar plates (with ampicillin)	
Reagent	**Final concentration**
Tryptone	0.50% (w/v)
Yeast extract	0.25% (w/v)
Sodium chloride (NaCl)	0.50% (w/v)
Agar	0.75% (w/v)
Ampicillin	100 µg/mL

The solution was autoclaved to 121°C for 20 min and then allowed to cool to no less than 55°C, to prevent setting, before the addition of ampicillin. Note that ampicillin was prepared as a 1000X solution, dissolved in ethanol. Agar solution was poured into 10cm^2 Petri dishes (Greiner Bio-One) and allowed to set inside a laminar flow hood. Dishes were stored at 4°C for a maximum of 4 weeks.

Terrific broth growth medium (with ampicillin)	
Reagent	**Final concentration**
Tryptone	1.2% (w/v)
Yeast extract	2.4% (w/v)
Glycerol	0.4% (v/v)
Monopotassium phosphate (KH_2PO_4)	17 mM
Dipotassium phosphate (K_2HPO_4)	72 mM
Ampicillin	100 µg/mL

Terrific broth was prepared as follows:

1. Tryptone, yeast extract and glycerol were dissolved in 90% the final volume of H_2O.
2. Both potassium phosphates were dissolved in $1/10^{th}$ the final volume of H_2O.
3. Both solutions were autoclaved at 121°C for 20 min.
4. The solutions were combined to make up the final volume.
5. Ampicillin was added once the broth had cooled to room temperature (RT). Broth was stored at 4°C for a maximum of 4 weeks

2.1.6.3 Protein lysis

RIPA buffer for protein lysis	
Reagent	**Final concentration**
NP-40	1% (v/v)
Sodium deoxycholate	1% (w/v)
SDS	0.1% (w/v)
Tris (pH 7.4)	25 mM
Sodium chloride (NaCl)	150 mM
Sodium fluoride (NaF)	10 mM
Protease inhibitor cocktail (PIC)	1X
PhosSTOP™	1X
Diisopropyl fluorophosphate (DIFP)	0.1 mM

Hypotonic buffer for protein lysis (cytoplasmic fraction)	
Reagent	**Final concentration**
HEPES	20 mM
Potassium chloride (KCl)	10 mM
Magnesium chloride ($MgCl_2$)	1 mM
Triton X-100	0.1% (v/v)
Glycerol	20% (v/v)

2.1.6.4 Flow cytometry (BrdU buffers)

Fixation/permeabilisation buffer for BrdU staining	
Reagent	**Final concentration**
Formaldehyde	4% (v/v)
Saponin	1% (w/v)

Freezing buffer for BrdU staining	
Reagent	**Final concentration**
FBS	90% (v/v)
DMSO	10% (v/v)

Wash/permeabilisation buffer for BrdU staining	
Reagent	**Final concentration**
TWEEN® 20	0.05% (v/v)
BSA	1% (v/v)

Dissolved in PBS.

2.1.6.5 Western blotting

Transfer buffer (20X)	
Reagent	**Final concentration**
Tris-HCl (pH 7.6)	25 mM
Glycine	192 mM

After diluting stock Transfer buffer in H_2O in 85-90% final volume, methanol was added to a final concentration of 10-15% (v/v), due to its volatile nature.

Ponceau S solution (stock)	
Reagent	**Final concentration**
Ponceau S	0.5% (w/v)
Glacial acetic acid	1% (v/v)

*Stock was diluted 5X in H_2O for use.

Tris-buffered saline (TBS) (10X)	
Reagent	**Final concentration**
Sigma 7-9®	200 mM
NaCl	1500 mM

After dissolving in H_2O the pH was adjusted to 7.6 using up to 1N HCl.

Additionally, to make TBST (1X), TBS was first diluted to 1X solution with TWEEN® 20 added to a final concentration of 0.1% (v/v).

2.1.6.6 Immunofluorescence

IF blocking/antibody solution	
Reagent	**Final concentration**
BSA	5% (w/v)
Ovalbumin	1% (v/v)
Triton-X100	0.2% (v/v)

These reagents were diluted in 1X TBS.

2.1.6.7 ChIP-Seq

All buffers were dissolved in H_2O, then protease inhibitor cocktail (PIC) and diisopropyl fluorophosphate (DIFP) were added immediately before use.

PBS with protease inhibitors	
Reagent	**Final concentration**
Protease inhibitor cocktail (PIC)	1X
Diisopropyl fluorophosphate (DIFP)	0.1 mM

Cytoplasmic lysis buffer (CLB)	
Reagent	**Final concentration**
Tris pH 8.0	10 mM
NaCl	10 mM
NP-40	0.4% (v/v)
PIC	1X
DIFP	0.1 mM

Nuclear lysis buffer (NLB)	
Reagent	**Final concentration**
Tris pH 8.1	50 mM
EDTA	10 mM
SDS	0.8% (w/v)
PIC	1X
DIFP	0.1 mM

Dilution buffer (DB)	
Reagent	**Final concentration**
Tris pH 8.1	20 mM
NaCl	150 mM
EDTA	2 mM
Triton-X100	1% (v/v)
SDS	0.01% (w/v)
PIC	1X
DIFP	0.1 mM

Note: a modified dilution buffer (DB^{MOD}) was created by mixing DB and NLB in a 4:1 ratio.

Wash buffer 1 (WB1)	
Reagent	**Final concentration**
Tris pH 8.1	20 mM
NaCl	150 mM
EDTA	2 mM
Triton-X100	1% (v/v)
SDS	0.1% (w/v)
PIC	1X
DIFP	0.1 mM

Wash buffer 2 (WB2)	
Reagent	**Final concentration**
Tris pH 8.1	20 mM
NaCl	500 mM
EDTA	2 mM
Triton-X100	1% (v/v)
SDS	0.1% (w/v)
PIC	1X
DIFP	0.1 mM

Wash buffer 3 (WB3)	
Reagent	**Final concentration**
Tris pH 8.1	10 mM
LiCl	250 mM
EDTA	1 mM
NP-40	1% (v/v)
Sodium deoxycholate	1% (w/v)
PIC	1X
DIFP	0.1 mM

2.1.7 Primers

2.1.7.1 Plasmid sequencing primers

Name	Forward Primer		Reverse Primer		Backbone/vector target(s)
	Sequence	Melt Temp (˚C)	Sequence	Melt Temp (˚C)	
LNCX	AGCTCGTTTAGTGAACCGTCAGATC	58.5	-	-	pMD2.G (VSVG)
pCAG-F	GCAACGTGCTGGTTATTGTG	55	-	-	psPAX2
SV40pro-F	TATTTATGCAGAGGCCGAGG	54.4	-	-	pMD2.G (VSVG) psPAX2 All pLKO.1 pMIG (o/e m*Nfatc2*) pMIG (o/e h*NFATC2*)
pCDH	-	-	GCATTCCTTTGGCGAGAG	53.9	pMIG (empty)
EXFP-R	-	-	GTCTTGTAGTTGCCGTCGTC	55.8	pMIG (empty) pMIG (o/e m*Nfatc2*) pMIG (o/e h*NFATC2*)
hU6 (LKO.1 5')	GACTATCATATGCTTACCGT	48.9	-	-	All pLKO.1

2.1.7.2 qRT-PCR primers: human target genes

Target	RefSeq	Forward Primer		Reverse Primer		Intron / exon junction	Product Length (bp)	T. Variant Coverage	# possible variants
		Sequence	Melt Temp (NCBI)	Sequence	Melt Temp (NCBI)				
NFATC2	NM_001258296.2	TGAATCCGAACGAAGAACCTC	58.04	TTGGCACCAGGCGATGAG	60.05	Y/Y	123	7, 8	8
NFATC2	NM_001136021.3	CTGGAGTAAGCCGGATCGC	60.30	GTTTGTATCGACCAGCAGCC	59.27	N/N	157	3- 6	8
NFATC2	NM_001258296.2	AAGACGAGCTTGACTTCTCCA	59.04	AGGCTGGTTCGAGGTGACAT	61.19	Y/Y	90	1, 2, 7, 8	8
NFATC2	NM_012340.5	AGACGAGCTTGACTTCTCCATC	59.83	AGACTAGCAAGGGGGCTGTA	59.96	Y/Y	159	1, 2	8
NFATC2	NM_001136021.3	TCTGTGGACCAAGAAGAGCC	59.31	GACATCATCGGGGTATGCGG	60.67	Y/Y	75	3, 4	8
NFATC2	NM_001258294.2	GCGGTAGAGAAGACGGCG	60.28	ATTGGCGAGGTTCTTGGTCC	60.32	Y/Y	171	5, 6	8
NFATC2	NM_001258296.2	CCAAGACGAGCTTGACTTCTC	58.67	TTGGCGAGGTTCTTCGTTCG	60.94	Y/Y	70	7, 8	8
NFATC2	NM_012340.5	ACCCTTGGAGCCCAAAAACA	60.03	CTTTCCGCAGCTCAATGTCG	59.90	Y/N	89	1-8	8
NFATC2	NM_173091.4	AAGTATTACCTGCGGGGGTG	59.46	GTCTGATTTCTGGCAGGAGGT	59.72	Y/N	118	1-8	8
NFATC2 (74050 vector)	N/A	AAGCCACGGTGGATAAGGAC	59.75	ACAGGTGTGCGGATATGCTT	59.75	N/A	88	N/A	8
NFATC1	NM_006162.5	TGT CTG GGA GAT GGA AGC GA	60.61	GTT TTT ATA ATT GGA ACG TTG GCG G	59.94	Y/Y	195	2-6, 10	10
NFATC1	NM_172390.3	TGCAAGCCGAATTCTCTGGTG	61.22	AAAGATGGCGTTACCGTTGG	58.84	Y/Y	156	1, 9	10
NFATC1	NM_172387.3	TTCGAGTTTAACCAGCGCGA	60.32	GAGGTCTGAAGGTTGTGGCA	59.89	Y/Y	143	3, 5, 8, 9	10
NFATC1	NM_001278669.2	AGTCCTGGAGATCCCACTCC	60.03	CGTGTGTTCTTCCTCCCGAT	59.75	Y/N	132	1-10	10

NFATC1	NM_001278669.2	AAAACTGACCGGGACCTGTG	60.18	TCTTCCCGTTGCAGACGTAG	59.76	Y/N	115	1-10	10
CCNA2	NM_001237.5	TGGCGGTACTGAAGTCCGG	61.64	CAAGGAGGAACGGTGACATGC	61.54	Y/N	121	1	1
CCNB1	NM_031966.4	CAGCTCTTGGGGACATTGGTAAC	61.43	ACTGGCACCAGCATAGGTACC	61.86	Y/N	148	1-3	3
CCNC	NM_005190.4	CCCCTTGCATGGAGGATAGT	58.86	TCTGCTGTACAACACAGGCT	59.24	Y/Y	112	1-3	3
CCND1	NM_053056.3	GATCAAGTGTGACCCGGACTG	60.67	CCTTGGGGTCCATGTTCTGC	60.97	Y/Y	101	1	1
CCND2	NM_001759.4	ACCAACACAGACGTGGATTGT	60.13	CTCCGACTTGGATCCGTCAC	60.18	Y/Y	111	1	1
CCND3	NM_001760.5	CCTCCTACTTCCAGTGCGTG	60.11	AGGCCAGGAAATCATGTGCA	59.96	Y/N	363	2, 3, 6	6
CCNE1	NM_001238.4	CAACGTGCAAGCCTCGGA	60.66	AAAGTGCTGATCCCTTAAGTATGTC	58.88	Y/N	131	1, 3-5	5
CCNE2	NM_057749.3	ATCCTTCACCTTTGCCTGATTT	58.22	CCTCATCTGTGGTTCCAAGTCA	59.96	Y/N	134	1	1
CDK1	NM_001170406.1	ATGAAGTGTGGCCAGAAGTG	58.10	CAGAAATTCGTTTGGCTGGATCA	59.81	Y/N	159	1, 2, 6	6
CDK2	NM_001798.5	CCCTGGATGAAGATGGACGG	59.89	GATGGGGTACTGGCTTGGTC	60.11	Y/N	126	1-3	3
CDK4	NM_000075.4	CCCATCAGCACAGTTCGTGA	60.32	AACACCAGGGTTACCTTGATCTC	59.99	Y/N	131	1	1
CDK6	NM_001259.8	CCGAAGTCTTGCTCCAGTCC	60.39	GTTGATCAACATCTGAACTTCCACG	60.62	Y/N	120	1, 2	2
CDC25A	NM_001789.3	GTCTAGATTCTCCTGGGCCATTG	60.50	CAGAATGGCTCCTCTTCAGAGC	60.74	Y/N	120	1, 2	2
CDC25C	NM_001790.5	CACTCAGCTTACCACTTCTGCAG	61.41	GGGCTACATTTCATTAGGTGCTGG	61.76	Y/N	117	1, 3-7	8
PRR7	NM_030567.5	CCGCGCCAAGCGGAAT	60.92	GTCCGTGAGCACCTCGCTAT	62.01	Y/Y	99	1-5	5
FAM216A	NM_013300.3	GACGGAGCGTAGCTCTTCTG	60.25	CAGCTGATCCGCCGCC	60.66	Y/Y	71	1	1

CD3EAP	NM_001297590.3	GTGAGGATGCTGCTCGGTT	60.08	CCAAGGAGAAACGAGGGGAC	60.04	Y/Y	81	1, 2	2
EEF1AKMT1	NM_174928.3	GAGGCGTTTTGGACTGGGTT	60.82	CTGCTAAGGCATGGGCAGAA	60.39	Y/Y	91	1	3
VDAC1	NM_003374.3	GACTCACGCAGGTCCTCCC	62.01	CAAGATCGGCATACGTGGGT	60.18	Y/N	118	1	3
EEF1E1	NM_004280.5	GGCGAGCGACAGATTCCAG	60.88	TGTTGGCTTGCTTGACTAGATGA	60.24	Y/Y	94	1, 2	2
ISOC2	NM_001136201.2	CGCCTACTTCCCACAGATCG	60.25	ATGACTGGCACCTCAAGCAG	60.32	Y/N	75	1, 2	3
PRR3	NM_025263.4	AGCGGGAAGAGACTGGAGAT	60.03	TGACTTAGGGTCGCCAGGTT	60.83	Y/N	104	1	2
QTRT1	NM_031209.3	CTGCCTGGGCAATACCTACC	60.18	TTCATGAAGCCGTGGAGACC	60.04	Y/N	84	1	1
EXOSC5	NM_020158.4	CCGAGGTGAAGGTCAGCAAA	60.25	TCTTCTCTGCAACACCAGGC	60.25	Y/Y	93	1	1
NOP16	NM_001256539.4	TACTCTGTCTCGGGACCTCATT	60.03	ACTCTGCTTATAGTCCTCCCCG	60.75	Y/Y	73	1-4, 6-8	10
SNRPA	NM_004596.5	ACCCGCCCTAACCACACTAT	60.62	GGATCTGGCCAAACTGGGAG	60.39	Y/N	106	1	1
PHB2	NM_001144831.2	GAAAATTGTGCAGGCCGAGG	60.11	CAGGGTTCTTGCTCAGTGCT	60.25	Y/N	71	1	3
RRP9	NM_004704.5	GTGGGGTCTCTCCAAGAAGC	60.04	CCGACGATATCCAGAAGGGC	60.04	N/N	98	1	1
MYC	NM_002467.6	CAAGAGGCGAACACACAACG	60.04	CAACTCCGGGATCTGGTCAC	60.11	N/N	90	1, 2	2
SNX16	NM_022133.4	GGTTTAACCGTCACCGGGAA	60.25	CCCTTCTGAAGCTTTATTCCATGC	60.20	Y/N	94	1, 4	8
RAB12	NM_001025300.3	AAGTCCACCGTGGGTGTTG	60.15	TCTCTCCTGACCTGCTGTGT	60.18	Y/Y	96	1	1
GBP3	NM_018284.3	CCAGCGATCCAGCGAAAGAA	60.74	GGGCCTGTCATGTGGATCTC	60.18	Y/N	120	1-4	5
ANKRD40	NM_052855.4	GGAGGTGCAGAAACTGGTGG	60.89	ACAAGTCCAGCCGTTGACC	60.23	Y/Y	70	1	1
RNF19A	NM_183419.4	TTGTGGCAACTGGGAACACT	60.03	GCGATTGTGAATCTTGCGGC	60.86	Y/Y	120	1-5	5
NBEAL1	NM_001114132.2	TTCAGCTGGGCAAAGAACCA	60.11	CCCAGGAGGCTGATGACAGA	60.98	N/N	119	1, 2	2

ACVR1	NM_001105.5	TTTGGAGAGAGGCAGCAAGC	60.61	TCACTGGGGTACTCGGAGAG	60.03	Y/Y	116	1	6
PANX1	NM_015368.4	CTGGAGCTGGCTGTGGAC	60.05	ACAGCTTATCTGTGTACCAATCGAG	60.68	Y/Y	111	1	1
SPNS3	NM_182538.5	CACCTCCTGGAGCCTGCC	62.11	CCAGCAGCACTCCTGCAAT	60.68	Y/Y	110	1, 2	2
HPDL	NM_032756.4	CCTCGAAATGACAGCAGGGT	60.04	GGAAGGGACTCAGCCAGAAC	60.04	Single exon	105	1	1
KLRG2	NM_198508.4	CAGGCTTTCTGCTCAGCCT	60.00	TGGGTATCTGCCCAGGAAGT	60.25	Single exon	75	1	1
ALOX5	NM_000698.5	CCGGCACTGACGACTACATC	60.53	TATGAATCCACCGCGCCAC	60.52	Y/Y	115	1-4	5
STK33	NM_030906.4	CCTTCCAGCTGAAATCAAGGGA	60.29	AGCAGGGTACTTGGTTGCTG	60.25	N/N	79	1-13, 17	17
YES1	NM_005433.4	TGGGAAGCAAGATCAATCGCT	60.07	AGCATCTTTTCTCCCCATTTTGC	60.06	Y/N	120	1	1
VLDLR	NM_003383.5	CAACAACCTGAATGATGCCCAA	59.70	TGGCAGGCATAGGTATTCACAT	59.56	Y/N	118	1-4	4
UBE3C	NM_014671.3	AGTCCAGAGACACGAGGAGA	59.31	TGCTGGCACATAGAGCTGAG	59.82	Y/N	101	1	1
TULP3	NM_003324.5	GACTTCAGGAGCGTCTCCAA	59.40	TGGCTTGATGCAGAATTGGGT	60.55	Y/N	115	1, 2	2
TGFBR2	NM_001024847.2	CCCCTGTGTCGAAAGCATGA	60.32	TCACACACCATCTGGATGCC	60.04	Y/N	102	1, 2	2
SNX16	NM_022133.4	ACTGCCTTGCAGTGAGAGAAT	59.65	TCTGTAAGCGGTAGTTTGTCTCT	59.17	Y/Y	117	1-4	4
SFXN3	NM_030971.6	TGGGGACAGCCTATGTGAGT	60.25	GCACAAATCTGCCGACCAAG	60.11	Y/N	102	1, 3-11	11
S1PR3	NM_001395848.1	GAGGAGCCCTTTTTCAACGC	59.76	GCCCCAGGAACATTCATTTCAA	59.43	Y/Y	105	1	1
RNF19A	NM_183419.4	ACTGGGAACACTGGTTGGTG	60.11	GATTGTGAATCTTGCGGCCC	59.90	Y/Y	110	1-5	5
RASA1	NM_002890.3	AGGAGAAACTCCAGAACAAGCA	59.56	TGACCTGACGAAGGCGTTTAT	59.73	Y/Y	107	1, 2	2

RAB15	NM_001308154.2	ATGAGTACGCACCAGAAGGC	60.11	TCCATGCCATACTCCTTCGC	59.89	Y/Y	118	1-3	3
RAB12	NM_001025300.3	TGCAGGTCATCATTATCGGCT	59.58	AACACCCACGGTGGACTTG	60.15	Y/Y	104	1	1
PRRG4	NM_024081.6	AGCATGCGGGAGAAGAAGTG	60.39	TTTCTAGGTTGCCGGGAGTG	59.68	Y/Y	114	1	1
PANX1	NM_015368.4	GTCTGGAAACCTCCCACTGT	59.23	TATGAGGAGCAGCTGCGAAAC	52.38	Y/N	113	1	1
OCRL	NM_000276.4	GAAAACCAGCGACCACAAGC	60.32	TCTGTCCATGATGCGTACACT	59.18	Y/N	112	a, b, c	3
NPEPPS	NM_006310.4	CCCCAACCAGGCCAAACTAA	60.18	TCCGATAAAACCCAACTGTTCCT	59.93	Y/N	119	1, 2	2
KDELC2	NM_024089.3	AGAAATATGCCGAGCGCCAG	60.88	TTGAAGGCTTTTTCCTGTGGC	59.59	Y/Y	114	1-3	3
GCNT2	NM_145649.5	TCCTGATGAGCATTTCTGGGTG	60.36	TGTCTGTCTTCCATGTCACTCC	59.70	Y/N	120	1-4	4
GBP3	NM_018284.3	CCAGCGATCCAGCGAAAGAA	60.74	GGGCCTGTCATGTGGATCTC	60.18	Y/N	120	1-4	4
CCNYL1	NM_001330218.2	GCAAGCACAATTTTCCTGAGCA	60.55	TTTTTCTCGCTGTTCTTTATGTGGT	59.70	Y/Y	117	1-3	3
BRWD3	NM_153252.5	CCTCAGAGTGTTCCTGGGGT	60.84	CTATGCAGAGCCGCAAAAGC	60.25	Y/N	119	1	1
BIN1	NM_139343.3	ACACGTTCCAGAGCATCGC	60.74	GAAGGTGTTGCTCCCGTGTT	60.82	Y/N	119	1-16	16
ATG9A	NM_001077198.3	TTGACCTCTTCTTCTCTCGAGTTT	59.41	GGAAGGTAGTGAAGGCAACCA	59.93	Y/Y	120	1, 2	2
ANKRD40	NM_052855.4	GGCCTTAGGGGACATTCGG	59.85	CCATGGTTTCGTTTACATGCCC	60.42	Y/N	117	1	1
AHNAK	NM_001620.3	GACCGAGATTCCCGACGAG	59.64	GGTTGTCTCCTCCTTCTCCATC	59.83	Y/Y	115	1-4	4
TMEM92	NM_153229.3	GGCTAAGTGCTTCTGTCGCA	60.67	AGAAAGGGATACTCTGACCCTCT	59.73	N/N	118	1, 2	2

SPNS3	NM_182538.5	AAGTGGTCTGGGCTACGTG	59.33	CCAGCAGGATAAGCAGGATCA	59.58	Y/Y	119	1, 2	2
SH2D3A	NM_005490.3	CCCATGGTTCGCCTACTGG	59.10	TGCGGAATTTGGGTGCGT	60.60	N/N	120	1-8	8
RGL4	NM_153615.2	GTGACAAAGAGAGCTACAAGCTG	59.57	GGTGCAGAGCCGGTGTT	59.93	Y/Y	118	1, 2	2
PRR7	NM_030567.5	ACATGTCCAAACCACCGTGT	60.11	GCGTGACGATCTTGCGGTA	60.52	N/N	111	1-5	5
KLF15	NM_014079.4	GTGAGAAGCCCTTCGCCTG	60.74	CACACAGGACACTGGTACGG	60.32	Y/N	118	1	1
HSH2D	NM_001382417.1	CATCAGGGTCAGTCACAGCC	60.39	CCCGGGGATCATGAAAGTCC	60.18	Y/N	112	1, 5-8, 15	15
EXOSC6	NM_058219.3	ATTCCTGGAAGGGCCCTGAT	60.63	CAGGGGCTGTTGAGTTTTGC	59.97	Single exon	116	1	1
COMTD1	NM_144589.4	CCTTGGAGACCCTGGACGA	60.61	CAGGCAGCGCTCGTAGTAG	60.30	Y/Y	110	1	1
SHISA5	NM_016479.6	GAGACCCTGGCTGGAGGA	59.96	GAGAGGCCAGGGAATGCTC	59.85	Y/Y	110	1-6	7
ETFRF1	NM_001001660.3	GCGTGCCGGAAAGTATGTTATG	60.29	TCTCGTCCAAGATACAGCAGATTT	59.84	Y/Y	120	1	1
PPP1R14C	NM_030949.3	AGCAGGGAAAAGTGACAGTGAA	60.09	GGCATTTCTTCTTCCTCGCAG	59.60	Y/Y	118	1	1
DGUOK	NM_080916.3	AGACCTCATGAGAGAGGTAAACAC	59.54	TGGTTGGGAGACACAACATTTTT	59.23	Y/Y	120	1-7	13
ELL2	NM_012081.6	TGTGAAGCTCACCGAGACG	59.71	TGGGAATTTTGACAAGCCCG	59.03	Y/Y	119	1	1
ADGRE5	NM_078481.4	AAATTAAAGAAGGCGAGGGCG	59.26	ATAGGTCAGCACCAAGCTCC	59.46	Y/Y	117	1-3	3
LMO2	NM_005574.4	CTGGACCCTTCAGAGGAACC	59.38	ATGGCCTTCAGGAAGTAGCG	59.82	Y/Y	110	1-3	3
PIGW	NM_178517.5	CATTTGGAGTACGTGAGGAAGAAA	59.01	GAAAGCACAATCCCTGGGTG	59.11	Y/Y	110	1	3
CUL4A	NM_001008895.4	CTGCCCTCCATCTGGGATATG	59.72	TCCTCTCGCGCTCGATCA	60.51	Y/Y	115	1-3, 5-9	11

FAM192A	NM_024946.4	AGCTGTGAAGCATAAGAGCTCAG	60.68	GTTTCCGAGAGACTTGCAGGA	60.00	Y/Y	112	1-15, 17-27	27
H2AFX	NM_002105.3	CAGGCCTCCCAGGAGTACTAA	60.34	AGCTCTTTCCATGAGGGCG	59.78	Single exon	110	1	1
BZW2	NM_014038.3	ACAGCAGTGATTGGTCTTCTGT	59.89	GGGGAGCATATTGCTTCAGGT	60.13	Y/Y	112	1-5	5
RAC3	NM_005052.3	GAATGTTCGTGCCAAGTGGT	59.05	CCGCTCAATGGTGTCCTTGT	60.61	Y/Y	112	1, 2	2
STAT5B	NM_012448.4	TCCGAGAAGCCAACAATGGTA	59.37	CTCTGTGTCCTGCGTGACC	60.37	Y/Y	119	1	1
MAGEF1	NM_022149.5	GGGGTGCAACCCTCAAAGTA	59.89	CTGGTGGATTGGTGTGAGGC	60.96	Single exon	118	1	1
FAM216A	NM_013300.3	GACTGGACGGAGCGTAGC	59.90	TCAGAACCTTTGGAATTCTGGTAAC	59.23	Y/Y	110	1	1
SLC25A22	NM_001191061.2	CTACTTCGGCATGTACCGGG	60.25	GCTTCTGCCCGTCCTTAGAG	60.18	Y/Y	119	1-3	3
ADGRG5	NM_001304376.3	TGCTGAATAACTACGTCCTGGG	59.83	GGTGTAGCCTTCCAGGCTTT	59.96	Y/Y	110	1-3	3
CTPS1	NM_001905.4	TGCTCATGGAGTGCTGGTTC	60.32	CCTAAGCACACGCCCAAAAA	59.33	Y/Y	114	1, 2	2
RRM2	NM_001034.4	TGGTCGACAAGGAGAACACG	59.97	CAGCTGCTTTAGTTTTCGGCT	59.46	Y/Y	111	1, 2	2
CDKN1A	NM_000389.5	CTCAAATCGTCCAGCGACCT	60.11	AGCCTCTACTGCCACCATCT	60.33	N/N	112	1-10	10
SVIP	NM_001320340.1	AATTCGGCGCGAAAAGACATT	59.80	CCCGAGATGCAGCCTCTTTTT	60.95	Y/Y	120	1	3
CALHM6	NM_001010919.3	GGCTCAGTCGCAGGTGTT	59.97	TTCAGCTGCAGAAAACTAACTGG	59.43	Y/Y	111	1	2
CD3EAP	NM_012099.3	GTGAGGATGCTGCTCGGTT	60.08	CCAAGGAGAAACGAGGGGAC	60.04	Y/Y	81	1, 2	2
VDAC1	NM_003374.3	GACTCACGCAGGTCCTCCC	62.01	CAAGATCGGCATACGTGGGT	60.18	Y/N	118	1	1

EEF1E1	NM_004280.5	GGCGAGCGACAGATTCCAG	60.88	TGTTGGCTTGCTTGACTAGATGA	60.24	Y/Y	94	1, 2	2
ISOC2	NM_001136201.2	CGCCTACTTCCCACAGATCG	60.25	ATGACTGGCACCTCAAGCAG	60.32	Y/N	75	1, 2	3
PRR3	NM_025263.4	AGCGGGAAGAGACTGGAGAT	60.03	TGACTTAGGGTCGCCAGGTT	60.83	Y/Y	104	1	2
KLRG2	NM_198508.4	GGGCAGATACCCAGTCTCCA	60.69	CCGTCCTCAGGGAGTAGCTG	61.39	Y/Y	111	1	1
HPDL	NM_032756.4	CCTCGAAATGACAGCAGGGT	60.04	GGAAGGGACTCAGCCAGAAC	60.04	Single exon	105	1	1
ALOX5	NM_000698.5	CCGGCACTGACGACTACATC	60.53	TATGAATCCACCGCGCCAC	60.52	Y/Y	115	1-4	5
NFATC3	NM_173165.3	CAGCGGTCTGCTCAAGAACT	60.32	TGAGGTCGTCCATCTTGTCC	59.10	Y/Y	152	1-3	3
KDM4A	NM_014663.3	TCCTTTGCTTGGCACACTGA	60.11	GGAAAAAGCCTTTGGCGAGG	60.04	Y/Y	133	1	1
PAF1	NM_019088.4	GGCTCAGATGAGGAGCAGGA	61.05	TCACCACTGCCACTCTTGTC	59.89	Y/Y	131	1	3
MCU	NM_138357.3	GGATGCAATTGCTCAGGCAG	59.90	CCAGGATTCAGAGGCTTTTTGC	60.09	Y/Y	119	1-3	3
SLC16A9	NM_194298.3	TGGCATTGTTGTAGGTCTTGGA	59.89	CCTGTTGAAATCAGGCCAAGC	60.07	Y/Y	111	1-6	6
CLCN3	NM_001829.4	TCTTTTTAGCCTGGAAGAGGTTAGC	60.80	CGGCTGTTACCAAATGGATTGA	59.25	Y/Y	120	b, c, e	4
PTK2	NM_001352699.2	GTGTGCTCTTGGTTCAAGCTG	60.00	AAGTCAGCAAGATGTGTGGGA	59.58	Y/Y	111	(123 variants)	>140
ADAM9	NM_003816.3	GAAGTGTGCCACTGGGAATG	59.12	GTGCCTCGACTAGGCGTTT	60.08	Y/Y	111	1	4
AMPH	NM_001635.4	GACTTTGATCCTTTCAAGCCCG	59.84	CCAAATCAGTGCTTGTCGTCC	59.80	Y/Y	112	1, 2	2
TMEM14A	NM_014051.4	AGGTGGTGTTCCGTCTTTGAT	59.58	AGGAAGAAAGCTGTAAACAGTGAC	59.18	Y/Y	120	1	1
SDK2	NM_001144952.2	GGCTGAGCTTACCTCCATGT	59.46	CACGCTCATCCGTATCTCGT	59.69	Y/Y	112	1	1
ARID4A	NM_002892.4	TACCTGACAGTGGGAACCGA	60.18	ATCCTGTTTCAGGAGTACCTTAACT	59.21	Y/Y	111	1-3	3

IST1	NM_001270975.2	CTGCCAAAGGGACCATCAGA	59.67	ACAGATTCATACGATGGGGGAG	59.37	Y/Y	110	1-3, 5, 6	6
RGS20	NM_170587.4	TTGTAGCTGCTCGTGTCTCAC	60.34	GTAGGAGCAGGGCTTTCTTCC	60.41	Y/Y	111	1-3	6
UBE2D2	NM_181838.2	CCATGGCTCTGAAGAGAATCC	58.15	GATAGGGACTGTCATTTGGCC	58.42	Y/Y	302	1, 2	5
B2M	NM_004048.4	GTCTTTCAGCAAGGACTGGTCT	60.22	CTTACATGTCTCGATCCCACTT	57.61	Y/Y	140	1	1
ATP5B	NM_001686.4	TCCATCCTGTCAGGGACTATG	58.32	ATCAAACTGGACGTCCACCAC	60.54	Y/Y	110	1	1
TYW1	NM_018264.4	CTCCTGATAGCACACAGAAAGTTTA	58.83	TGCGCTGAACGTTTTTGATCC	60.33	Y/Y	123	1	2
ENOX2	NM_006375.4	GAGCTGGAGGGAACCTGATTT	59.72	CACTGGCACTACCAAACTGCA	61.08	Y/Y	123	1, 2, 4, 6, 7, 10	10
GAPDH	NM_002046.7	GACAGTCAGCCGCATCTTCT	60.11	GCCCAATACGACCAAATCCGT	61.02	Y/Y	102	1, 3, 4, 7	7
ACTB	NM_001101.5	CGCCGCCAGCTCACC	60.56	CACGATGGAGGGGAAGACG	59.86	Y/Y	120	1	1
GAPDH	NM_002046.7	GTCAACGGATTTGGTCGTATTG	58.00	TGTAGTTGAGGTCAATGAAGGG	57.71	Y/Y	106	1-4, 7	7
ACTB	NM_001101.5	CACAGAGCCTCGCCTTT	56.78	GCGGCGATATCATCATC	52.58	Y/N	76	1	1

Note: some primer targets are duplicated due to isoform-specific versions, or more optimised primers were generated for the Fluidigm® BioMark™ platform.

2.1.7.3 qRT-PCR primers: mouse target genes

Target (mouse)	RefSeq	Forward primer		Reverse primer		Intron/exon junction	Product length (bp)	Transcript variant coverage	# Possible variants
		Sequence	Melt temp (˚C)	Sequence	Melt temp (˚C)				
Nfatc2	NM_001136073.2	GAAGGGTGATGAGGGTTCGG	60.11	CCCTCATGTGCAAAACGTGG	60.04	N/N	73	1, 4-8, 10-15	18
Nfatc2	NM_001037177.2	AGCGGAGTCCAAGGTTGTGT	61.7	AAGACAGAGCCAGGAGGGTTT	61.05	Y/N	147	2, 3, 9, 16	18
Nfatc2 (11100 vector)	N/A	AGCGGAGTCCAAGGTTGTGT	61.7	AGGCTGGCTCTTGTCTTTATCC	60.09	N/A	94	N/A	18
Nfatc1	NM_016791.4	ACCGATAGCACTCTGGACCT	60.03	GTCAGAAGTGGGTGGAGTGG	59.96	N/N	135	1- 6	6
Actb	NM_007393.5	CACTGTCGAGTCGCGTCC	60.5	CGCAGCGATATCGTCATCCA	60.39	Y/N	102	1	1
Gapdh	NM_001289726	GGGTCCCAGCTTAGGTTCATC	60.13	AATCCGTTCACACCGACCTT	59.6	Y/Y	87	1	2
Hoxa9	NM_010456.3	GTATATGCGCTCCTGGCTGG	60.67	CCGAGAGCGGTTCAGGTTTA	59.75	N/N	98	1	2
Meis1	NM_010789.3	GTCCCCATGCAACAACAACC	59.97	GCTCCAAGGTGGGACTATGG	59.82	N/N	155	A, B	2
Ccna2	NM_009828.3	TCTGGGATTAAAGGCGCCAC	60.39	CTGCCGGAGCCGCTG	60.2	Y/Y	118	1	1
Ccnb1	NM_172301.3	ACAACGGTGAATGGACACCA	59.82	GAGGCCACAGTTCACCATGA	59.96	Y/Y	113	1	1
Ccnd1	NM_001379248.1	CCATGCTCAAGACGGAGGAG	60.18	CACAGACCTCCAGCATCCAG	60.11	Y/Y	117	1, 2	2
Ccnd2	NM_009829.3	GCAGTGTGCATGTTCCTAGC	59.55	TACCAGTTCCCACTCCAGCA	60.47	Y/Y	120	1	1
Ccnd3	NM_007632.2	GCCCTCTGTGCTACAGATTACA	59.83	GTGAGCTCATCCGCAGACAT	60.18	Y/Y	119	1-3	3
Ccne1	NM_007633.2	CCATGCCAAGGGAGAGAGAC	59.82	TGCAAAAACACGGCCACATT	59.82	Y/Y	112	1	1
Ccne2	NM_001037134.2	TGTGCATTCTAGCCATCGACT	59.52	CATCCCATTCCAAACCTGAAGC	59.83	Y/Y	117	1-3	3

Bin1	NM_009668.2	CCCTGATATCAAGTCGCGCA	60.25	TTCTCAAGCAGCGAGACAGG	60.04	Y/Y	141	1, 3	3
Cd3eap	NM_145822.2	GATGTCGCCAGACTCGGAAC	60.8	CCGCCCATTGAGACATTGTG	59.55	Y/Y	118	1	1
Hsh2d	NM_197944.1	ACACCCTTTCCTACAAAGCCC	60.2	AGAGAGGCGTGGGTCATGTG	61.89	Y/Y	106	1	1
Spns3	NM_029932.3	GCTGCAGCTGTTCTCTGTTAC	59.54	TGTCTGCAGCAAACCAGCAT	60.82	Y/Y	125	1	1
Vldlr	NM_013703.2	TGCAAGGCAGTAGGCAAAGA	59.89	GAGCCACCGTGTTCCTTAGT	59.68	Y/Y	121	1-3	3
Yes1	NM_009535.3	TGGAGCGAGCGGATTTGATA	59.25	AATGACTGGCACTTGGGCTT	60.18	Y/Y	114	1	3
Lmo2	NM_008505.4	GATTGCCTCAGCTGTGACCT	60.04	ATCCTGACCAAAAAGCCTGAGA	59.62	Y/Y	117	1-4	4
Cdkn1a	NM_007669.5	TATCCAGACATTCAGAGCCACA	58.89	CACGGGACCGAAGAGACAAC	60.67	Y/Y	100	1	2
Cul4a	NM_146207.3	AGAACTTCCGAGGCTGTTGA	58.95	TCTGAATGGGAGGATCTGGGC	61.32	Y/Y	114	1	3
Npepps	NM_008942.3	ACTCTGCAAACAGGTACAGGA	58.95	TGTGTGACAGCAGCATAGCG	60.68	Y/Y	134	1	1

2.2 Methods

2.2.1 Cell culture

2.2.1.1 Culture of human cell lines

All cell culture work was carried out under aseptic conditions, using sterilised materials and reagents. Cell lines were maintained at 37°C and 5% CO_2 incubation and were tested for mycoplasma using a MycoAlert™ detection kit. Culture media for all cell lines contained a base medium (RPMI, DMEM or IMDM) and FBS as shown in Tables 2-1, 2-3 and 2-4, in addition to 2mM L-glutamine. Biological and clinical information on human AML cell lines is given in Table 2-2. Suspension cell lines were sub-cultured by centrifugation of cell suspension at 300g for 5 min and resuspension in the appropriate medium to the suggested cell density (Tables 2-1&2-3, density not standardised for murine cells).

Adherent cell lines (Table 2-3) were sub-cultured by rinsing cells in PBS and incubation in Trypsin-EDTA (0.25%) Solution for 10 min at 37°C. The trypsin reaction was inhibited by adding 1.5X volumes of culture medium and a single cell suspension was obtained by gentle pipetting. Cell suspension was centrifuged at 300g for 5 min and resuspended in an appropriate volume of medium, before re-seeding in tissue culture flasks.

Two adherent cell lines were used: HEK-293T or phoenix-AMPHO, which is a modified version of HEK-293T, stably expressing amphotropic retroviral envelope and retroviral gag-pol proteins for the generation of retrovirus using a helper-free protocol. Phoenix-AMPHO cells were maintained in culture with Hygromycin B (200 µg/mL) and Diphtheria toxin (2 µg/mL) to select for envelope and gag-pol expression (Pear *et al.*, 1993). HEK-293T were maintained in antibiotic-free media.

Biological and clinical information on AML cell lines is given in Table 2-11, below.

2.2.1.2 Human suspension cell lines

Cell Line	Supplier	Catalogue #	Base media	FBS (% v/v)	Doubling time	Cell density
THP-1	ATCC®	TIB-202™	RPMI	10.0	26 hr	0.1-1.0x10^6
MOLM-13	DSMZ	ACC-554	RPMI	10.0	50 hr	0.1-1.0x10^6
MV4-11	ATCC®	CRL-9591™	RPMI	10.0	50 hr*	0.1-1.0x10^6
NOMO-1	DSMZ	ACC-542	RPMI	10.0	35-40 hr	~0.5x10^6
HL-60	ATCC®	CCL-240™	IMDM	10.0	40 hr*	0.1-1.0x10^6
Kasumi-1	ATCC®	CRL-2724™	RPMI	20.0	48-72 hr*	0.3-2.0x10^6
OCI-AML3	DSMZ	ACC-582	RPMI	20.0	30-40 hr	0.5-2.0x10^6

Table 2-1. Human suspension cell lines used in the study.
The base medium conditions used to culture cell lines used in the study, together with supplier, are shown. The doubling time given for is either from the manufacturer, where available, or from DSMZ where not available from ATCC® (indicated by *) Cell density is the range in which they were maintained, based on suppliers' guidance.

Cell Line	Age of Patient (Years)	FAB Class.	Disease stage	Key Cytogenetic and Molecular Features
THP-1	1	M5	Relapse	MLL-AF9; *NRAS*^{mut}; *TP53*^{mut}
MOLM-13	20	M5a	Relapse, progressed from prior MDS	FLT3^{ITD} (heterozygous); MLL-AF9
MV4-11	10	M5	Diagnosis	FLT3^{ITD} (homozygous); MLL-AF4; *KDM4A*^{mut}
NOMO-1	31	M5a	Relapse	MLL-AF9; *TP53*^{mut}; *KRAS*^{mut}
HL-60	35	M2	Diagnosis	Amplified *MYC* and *NRAS*; *TP53*^{del}; *NRAS*^{mut}
Kasumi-1	7	M2	Relapse	AML1-ETO; *TP53*^{mut}
OCI-AML3	57	M4	Relapse	*NPM1*^{mut}; *DNMT3a*^{mut}; *NRAS*^{mut}

Table 2-2. Biological and clinical summary of AML cell lines.
This table summarises the reported clinical features of the patient from which the cell line models of AML were derived. This includes the patient's age at time of cell acquisition, the FAB classification of disease and a descriptor of whether their disease was a new diagnosis, relapse or other key features about its progression. Also shown are key mutations, which highlights lesions in genes well-documented in AML pathology. 'mut' = mutation and 'del' = deletion.

2.2.1.3 Human adherent cell lines

Cell Line	Supplier	Catalogue #	Base media	FBS (% v/v)	Antibiotic	Subculture Ratio
(HEK-)293T	ATCC®	CRL-3216™	DMEM	10.0	No	1:3-1:8
Phoenix-AMPHO	ATCC®	CRL-3213™	DMEM	10.0	Yes	1:5-1:8

Table 2-3. Human adherent cell lines used in the study.
As above for suspension cells, but the recommended ratio of sub-cultivation is given, instead of a cell density. The need for selection antibiotics is also suggested, with further detail given in Section 2.2.1.1.

2.2.1.4 Mouse (suspension) cells

Cells	Base media	FBS (% v/v)	Cytokines	Relevant publication(s)
MLL-AF9 murine BM	RPMI	10.0	X63/mIL-3 media (10%)	(Somervaille and Cleary, 2006)
Primary murine BM	RPMI	20.0	mIL-3 (10 ng/mL) mIL-6 (10 ng/mL) mSCF (20ng/mL) mGM-CSF (10 ng/mL)	-
X63-omIL-3	RPMI	10.0	-	(Mitchell *et al.*, 1991)

Table 2-4. Murine cells used in the study.
As for human suspension cells. Publications describing the cells' uses or culture are shown.

2.2.1.5 Culture of murine (suspension) cells

MLL-AF9 murine BM cells were derived from C57BL/6J mice, with stable retroviral expression of the MLL-AF9 oncogene, as described by Somervaille and Cleary (Somervaille and Cleary, 2006). Culture media for these cells was supplemented with murine IL-3 (mIL-3) derived from a modified mouse hybridoma cell line expressing mIL-3; named 'X63-omIL-3'. MLL-AF9 murine BM were maintained as for other suspension cell lines, in the appropriate medium (Table 2-4).

2.2.1.6 Cryopreservation of cells

Cells were cryopreserved in liquid nitrogen storage, held at approximately -196°C, for long-term storage. For shorter-term storage cells were retained at -80°C. To cryopreserve cells the suspension was centrifuged at 200g for 10 min. The pellet was resuspended in room-temperature freeze media (RPMI with 30% (v/v) FBS and 5% (v/v) DMSO) to a density of 5-10x10^6 cells/mL and left to equilibrate for 10-20 min inside a laminar flow hood. The suspension was then pipetted into cryogenic vials and placed in a Mr Frosty™ Freezing Container part-filled with absolute isopropanol and pre-chilled to 4°C. The container was placed in a -80°C freezer to allow gradual freezing of the cell vials at a rate of approximately 1°C/min. After cooling to -80°C these vials were transferred to liquid nitrogen storage.

2.2.2 Derivation of primary murine BM tissue

2.2.2.1 Animal husbandry and maintenance

Experiments using mice were approved by the local animal ethics review board and performed under a project licence issued by the Home Office, in keeping with the Home Office Animal Scientific Procedures Act 1986 (PPL No. PD40605B1). C57BL/6J mice (The Jackson Laboratory, strain #000664) were kept in animal housing facilities at the Beatson Institute of Cancer Research (BICR). Mice were culled using an approved Schedule 1 method. Technical support for *in vivo* work was provided by Mrs Karen Dunn and the facility staff.

2.2.2.2 Processing of BM tissue

Long bones from hind limbs were removed from culled mice and flushed using designated wash buffer (PBS with 1% FBS and 0.1 mM EDTA) and a 26G needle, to release BM tissue. BM cells were washed twice by resuspending in wash buffer and centrifuging at 300g for 5 min. A single cell suspension was obtained by resuspending the final cell pellet in the final culture media and filtration through a 70 µm cell strainer.

2.2.2.3 Enrichment of $CD117^+$ cells

$CD117^+$ BM cells were enriched from primary murine BM tissue using CD117 MACS® MicroBeads, MACS® LS Columns, a MidiMACS™ Separator and a MACS® magnetic stand, using the protocol supplied. A 'MACS' buffer was made containing PBS (pH 7.2), 0.5% (w/v) BSA, 2mM EDTA for washing and column flowthrough.

In summary, a maximum of $2x10^9$ cells was suspended in 80 µL MACS buffer and 20 µL CD117 MicroBeads per 10^7 cells. After a 15 min incubation at 4°C cells were washed in MACS buffer and applied to a pre-washed LS column, while on the magnet. These were washed with MACS buffer and finally removed from the magnet before flushing out CD117 bead-labelled cells. The volumes of buffer for cell suspension and column washes are given in the protocol for LS columns.

To assess enrichment, CD117 bead-labelled cells, unlabelled cells from the flowthrough and a $CD117^-$ cell line were stained with anti-CD117-PerCP-Cy5.5 antibody and assessed by flow cytometry.

2.2.3 Bacterial culture and plasmid generation

2.2.3.1 Stbl3™ competent bacterial cell propagation

Stbl3™ Chemically Competent *E. coli* were propagated using a protocol by Green & Sambrook (Green, 2012). Briefly, Stbl3™ cells were thawed on ice and incubated overnight in 2.5 mL LB growth medium at 37°C, with shaking at 225 rpm. The culture was then diluted into 1 L LB medium with 20 mM $MgSO_4$ and incubated as above until the culture absorbance reached OD_{600} in the range 0.4-0.6, as measured by a SpectraMax® M5 Plate Reader. Cultures were centrifuged at 4500g for min, at 4°C.

Bacterial pellets were initially resuspended in 200 mL Stbl3™ buffer 1 and incubated on ice for 5 min and centrifuged again, using the same settings. Pellets were then resuspended in 40 mL Stbl3™ buffer 2 and incubated on ice for 2 hr. Finally, these cell suspensions were snap frozen in 100 µL aliquots using liquid nitrogen.

2.1.1.1. Transformation of Stbl3™ competent bacterial cells with plasmid

100 µL Stbl3™ competent cells were thawed on ice for 20-30 min. 5 µL appropriate plasmid was added to the cell suspension, mixed by flicking the tube, and subsequent incubation on ice for 30 min. Cells were heat shocked at 42°C for 45 sec, using a thermoblock, before returning them to the ice for a 2 min incubation. 300 µL SOC medium was added to the cell suspension, and this was incubated at 37°C with shaking at 225 rpm for 1 hr. Finally, 150 µL cell suspension was spread on a LB agar plate, with ampicillin (100 µg/mL), and incubated overnight at 37°C with 5% CO_2.

2.1.1.1. Growth and purification of plasmids from Stbl3™ competent bacterial cells

After overnight incubation a single colony was picked from each LB agar plate, for the relevant plasmid. This was mixed with 5 mL Terrific broth (with ampicillin, 100 µg/mL) and incubated at 37°C with shaking at 225 rpm for up to 8 hr. After this, 1 mL cell suspension was mixed with glycerol to a final concentration of 15% (v/v) and stored at -80°C as a stock.

3mL cell suspension was centrifuged at 3500g for 10 min to obtain a cell pellet for initial plasmid preparation and restriction digestion. If required, the remaining cell suspension was diluted ~1:500 in Terrific broth (with ampicillin, as above) and incubated overnight, in conditions as above. This larger cell culture was centrifuged at 3500g for 10 min to obtain cell pellets for larger scale plasmid preparation.

Plasmid was extracted from the initial cell pellet for restriction digestion using a QIAprep Spin Miniprep Kit as per the manufacturer's instructions. In summary, this process consisted of RNase digestion, bacterial cell alkaline lysis and neutralisation, DNA precipitation and a series of wash steps using QIAprep 2.0 spin columns and a microcentrifuge. For larger cell pellets (e.g. from the second culture) a Plasmid Maxi Kit was used to extract plasmid DNA, as per the manufacturer's instructions, following a similar process to the Plasmid Mini Kit.

Harvested DNA was quantified using a NanoDrop™ 1000 Spectrophotometer. DNA quality was assessed using the given A260/A280 and A260/A230 ratios given, whereby an A260/A280 ratio ≥1.8 was considered pure.

2.2.3.2 Restriction digest and gel electrophoresis of plasmids

To assess whether plasmid preparations contained the expected vector, restriction enzymes were used to digest plasmids at known cut sites. Enzymes used in each restriction digest are specified in Table 2-5, with the expected fragment sizes after digestion.

Construct	Backbone	Restriction digest		
		Enzyme 1	Enzyme 2	Expected fragments (kilobases)
VSVG	pMD2.G	BamHI	EcoRI	3.0, 1.5, 0.8
PAX2	psPAX2	BamHI	EcoRI	4.0, 3.0, 1.0
Scrambled control	pLKO.1	BamHI	EcoRI	6.3, 0.8
sh*NFATC2*-143	pLKO.1	BamHI	EcoRI	6.3, 0.8
sh*NFATC2*-144	pLKO.1	BamHI	EcoRI	6.3, 0.8
sh*NFATC2*-145	pLKO.1	BamHI	EcoRI	6.3, 0.8
sh*NFATC2*-146	pLKO.1	BamHI	EcoRI	6.3, 0.8
sh*Nfatc2*-356	pLKO.1	BamHI	EcoRI	6.3, 0.8
sh*Nfatc2*-357	pLKO.1	BamHI	EcoRI	6.3, 0.8
Empty vector	pMIG	NdeI	EcoRI	4.5, 2.0
o/e m*Nfatc2*	pMIG	NdeI	NotI	7.3, 2.1
o/e h*NFATC2*	pMIG	NdeI	NotI	4.5, 2.8, 2.1, 0.5

Table 2-5. Restriction enzymes used per plasmid vector for validation.
The expected fragment sizes observed on gel electrophoresis are indicated.

An agarose gel was made by dissolving 0.8% agarose into Tris-acetate-EDTA (TAE) buffer and heating in a microwave until just below its boiling point. After cooling for 10-15 min, SYBR™ Safe DNA Gel Stain was added to a final 1X concentration (1:10,000 dilution) and the solution was poured into a gel case, which contained a well comb. After setting, the gel was bathed in TAE buffer in a gel tank. 500 ng digested plasmid was mixed with Purple Loading Dye to 1X concentration (1:6 dilution) and loaded into one well per plasmid. 5 µL 1 kb Plus DNA Ladder was loaded into the final well of the gel.

The gel tank was run at 120 V for 30-60 min, until the distal bands in the loading buffer had moved ~2/3 the length of the gel. The gel was imaged using a LI-COR® Odyssey Imaging System, using the 600 nm channel. Image parameters were adjusted and images saved using ImageStudio Lite software.

2.2.3.3 Plasmid sequencing

For confirmation that plasmid preparations contained the expected sequences, plasmid DNA was sequenced externally by Eurofins Genomics. The primers used are detailed in Section 2.1.7.1. Sequencing quality was assessed visually by inspection of chromatograms using SnapGene® Viewer. Example chromatogram plots are shown in Figure 2-1. Sequences were aligned to the expected sequences, provided by Addgene and/or Merck, using the EMBOSS Needle web tool.

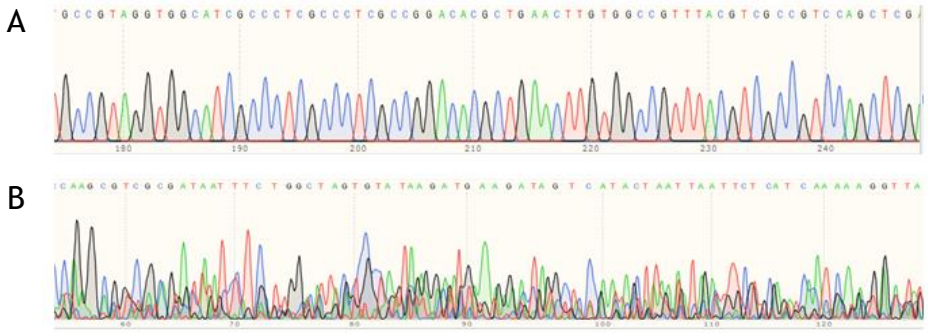

Figure 2-1. Example chromatograms from plasmid DNA Sanger Sequencing.
Two examples from Sanger Sequencing conducted on plasmid DNA, derived from SnapGene® Viewer. **A:** An example of good-quality sequencing, where base call peaks are sharp and evenly spaced per base. **B:** An example of poor-quality sequencing, as base call peaks are overlapping, irregular and not well-defined.

2.2.4 Generation of lentivirus and retrovirus

2.2.4.1 Lentivirus production using PEI-mediated transfection

Lentivirus was produced by transfection of HEK-293T cells either in 6-well plates or 10 cm^2 cell culture dishes, depending on the volume of lentiviral supernatant required.

For 6-well plate transfection HEK-293T cells were harvested from cell culture flasks using trypsin, as per the described procedure. After resuspension in culture media the cell suspension was passed through a 70 µm cell strainer, then seeded into wells at a density of $8x10^5$ cells/2 mL culture media/well. After 18-24 hr in culture the confluence of cells was inspected visually; transfection proceeded if cells were approximately 70-90% confluent in the well.

Around 1 hr prior to transfection the media was gently replaced with 1.5 mL culture media/well. Plasmids were complexed with PEI (1 mg/mL) in a total mass ratio of 12 µg PEI to 4 µg total DNA/well of HEK-293T for transfection. Plasmid details are in Table 2-6. The 4 µg plasmid mix contained: 1.8 µg transgene (pLKO.1/shRNA), 1.8 µg packaging (psPAX2) and 0.4 µg envelope (pMD2.G) plasmids. The total volume of PEI/DNA mix/well was 250 µL. These were incubated for 20-30 min at RT, before adding dropwise to each well. Note that 1 well was transfected with a scrambled control expressing GFP as a positive transfection control.

After a maximum of 18 hr post-transfection media was gently changed to 2 mL/well and supernatant discarded. Following another 24 hr the viral supernatant was harvested and replaced with culture media, with reduced FBS to prevent over-growth of cells (DMEM with 5% FBS and 2 mM L-glutamine). At this point the GFP scrambled control well was visualised using a Zeiss microscope to observe fluorescence and estimate transfection efficiency. Finally, viral supernatant was harvested again after 24 hr. Viral supernatant from different timepoints was pooled and centrifuged at 1000g for 10 min, to pellet cells and debris. The supernatant was harvested again and stored at 4°C for up to 1 week, or -80°C for long-term storage.

For transfection in 10 cm^2 dishes the process was similar, but with differing DNA and PEI quantities, and volumes of supernatant. Each plate was transfected with

48 µg PEI and 16 µg plasmid (8 µg transgene, 6µg packaging and 2 µg envelope). Cells were seeded in 7.5 mL culture media per well and transfected in 5 mL media, with 1 mL of PEI/DNA mix. Supernatant was replaced with 7.5 mL culture media for subsequent viral harvests.

2.2.4.2 Retrovirus production using PEI-mediated transfection

Retrovirus was produced in the same manner as lentivirus, using the phoenix-AMPHO cell line instead of HEK-293T. Phoenix-AMPHO cells were seeded in culture media (DMEM with 10% FBS and 2 mM L-glutamine) excluding selection antibiotics. There was no requirement for transfection of packaging or envelope plasmids due to endogenous expression. Retroviral plasmid details are in Table 2-6. PEI/DNA quantities used were as follows: 5.4 µg PEI and 1.8 µg transgene plasmid per well of a 6-well plate, or 24 µg PEI and 8 µg transgene plasmid per 10 cm^2 dish. Otherwise, the transfection process was the same as for lentivirus.

Construct	Retro/ lentivirus	Function	Backbone	Supplier	Catalogue #/ID	shRNA sequence (if applicable)
VSVG	Lentivirus	Viral envelope	pMD2.G	Addgene	12259	N/A
PAX2	Lentivirus	Viral packaging	psPAX2	Addgene	12260	N/A
Scrambled control	Lentivirus	Non-targeting shRNA	pLKO.1	Merck	SHC002	N/A
Scrambled control (with GFP)	Lentivirus	Non-targeting shRNA/GFP control	pLKO.1	Merck	SHC001	N/A
sh*NFATC2*-143	Lentivirus	h*NFATC2*-targeting shRNA	pLKO.1	Merck	TRCN0000016143	CCGAGTCCAAAGTTGTGTTTA
sh*NFATC2*-144	Lentivirus	h*NFATC2*-targeting shRNA	pLKO.1	Merck	TRCN0000016144	CGCCAATAATGTCACCTCGAA
sh*NFATC2*-145	Lentivirus	h*NFATC2*-targeting shRNA	pLKO.1	Merck	TRCN0000016145	GCACATCATGTACTGCGAGAA
sh*NFATC2*-146	Lentivirus	h*NFATC2*-targeting shRNA	pLKO.1	Merck	TRCN0000016146	CCTCTTCGACTATGAGTATTT
sh*Nfatc2*-356	Lentivirus	m*Nfatc2*-targeting shRNA	pLKO.1	Merck	TRCN0000012356	GCCCGTGAAAGTCAACTTCTA
sh*Nfatc2*-357	Lentivirus	m*Nfatc2*-targeting shRNA	pLKO.1	Merck	TRCN0000012357	CCCTATCGAAGAAGAACCGAT
Empty vector	Retrovirus	Overexpression (empty) backbone	pMIG	Addgene	9044	N/A
o/e m*Nfatc2*	Retrovirus	Overexpression of m*Nfatc2*	pMIG	Addgene	11100	N/A
o/e h*NFATC2*	Retrovirus	Overexpression of h*NFATC2*	pMIG	Addgene	74050	N/A

Table 2-6. Table of lentiviral and retroviral plasmid vectors used in the study.

2.2.5 Transduction of cell lines with shRNA-containing lentivirus

Cells for lentiviral transduction were sub-cultivated 1 day prior to transduction, to allow cells to enter a log-growth phase. On the day of transduction 1 mL lentiviral supernatant was added to each well of a 6-well plate and incubated at 37°C for up to 1 hr, to allow equilibration of temperature and coating of the wells.

Cell suspension was centrifuged at 300g for 5 min and resuspended in transduction medium, which consisted of standard culture media with double the recommended concentration of FBS and 16 µg/mL of hexadimethrine bromide (also known as Polybrene). 1 mL cell suspension was added to each well containing lentiviral supernatant (1:1 volumetric ratio; final Polybrene concentration 8 µg/mL). Plates were wrapped in Parafilm® and centrifuged at 900g for 30 min, before returning to incubation at 37°C with 5% CO_2.

After 18-24 hr the cell suspensions with lentivirus were centrifuged at 300g and resuspended in an equivalent volume of standard cell culture media plus puromycin, for selection of transduced cells, as indicated in Table 2-7. The concentration of puromycin used was determined empirically using kill curves (Figure 2-2). The puromycin concentration for THP-1 had been determined in previous work by Dr. Matthew Massett.

Cell line / cells	Puromycin concentration (µg/mL)
THP-1	2.5
MOLM-13	1.0
MV4-11	1.5
NOMO-1	3.0
HL-60	4.5
OCI-AML3	2.0
Kasumi-1	3.0
MLL-AF9 murine BM	1.5

Table 2-7. Puromycin concentrations used for selection in each cell line.
The concentration of puromycin required to achieve '0' cell count 24 hr after treatment for each cell line (or for MLL-AF9 murine bone marrow (BM)).

Cells were counted (see Section 2.2.8.1) immediately prior to resuspension in puromycin media ('0 hr post-selection') and counted 24 hr later, to determine the selection and efficiency of transduction. The puromycin media was replaced again at 24 hr post-selection, as above, and counted again at 48 hr post-selection. If measurement at timepoints later than 72 hr post-selection were required, the puromycin media was replaced again at 72 hr post-selection, as above.

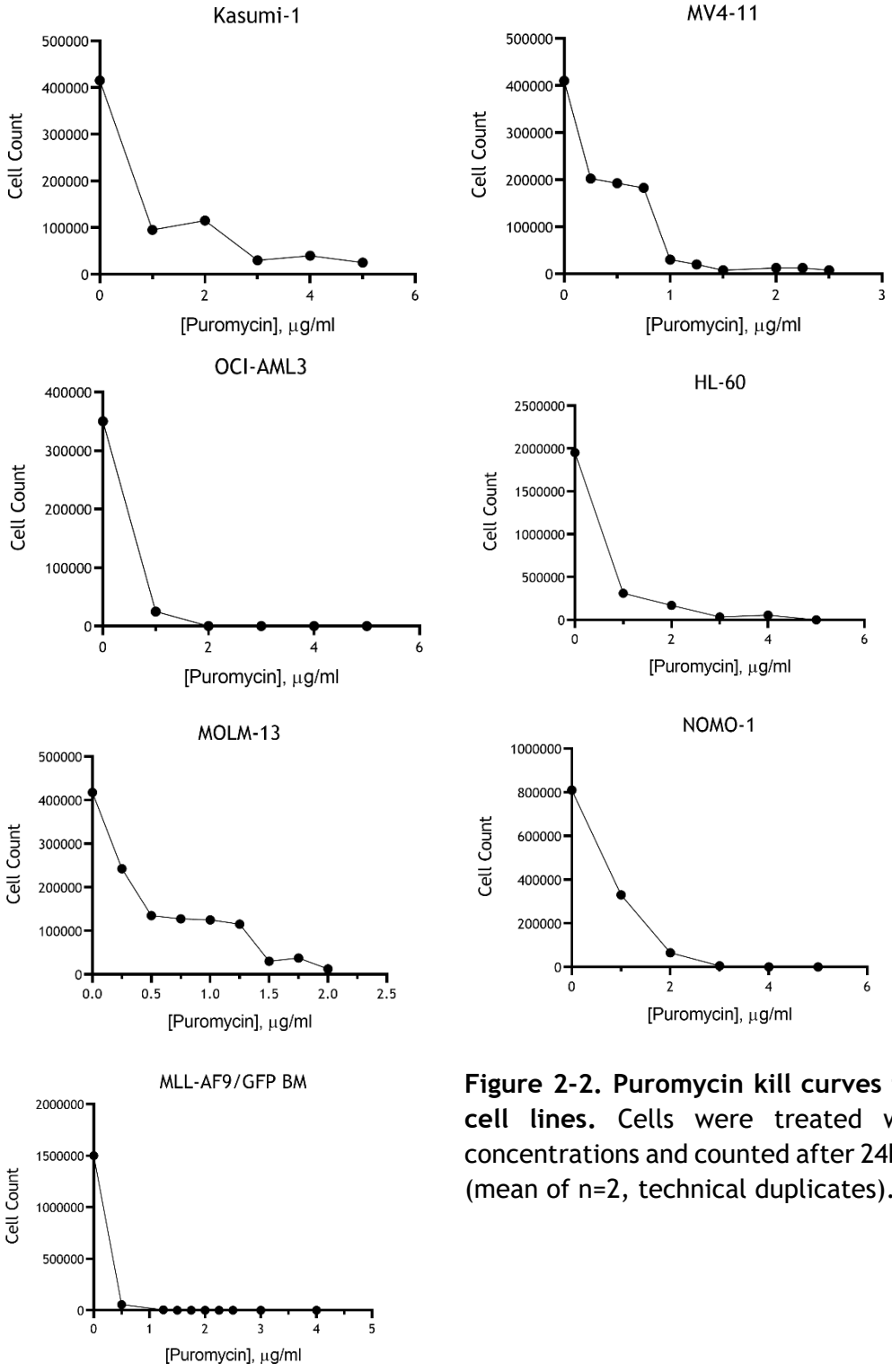

Figure 2-2. Puromycin kill curves for selected cell lines. Cells were treated with varying concentrations and counted after 24hr in culture. (mean of n=2, technical duplicates).

2.2.6 Establishment of stable vector expression in cell lines

2.2.6.1 Transduction of cell lines with retrovirus

After 24 hr of transduction, cells were resuspended in the appropriate culture media for the cell line, without antibiotics.

48 hr from centrifugation, cells were assessed for GFP expression using flow cytometry. If >0.1% GFP expression was observed in the live cell population, GFP^+ cells were selected using either a dilution method or fluorescence-activated cell sorting (FACS), to achieve a homogenous GFP^+ population.

In the dilution method, cell suspensions were diluted to 5 cells/mL and pipetted into a 96-well plate at 100 µL/well with the aim of achieving 1 cell/2 wells and therefore maximise the likelihood of any well being inoculated with single cells. Cells were incubated at 37°C with 5% CO_2 for 2-4 weeks, during which time the media was refilled to prevent drying out.

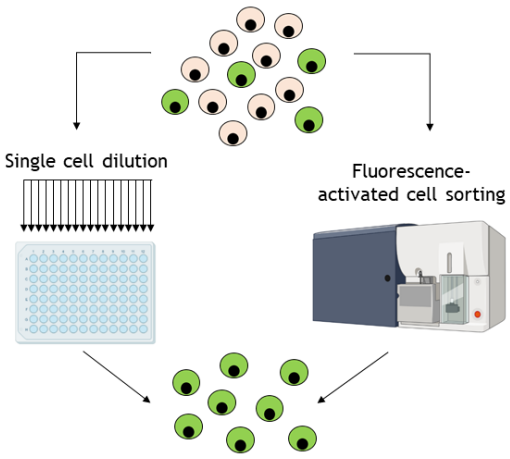

Figure 2-3. Schematic of GFP^+ cell selection. Made in Biorender.

Upon observation of cell growth, using an inverted light microscope, wells containing expanded cell populations were sampled for flow cytometry. These samples were assessed for GFP expression and any population exhibiting >90% positivity in their live population was taken forward for further incubation and expansion in culture.

Alternatively, samples were sorted to isolate the GFP^+ population by flow cytometry. GFP-selected cells, using either method, were expanded in culture and validated for GFP expression using flow cytometry, before cryopreservation in freezing media (RPMI with 30% FBS and 5% DMSO) for liquid nitrogen storage. These methods of GFP^+ cell selection are shown schematically in Figure 2-3.

2.2.7 Phenotypic cell assays and measurements

2.2.7.1 Cell counting

Cells were counted using Trypan Blue dye exclusion. Trypan Blue (Merck) solution (0.4% v/v) was mixed with cell suspension in a 1:1 ratio and incubated for up to 5 min. 10µL of the mix was pipetted into a haemocytometer and visualised using an inverted light microscope with phase contrast (Figure 2-4). The number of cells counted in one 4x4 grid (each highlighted in blue) gives the density in 100 nL of liquid. In each 4x4 grid, cells overlapping the edges must only be counted on 2 of the edges (e.g., the outer edges only), to avoid double counting. To calculate the cell density in the original sample an average of counts from all 4 corner grids is taken, then corrected for the 1 in 2 dilution with Trypan Blue. Multiplying this value by $1x10^4$ provides the cell density/mL.

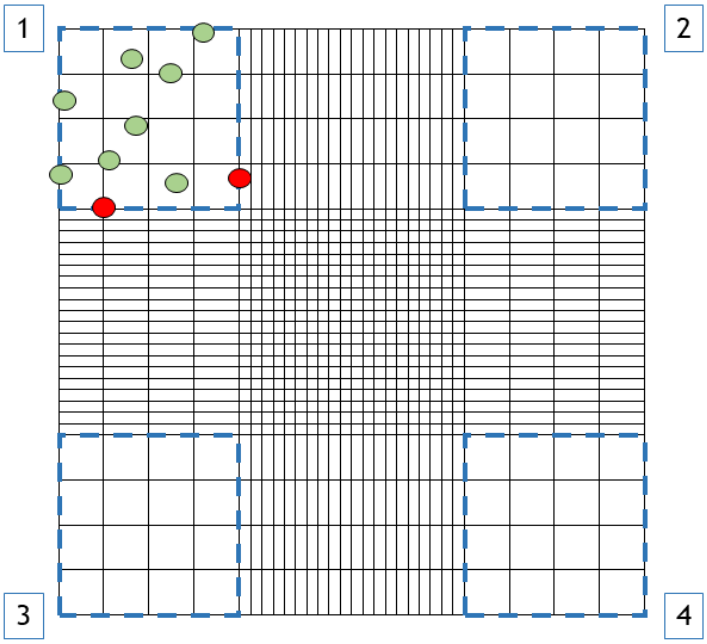

Figure 2-4. Example haemocytometer grid for cell counting.
The diagram represents the haemocytometer grid layout. The cells were counted in the numbered (blue) 4x4 grids. In grid 1 there are some example cells, whereby green cells can be included in the count and red cells cannot - cells overlapping the inner edges of the 4x4 grid are not counted.

2.2.7.2 Colony-forming cell (CFC) assays

For seeding human cells, MethoCult™ H4230 was used as a semi-solid medium, while MethoCult™ M3231 was used for murine cells. Both medias were cytokine-free. Prior to use, MethoCult™ was mixed with IMDM to a final concentration of 20% (v/v) IMDM. After cell counts, 1000 cells were mixed with 100 µL RPMI. If required for the experiment, puromycin was added at the desired concentration and mixed using a 1 mL syringe and a 19G needle. The 100 µL cell suspension was later added to 900 µL of MethoCult™/IMDM mix. Each mix was then left for 5 min to allow bubbles to rise to escape the solution. A summary of the cell/media mix is shown in Figure 2-5.

Each of 6 wells of a 24-well plate was scored along the bottom using a scalpel, to create a grid for counting colonies against (Figure 2-5). Each 1 mL of cell/media mix was divided between 3 wells using the syringe (~300 µL/well), providing technical triplicates/condition. The surrounding wells were filled with 1 mL PBS. The plate was incubated at 37°C with 5% CO_2 until sufficient colonies had formed, at least in control samples. This period was determined for each cell line and ranged from ~7-12 days post-seeding.

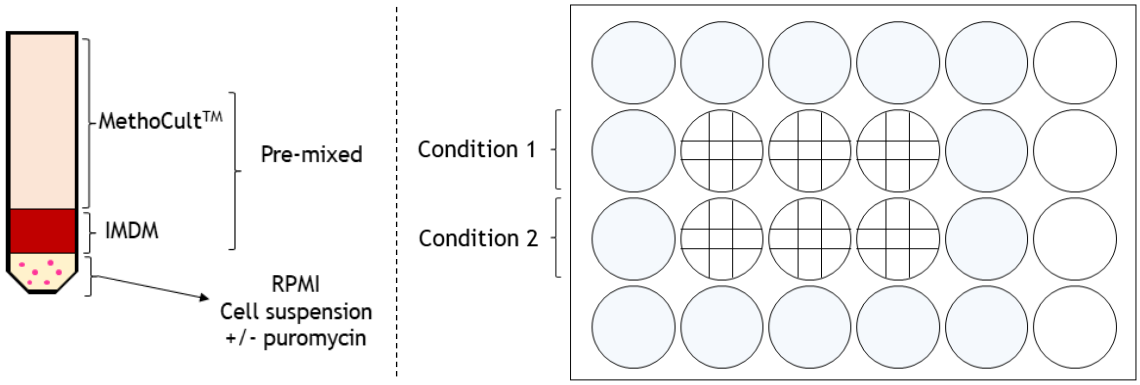

Figure 2-5. Schematic diagram of CFC assay setup.
On the left-hand side is a representative diagram of the cell/media mix used in each CFC assay. On the right-hand side is a plate layout, showing scored wells and position of PBS-filled wells. Each condition is laid out in technical triplicate.

Colonies were imaged and counted using an EVOS cell imaging system. Scale bars were added retrospectively using a reference size image. Cell clusters with >50 cells were counted as colonies and their morphology used to classify the type of colony.

2.2.7.3 Cytospin preparation for cell morphology

For visualisation of individual cell morphology, cells were centrifuged onto slides using a Shandon Cytoclip system. The sample chamber was attached to a SuperFrost® slide using the cytoclip and a piece of filter card was inserted between the slide and sample chamber. Cell suspension was diluted to $2x10^5$/mL and 100 µL was loaded into the sample chamber. The assembled slide/clips were inserted to a cytospin centrifuge and centrifuged at 450g for 5 min, then allowed to air-dry at RT.

Each slide was fixed in methanol for 10 min and allowed to air-dry for 5 min. May-Grünwald and Giemsa stains were diluted in Sorensen's phosphate buffer (Section 2.1.6.1), 2X and 10X respectively. Both stains and Sorensen's buffer were poured into separate glass chambers. Slides were incubated in diluted May-Grünwald stain for 30 min and then immediately incubated in diluted Giemsa stain for 30 min. Next, slides were gently rinsed in tap water and incubated in Sorensen's buffer for 3 min, prior to further gentle rinsing in tap water and air-drying overnight at RT.

Finally, a drop of Pertex® mounting medium was added over the cells on each slide, and a glass coverslip placed on top. These were allowed to set overnight before imaging using an EVOS cell imaging system at 40X magnification. Scale bars were added retrospectively using a reference size image.

May-Grünwald and Giemsa stains were used to identify morphological features of cells. Basic dye components, such as methylene blue, stain acidic structures in the cell such as DNA. Acidic dye components, which includes eosin, stain basic proteins such as those found in cytoplasmic granules (Mopin *et al.*, 2016). For example, a typical monocyte would show a large, round nucleus and a pale granular appearance in the cytoplasm (Young, 2006).

The area of individual cells was quantified using ImageJ software. Each image size was quantified using the scale bar as a reference. The 'Analyze Particles' feature was used to highlight cells and area quantification was produced automatically. Cells on the image edges or those with a highly irregular appearance were removed from analysis. Technical replication was not used in cytospin analyses.

2.2.7.4 Alamar Blue assay

Alamar Blue dye contains resazurin, which is non-toxic to cells and cell-permeable in addition to being non-fluorescent in its native state. Resazurin readily accepts electrons from cellular metabolic activity and is also reduced by various enzymes, which leads to formation of the highly fluorescent resorufin (Rampersad, 2012). As such, Alamar Blue was used to measure the metabolic activity and so viability of cells in culture after various treatments.

At the experimental timepoint cell suspensions were mixed with Alamar Blue to 50μM and pipetted into a 96-well flat-bottomed plate, with each condition in technical triplicate. A media-only control was used on each plate. Cells were incubated at 37°C with 5% CO_2 for 4 hr. Finally, the fluorescence was measured using a SpectraMax® M5 Plate Reader at $535nm_{Ex}$ and $590nm_{Em}$. The reading for each well was corrected using the media-only control.

2.2.7.5 Treatment of cells with compounds

Inhibitors were pre-diluted in the appropriate diluent so that each condition would contain the same final concentration of solvent. A vehicle control was included for every experiment. Pharmacological information on calcineurin-NFAT inhibitors are shown in Table 2-8.

The control and treatments were added to cell suspensions and mixed thoroughly. The cell phenotype was then assessed using various assays, including Alamar Blue viability assays to estimate the IC_{50}. To estimate the IC_{50} the fluorescence measured per condition was normalised to the vehicle control as a %. Using the '[Inhibitor] vs. normalized response – Variable slope' algorithm in GraphPad Prism a sigmoidal curve was fitted to the data, constrained between 0% and 100%. The IC_{50} was calculated using this curve.

Inhibitor	Target Molecule	Mechanism of Action	Licenced Clinical Uses (UK)
Cyclosporine A	Calcineurin (CnA and CnB subunits)	Formation of a ternary complex with cyclophilin A and calcineurin. Binding blocks access of phosphatase site to substrates. (Huai *et al.*, 2002)	Organ and BM transplantation; severe inflammatory conditions
VIVIT-11R	Calcineurin (NFAT docking site)	Mimics PxIxIT domain of NFAT1-4. Binds to calcineurin at NFAT-docking site and blocks calcineurin-NFAT interaction. (Aramburu *et al.*, 1999)	None
INCA-6	Calcineurin (NFAT docking site)	Shown to displace VIVIT from calcineurin binding *in vitro*: blocks calcineurin-NFAT interaction (putative). (Roehrl *et al.*, 2004)	None

Table 2-8. Inhibitors of calcineurin-NFAT signalling.
The molecular targets of selected inhibitors of the calcineurin-NFAT signalling axis, their mechanism(s) of action and any licensed uses in the clinic (UK only) are shown. Publications evidencing these are given.

2.2.8 Flow cytometry

2.2.8.1 General data acquisition and gating strategies

Analyses of cells using flow cytometric assays was conducted on a FACSCanto™ II. Data were acquired using BD FACSDiva™ software and analysed using FlowJo software. The appropriate machine settings were determined using unstained, single stained and isotype controls as indicated. Compensation matrices were determined using single stained cell samples, or compensation beads.

To analyse the fully stained cells, doublets were first excluded using the FSC-A vs. FSC-H plot, where for single cell events these parameters should have a linear relationship. The FSC-A vs. SSC-A plot was then used to identify homogenous population(s) and gate on these, excluding debris. If required, live cells were gated by excluding cells which absorbed a viability dye, such as DAPI (Figure 2-6).

Note also that technical replication was not used for any flow cytometry assays.

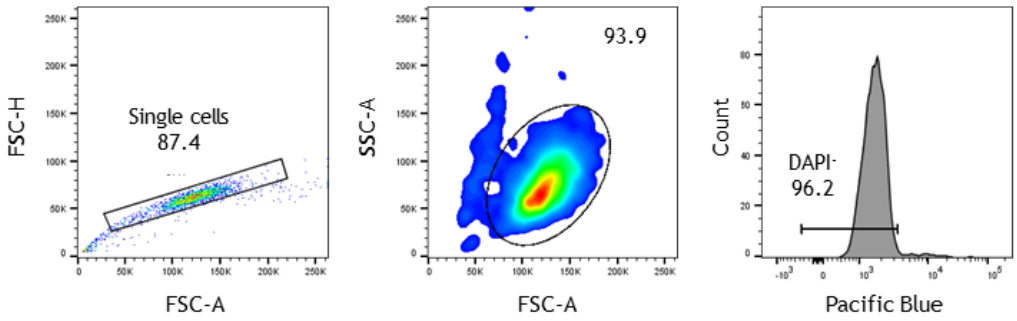

Figure 2-6. General gating strategy for flow cytometry.
Plots from FlowJo illustrate the general gating strategy for DAPI-stained THP-1 cells. Left to right: selecting single cells, excluding debris, excluding dead ($DAPI^+$) cells.

2.2.8.2 Annexin V apoptosis assay

1-5x10^5 cells were pelleted at 300g for 5 min. Cells were washed by resuspending in 0.5 mL HBSS and after aspirating HBSS, the cell pellet was resuspended in a solution with 1 μL Annexin V (conjugated to FITC or APC) per 100 μL 1X annexin binding buffer and 1 μg/mL DAPI. Annexin V-APC was used instead of Annexin V-FITC when assessing cell lines expressing GFP.

Cells were incubated in the staining solution for 15 min at RT and then pelleted as above, before resuspending in 100 μL HBSS and transferring to a tube for analysis.

Events were gated by isolating single cells using the FSC-A vs. FSC-H plot, as described previously. Cells were gated by size (FSC-A vs. SSC-A) to capture all live and dead cells but exclude debris. The DAPI vs. Annexin V plot was used to divide cells into four quadrants; whereby DAPI discriminates live and dead cells, and Annexin V discriminates apoptotic cells. $DAPI^+$ Annexin V^- cells were denoted as necrotic. This gating strategy is shown in Figure 2-7.

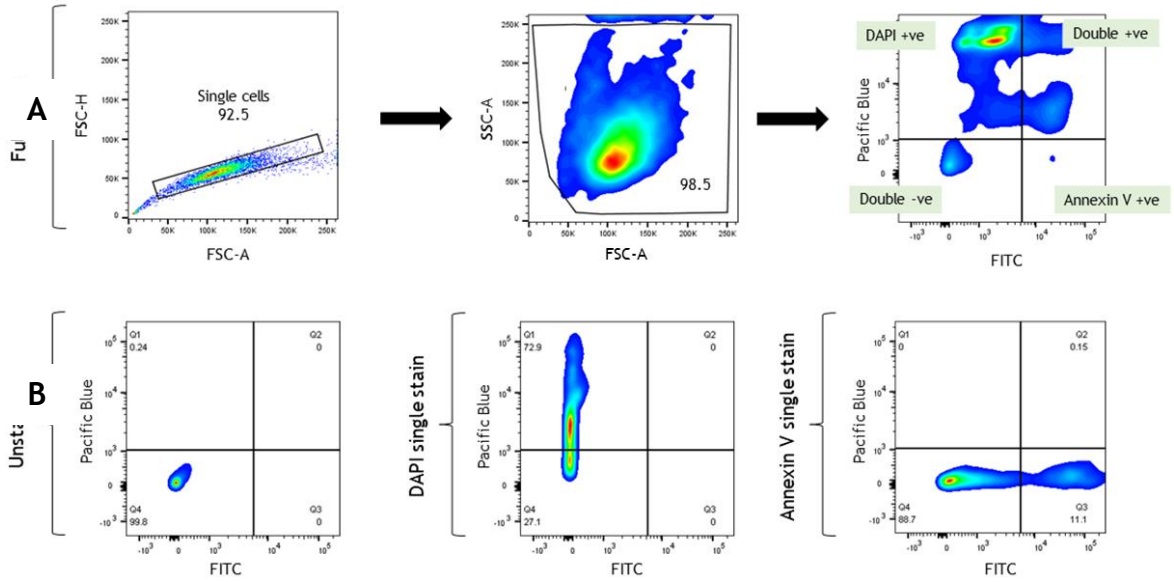

Figure 2-7. Gating strategy for Annexin V apoptosis assay.
A: FlowJo plots illustrate the gating strategy for THP-1 cells. To generate dying cells as a positive control, THP-1 cells were heated at 95°C for 5 min, and then stained with Annexin V-FITC and DAPI. Left to right: selecting single cells (FSC-A vs. FSC-H), excluding debris (FSC-A vs. SSC-A), quadrant gating for Annexin V^+/$DAPI^+$ cells. **B:** Quadrant plots as described in A: unstained cells (left), DAPI stain only (middle), Annexin V stain only (right).

2.2.8.3 PI staining for cell cycle analysis

0.5-1.x10^6 cells were harvested and pelleted at 300g for 5 min. Cells were then washed twice in PBS. To fix cells, the cell pellet was resuspended in 500 µL ice cold 70% ethanol/PBS solution, by dropwise addition with vortexing, to prevent aggregation.

The cell fixation mix was incubated for a minimum of 24 hr at -20°C. Cells were washed twice by centrifuging at 850g for 5 min and resuspending in PBS. The final cell pellet was resuspended in 250µL 40 µg/mL PI and 20 µg/mL RNase A in H_2O and mixed by pipetting. The staining cells were incubated at 37°C for 20-30 min. Finally, 150µL HBSS was added and cells transferred to cytometry tubes for analyses.

PI-stained cell data was acquired on the flow cytometer at the lowest flow rate, for optimal signal acquisition. Cells were gated as described above. The cell size was different from native cells, due to fixation.

Gated cells were plotted using a histogram in the PE channel, on a linear scale. The signal/cell represents the quantity of DNA present, thereby allowing separation of cells by phase of the cell cycle. Gates were set on each region of the plot, corresponding to these (Figure 2-8).

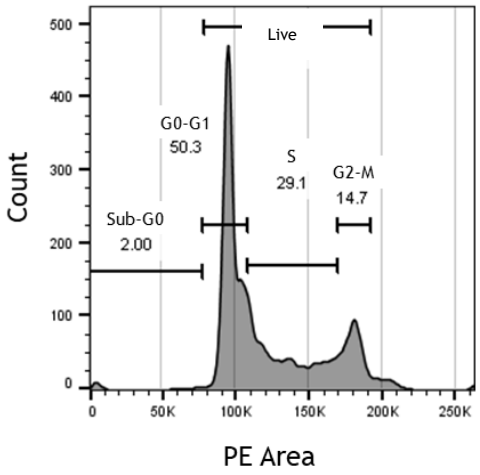

Figure 2-8. Cells stained with PI were gated into cell cycle phases. Shown are the gates applied to the PE histogram, gated from single cells and excluding debris. The data were then presented as fractions of 'live' cells. Voltages were adjusted so that the prominent G0/G1 peak and smaller G2/M peak were visualised centrally. The region between these was denoted as cells in the S-phase and cells below the G0/G1 peak were denoted as 'sub-G0/G1' cells. Cells beyond the G2/M peak were excluded from analysis.

2.2.8.4 BrdU assay for cell cycle analysis

BrdU is a thymidine analogue and can incorporate into DNA when cells are undergoing mitosis, during the S-phase. Detection of incorporated BrdU is another means of determining cell cycle status of cells, in a cumulative manner.

The buffers used in this assay are detailed in Section 2.1.6.4. BrdU stock (in DMSO) was added to cell suspension ($2x10^5$ cells in 1 mL/condition) to 10 µM and incubated at 37°C with 5% overnight. Cells without BrdU were incubated also, as a negative control. Next, cells were washed 2x by centrifuging at 500g for 5 min and resuspending in PBS with 3% (v/v) BSA. To permeabilise and fix, the pellet was resuspended in 250 µL permeabilisation/fixation buffer and incubated in the dark for 30 min, on ice.

Cells were centrifuged at 800g for 5 min and washed again with PBS/3% BSA, before resuspension in 1 mL freezing buffer. Cells were left overnight at -80°C. These were thawed rapidly at 37°C in a water bath and pelleted again by

centrifuging at 800g for 5 min, before resuspension in 250 µL permeabilisation/fixation buffer and 10 min incubation on ice.

DNA was fragmented by pelleting and resuspension in 100 µL of a DNase I solution, allowing 6 µg DNA per condition, before incubating at 37°C for 1 hr. Cells were washed in wash/permeabilisation buffer and resuspended in 100 µL buffer with anti-BrdU antibody, conjugated to APC, at 1:50 dilution. DAPI was also added at 1:500. After 30 min incubation at RT, in the dark, cells were washed 1x in wash/permeabilisation buffer and prepared in tubes for flow cytometry.

As described for other assays, cells were gated on single cells and debris excluded. Cells were then viewed for BrdU/APC vs. DAPI/Pacific Blue and 3 panels constructed, to gate on the main phases of the cell cycle, as shown in Figure 2-9.

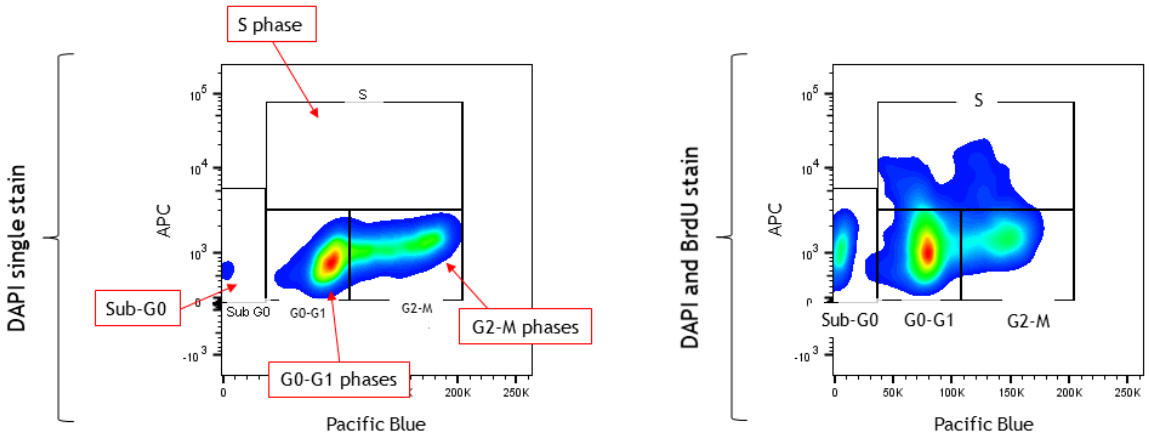

Figure 2-9. Example gating strategy for BrdU assay.
Left: DAPI single stain with labels. Right: full DAPI/anti- BrdU-APC stain.

2.2.8.5 CFSE assay for cell proliferation

CFSE stain stock solution was made by dissolving powder in DMSO to 5 mM, as recommended, then diluting the CFSE to 5 µM in the appropriate base medium for the desired cell line. $2x10^5$ cells were dissolved in 1 mL staining medium and incubated at 37°C with 5% CO_2 for 20 min, before adding 5 mL of complete cell culture medium, to inhibit the reaction. Cell suspension was then centrifuged at 300g for 5 min and resuspended in 1 mL complete culture medium and returned to incubation at 37°C with 5% CO_2.

To establish a baseline fluorescence signal, up to 500 µL of cell suspension were stained with DAPI and analysed by flow cytometry. After viability and size gating, a histogram of FITC signal was used to visualise the CFSE stain and the voltage set to position the main peak at the far-right side.

This process was repeated for every timepoint of interest, using the same voltages, and the signal compared to the baseline to visualise proliferation (Figure 2-10). The fold change in signal was calculated per sample using the geometric mean signal in the FITC channel. Conversion to $\log_2$ fold change gave the estimated number of cell divisions.

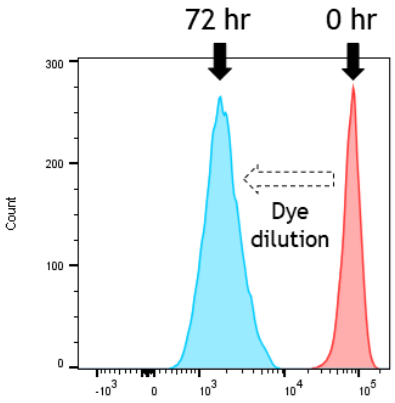

Figure 2-10. Example CFSE data.

2.2.8.6 Cell sorting

Sorting of GFP-expressing cells was conducted with the technical support of Ms. Jennifer Cassells. 24 hr prior to sorting, cell medium was supplemented with penicillin-streptomycin to 100 U/mL, to minimise risk of contamination, and maintained in this for 48 hr after.

Cells were sorted using a FACSAria™ III. Cells were gated by size and on live cells, and GFP^+ cells were selected for separating on the FITC channel. Bulk cells were sorted into a single culture and their GFP expression measured after sufficient outgrowth, using a FACSCanto™ II.

2.2.9 Protein analysis

2.2.9.1 Whole cell lysate (WCL) protein extraction

To obtain WCL, cells were washed twice in PBS by centrifuging at 300g for 5 min at 4°C and then the cell pellet was resuspended in 50 µL 1 mM DIFP per $1x10^6$ cells. DIFP is a potent serine protease inhibitor, which was used during lysis due to the high protease activity of myeloid cells. Cells were incubated on ice for 30 min before centrifuging at 300g for 5 min, at 4°C.

DIFP was aspirated and the pellet resuspended in RIPA buffer (Section 2.1.6.3). Buffer was prepared freshly immediately prior to extraction. The cell/RIPA buffer mix was vortexed at high speed for 10 sec and then incubated on ice for 30 min, with occasional vortexing. The mix was centrifuged at 16,000g for 20 min, to separate remaining precipitates, and the cell lysate was aspirated. Lysates were stored at -80°C.

2.2.9.2 Cell fractionation

Lysates from the cytoplasmic and nuclear fractions of the cell were obtained using a protocol, adapted from that described by Healy and O'Connor (Healy and O'Connor, 2009). The cell pellet was stored at -80°C for at least 72 hr and then frozen and thawed using liquid nitrogen three times, to weaken the outer cell membrane. These cells were then resuspended in 50 µL/$1x10^6$ cells of hypotonic lysis buffer (see 2.1.6.3). Cells were vortexed at medium speed for 10 sec and incubated on ice for 10 min, before centrifuging at 2.300g for 2 min, at 4°C, to pellet the nuclei. The supernatant, containing cytoplasmic lysates, was pipetted into separate tubes. DIFP (0.1 mM) was added immediately to the cytoplasmic lysates, to block protease activity.

The pelleted nuclei were resuspended in 50 µL/$1x10^6$ cells of RIPA buffer and vortexed at high speed for 10 sec, before incubating on ice for 30 min, as for WCL. These were centrifuged as described previously and the supernatant, containing nuclear lysates, was harvested by pipetting. Lysates were stored at -80°C.

2.2.9.3 Protein quantification: Bradford assay

A set of standards was prepared using BSA and kept at -20°C for repeated use. These ranged in concentration from 25-2,000 µg/mL. A H_2O-only and a buffer-only sample was also quantified in each run as controls. The buffer-only sample was used to subtract background absorbance from all samples and the H_2O was used to set the origin of the standard curve.

2.2.9.4 Western blotting

Equal quantities of protein were loaded for each sample. Western blots were run and transferred in a Mini Gel Tank and loaded into NuPAGE™ 4-12%, Bis-Tris, 1 mm protein gels as described by the manufacturer. MOPS SDS running buffer was used to run the gel, alongside a PageRuler™ Plus Prestained Protein Ladder. The gel was run at 120-140 V for 1-1.5 hr, and the protein was transferred at 10 V for 1 hr, onto nitrocellulose membranes.

Protein bands were visualised on the membrane by soaking in 0.1% Ponceau S solution for >1 min and were inspected to determine the evenness of transfer.

Membranes were rinsed using TBST and then blocked in 5% BSA/TBST for 1 hr, to prevent non-specific binding of antibodies. Antibody solutions were prepared in 5% BSA/TBST solution, with dilutions based on the manufacturer's recommendations (Section 2.1.5.10).

After blocking the membranes were incubated with the appropriate antibody solution and placed on a rocker at 4°C overnight. If multiple antibodies derived from the same species were tested on the same membrane, the membrane was cut along expected size boundaries, using a scalpel, to separate proteins of interest.

After antibody incubation the antibody solution was removed, and the membranes washed twice using TBST. Secondary antibodies with fluorescent conjugates were used to visualise these, by diluting these in TBST 1:1000. Membranes were placed in secondary antibody solutions for 1 hr at RT and washed twice as described previously.

Technical replication was not used for any Western blotting.

Each membrane was visualised using a LI-COR® Odyssey Imager, with ImageStudio software. Images were processed for maximum visual quality in ImageStudio Lite software.

If re-probing of any membrane was required, ReBlot Plus Strong Antibody Stripping Solution was used to strip the membrane of existing antibodies. The membrane was blocked using 5% BSA/TBST as before, for 15 min, before rinsing with TBST briefly. The membrane was submerged in stripping buffer (1X, dissolved in H_2O) and placed on a rocker for 10 min. It was then washed twice with TBST for 10 min, as before, and finally re-probed using primary and secondary antibodies.

2.2.10 Immunofluorescence

Visual detection of protein was carried out on fixed cells using antibodies with fluorescent conjugates. Multi-spot microscope slides were coated with 30 µL PLL solution/spot and left for at least 1 hr at RT. After removing the PLL each spot was washed in 20 µL PBS, for 2-5 min.

Cells were taken from culture and prepared as suspensions of $6x10^4$ cells/20 µL, which were then pipetted onto a PLL-coated slide spot. After 45 min cells were removed, washed once with PBS (as described previously) and fixed in 30 µL 4% (w/v) paraformaldehyde solution, for 10 min. After removing fixative, the fixed cells were washed on the slide in PBS 3 times. Cells were then permeabilised using 20 µL 0.5% Triton-X100/PBS, and incubated for 15 min at RT.

After removing Triton-X100, cells were washed in PBS. IF blocking solution (Section 2.1.6.6) was added at 20 µL per spot and left to incubate for 1-2 hr. Meanwhile, primary antibodies were diluted 1:500 in IF blocking/antibody solution. Once the block was removed and cells washed in PBS, 20 µL primary antibody was added per spot. These were incubated overnight at 4°C, in a chamber humidified with wet paper towel, to prevent drying out.

After removal of primary antibodies, each spot was washed 5x using 0.1% TWEEN® 20/PBS (PBST), to remove background antibody binding. Secondary antibody solutions with fluorescent conjugates (Section 2.1.5.12) were pipetted on at 20 µL/spot and incubated for 1 hr at RT, in the dark. After removal and washing as before, a drop of ProLong™ Diamond Antifade Mountant with DAPI was added to

stain the DNA. A glass cover slip was placed over the spots and allowed to set overnight at 4°C. Finally, the slide was sealed using nail polish.

A Zeiss Axio Imager M1 Epifluorescence and Brightfield Microscope was used to visualise and image slides, using AxioVision Rel 4.8.2 software. Images were taken at 40x and 100x magnification, the latter of which required a drop of immersion oil to be placed on the slide. Each spot was imaged in 15 'stacks' and the best image selected, with scale bars added in the software.

2.2.11 Extracting and processing RNA

2.2.11.1 RNA extraction

For cell numbers >$5x10^5$ RNA was extracted using an RNeasy® Mini Plus Kit. For cell numbers <$5x10^5$ an RNeasy® Micro Plus Kit was used. Both extractions were carried out as described in the manufacturer's instructions. Of note, lysates were homogenised using QIAshredder spin columns as per protocol to maximise the concentration of RNA isolated. Genomic DNA (gDNA) was removed using the spin columns supplied with the RNeasy® kits. The RNA sample was eluted using RNase-free water.

RNA was quantified using a NanoDrop™ 1000 spectrophotometer. The RNA quality was assessed using the given A260/A280 and A260/A230 ratios given. An A260/A280 ratio ≥2.0 was considered to be pure.

2.2.11.2 cDNA synthesis

RNA was converted to cDNA using a first-strand synthesis reaction. This was based on the two-step reaction required for the SuperScript™ IV Reverse Transcriptase.

In the first step 0.5-1.0 µg RNA was diluted in RNase-free H_2O to 11 µL in 0.2 µL thin-walled tubes. Random hexamers were diluted to 3.8 µM and a dNTP mix to 769 µM to make a final volume of 13 µL. This was incubated at 65°C for 5 min, briefly centrifuged and then cooled on ice for 1-2 min.

SuperScript™ IV was added to 10 U/µL and the provided buffer to 1X. DTT was added to 5 mM and RNaseOUT – an RNase inhibitor – to 2 U/µL, in a final volume of 20 µL. These tubes were heated as follows: 23°C for 10 min (for hexamer annealing), 52.5°C for 10 min (for cDNA synthesis) and 80°C for 10 min (for

termination of the reaction). The finished reaction was cooled to 4°C, briefly centrifuged and either used for further application or stored at -20°C.

2.2.12 qRT-PCR

2.2.12.1 Primer design

The RefSeq given in Section 2.1.7.2 & 2.1.7.3 is that which was used to generate the primer sequences using the NCBI Primer-BLAST tool. The predicted melting temperature (T_m) was set to range between 58-62°C and the desired PCR product size between 80-120 bp. For targets with multiple exons, primers sitting across at least 1 exon-exon junction were preferred, to minimise off-target amplification of gDNA. Primers which targeted all known transcript variants (excluding computationally derived variants) were also preferred. Meeting all of these criteria was not always possible and so a balance of factors was considered for each. The length of each primer was within the range of 18-24 bases.

Primers were supplied as 2 nmol lyophilised powder and diluted to 100 µM each in RNase-free H_2O, before storing at -20°C.

2.2.12.2 Data acquisition using a 384-well plate

RNA abundance was quantified by amplifying cDNA using a QuantStudio™ 7 Pro. PowerUp™ SYBR™ Green Master Mix was used to amplify cDNA targets. The master mix was diluted to 1X and primers to 500 nM, for each forward and reverse. The completed cDNA reaction mix was initially diluted 1:100 in RNase-free H_2O and then entered into the qRT-PCR reaction as 40% of the total reaction volume.

Each sample/primer combination was pipetted into a 384-well plate in technical triplicates. For each primer 1 replicate with H_2O, was used to control for primer or master mix contamination. Thermocycling conditions were as follows: 50°C for 2 min, 95°C for 2 min, and then 40 cycles of 95°C for 15 sec and 60°C for 1 min. To produce a melt curve an additional heat step was added of rapid heating to 95°C and subsequent cooling to 60°C.

2.2.12.3 Analyses of 384-well plate data

The qRT-PCR data were analysed using the $\Delta\Delta C_t$ method, which firstly compares mean C_t values (from technical triplicates) to those of selected housekeeping genes, then compares these values for test samples to those for control samples. The first step is to normalise samples and account for variation in quantity, by comparing to genes which are not expected to vary with experimental treatment. For all human genes *ACTB* and *GAPDH* were used as housekeeping genes, whereby the mean C_t values of the 2 was used. For mouse genes only *Actb* was used. The equation for this step is as follows:

$$\Delta Ct = C_t \text{ for gene of interest (GOI)} - C_t \text{ for housekeeping gene(s)}$$

The subsequent step was to compare test samples to a control sample, therefore producing a value for the difference in expression between the 2. This was calculated as follows:

$$\Delta\Delta C_t = \Delta C_t \text{ test sample} - \Delta C_t \text{ control sample}$$

The $-\Delta\Delta Ct$ value was then taken as the $\log_2$ fold change for the difference between samples.

Where there was a minimum of 3 replicates the C_t values from each were pooled and analysed together. To do so the ΔC_t for the control sample was calculated by subtracting the mean C_t of control sample replicates for the GOI from the mean C_t of the control samples' housekeeping gene(s). This provided a pooled ΔC_t control value (for example, a ΔC_t for all 3 replicates for 'vehicle control').

The $\Delta\Delta C_t$ for each individual replicate was then calculated relative to this pooled ΔC_t control value. These $\Delta\Delta C_t$ values could then be used to produce a mean ± SEM for each control and treatment sample, for statistical testing. The equation below summarises this method of pooling (Livak and Schmittgen, 2001), where the square brackets contain the calculation for the pooled ΔC_t control sample value.

$$\Delta\Delta C_t^{\text{pooled}} =$$

$$\Delta C_t \text{ control/test sample} - \Delta C_t \text{ control sample } [\text{pooled } C_t^{GOI} - \text{pooled } C_t^{housekeeping}]$$

Where only 1 replicate was available, this method was applied using the technical triplicates from the qRT-PCR plate instead of experimental replicates, producing a mean ± SD for each sample, instead of a mean ± SEM.

2.2.12.4 Multiplexed qRT-PCR

Multiplexed qRT-PCR was conducted using a Fluidigm® Biomark™ HD platform and samples were prepared for a 96x96 plate format, using the 96.96 Dynamic Array kit. Primers were designed to meet a more stringent T_m criteria of 60°C. cDNA was synthesised using 500ng of RNA per sample and these were not diluted 1:100 prior to the reaction, as for standard qRT-PCR.

To pre-amplify cDNA a QIAGEN Multiplex PCR Kit was used with a solution containing all primers pooled in H_2O, to 50nM. For each sample, cDNA was diluted with primer mix at a 1:4 ratio. These reactions were then amplified using the following parameters: 95°C for 10 min, and 12 cycles of 95°C for 15 sec and 60°C for 4 min, before a final cooling to 4°C. In order to remove primers, Exonuclease was added to the cDNA mix at 1.1 U/µL, with the appropriate reaction buffer. This was heated to 37°C for 30 min and the reaction inactivated at 80°C for 15 min, before cooling to 4°C.

The cDNA sample mixes were diluted 0.45X in a mix of DNA Binding Dye Sample Loading Reagent and SsoFast EvaGreen Supermix. Individual primers were diluted to 5 µM in separate mixes, using the provided Assay Loading Reagent and DNA Suspension Buffer. The final concentration of the primer in each reaction was 500 nM.

5 µL of each cDNA sample mix and primer solution were pipetted into separate wells, totalling 96 wells each per sample and primer. The housekeeping genes included on the plate were: *UBE2D2*, *B2M*, *ATP5B*, *TYW1*, *ENOX2*, *GAPDH* and *ACTB*. The plate was run in the machine under the conditions given below.

Phase		Number of cycles	Temperature (°C)	Duration (sec)	Ramp rate (°C/s)
1	Thermal mix	1	70	2400	5.5
			60	30	5.5
2	Hot start	1	95	60	5.5
3	PCR	30	96	5	5.5
			60	20	5.5
4	Melting curve	1	60	3	1
			60-95	-	0.33

Signals from each sample/primer reaction in the plate were visualised using the Fluidigm® Real-Time PCR Analysis Software and BioMark™ HD Data Collection Software. Melt curves and amplification curves were inspected visually to filter out low-quality data. The data were treated as for qRT-PCR, except that 7 housekeeping genes were pooled for the multiplexed data.

2.2.13 RNA-Seq

Data regarding the determination of RNA harvest timepoints, experimental quality, sample QC and read QC are described more fully in the Appendices (Section 9.2).

2.2.13.1 Data analysis

The experimental and analysis pipeline is shown in Figure 2-11. In summary, the cDNA libraries were prepared by Novogene using a Next® Ultra™ RNA Library Preparation Kit (NEB) and sequenced using a NovaSeq 6000 platform (Illumina). Novogene provided read and mapping quality statistics (Table A-1) and reads were filtered to remove adapter reads and reads with low quality base read scores (>50% of bases with a base score<5). Reads were aligned to the hg38 human genome build using the *STAR* alignment tool and then expression was quantified using the *HTseq* package, with read counts expressed as FPKM. Differential expression between samples transduced with sh*NFATC2* and the scrambled control was conducted in a pairwise manner, using the *DESeq2* R package, which utilised all 3 biological replicates in the calculation. The resulting *p* value for a difference in means was corrected in the *DESeq2* algorithm with the Benjamani and Hochberg method. Next, parsing and filtering of differential expression data, and production of most diagrams were conducted in RStudio. Tools and software are described in 2.1.2.

Scatterplots (including volcano plots) were drawn using *ggplot2* and Venn diagrams with the package *VennDiagram*, both in R. Heatmaps were created using the *heatmap* function from the base *stats* package. These were used to explore the differential expression patterns after *NFATC2* KD and identify significantly deregulated genes.

The STRING database provided information on protein-protein interactions, based on known interactions, co-expression, co-occurrence in the literature and other means of prediction. The DAVID Bioinformatics Resources website provided

functional annotation of genes, as a means of grouping significantly deregulated genes. The *SPIA* R package provided access to the 'signaling pathway impact analysis' (SPIA) platform, which detects enrichment of known pathways based on both the presence of genes in the data, and the strength of their deregulation relative to their position in the pathway. Other databases, such as KEGG and PANTHER were also used to establish enrichment of known pathways in the data, using their web tools as appropriate.

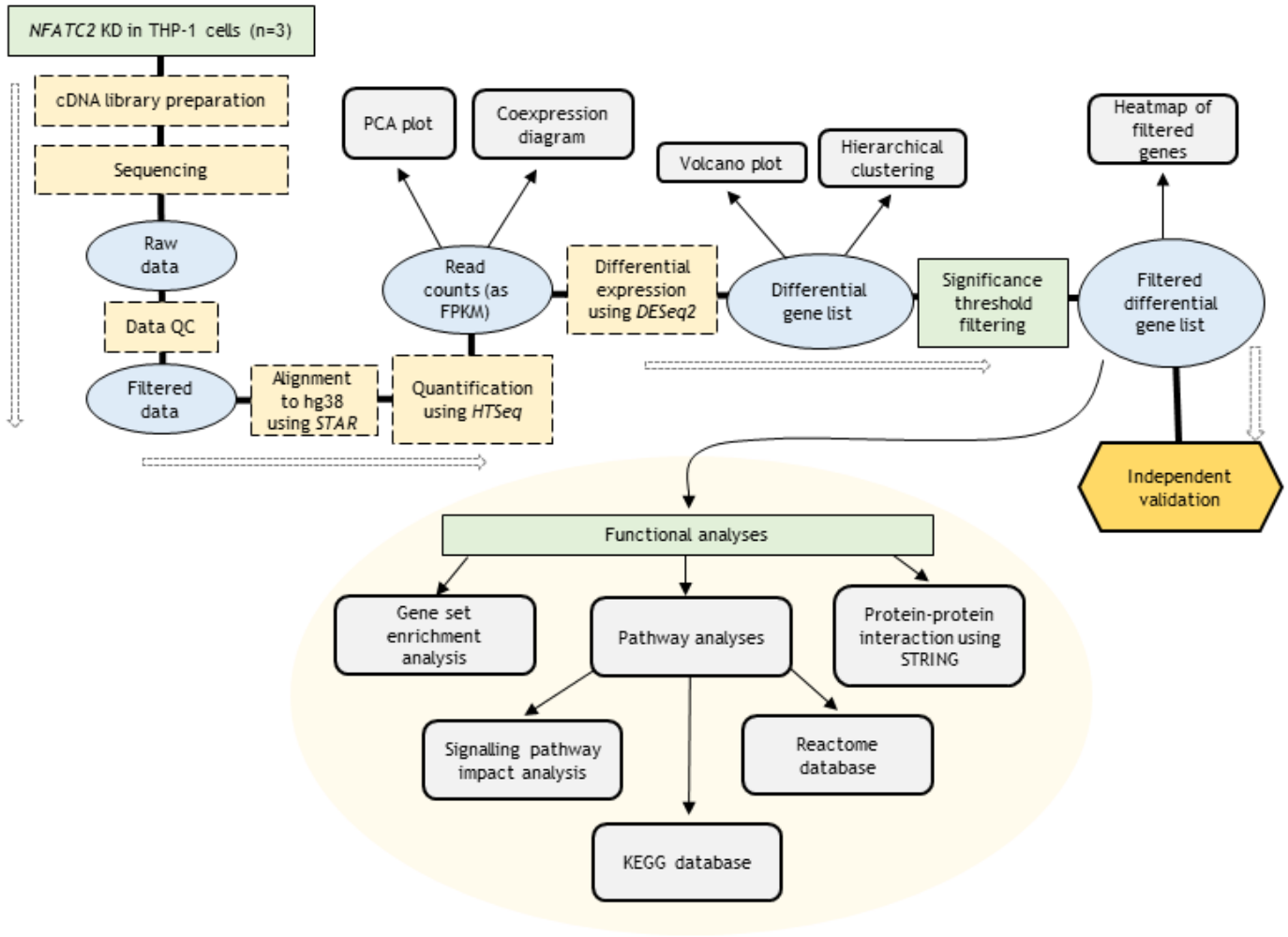

Figure 2-11. Schematic flowchart depicting the experimental and data analysis strategy for RNA-Seq data. Elements conducted by external providers are highlighted in yellow, with dotted lines.

GSEA software was used to determine patterns of deregulated expression across the whole dataset, identifying enriched pathways or putative upstream regulators of genes in the data. The genes which contribute most highly to the deviation of the enrichment statistic from zero are described as the 'leading edge subset'. This package provides multiple statistical measures of significance. The familywise error rate (FWER) is a more conservative means of determining statistical significance than false discovery rate (FDR) (Benjamini and Hochberg, 1995) and was used primarily in this study.

Note that reads can also be normalised in a way that is more optimal for differential expression between samples, which produces the trimmed mean of M values (TMM) (Robinson and Oshlack, 2010). This was used for cross-sample heatmap comparisons. TMM was derived from read counts using the *edgeR* package.

2.2.14 ChIP-Seq

NFATC2-bound DNA was precipitated from untreated THP-1 cells. The buffers and commercial reagents in this protocol are described in Sections 2.1.8.7 & 2.1.5.7. For each replicate, NFATc2, total H3 and non-targeting IgG antibodies were used. For each antibody IP, $11x10^6$ cells were lysed, with around 10% of the total being lost to input samples and shearing analyses. The experimental and analysis pipeline is shown in Figure 2-12.

2.2.14.1 THP-1 lysis

All replicates' lysates were prepared simultaneously, and cell numbers were scaled accordingly. Cell suspensions were harvested and centrifuged at 300g for 3 min, with a maximum of 18 x 10^6 THP-1 cells/50 mL tube and resuspended in 43 mL PBS, pre-warmed to 37°C. Formaldehyde was added to a final concentration of 1% before incubation for 10 min at RT and immediately supplemented with 125 mM glycine solution and agitated for 5 min, to inhibit the formaldehyde fixation reaction.

The fixed cells were centrifuged at 300g for 3 min, at 4°C, before discarding supernatant. Fixed cells were combined into one volume and resuspended in ice-cold PBS with PI/DIFP, to ~12 x 10^6 cells/mL. After washing the cell pellet was resuspended in the same volume of CLB, mixed by pipetting and incubated on ice for 10 min, to lyse the outer membrane. After centrifuging at 500g for 5 min, the

cell pellet was resuspended in ~1.5 mL NLB/100 x 10^6 cells, mixed by pipetting and incubated on ice for 10 min with frequent vortexing. Finally, cells were split into 15 mL tubes at ~33x10^6 cells/tube and DB was added to make the volume up to 1 mL each.

2.2.14.2 DNA sonication

An EpiShear™ Probe Sonicator was first cleaned using solutions of 0.1% (w/v) SDS, 0.25 M HCl and dH_2O. Each tube from the lysis step was vortexed, placed on ice and positioned with the sonicator probe just below the level of the liquid. The cells were given 30% amplitude for 30 sec/burst, for 18 bursts in total. 50 µL aliquots were taken at the end to assess adequate shearing. Sonicated samples were centrifuged at 10000g for 10 min and used immediately or stored at -80°C.

2.2.14.3 IP

Sonicated samples were diluted 1:2 using DB^{MOD}, before adding 2 µg rabbit IgG antibody/sample and rotating at 4°C, for 1 hr, 'pre-clear' samples. Meanwhile, PBST was used to wash protein G magnetic Dynabeads® twice (30 µL beads/sample), by placing the beads in a 1.5 mL tube and within a magnetic stand to separate the beads from supernatant. Beads were resuspended in 100 µL PBST. After sample/IgG incubation the washed beads were added to each sample and rotated at 4°C for 1 hr, to bind the IgG/DNA complexes.

IgG-bound DNA was removed by placing tubes in the magnetic stand and harvesting the supernatant for further IP. A sample comprising ~2% of the input quantity of chromatin was harvested as an input control sample, and stored at -20°C. Next, antibodies targeting either NFATc2, total H3 or non-targeting rabbit IgG were added to pre-cleared supernatants; 2 µg each. They were incubated overnight with rotation at 4°C. Pull-down of antibody-bound DNA was conducted using washed magnetic beads, as described for the pre-clear step, discarding the supernatant.

Beads were washed using a repetition of the following: addition of wash buffer, rotation for 5 min at 4°C, brief centrifugation, magnetic separation and discard of wash buffer. The buffers were used in the following order: WB1, WB2, WB3, TE buffer twice.

DNA was eluted from washed beads using a Diagenode IPure V2 Kit, as per protocol. Briefly, incubating in an elution buffer for 4 hr at 65°C with shaking, to induce reverse-crosslinking of DNA, and isopropanol-based wash steps. Eluted DNA was quantified using a Qubit® dsDNA HS Kit, due to the expected low quantity of yield.

2.2.14.4 DNA library preparation

A MicroPlex Library Preparation Kit was used to generate a DNA library for sequencing. This was followed as per protocol, with 12 PCR cycles. Briefly, this involves the ligation of ~140 bp adapters to the DNA ends and PCR amplification. The libraries were then purified using AMPure® XP beads, which removes contaminating adapters/primers. Quality control steps are included in the Appendices (Section 9.3).

2.2.14.5 Data parsing

Raw data were processed using tools in the Galaxy platform. Reads were imported as FastQ files and adapter sequences were trimmed using Trimmomatic, which was run in palindrome mode as described for paired-end reads (Bolger *et al.*, 2014). Parameter settings included: clipping of known Illumina adapters using the Truseq3 set, a maximum mismatch count of 2 bases (for full match), a minimum adapter length of 8 bases and a quality threshold of 20. Trimmed reads were aligned to the hg19 human genome build using the BWA-MEM alignment tool for reads >100 bp (Li, 2013) using standard settings for an Illumina-based library.

PCR duplicates were removed from the alignment output BAM files using the RmDup tool from the samtools package. BAM files were filtered further by excluding reads with a Phred score of <20 and reads with multiple mapping, using the bamtools package. BAM files were also sorted by coordinates using the SortSam package. MACS2 was used as a peak-calling package, as described by (Feng *et al.*, 2012), for pooled NFATc2 IP and input samples. This was run using a band width of 300 bp and a *q*-value threshold of 0.1 for differential enrichment of regions in the NFATc2 IP samples. This was also set to output both narrow and broad peaks. ChIPseeker was used to annotate MACS2 peaks with genomic loci and produce plots to describe the peaks' distribution across the genome (Yu *et al.*, 2015).

Blacklisted genomic regions for the hg19 build were removed from the MACS2 peaks to prevent data artefacts. The published list of 880 regions was downloaded

from the ENCODE database. The MACS2 and blacklist BED files were compared for region overlap of ≥1 bp and blacklisted regions removed from the MACS2 file, using the setdiff() function of the *GenomicRanges* package.

The *ChIPQC* package also generates a PCA plot, using the underlying dba.PCA function from the *DiffBind* package. This generates eigenvectors based on the presence and strength of intersections between read counts and peak calls in any of the NFATc2 IP or input DNA replicates.

2.2.14.6 Data analyses

The *ChIPseeker* package was used in Galaxy to generate plots showing the distribution of peaks across the genome. This package also annotated peaks with Ensembl gene IDs and gene loci information. Genes were further annotated manually using the Ensembl database. Coverage plots for peak summits were generated using *ChIPseeker* in the R platform.

Metagene plots were generated using the R package *metagene2*. *GenomicFeatures* was used to extract GRanges files from the UCSC genome browser hg19 build, for the TSS±1000 bases or TSS±5000 bases, per gene. Blacklisted regions were removed from these GRanges files and these were then used as template regions for *metagene2*. For each ChIP-Seq replicate the NFATc2 IP BAM file was normalised to the input BAM file and the metagene plots were generated from these files together.

Functional enrichment in the genes containing peaks was conducted on GSEA using a preranked analysis. Ensembl gene IDs were uploaded with their associated (peak) *MACS2* enrichment scores, which were used to rank genes. Standard settings were used and inclusion of gene sets in the range of 5-500 genes.

DNA binding motifs were identified using the MEME-ChIP platform (available at meme-suite.org). To prepare 500 bp sequences of interest, as is optimal for the platform, peak summit genomic locations were extracted from the *MACS2* peaks and entered into a bed file. This bed file was uploaded to the UCSC Table Browser (available at genome.ucsc.edu) as a custom track. 500bp regions were extracted centred on these peak summits and parsed in RStudio using the *Biostrings* package (version 2.58.0).

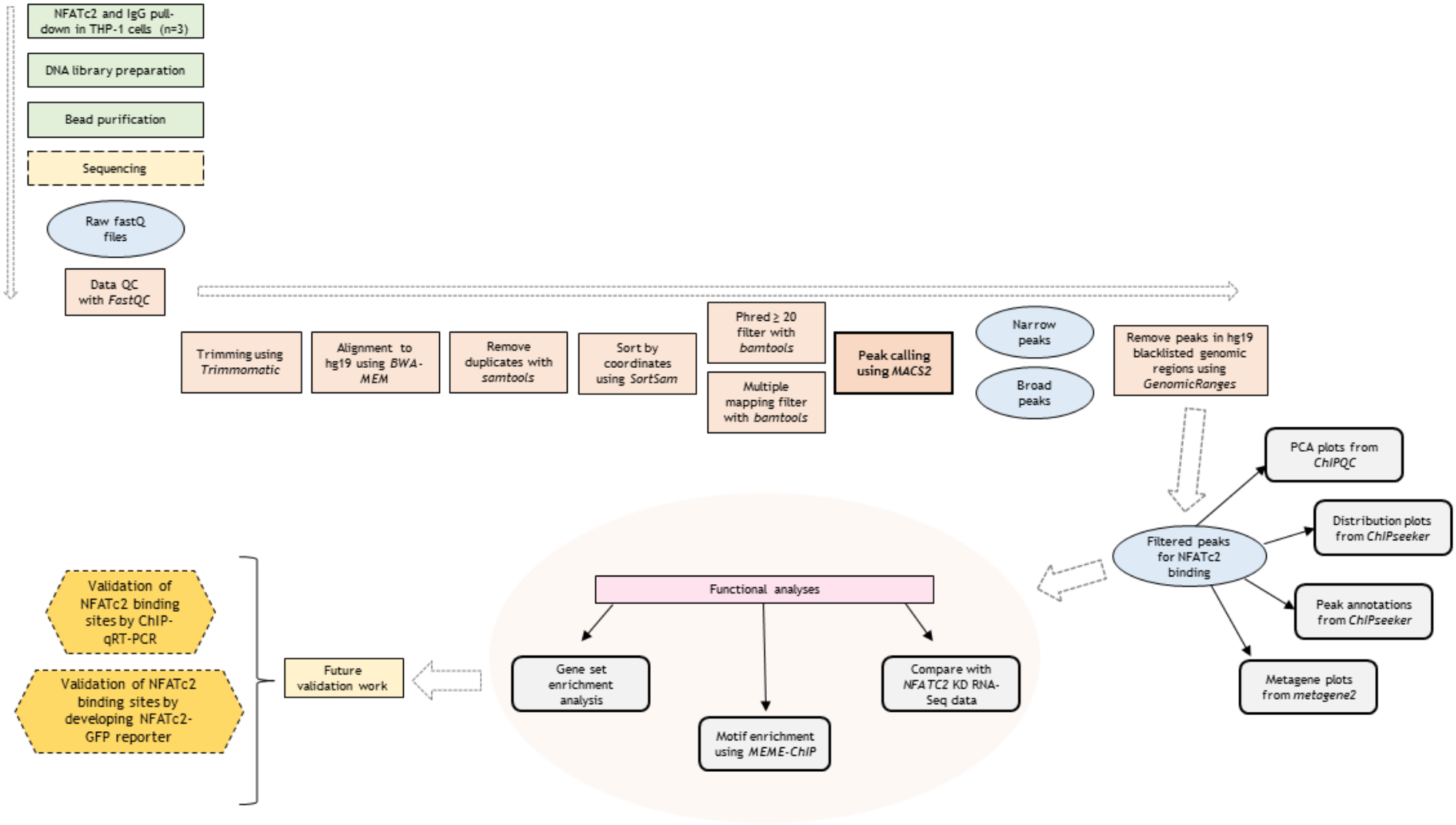

Figure 2-12. Schematic flowchart depicting the experimental and data analysis strategy for ChIP-Seq data.
Only the sequencing was performed by the external provider (Novogene). The bottom left elements (orange) indicate possible future work.

2.2.15 Extraction of patient data

Data were obtained from 4 sets, detailed in 2.1.4 and primarily analysed using RStudio. The TCGA-AML data (also 'TCGA-LAML') were downloaded using *TCGABiolinks* from the GDC database. Supplemental clinical information was derived from the associated publication (Ley *et al.*, 2013). These expression data were provided as 'normalised expected read counts', which were derived from the RNA-Seq by Expectation Maximisation (RSEM) package (Li and Dewey, 2011). This is a means of quantifying reads without the need for a reference genome.

Data from the TARGET-AML set were also obtained using *TCGABiolinks*, which are expressed as fragments per kilobase of transcript per million mapped fragments (FPKM), which corrects read counts for sequencing depth and gene length. Data from the BEAT-AML cohort were obtained directly from the source publication (Tyner *et al.*, 2018) and are expressed as 'reads per kilobase of transcript per million mapped reads' (RPKM), which is very similar to FPKM. Finally, data were extracted from GSE83533 directly from the GEO platform, and were given as RPKM.

Survival analyses were created by dividing patient cohorts by a defined expression threshold and comparing the overall survival (OS) or event-free survival (EFS) of these. Testing the null hypothesis of no difference in survival between the 2 cohorts was conducted using a log-rank test, in Prism.

2.2.15.1 Comparison of RNA-Seq, ChIP-Seq and patient data

Overlapping gene lists from RNA-Seq and ChIP-Seq data was conducted using the *intersect*() function in R. Patient survival and expression data were parsed and analysed as previously described. Patient expression profiles were correlated using the *corrplot* package, and a heatmap produced using the *heatmap* function, using standard settings. The clustering used within this package is based on the *hclust* R function, which uses the complete linkage method of agglomerative hierarchical clustering as standard. Agglomerative hierarchical clustering is based on the principal of sequentially grouping together objects by clusters and repeating this process until all clusters are in one large cluster. 'Agglomerative' refers to the way in which clusters are gathered in a 'bottom-up' manner to achieve the final cluster. Complete linkage is one method of calculating the distance between objects (Murtagh, 1983).

2.2.16 Statistical tests

Data were presented as mean values ± standard error of the mean (SEM) if ≥3 independent replicates were done. Technical replicates were presented as the mean ± standard deviation (SD). Most statistical tests were conducted using the appropriate parametric test for a difference in means, since non-parametric tests are not powerful at low replicate numbers, for which most of these data were. For data with replicates in an approximate range of 6-30 the equivalent non-parametric test for a difference in medians, or equivalent, was applied.

Where multiple groups were being compared to the control condition, a one-way ANOVA was applied to test for an overall difference between all comparable means. The post-hoc Dunnett's test (a modified *t*-test) compared each treatment condition with the control sample in a pairwise manner. The non-parametric equivalents to these tests, which were used, are the Kruskal-Wallis test for a difference in medians and post-hoc Dunn's pairwise tests. Where only two conditions were being compared an unpaired two-sided *t*-test was used, with the application of Bonferroni's correction in the scenario of multiple simultaneous tests. A non-parametric equivalent to a paired *t*-test, the Wilcoxon matched-pairs signed rank test, was also used in the case of paired data. Specific statistical tests are indicated in the legends.

3 Results (I): Characterisation of *NFATC2* in AML

3.1 Introduction

Much of the published data into *NFAT* family members' involvement in myeloid leukaemia focuses on AML harbouring a *FLT3*^{ITD} mutation and their role in this context. The research focuses predominantly on *NFATC1* (Fric *et al.*, 2014, Metzelder *et al.*, 2015, Solovey *et al.*, 2016). The novel discovery of *NFATC2* as a key target of histone lysine demethylase *KDM4A* in MLL-AF9 AML suggests a role for *NFATC2* in *KDM4A*-mediated survival pathways, and so it warrants further investigation. NFATs are known to regulate multiple aspects of myeloid cell function (Kiani *et al.*, 2004, Kiani *et al.*, 2007) and the same may be true of *NFATC2* in AML cells.

The first priority of this study was to examine the relationship of *NFATC2* with outcomes and pathology in clinical AML, using open-source data, to determine if there might be a valid rationale to investigate further.

Using the existing knowledge about NFAT signalling in T cells, it was important to determine if the calcium-calcineurin-NFAT axis functioned as expected in AML cells, prior to investigation using established inhibitors which target these signalling axes. Published data in T cells show that NFATc2 resides predominantly in the cytoplasmic compartment, with a clear nuclear shift upon calcium influx, secondary to ionomycin stimulation. Changes in global NFATc2 phosphorylation can also be observed by changes in the protein size, whereby increased phosphorylation implies functional inhibition (Bécart *et al.*, 2007, Sieber *et al.*, 2007, Ren *et al.*, 2008). In contrast, phosphorylation of NFATc2 at Ser54 (p-NFATc2^{ser54}) is a marker of transactivation, which can be induced by PMA and ionomycin together in T cells (García-Rodríguez and Rao, 2000, Alam *et al.*, 2018).

It was also considered whether blockade of PLC signalling using established inhibitors would impact upon NFATc2 function in AML cells, since PLC-mediated calcium influx from the ER by SOCE can activate the calcineurin-NFAT pathway (Gwack *et al.*, 2007, Wang *et al.*, 2009a).

Some consideration was also be given to variants of *NFATC2* in AML. Splice variants of *NFATC1* have been shown to have differential distribution in some T cell subtypes and can exert differing functions, depending on the protein subdomains

translated (Chuvpilo *et al.*, 1999). Characterising *NFATC2* variants in AML is therefore important to understanding NFATc2 function and its manipulation *in vitro*.

Human *NFATC2* (h*NFATC2*) has been successfully overexpressed in T cells to determine protein binding partners by immunoprecipitation (Gabriel *et al.*, 2016). Additionally, expression of a constitutively dephosphorylated form of NFATc2 in fibroblasts was shown to induce cell cycle arrest (Robbs *et al.*, 2008). As such, the role of NFATc2 in AML cells' growth and survival was evaluated by overexpressing *NFATC2* in cell line model(s) and observing any phenotypic changes *in vitro*.

Murine *Nfatc2* (m*Nfatc2*) has significant sequence homology with h*NFATC2* although the tissue expression patterns of common structural variants are somewhat divergent between the two species, indicating that they may have functionally divergent roles also. Exogenous expression of m*Nfatc2* and its function in human cells has not been published and so this was also expressed in human cell lines here, to establish if any observed phenotype was common between h*NFATC2* and m*Nfatc2*. This could provide an opportunity to hypothesise further around the relationship between any phenotype and common structural properties or differences of the orthologous proteins.

This chapter aims to establish whether *NFATC2* might have a clinically important role in AML and to examine its expression and function in some of the available *in vitro* cell line models. These data were subsequently used to support further investigation of *NFATC2* as an important gene in AML cell survival and function.

3.2 Chapter objectives

1. Determine if there is a relationship between *NFATC2* transcript expression and AML subtype and/or patient survival, using open-source patient data.
2. Survey transcript and protein expression of *NFATC2*/NFATc2 in cell line models of AML, including transcript variants.
3. Determine whether NFATc2 functions downstream of the calcium-calcineurin axis, as published in T cells, in a model of AML.
4. Overexpress human *NFATC2* and murine *Nfatc2* in a cell line model of AML and examine the effect(s) on cell behaviour *in vitro*.

3.3 Results

3.3.1 Higher *NFATC2* expression is associated with reduced survival in a subset of AML patients

RNA-Seq and survival data were extracted from 3 independent AML patient datasets to include a range of disease phenotypes. The TARGET-AML dataset is derived from a 'relapse-enriched' cohort of paediatric patients with BM samples taken at diagnosis. The TCGA dataset included adults with *de novo* AML and the BEAT-AML dataset included adults and paediatric AML cases. Taken together, these datasets account for inter-patient heterogeneity and the wide age distribution of AML (Ley *et al.*, 2013, Tyner *et al.*, 2018, Fan *et al.*, 2020).

Firstly, somatic mutations of *NFATC2* were examined in each dataset using either the GDC data portal or the annotated data. Across the entire unfiltered TARGET-AML cohort (n=684 patients with validated mutational profiling data), no somatic variants were recorded in *NFATC2*. Similarly, in the TCGA cohort (n=150 patients with whole exome sequencing) there were no variants in *NFATC2*. Finally, in the BEAT-AML curated set of high-confidence somatic mutations (derived from n=531 patients) 2 patients were found to have somatic mutations in *NFATC2*; 1 missense substitution and 1 deletion. In summary, somatic mutations of *NFATC2* were found to be rare in these cohorts of AML patients.

For gene expression analyses, data from these cohorts are described in Figures 3-1, 3-2 and 3-3, respectively. Flowcharts for the selection of the sample data included are shown in part A of the figure. Only BM samples were taken to account for inter-tissue expression differences. In the BEAT-AML cohort there was substantial heterogeneity in patients' treatment background, and so only therapy naïve patients were included. Detailed characteristics of the selected patients' cytogenetic, molecular and demographic backgrounds are shown in the Appendices (Section 9.1, Figure A-1).

RNA-Seq data were subdivided by the FAB classification recorded for each patient, as shown in part B of each figure. Statistical testing for an overall difference in medians found a significant difference in *NFATC2* expression, across all FAB groups in each dataset. In the TARGET-AML dataset (Figure 3-1B), M5 AML patient samples expressed the lowest *NFATC2* of all groups, but no pairwise differences were found

to be statistically significant. In the TCGA-AML data (Figure 3-2B) the most significant differences were between M0 and either M4 or M5 (p<0.0001 for both) but significant differences were also found between M1 and M4 (p=0.015), M1 and M5 (p=0.0002) and M2 and M5 (p=0.006). Of groups M1 through to M5 each had a sequentially lower median *NFATC2* expression, suggesting that this could be related to differentiation status of the patient's AML blasts.

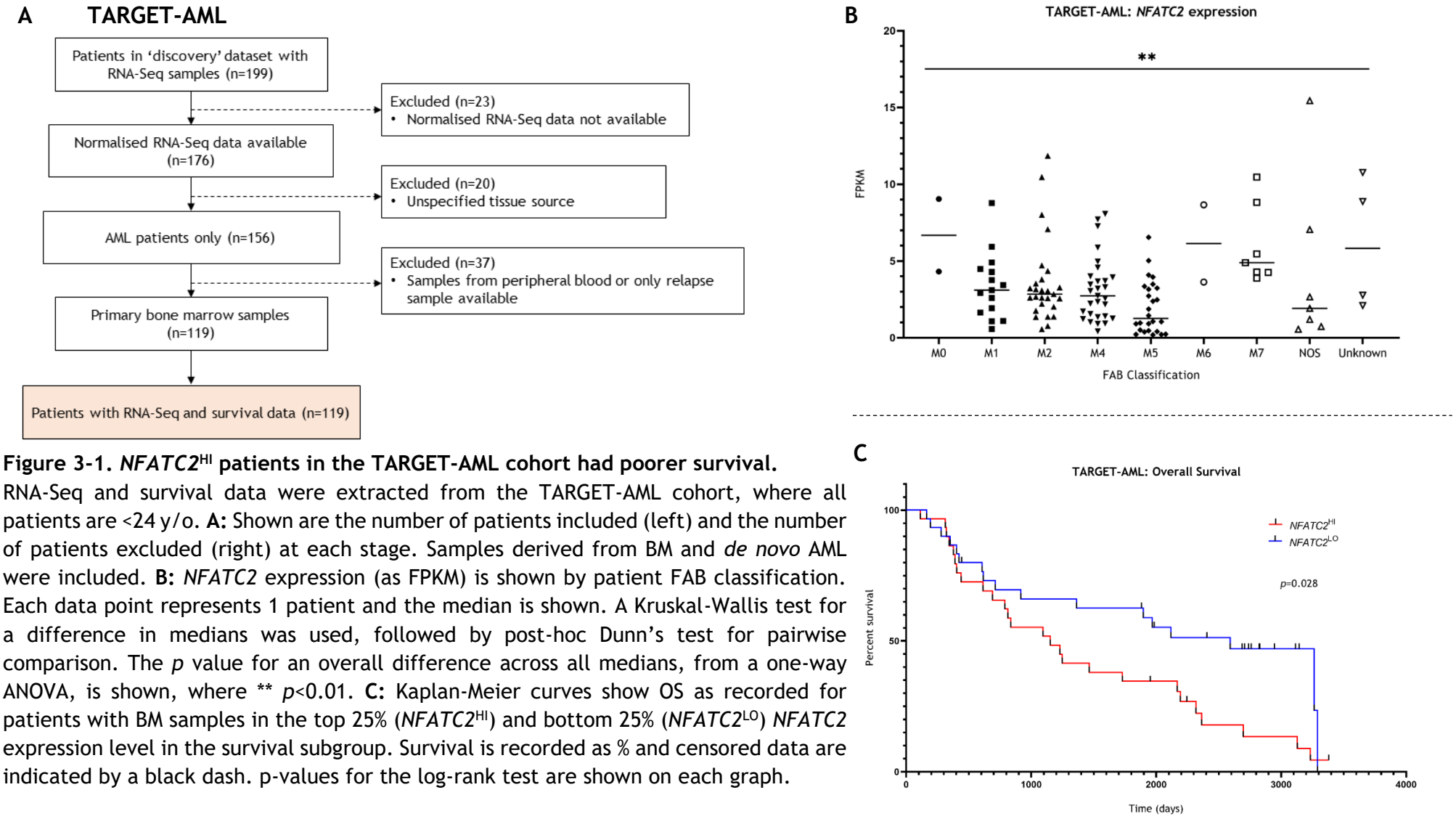

Figure 3-1. *NFATC2*^{HI} patients in the TARGET-AML cohort had poorer survival. RNA-Seq and survival data were extracted from the TARGET-AML cohort, where all patients are <24 y/o. **A:** Shown are the number of patients included (left) and the number of patients excluded (right) at each stage. Samples derived from BM and *de novo* AML were included. **B:** *NFATC2* expression (as FPKM) is shown by patient FAB classification. Each data point represents 1 patient and the median is shown. A Kruskal-Wallis test for a difference in medians was used, followed by post-hoc Dunn's test for pairwise comparison. The *p* value for an overall difference across all medians, from a one-way ANOVA, is shown, where ** $p<0.01$. **C:** Kaplan-Meier curves show OS as recorded for patients with BM samples in the top 25% (*NFATC2*^{HI}) and bottom 25% (*NFATC2*^{LO}) *NFATC2* expression level in the survival subgroup. Survival is recorded as % and censored data are indicated by a black dash. p-values for the log-rank test are shown on each graph.

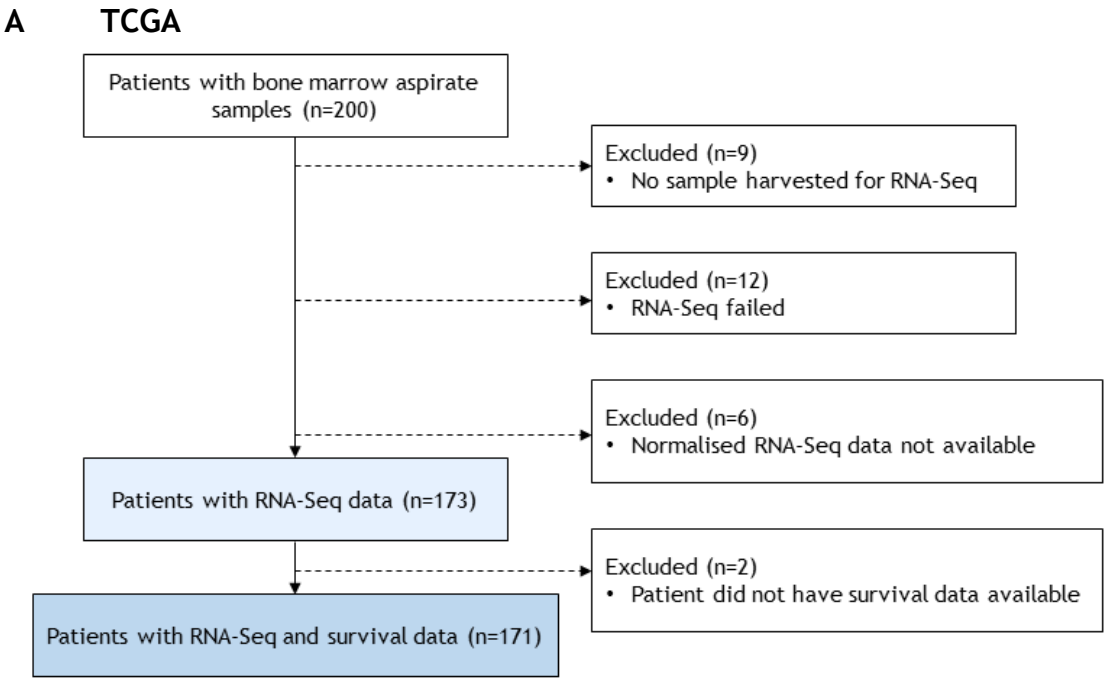

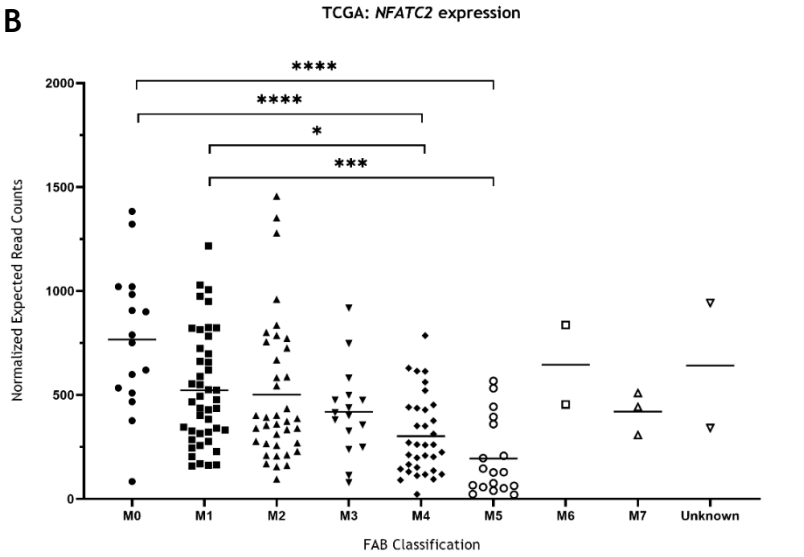

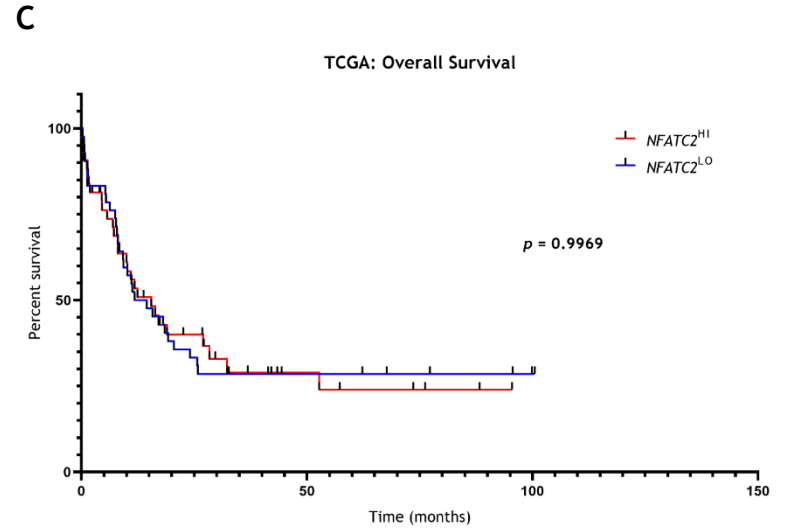

Figure 3-2. Patients in the TCGA-AML cohort with poorly differentiated AML had higher *NFATC2* expression. Data were extracted from the TCGA-AML set and presented as for TARGET-AML in Figure 3-1. **A:** Patients were excluded due to an absence of survival and/or adequate RNA-Seq data. **B:** *NFATC2* expression (as normalised expected read counts) is shown by patient FAB classification. A Kruskal-Wallis test for a difference in medians was used, followed by post-hoc Dunn's test for pairwise comparison. In limited space, only the most significant *p* values for an overall difference in medians are shown. * $p<0.05$, *** $p<0.001$, **** $p<0.0001$. **C:** Kaplan-Meier curves show *OS* as recorded for patients with *BM* samples *in* the top 25% ($NFATC2^{HI}$) and bottom 25% ($NFATC2^{LO}$), with the *p* value given for the difference in hazard functions, as previously.

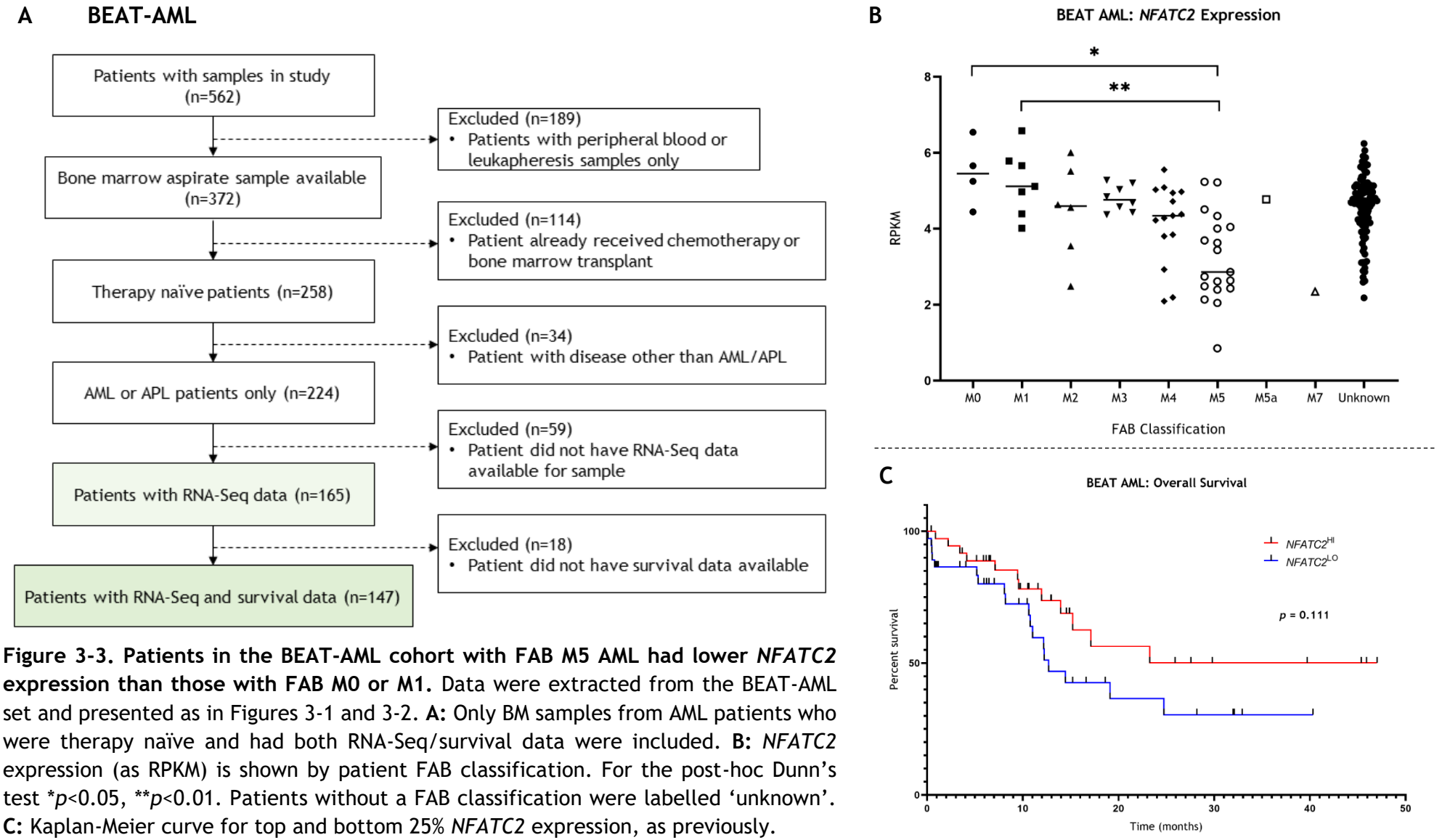

Figure 3-3. Patients in the BEAT-AML cohort with FAB M5 AML had lower *NFATC2* expression than those with FAB M0 or M1. Data were extracted from the BEAT-AML set and presented as in Figures 3-1 and 3-2. **A:** Only BM samples from AML patients who were therapy naïve and had both RNA-Seq/survival data were included. **B:** *NFATC2* expression (as RPKM) is shown by patient FAB classification. For the post-hoc Dunn's test *p<0.05, **p<0.01. Patients without a FAB classification were labelled 'unknown'. **C:** Kaplan-Meier curve for top and bottom 25% *NFATC2* expression, as previously.

In the BEAT-AML data (Figure 3-3B), M5 AML showed the lowest expression and was significantly lower than in M0 and M1 AML (p=0.011 and p=0.004, respectively). In these data a larger proportion of patients were grouped as 'unknown' (n=104) as this study primarily used the WHO classification of myeloid neoplasms as a basis to group patients. By the WHO classification patients were grouped into 11 disease types, primarily as defined by cytogenetic status, between which no statistically significant difference was found for median *NFATC2* expression (data not shown).

Together these data reveal a relationship between FAB classification of patient AML and *NFATC2* expression which is observed in three distinct populations. The largest difference in *NFATC2* expression in these datasets is between samples from M0 AML and from M5 AML, between which expression is lower in M5 AML.

Next, survival data were compared between groups of patients with differing *NFATC2* expression, in part C of each figure. The number of patients with both survival data and BM sample RNA-Seq data available are detailed in the flowchart of part A. For each dataset patients which met these criteria were divided into quartiles by *NFATC2* expression, denoting the top and bottom 25% as *NFATC2*^{HI} and *NFATC2*^{LO}, respectively. Quartiles were selected initially as an arbitrary threshold, by which to separate patients with greater extremes of *NFATC2* expression than separation into halves by the median, with the aim of observing a maximal biological but still statistically powered effect. These two groups were then compared for overall survival and plotted using Kaplan-Meier curves.

Of the 3 datasets a significant difference in survival was found in the paediatric TARGET-AML dataset only (Figure 3-1C, p=0.028), in which *NFATC2*^{HI} patients had a reduced survival compared to *NFATC2*^{LO} patients (median survival 1152 days vs. 2592 days, respectively). The hazard ratio for high to low expressing patients was 1.95, as determined by a log-rank test. Event-free survival was also found to be significantly different between these two groups (p=0.015, data not shown). Note, however, that *NFATC2*^{HI} patient data contained fewer censored events compared with *NFATC2*^{LO} patient data (n=4 and n=13, respectively).

No statistically significant difference in survival was found for either the TCGA-AML (Figure 3-2C) or BEAT-AML (Figure 3-3C) datasets (p=0.9969 and p=0.111, respectively). Regrouping the data to divide patients into halves by *NFATC2* expression (*NFATC2*$^{LO\text{-}50}$, *NFATC2*$^{HI\text{-}50}$) also revealed no statistically significant difference between these groups for either the TCGA or BEAT AML data (p=0.150

and p=0.331, respectively, data not shown). However, regrouping of the TARGET-AML dataset into halves still revealed a significantly lower survival for *NFATC2*$^{HI\text{-}50}$ patients (p=0.048, median 1229 vs. 2492 days, data not shown), albeit less so.

Together these data suggest that some AML patients with high *NFATC2* expression in bone marrow tissue have poorer disease outcomes, but this has not been reproduced across all selected datasets. Given the ages of the TARGET-AML cohort this may suggest that *NFATC2* expression and survival outcomes are more closely linked in paediatric AML patients compared to adults. Alternatively, it was hypothesised that the observed differences may be correlated with patient relapse.

The samples included in TARGET-AML were selected for the study retrospectively and are described as a 'relapse-enriched' cohort. Of the 119 patients included, 78 underwent a relapse during the period of patient follow-up, while 38 patients' event and survival data were censored. The remainder either died or their induction therapy failed during this period. To investigate whether *NFAT* expression has a relationship with AML relapse, data from paired samples at diagnosis and relapse were extracted from an independent dataset, via the GEO database (GSE83533, n=19) (Li *et al.*, 2016).

The data in Figure 3-4 show that *NFATC2* is more highly expressed at relapse in this cohort (p<0.0001). Together with the survival data, these data suggest that *NFATC2* is important in relapsed AML. However, these conclusions are drawn from gene expression data, which alone do not provide information surrounding *NFAT* function in these tissues and disease states.

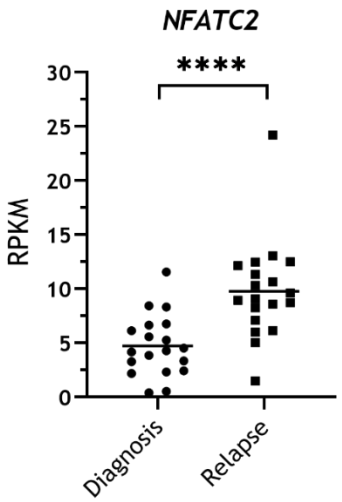

Figure 3-4. *NFATC2* expression was higher at relapse in the GSE83533 cohort. *NFATC2* expression is shown for paired diagnosis and relapse samples in a cohort of AML patients (n=19). Statistical significance for a difference between the two groups is shown for a Wilcoxon matched-pairs signed rank test (p<0.0001). Gene expression is given as RPKM.

3.3.2 *NFATC3*, but not *NFATC1* expression is associated with survival in a subset of AML patients

The relationship observed with survival in the TARGET-AML dataset was compared to the calcium-dependent NFAT family members *NFATC1* and *NFATC3*, to determine if this effect was unique to *NFATC2* expression. *NFATC4* is not well expressed in the myeloid lineage and was not examined. As shown in Figure 3-5, there was no statistically significant survival difference between $NFATC1^{HI}$ and $NFATC1^{LO}$ patients (p=0.937), but in the case of *NFATC3* the difference was significant (p=0.010), by log-rank test. The median survival was 689 days in the $NFATC3^{HI}$ group vs. 3149 days in the $NFATC3^{LO}$ group.

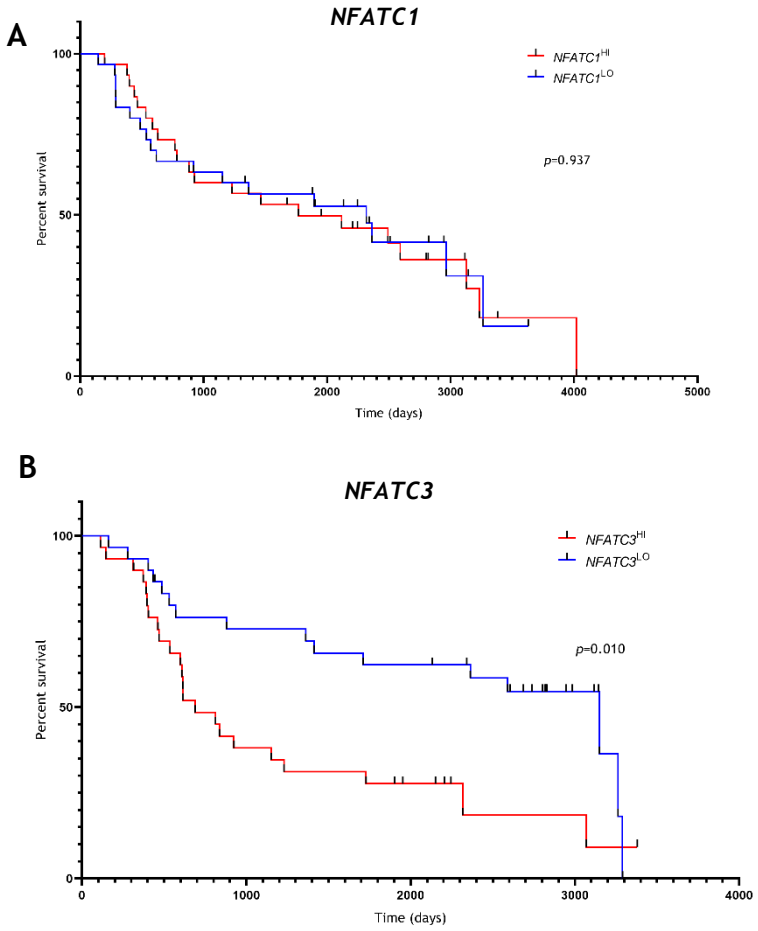

Figure 3-5. $NFATC3^{HI}$ patients in the TARGET-AML cohort have a poorer overall survival. Patients in the TARGET-AML cohort included in Figure 3-1C (n=119) were divided into groups containing the top and bottom 25% expression of **A:** *NFATC1* and **B:** *NFATC3*. The Kaplan-Meier curves were plotted as previously, and the *p* value for the difference in hazard functions is shown.

To build on this finding the expression of *NFATC1* and *NFATC3* were examined in the GSE83533 cohort. As shown in Figure 3-6, *NFATC3* is also more highly expressed in relapsed samples (p=0.023), while *NFATC1* is not significantly different between the two sample groups.

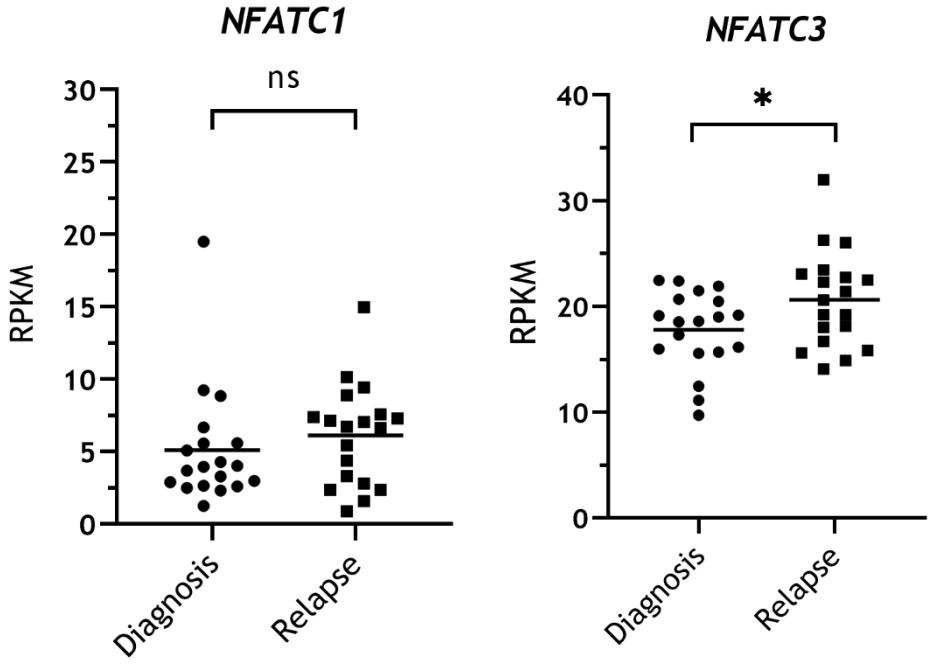

Figure 3-6. *NFATC3* is higher in a cohort of AML patients after relapse.
Gene expression was extracted from paired diagnosis/relapse samples, from the GSE83533 cohort (n=19) as previously. Shown are expression plots for **A:** *NFATC1* and **B:** *NFATC3*, at diagnosis and relapse. Statistical significance for a difference between the two groups is shown for a Wilcoxon matched-pairs signed rank test, where *p<0.05, 'ns'= p>0.05. Gene expression is given as RPKM.

In the TARGET-AML dataset expression values for *NFATC2* and *NFATC1* were correlated with statistical significance (r=0.282, p=0.002), in addition to expression values for *NFATC2* and *NFATC3* (r=0.536, p<0.0001). The correlation between *NFATC2*/*NFATC3* may therefore underpin some of the relationship of *NFATC2*/*NFATC3* expression with relapse and survival.

Overall, these interesting data show similar expression patterns of *NFATC2* and *NFATC3* in these AML cohorts which warrant further investigation, particularly in the context of patient relapse. In the context of the *KDM4A-PAF1-NFATC2* axis in THP-1 cells, *NFATC2* is of particular importance to carry forward for investigation in this study, supported by the *in silico* patient data.

3.2.2 NFATc2 is active downstream of calcineurin signalling in MLL-AF9 THP-1 cells

Of the AML cell lines available, THP-1 cells were chosen as a primary model in which to study *NFATC2* due to the discovery of the putative *KDM4A-PAF1-NFATC2* axis in this model. THP-1 was derived from a paediatric patient with acute monocytic leukaemia harbouring an MLL-AF9 fusion gene, in addition to *NRAS* and *TP53* mutations.

To test whether NFATc2 phosphorylation is dependent on known calcium signalling pathways, as in T cell models, THP-1 cells were treated with inhibitors and/or stimuli of these pathways. An upward band shift in total NFATc2 protein on a Western blot suggests an increase in protein size, which is an established means of assessing phosphorylation status of NFATc2. Phosphorylation at ser54 (pNFATc2^{ser54}) was also examined, as a marker of transactivation, often downstream of MAPK signalling.

On inspection of the Western blot (Figure 3-7), NFATc2 is visible in THP-1 lysates as bands ranging from approximately 85-115kDa. The uppermost and lowest bands are the most prominent, which likely correspond to fully phosphorylated and dephosphorylated NFATc2 protein, respectively. pNFATc2^{ser54} occurs mainly at the upper band size (~115kDa), which would corroborate this assumption. The smear seen between bands may represent differing phosphorylation states of NFATc2. There may also be contribution from varying sizes of protein which arise from transcript variants. Band intensities, measured by densitometry, are shown above and below the blot.

THP-1 cells were pre-treated for 1 hr with EGTA, a chelator of calcium and inhibitor of signalling, or U73122, a pan-inhibitor of PLC and associated signalling. Cells were then treated for 1 hr with either ionomycin, a calcium ionophore and activator of the calcium-NFAT in T cells, and/or PMA, a MAPK pathway and NFAT signalling activator. Vehicle controls were included for each stage of treatment. Inhibitor concentrations were determined empirically by measuring cell viability, using an Alamar Blue assay, in a range of concentrations. This was to determine the concentration which would stimulate a minimal observable effect. Ionomycin, PMA and EGTA concentrations were selected to be marginally sub-lethal concentrations, again determined by Alamar Blue assay (data not shown).

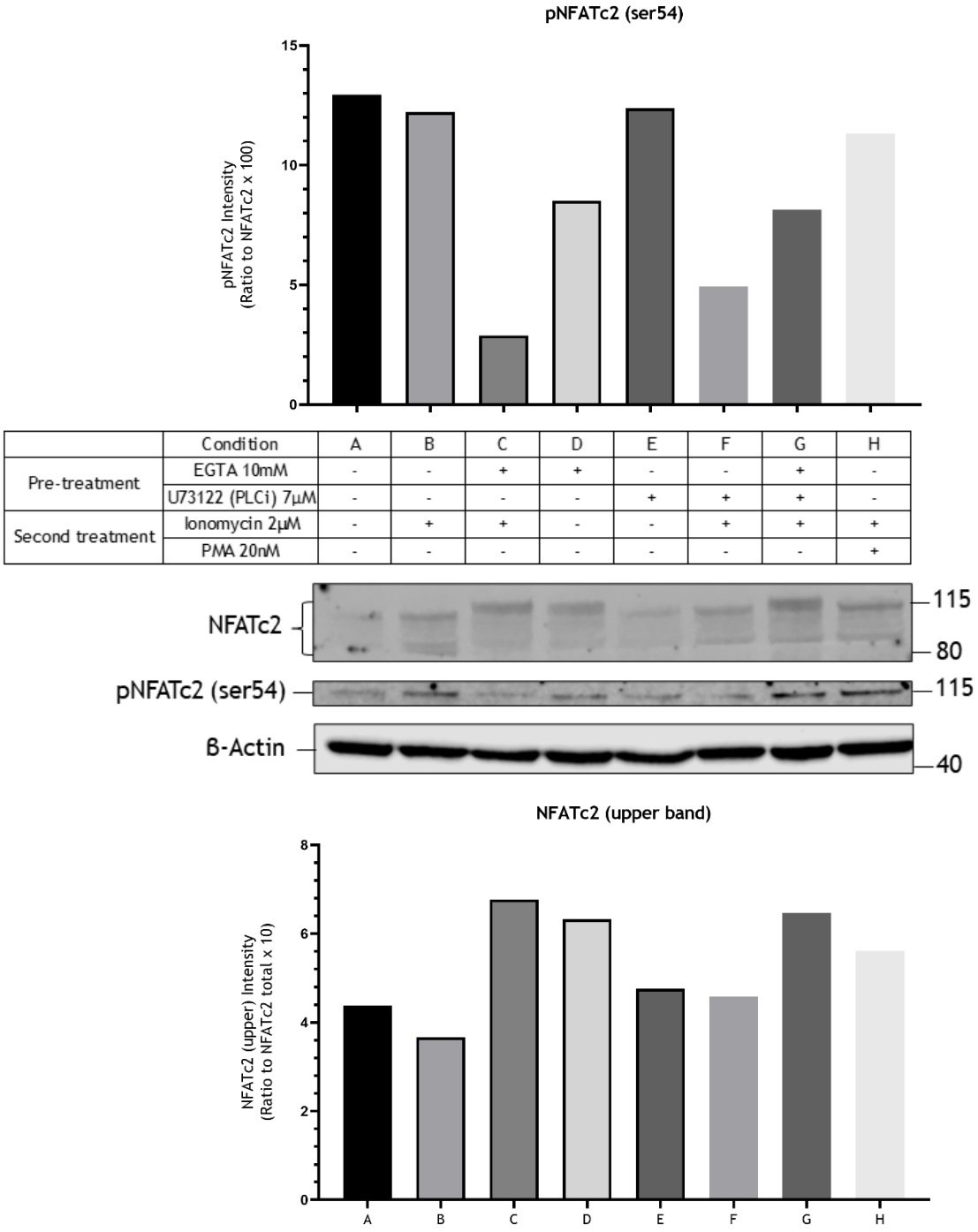

Figure 3-7 EGTA treatment of THP-1 cells leads to global NFATc2 phosphorylation. THP-1 cells were pre-treated for 1 hr with EGTA (a calcium chelator) and/or U37122 (a PLC inhibitor), followed by 1 hr treatment with ionomycin (a calcium ionophore) and/or PMA (a MAPK pathway stimulator); n=1 biological replicate. Concentrations are given and DMSO was matched in each condition as a vehicle control. Whole cell lysates (25 µg/well) were immunoblotted with anti-NFATc2 or anti-pNFATc2^{ser54} as shown. Anti-ß-actin was used as a loading control. Protein size is shown on the right-hand side in kDa. Bar graphs show protein signal intensity as measured by densitometry. Above: pNFATc2^{ser54} normalised to total NFATc2. Below: NFATc2 (upper band only) normalised to total NFATc2.

Treatment with EGTA results in an upwards shift and increased intensity of the upper NFATc2 band in all conditions (C, D and G). This likely reflects increased global phosphorylation of NFATc2. There is, however, a reduction in phosphorylation at pNFATc2^{ser54} relative to total NFATc2. Treatment with ionomycin (condition B) has no effect on pNFATc2^{ser54} or the upper band of NFATc2. The addition of PMA with ionomycin (condition H) increases upper band NFATc2 intensity as a proportion of total NFATc2 more than with ionomycin mono-treatment, but does not impact pNFATc2^{ser54}, contrary to expectations. The effect of EGTA on the upwards band shift (condition D) is not reversed in the presence of ionomycin (condition C).

Mono-treatment of THP-1 with U73122 (condition E) does not substantially change the upper NFATc2 band or pNFATc2^{ser54}. This suggest that NFATc2 phosphorylation status is not directly related to PLC activity in THP-1. U73122 treatment with the addition of either ionomycin (condition F) or ionomycin and EGTA together (condition G) does not alter the size of NFATc2 protein compared with conditions B and C, respectively.

The upward NFATc2 band shift with EGTA treatment suggests that global blockade of calcium in the cell is sufficient to increase NFATc2 global phosphorylation and therefore translocation to the cytoplasm and inactivation. However, phosphorylation specifically at ser54 is reduced relative to total NFATc2 after EGTA treatment, which may imply that phosphorylation at this site is also dependent on active calcium signalling.

To characterise better the nature of the effects of EGTA on THP-1 cells a time-course was established for EGTA treatment. Figure 3-8 reveals an upward shift in the upper NFATc2 band at 30 and 60 min, with either 1 mM or 10 mM of EGTA. This confirms the previous finding of the band shift (Figure 3-7) and demonstrates that this occurs as early as 30 min post-treatment. This is an important finding as it is consistent with global blockade of calcium leading to a rapid dephosphorylation event. There is also visibly reduced total protein level of NFATc2 at 10 min post-treatment, of which the significance is not clear.

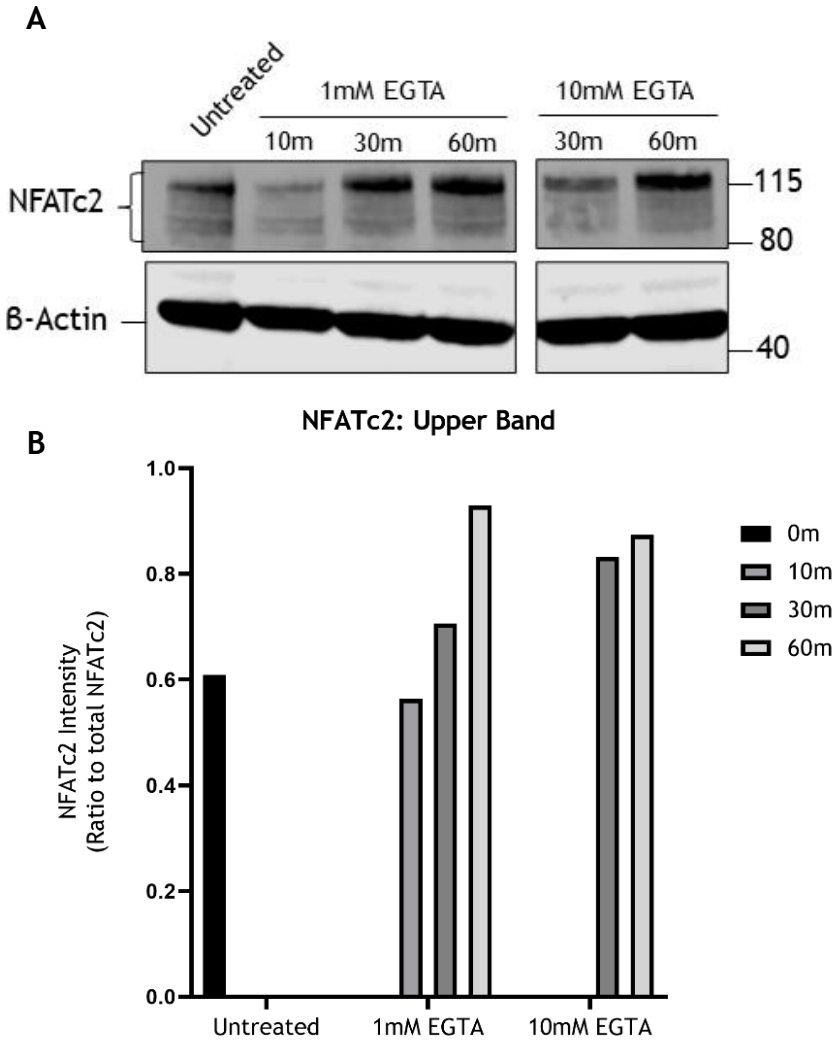

Figure 3-8. EGTA-mediated NFATc2 phosphorylation in THP-1 cells occured as early as 30 min post-treatment. THP-1 cells were treated with EGTA for varying lengths of time, as shown in min; n=1 biological replicate. Concentrations are given. **A:** Whole cell lysates (20 µg/well) were immunoblotted with anti-NFATc2. Anti-β-actin was used as a loading control. Protein size is shown on the right-hand side in kDa. **B:** Bar graph showing protein signal intensity as measured by densitometry, for the upper NFATc2 band intensity relative to total NFATc2 intensity.

Fractionation of THP-1 cells into cytoplasmic and nuclear lysates was carried out to determine whether NFATc2 was in its functional nuclear compartment under some of the treatment conditions. THP-1 cells were treated with ionomycin, PMA, EGTA and/or CsA; a calcineurin-NFAT activation inhibitor. Figure 3-9 shows NFATc2 protein to be of a similar size to those in Figure 3-7. Overall, the nuclear protein was of a higher quantity compared with the cytoplasmic, which may suggest that NFATc2 is predominantly nuclear at resting conditions in THP-1. These also appear to correspond to the smaller un-phosphorylated proteins, as expected in the nucleus.

Treatment of THP-1 with ionomycin, with or without PMA co-treatment, resulted in an apparent cytoplasmic shift of NFATc2 by densitometry (Figure 3-9B); this is contrary to expectations. This may suggest that NFATc2 is already maximally translocated in THP-1 cells and this represents some technical variation, and/or that ionomycin has unexpected effects in THP-1 cells which disrupt the normal balance of calcium and/or NFAT signalling. However, this cytoplasmic shift is not observable by eye and there is some contamination of the nuclear lysates with ß-tubulin, suggesting that the fraction separation is not optimal.

Interestingly, co-treatment with ionomycin and EGTA reduced the nuclear fraction of NFATc2 overall, relative to the cytoplasmic fraction. Additionally, the upper bands are more visible in both fractions with the addition of EGTA. This upward band shift is consistent with the findings in Figure 3-7 (condition C), but its presence in the nucleus is unexpected, since nuclear NFATc2 is expected to be mostly un-phosphorylated. Together with the ionomycin mono-treatment these data are inconclusive. The relationships between protein band size, phosphorylation status and nuclear translocation are not clear and require further replication, in addition to improved cellular fractionation, in order to make firm conclusions.

Treatment of THP-1 with CsA leads to a marked cytoplasmic translocation and disappearance of nuclear NFATc2 (Figure 3-9). This is consistent with expectations and supports the hypothesis that NFATc2 is activated by calcineurin, allowing its dephosphorylation and shuttling to the nucleus, in THP-1 cells.

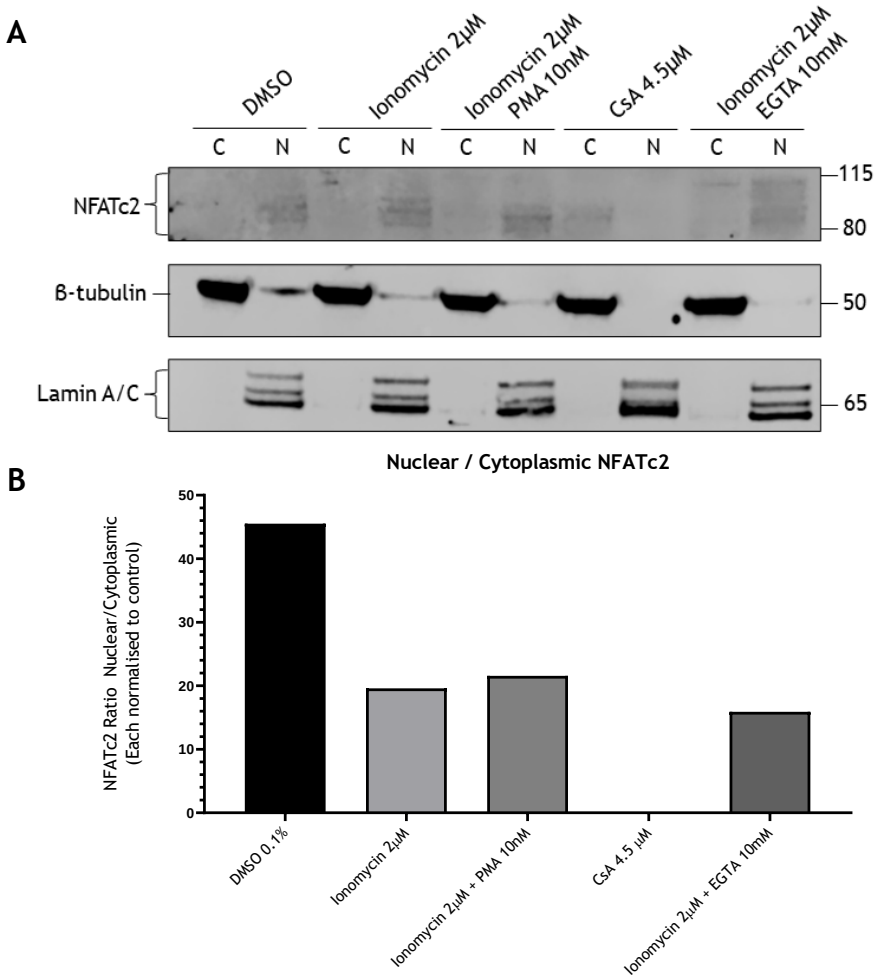

Figure 3-9. CsA treatment of THP-1 cells blocked NFATc2 nuclear translocation. THP-1 cells were pre-treated for 1 hr with EGTA and/or CsA (a calcineurin-NFAT activation inhibitor), followed by 1 hr treatment with ionomycin and/or PMA; n=1 biological replicate. Concentrations are given and DMSO was used as a vehicle control. **A:** Fractionated lysates for either the cytoplasmic or nuclear cell compartment (30 μg/well) were immunoblotted with anti-NFATc2. Anti-ß-tubulin or anti-lamin A/C were used as loading controls for cytoplasmic or nuclear lysates, respectively. Protein size is shown on the right-hand side in kDa. **B:** Bar graph showing protein signal intensity as measured by densitometry, expressed as a ratio of nuclear to cytoplasmic lysates, after normalisation. Cytoplasmic lysates were normalised to ß-tubulin and nuclear were normalised to lamin A/C.

To compare these observations in THP-1 cells with an established model, the Jurkat T cell line was treated with inhibitors and stimuli of the calcium-calcineurin-NFAT axis (Figure 3-10). Both NFATc2 and NFATc1 were visible by immunoblotting with 2 distinct bands visible, though NFATc1 appeared to be less well expressed. The NFATc2 bands were around 120 and 90 kDa, while the NFATc1 bands were around 110 and 90 kDa. Treatment with ionomycin, under the same conditions as for THP-1, did not appear to change the intensity of the upper band

of either NFATc2 or NFATc1, suggesting that no global changes to phosphorylation occurred at this point. Minimal change was seen with 4.5 µM CsA. Treatment with 10 mM EGTA, with or without ionomycin, did increase the ratio of the upper bands' intensities to the total protein, indicating that global phosphorylation did increase at this timepoint. Furthermore, as observed in THP-1, ionomycin did not reverse the effect of EGTA, which might also be expected from the data in condition B.

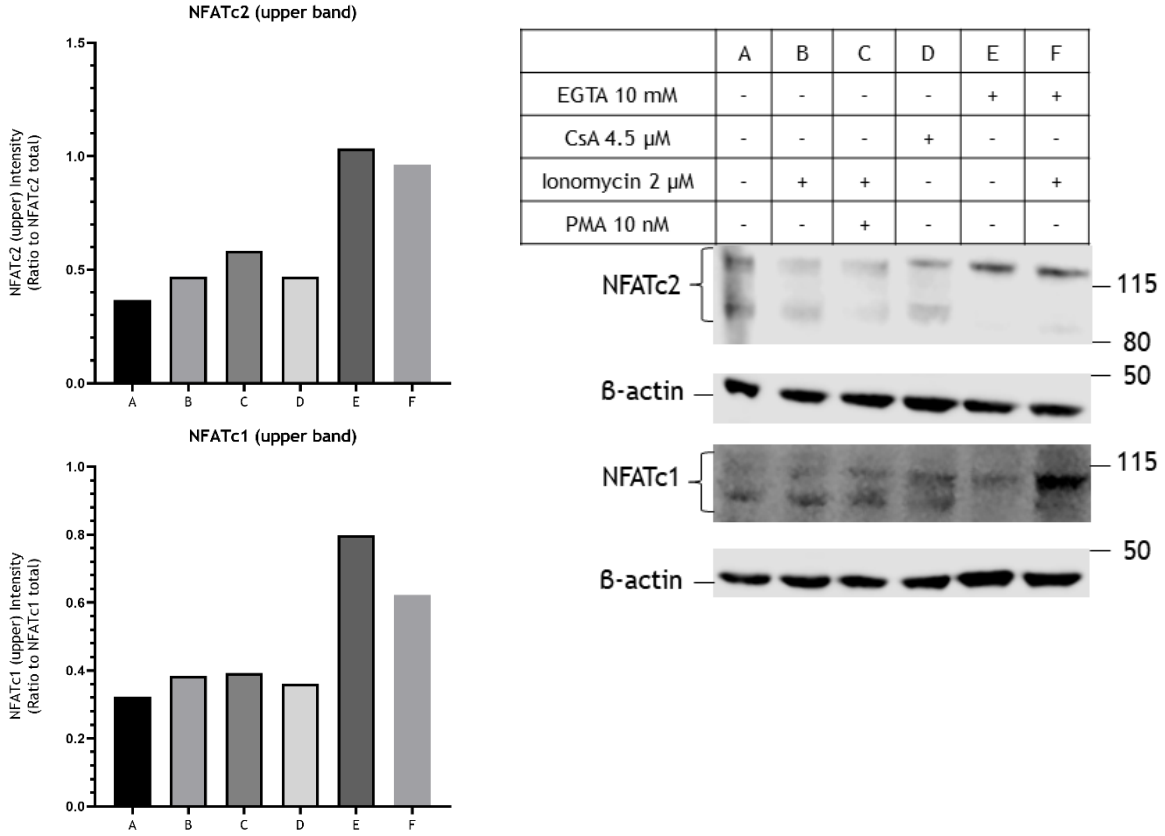

Figure 3-10. Treatment of Jurkat cells with 2 µM ionomycin did not change global NFATc2 phosphorylation status after 1 hr. Jurkat cells were pre-treated for 1 hr with EGTA or CsA, followed by 1 hr treatment with ionomycin and/or PMA; n=1 biological replicate. Concentrations are given and DMSO was matched in each condition as a vehicle control. WCL (18 µg/well) were immunoblotted with anti-NFATc2 or anti-NFATc1 as shown. Anti-ß-actin was used as a loading control. Protein size is shown on the right-hand side in kDa. Bar graphs show protein signal intensity as measured by densitometry for the upper band of NFATc2, normalised to total NFATc2.

To examine these results further, fractionated lysates of Jurkat cells, under the same treatment conditions, were immunoblotted for NFATc2 (Figure 3-11). The protein bands were of a similar size as in the WCL and are visible in both fractions of condition A, suggesting the presence of phosphorylated and unphosphorylated NFATc2 in each. Additionally, the proteins appear marginally larger at both bands in the nuclear fraction. However, contamination of ß-tubulin within the fractions

denoted ‘nuclear’, indicating poorer cytoplasmic/nuclear lysate separation, indicates that caution should be taken when interpreting this blot. In addition, quantification by densitometry would not accurately reflect the changes in each fraction relative to one another.

CsA treatment appears to lead to an increase in the cytoplasmic NFATc2 fraction, but the change is subtle. EGTA treatment led to marked reduction in the smaller NFATc2 protein band, suggesting a loss of unphosphorylated protein in both fractions. However, in the absence of further replication with clear cytoplasmic and nuclear separation, these suggestions are not conclusive.

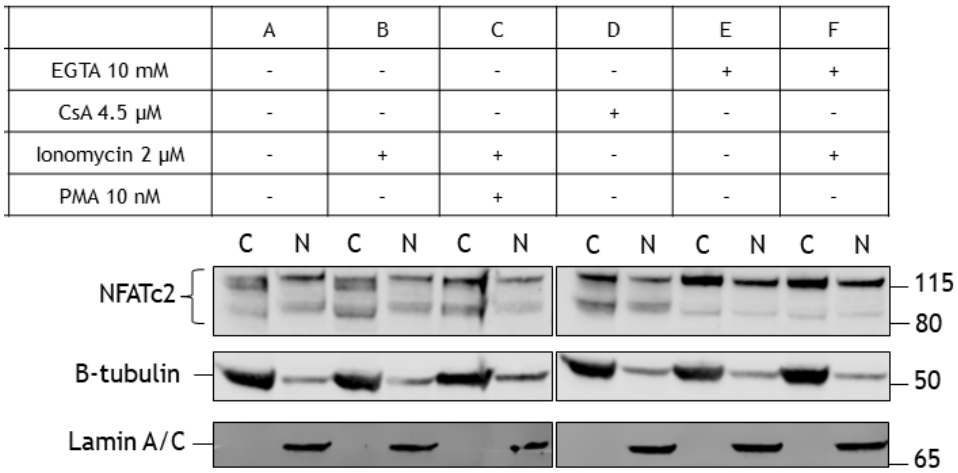

Figure 3-11. CsA and EGTA treatment of Jurkat cells increased the NFATc2 cytoplasmic fraction. Jurkat cells were treated as in Figure 3-9; n=1 biological replicate. **Bottom:** Fractionated lysates for either the cytoplasmic or nuclear cell compartment (25 µg/well) were immunoblotted with anti-NFATc2. Anti-β-tubulin or anti-lamin A/C were used as loading controls for cytoplasmic or nuclear lysates, respectively. Protein size is shown on the right-hand side in kDa.

To determine the relative contributions of *NFATC2* transcript variants to the observed protein band sizes, primers were designed to amplify specific transcript variants. Transcript abundance was measured in THP-1 by qRT-PCR and expressed as the $-\Delta C_t$ value, converted to a Z-score (Figure 3-12). The C_t values associated with variants 3-6 were in the range 35.0-40.0 and so are determined to be poorly expressed variants in THP-1. These data suggest that either or both variants in each pair of variants 1/2 and 7/8 are predominant in THP-1, though more specific primers were not designed. Based on the sequences alone the predicted sizes of the associated protein isoforms (1, 2, 7, 8) are 99.3, 98.1, 76.2 and 75.0 kDa, respectively, as determined using the 'Protein Molecular Weight' tool (via bioinformatics.org). This does not take account of post-translational modifications.

The antibody recognition sites for both total NFATc2 and pNFATc2^{ser54} are in regions which are not present on the shorter isoforms (F and G) translated from transcript variants 7 and 8. These regions – at glycine 87 and serine 54, respectively – are present in the N-terminal region which is absent in isoforms F and G (see Table 1-2C, for which alignment was derived from publicly available sequences). Therefore it is likely that the variation in band size is accounted for by variation in phosphorylation status and not protein isoform size differences. This also has practical implications when assessing the contribution of protein isoforms F and G in THP-1 cells using these antibodies, given that there is a higher abundance of these transcripts as shown in Figure 3-12.

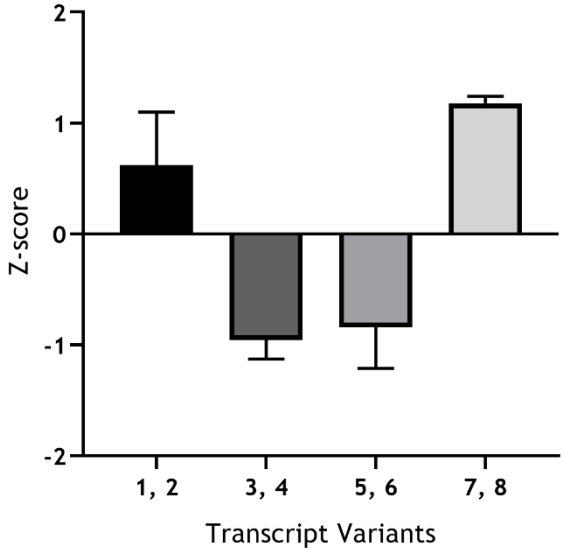

Figure 3-12. *NFATC2* transcript variants 7 and 8 were most highly expressed in THP-1. Transcript abundance as measured by qRT-PCR. Expression is normalised to *ACTB* and *GAPDH* as housekeeping genes, expressed as the $-\Delta C_t$ value and then converted to a Z-score. Error bars represent the SD for technical replicates (n=3) in assay.

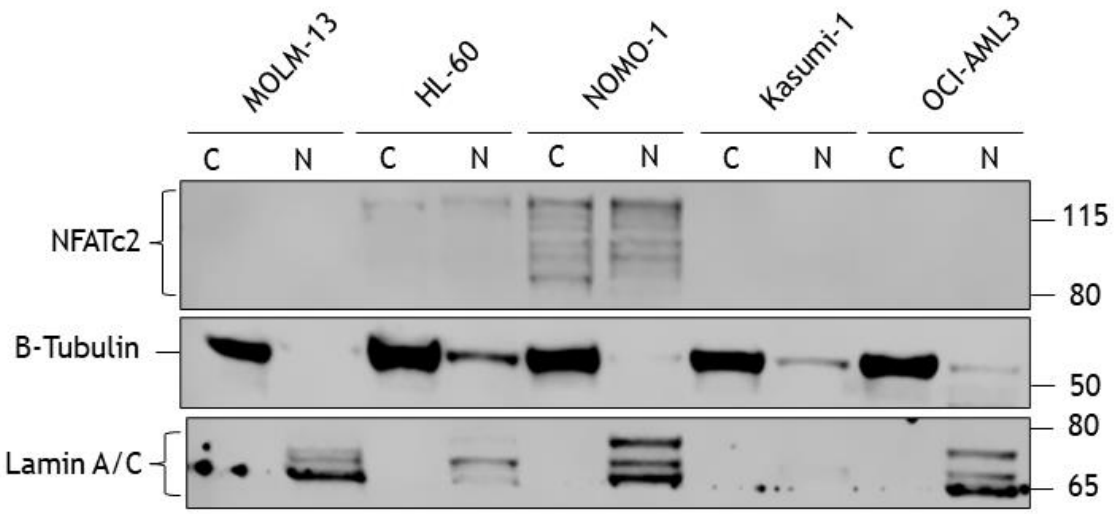

Figure 3-13. NOMO-1 had high protein expression of NFATc2 in both the cytoplasm and nucleus. A: The following AML cell lines were fractionated into cytoplasmic and nuclear lysates: MOLM-13, HL-60, NOMO-1, Kasumi-1, OCI-AML3; n=1 biological replicate. 15 µg protein was loaded per well and immunoblotted with anti-NFATc2. Anti-ß-tubulin or anti-lamin A/C were used as loading controls, for cytoplasmic or nuclear lysates, respectively. Protein size is shown on the right-hand side in kDa.

Finally, NFATc2 protein was characterised in a selection of other AML cell lines (Figure 3-13). NFATc2 was not observable by eye above background signal for any of OCI-AML3, Kasumi-1 or MOLM-13. NOMO-1 expressed the highest quantity of NFATc2 in both fractions, with a number of distinct bands visible in the approximate range of 85-120kDa. As with THP-1 it is likely that these represent proteins with differing amounts of phosphorylation. Both HL-60 and NOMO-1 appear to express the uppermost bands in both cytoplasmic and nuclear fractions evenly. This suggests that these bands do not exclusively represent phosphorylated protein and/or there may be phospho-sites which are abundant within the nucleus, in these cell lines. However, as in Figure 3-11, there is some contamination of the nuclear fraction with ß-tubulin for NOMO-1 and HL-60, and so these suggestions are not conclusive. In addition, the Lamin A/C loading control is absent from the Kasumi-1 nuclear lysate, and so it cannot be ruled out that NFATc2 is not expressed in this compartment.

In MOLM-13, Kasumi-1 and OCI-AML3, where NFATc2 protein expression appears to be low, *NFATC2* transcript expression was measured by qRT-PCR. These were expressed relative to THP-1 (Figure 3-14). MOLM-13 expression is 1.25X log_2fold lower than THP-1, while Kasumi-1 8.96X log_2fold lower. *NFATC2* transcript was undetectable by qRT-PCR (C_t value fixed at 40) in OCI-AML3.

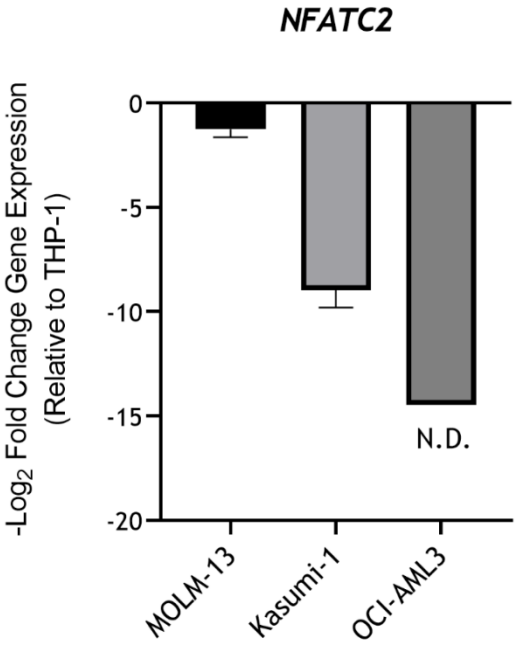

Figure 3-14. *NFATC2* was undetectable by qRT-PCR in OCI-AML3 cells.
NFATC2 expression was measured by qRT-PCR for MOLM-13, Kasumi-1 and OCI-AML3. Expression is relative to THP-1 cells, normalised to *ACTB* and *GAPDH* as housekeeping genes, using the ΔΔCt method. Error bars represent SD for technical replicates (n=3) in assay. 'N.D.' = not detectable, Ct value set at 40.

3.2.3 NFATc2 was found to be predominantly nuclear when overexpressed in THP-1 cells

To better characterise the function of *NFATC2*, human *NFATC2* was overexpressed in THP-1 and MOLM-13 cells, which are both cell line models of MLL-AF9 AML. Murine *Nfatc2* was also expressed in these cell lines, to subsequently measure any rescue effect following KD of h*NFATC2* (see 4.3.3) and, due to the sequence homology between species, the functional consequences of m*Nfatc2* expression were assessed also to determine if any common phenotype could be observed.

Both vectors express truncated versions of their respective transcripts, tagged with IRES-eGFP. The proteins coded by each vector are shown schematically in Figure 3-15, with comparison to the native proteins. An empty vector was used to create a control cell line. Cells transduced with retrovirus containing the vectors were first analysed for GFP expression and then either sorted using FACS for the GFP^+ populations, or plated as single cells and grown in liquid culture, with subsequent validation of GFP expression by flow cytometry.

The GFP^+ cell lines are denoted as either 'o/e m*Nfatc2*' or 'o/e h*NFATC2*' for those transduced with the murine and human transcript vectors, respectively. The cell lines were validated for either m*Nfatc2* or h*NFATC2* transcript expression by qRT-PCR (Figure 3-16). Given the known functional redundancy of NFAT family members *NFATC1* expression was also measured, to assess whether *NFATC2* might co-regulate *NFATC1* expression in this manner.

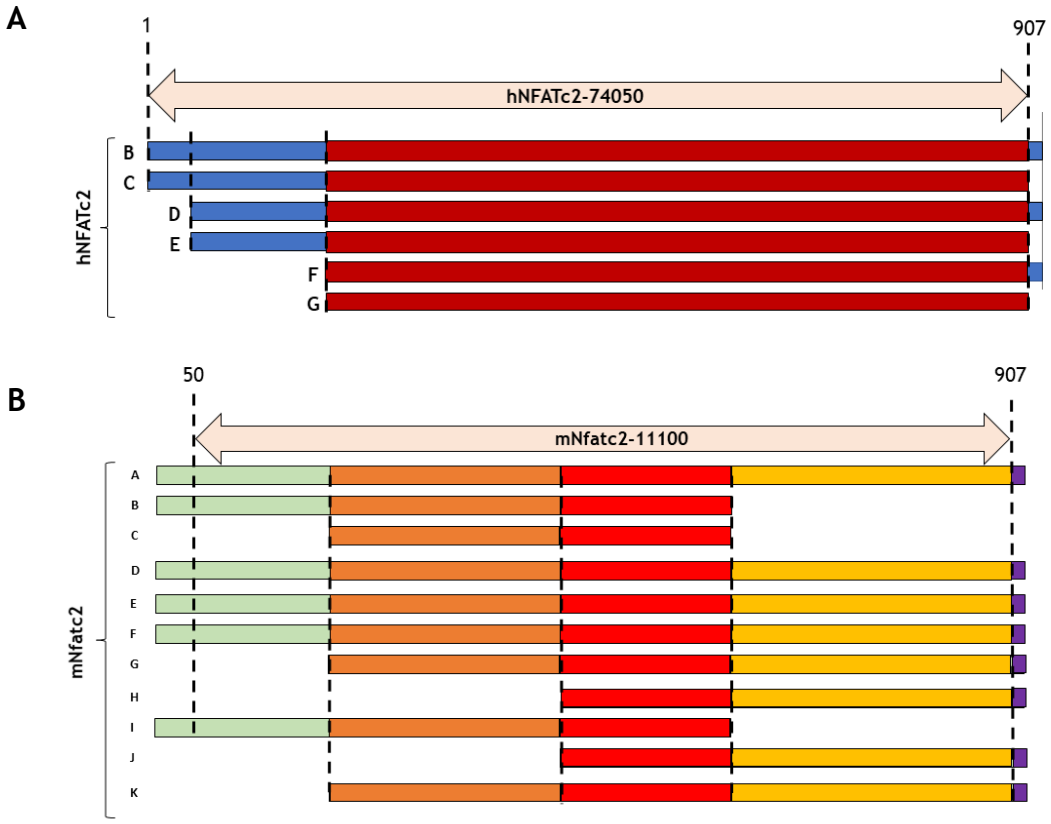

Figure 3-15. The protein derived from the h*NFATC2* vector is similar to the native protein derived from variants A and B. Schematic diagrams represent the approximate sizes of protein transcribed by each transcript variant of h*NFATC2*/m*Nfatc2*. Protein sequences were derived from transcript variants via NCBI and aligned to the native protein isoforms using the PRALINE tool. Approximate regions of alignment are shown by colour, where red and orange represent the highest alignment scores. The position of the arrow indicates the position of 100% sequence alignment of either **A:** h*NFATC2*-74050 vector to variants A and B of native h*NFATC2* or **B:** m*Nfatc2*-11100 to variant A of native m*Nfatc2*. For both, the position relative to variant A is given.

m*Nfatc2* was expressed 477.7X and 724.1X more in THP-1 o/e m*Nfatc2* and MOLM-13 o/e m*Nfatc2*, respectively, compared to their empty vector counterparts (8.9X and 9.5X on the $\log_2$fold scale, Figure 3-16A). The primers designed to amplify the vector-specific m*Nfatc2* transcript were found to bind to a region with 95% sequence homology with h*NFATC2*, and so there may have been some background amplification over and above true m*Nfatc2* expression. h*NFATC2* was also 3.2X and 1.0X more expressed in these cells than with the empty vector.

h*NFATC2* was expressed 90.5X and 16.3X more in THP-1 o/e h*NFATC2* and MOLM-13 o/e h*NFATC2,* respectively, compared to their empty vector counterparts (6.5X and 4.0X on the $\log_2$fold scale, Figure 3-16B). *NFATC1* expression increased by 2.7X and 1.4X, respectively.

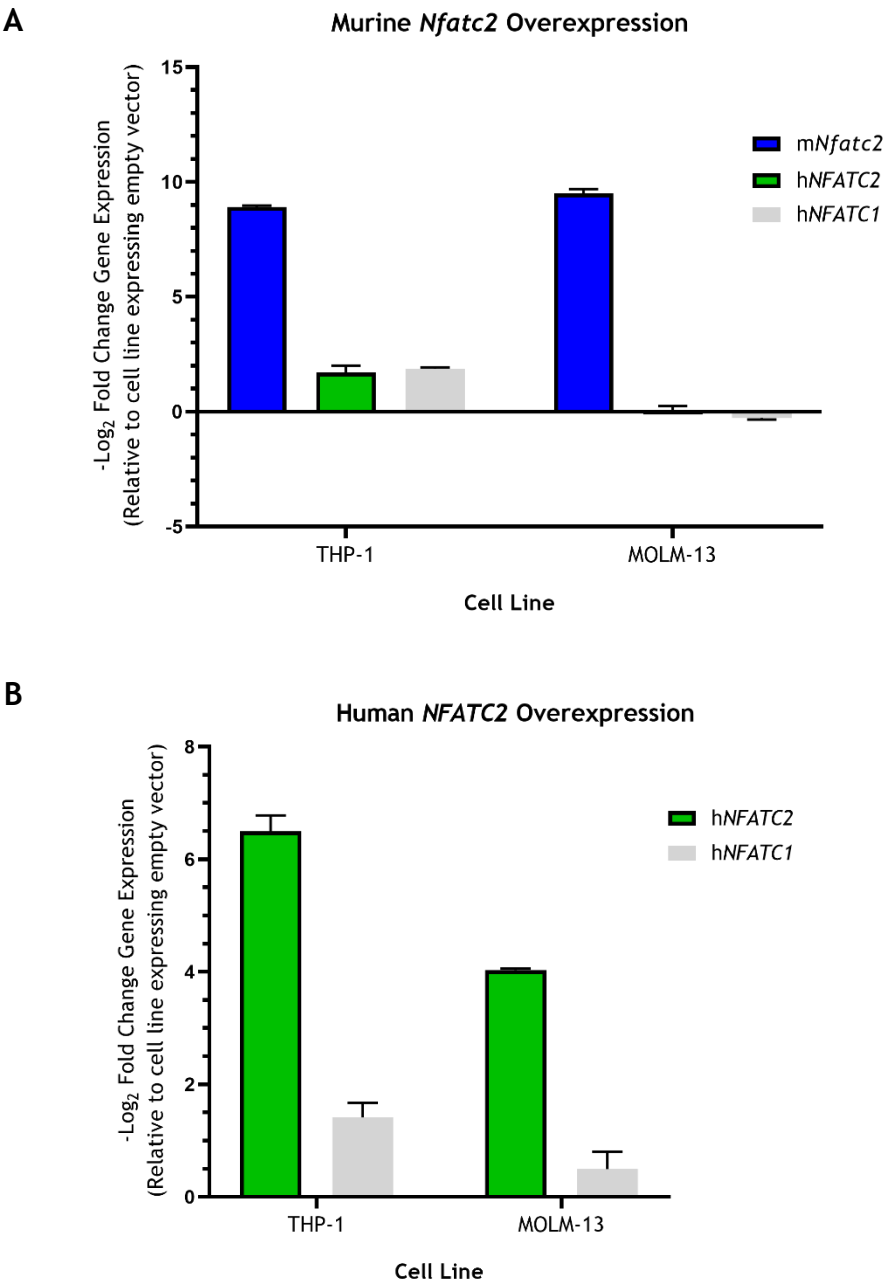

Figure 3-16. m*Nfatc2* and h*NFATC2* were successfully overexpressed in retrovirally-transduced THP-1 and MOLM-13. Gene expression was measured by qRT-PCR. Expression is relative to either THP-1 or MOLM-13 cells expressing an empty retroviral vector. Expression is normalised to *ACTB* and *GAPDH* as housekeeping genes, using the ΔΔCt method. Error bars represent standard deviation for technical replicates (n=3) in assay. m*Nfatc2* = murine *Nfatc2*; h*NFATC2* = human *NFATC2*; h*NFATC1* = human *NFATC1*. **A:** THP-1 or MOLM-13 expressing murine *Nfatc2*, as selected by GFP expression. **B:** THP-1 or MOLM-13 expressing h*NFATC2*, as selected by GFP expression.

To validate the overexpression of Nfatc2 and NFATc2 protein, whole cell lysates were obtained from untreated cells expressing these vectors, in addition to untransduced THP-1 and MOLM-13 cells. The NFATc2 antibody is expected to bind both hNFATc2 and mNfatc2, which share 81% protein sequence homology in the 21 amino acid region containing the antibody binding site (glycine 87). Details of this are shown in Table 3-1. The expression vector proteins are also expected to express these regions containing this site, as predicted by translation from the DNA sequence.

Vector	Protein sequence: 21 amino acid region containing glycine 87
hNFATc2	SLSGEPPGRFGEPDRVGPQKF
mNfatc2	SLSGEPPGRFGEPDSIGFQNF

Table 3-1. hNFATc2 and mNfatc2 proteins share 81% sequence homology around the antibody-binding site. 21 amino acid regions containing the glycine 87 residue**, against** which the NFATc2 antibody is raised, were extracted from the respective native human NFATc2 and murine Nfatc2 protein sequences via NCBI. The canonical, and longest, protein isoform was chosen for each.

To control for endogenous murine Nfatc2 antibody cross-reactivity, BM cell lysates derived from C57Bl/6 (expressing an MLL-AF9 retroviral vector) and NSG mice were included. However, the Nfatc2 expression in these cells was not tested by another method at this stage and so these samples are not strong controls.

There was markedly higher expression of h*NFATC2* in both the THP-1 and MOLM-13 o/e h*NFATC2* lines (Figure 3-17). As quantified by densitometry, relative to the β-actin loading control, the expression of NFATc2 protein was 47.6X and 21.9X higher than in the respective cell lines expressing the empty vector. This protein expression difference is 2.2X higher in THP-1 than in MOLM-13. This is lower than the difference observed in transcript of 5.6X higher in THP-1, in comparison to MOLM-13. Overexpression of h*NFATC2* using the same vector was performed in HEK-293T due to the ease with which these cells can be transfected. As such, HEK-293T cells express NFATc2 protein at a level intermediate to THP-1 and MOLM-13, relative to β-actin.

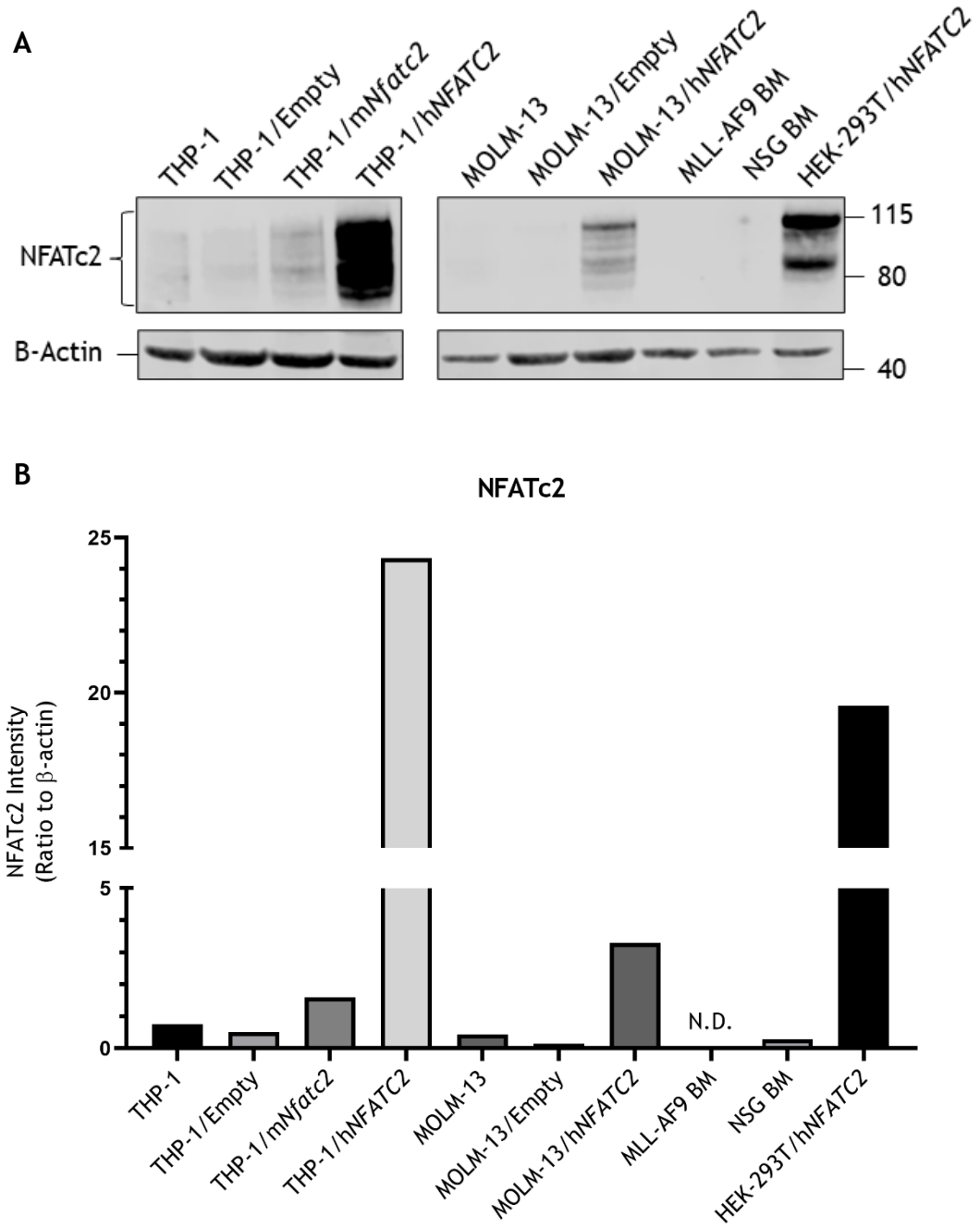

Figure 3-17. THP-1 and MOLM-13 expressing retroviral h*NFATC2* expressed markedly increased NFATc2 protein. A: WCL from untransduced THP-1 or MOLM-13 or cells expressing an empty retroviral vector, m*Nfatc2* or h*NFATC2*. Lysates from murine BM expressing MLL-AF9, BM from NSG mice or HEK-293T overexpressing h*NFATC2* were also loaded. 22µg protein was loaded per well and immunoblotted with anti-NFATc2. Anti-β-actin was used as a loading control. **B:** Bar graph showing protein signal intensity as measured by densitometry, normalised to ß-actin; n=1 biological replicate. 'N.D.' = not detectable.

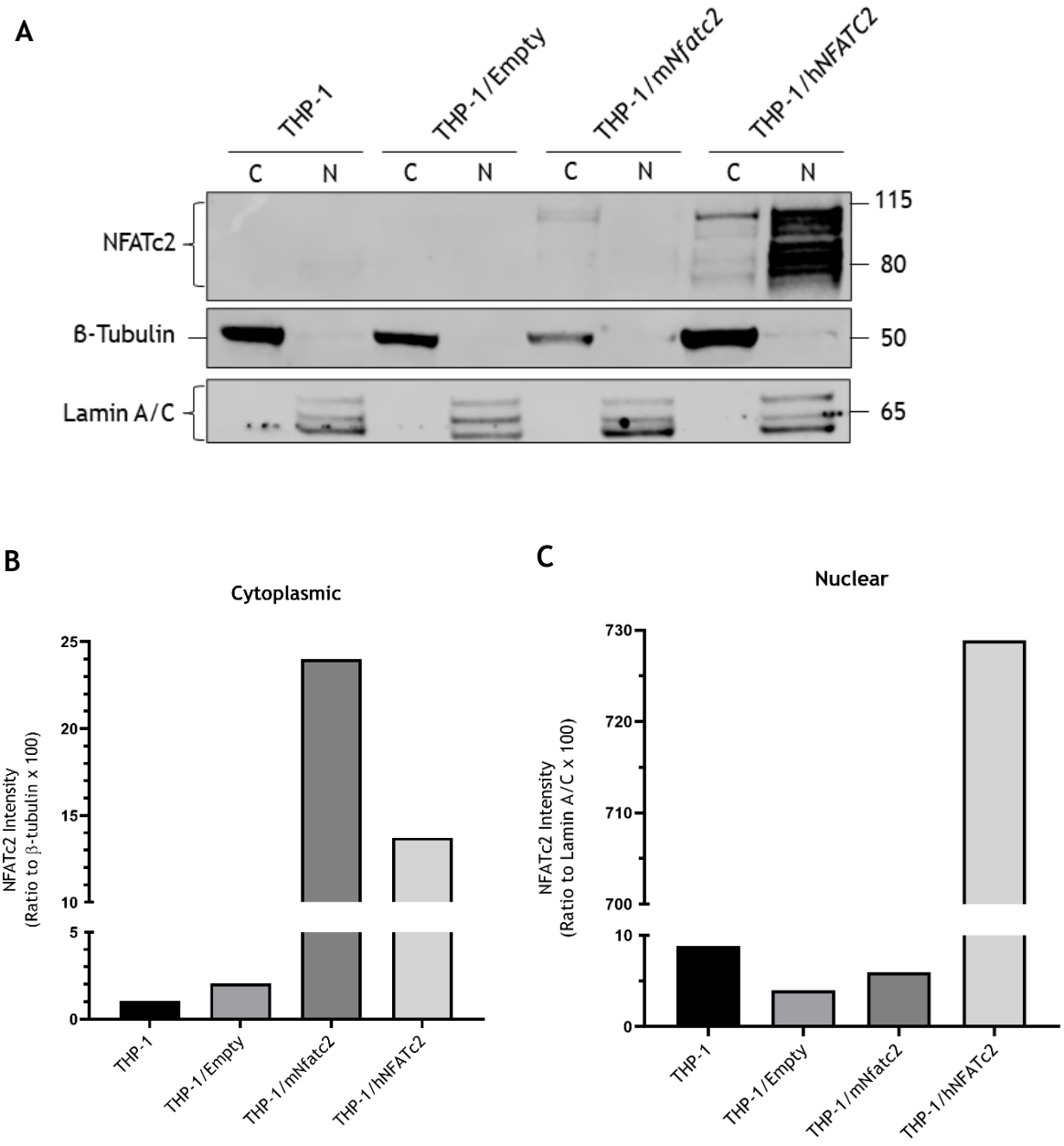

Figure 3-18. THP-1 expressing retroviral h*NFATC2* showed protein residing predominantly in the nucleus. A: Fractionated cell lysates from untransduced THP-1 or THP-1 expressing an empty retroviral vector, m*Nfatc2* or h*NFATC2*. 20 µg protein was loaded per well and immunoblotted with anti-NFATc2. Anti-β-tubulin or anti-lamin A/C were used as loading controls for cytoplasmic or nuclear lysates, respectively. Protein size is shown on the right-hand side in kDa. **B-C:** Bar graphs showing protein signal intensity as measured by densitometry, normalised to β-tubulin or lamin A/C, respectively; n=1 biological replicate.

Protein was expressed 3.1X more in THP-1 expressing m*Nfatc2* than in the empty vector. This could be accounted for by h*NFATC2* transcript being 3.2X more expressed in the THP-1 o/e m*Nfatc2* vector, which may reflect some activity of m*Nfatc2* in the regulation of *NFATC2* transcription. There is minimal or absent protein detected by this antibody in the murine BM controls, which suggests either poor reactivity to endogenous mNfatc2, or that it is poorly expressed in these cells. MOLM-13 expressing the empty vector and m*Nfatc2* did not survive well in culture over a long period, potentially due to retrovirus-induced stress, and were excluded from further protein analyses.

Finally, to validate whether the hNFATc2/mNfatc2 protein expressed in THP-1 cells was present in the functional compartment, cells were fractionated into cytoplasmic and nuclear lysates. Western blotting analysis for hNFATc2 shows that the protein appears predominantly in the nuclear compartment (Figure 3-18), with protein abundances of 13.7X and 728.9X relative to either β-tubulin or lamin A/C, for the cytoplasmic and nuclear compartments respectively. This indicates that NFATc2 is highly functional in this cell line, but no direct assessment of transcriptional or partner binding activity has been made due to a lack of known targets.

As assessed in whole-cell lysates there is detectable protein in THP-1 o/e m*Nfatc2*. This is more evident in the cytoplasmic fraction, with protein abundances of 24.0X and 6.0X relative to either ß-tubulin or lamin A/C, for the cytoplasmic and nuclear compartments respectively. This may reflect the detection of mNfatc2, which is less functional and not well-translocated to the nucleus, or hNFATc2 which is expressed at a level below a threshold for active nuclear translocation.

3.2.4 Overexpression of h*NFATC2* led to increased cell expansion in THP-1

THP-1 and MOLM-13 containing either the empty vector, o/e m*Nfatc2* or o/e h*NFATC2* were seeded in semi-solid media, in order to determine their ability to form colonies over a period of 9-10 days, as a measure of both proliferation and differentiation (Figure 3-19). This was performed in a single replicate and so a direct quantitative assessment was not used, due to the variability introduced when seeding low numbers of cells. On inspection it appears that all cell lines are capable of colony formation.

In THP-1 cells the empty vector and o/e h*NFATC2* cells appear to form a similar size and density of colony, while the o/e m*Nfatc2* colonies have a more compact and dense appearance. In MOLM-13 the empty vector cells form the least dense colonies and o/e m*Nfatc2* the highest, with o/e h*NFATC2* colonies being intermediate to these. However, these are subjective assessments. In all cases colonies appear similar to CFU-GM progenitor-derived colonies due to their round shape, less dense appearance and visibility of individual peripheral cells, at close magnification. This is expected since THP-1 and MOLM-13 are of monocytic origin and should be homogenous. Furthermore, there is little evidence of macrophage differentiation, which might be indicated by wide spreading of colonies. The higher density in o/e m*Nfatc2* colonies may reflect higher proliferation.

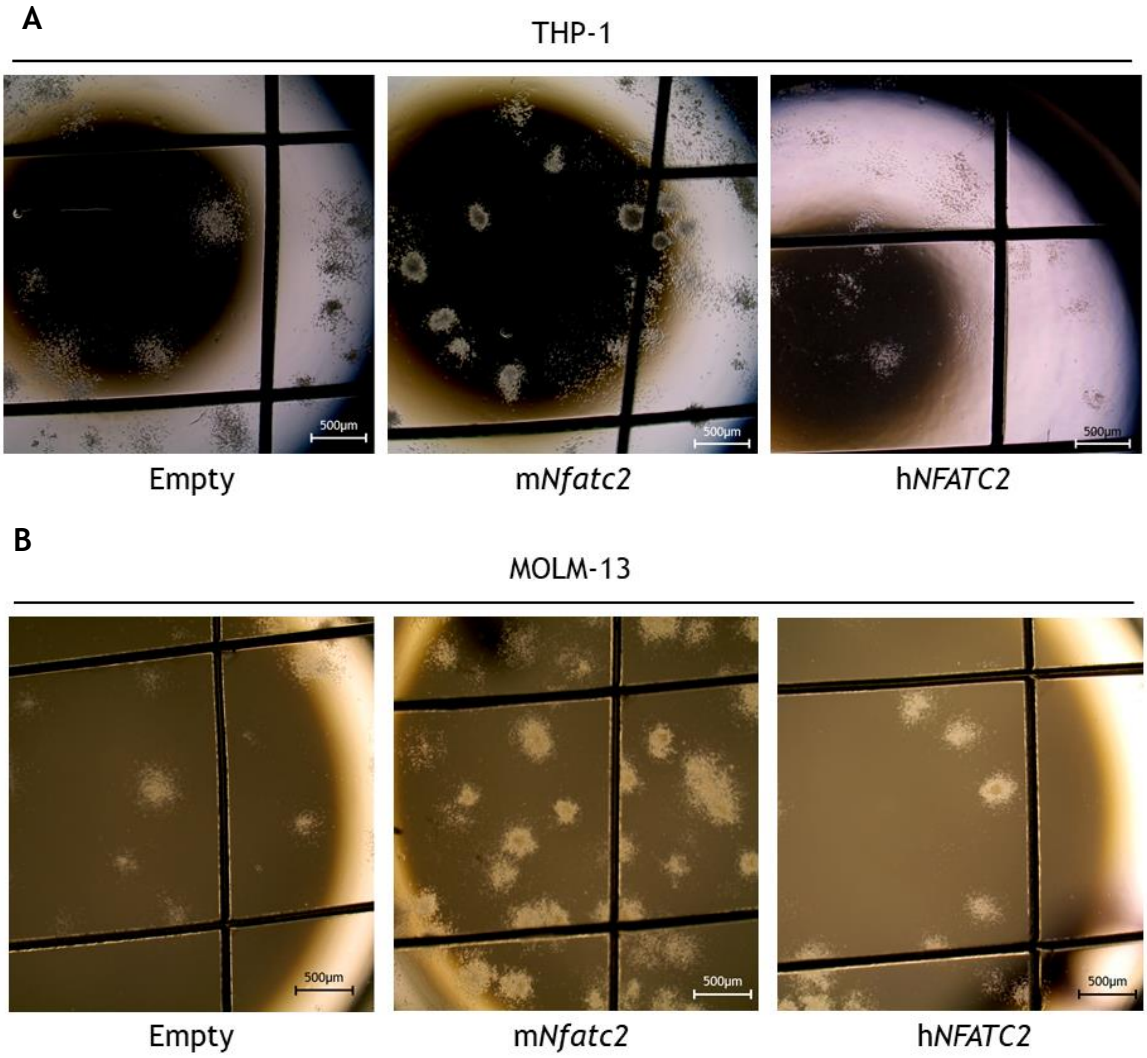

Figure 3-19. Colony-forming cell assays with cell lines overexpressing human *NFATC2* and murine *Nfatc2*. THP-1 (**A**) and MOLM-13 (**B**) expressing either an empty retroviral vector, m*Nfatc2* or h*NFATC2* were seeded in semi-solid media. Representative images (n=1 biological replicate) were taken at 9-10 days post-seeding. 500 µm scale bars are shown on each.

To assess proliferation, cells were also seeded in liquid culture and counted every 24 hours for a period of 72 hr (Figure 3-20). The mean cell count fold change of THP-1 o/e h*NFATC2* was shown to be 1.36X higher at 72 hr than in the empty vector (p=0.007) but was not significant for THP-1 o/e mNfatc2 (p=0.323). The mean fold change at 72 hr was not significantly different in either MOLM-13 o/e h*NFATC2* (p=0.337) or m*Nfatc2* (p=0.265). This could suggest that overexpression of h*NFATC2* in THP-1 leads to an upregulation of proliferation, or that there is a reduction in basal cell death. The differences in the other cell lines may have been masked by high variability.

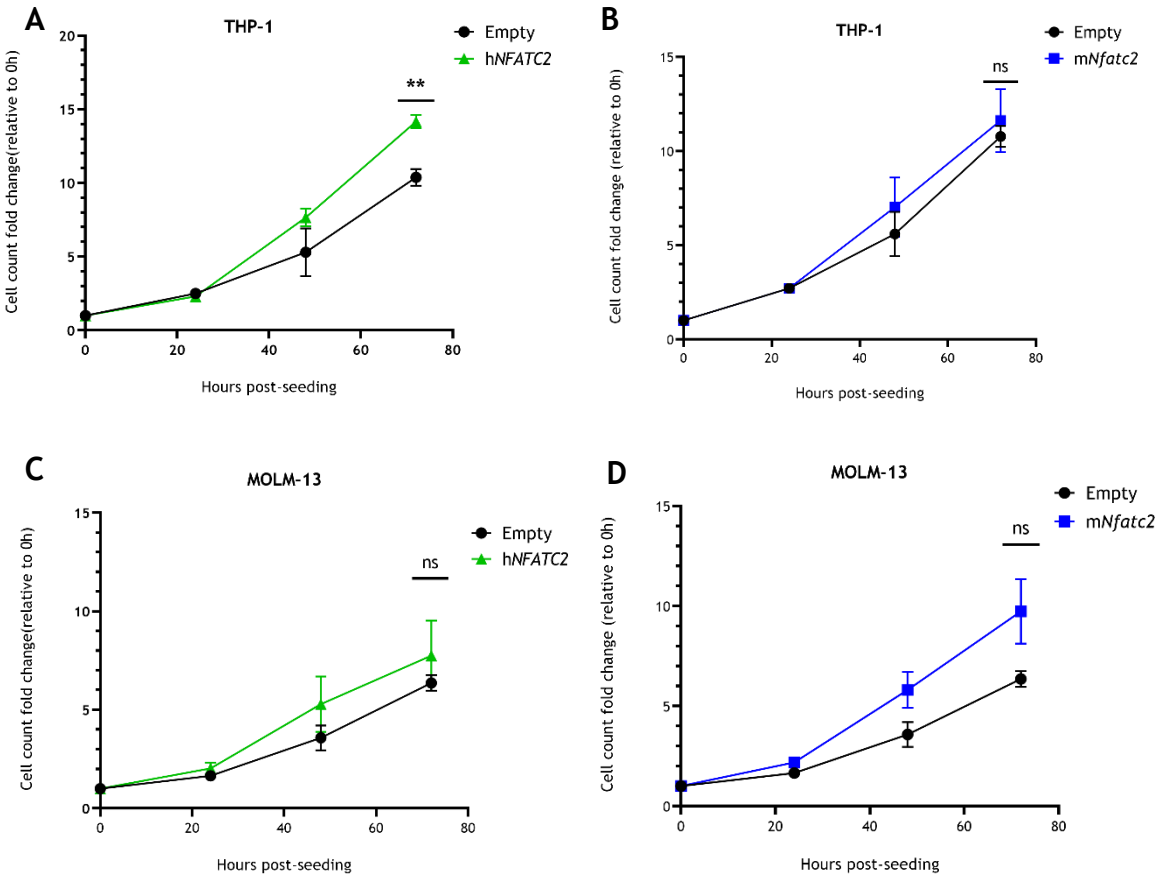

Figure 3-20. THP-1, but not MOLM-13, expanded more in culture with o/e h*NFATC2*. Cell lines were seeded at 1x10^5 cells/mL in liquid culture and counted every 24 hr, for a period of 72 hr. Cell counts are shown as a mean±SEM fold change from 0 hr at each time point. For each cell line the mean difference between fold changes at 72 hr was compared to that of the empty vector control using an unpaired two-sided t-test. Significance is shown as *p* values (**<0.1, 'ns' = *p*>0.05). Biological replicates are as follows: **A:** THP-1 o/e h*NFATC2*, n=3; **B:** THP-1 o/e m*Nfatc2*, n=4; **C:** MOLM-13 o/e h*NFATC2*, n=3; **D:** MOLM-13 o/e m*Nfatc2*, n=3. All technical replicates n=2.

3.2.5 Chapter Discussion

3.2.5.1 *NFATC2* and survival outcomes

The findings in this chapter demonstrate that there may be a role for *NFATC2* in AML biology. The first aim was to elucidate whether *NFATC2* expression would impact upon clinical course. From the TARGET-AML paediatric cohort it was shown that patients in the upper quartile of *NFATC2* expression had a worse overall or event-free survival than in the lower quartile. This was not seen in the TCGA or BEAT-AML data, which are comprised largely of adults. This initially suggests, from limited data, that *NFATC2* could have a more important role in the course of paediatric AML than in adult disease. Also, higher *NFATC2* expression appeared to be associated with better overall survival in the BEAT-AML cohort, although without statistical significance, potentially highlighting further differences between these cohorts which require further exploration.

The TARGET-AML cohort is retrospective and described as 'relapse-enriched' (Fan *et al.*, 2020). For the patient samples selected, 65.5% underwent relapse during the ~9-year course of follow-up. In the AML10 paediatric AML trial, whereby follow-up lasted ~7 years, only 34.8% of patients relapsed after chemotherapy or transplantation (Webb *et al.*, 1999). While clinical protocols and classification of remission have changed since AML10, it is clear that TARGET-AML cohort has a substantially higher proportion of patient relapse than might be expected.

The analysis of the BEAT-AML cohort focused on therapy-naïve patients and the TCGA-AML cohort looked at *de novo* AML only. It is possible that the correlation of survival outcomes with *NFATC2* expression in the TARGET-AML cohort may therefore be related to the high rate of relapse in these patients. Subgroup analysis of TARGET-AML patients who went on to relapse might reveal whether high *NFATC2* expression is correlated with relapse risk, and whether this explains the finding that these *NFATC2*^{HI} patients have poorer OS.

In the GSE83533 cohort of patients, *NFATC2* was found to be higher at relapse than at diagnosis in paired sample, which supports the hypothesis that *NFATC2* may play a role in AML relapse. However, the data suggest that high *NFATC2* was correlated with the relapse phenotype when it occurred, as opposed to being a predictive marker of relapse or outcome.

Previous studies have shown that *NFATC1* is involved in driving 'escape' mechanisms leading to resistance to TKIs in myeloid leukaemia (Gregory *et al.*, 2010, Metzelder *et al.*, 2015). It is possible that, in the GSE83533 cohort, *NFATC2* is driving similar mechanisms of acquired resistance and leading to the selection of *NFATC2*^{HI} clones at relapse. However, this does not explain the poorer outcomes observed for *NFATC2*^{HI} patients at diagnosis in the TARGET-AML cohort. A variety of other factors are implicated in AML resistance, including AML stem cell resistance to chemotherapy (Yeung and Radich, 2017).

3.2.5.2 *NFATC2* and *NFATC3*

It is also interesting to note that high expression of *NFATC3*, but not *NFATC1*, was detrimental to survival in the TARGET-AML cohort and also higher at relapse in the GSE83533 cohort. These similarities between *NFATC2* and *NFATC3* suggests that they may have similar functional properties driving these correlative relationships observed. The finding that *NFATC2* and *NFATC3* expression values are correlated with $r>0.5$ could support the idea that these genes share some functional properties and explain some of the common patterns observed in the TARGET-AML data.

Given the structural homology between differing NFATs it is unsurprising that some functional redundancy has been observed in some tissues. *NFATC2* and *NFATC3* double KO mouse models have shown that their repressive effects on cells of the lymphoid system are redundant to some extent (Ranger *et al.*, 1998), though the applicability of this to myeloid tissue is not clear. In contrast, mouse single knockout (KO) models have shown that inter-NFAT redundancy is not always the case, particularly in immune system development and function.

Various *NFAT* KO mouse models demonstrate that NFATc1, NFATc2 and NFATc3 have critical roles in the immune system, including thymic development, lymphocyte expansion, allergic responses (including eosinophil and mast cell function) and T cell activation. NFATc4 appears to be less important in immune cells. Also, *NFATC1* KO mice are non-viable due to lethal cardiac defects and so the KO must be expressed conditionally in transgenic mice, highlighting that NFATs have key roles in multiple cell types and in development. The different KO mouse models are summarised by Crabtree and Olson (Crabtree and Olson, 2002).

In this study, the finding that *NFATC3* may be involved in AML clinical outcome is also novel, however this study aimed to focus on *NFATC2*, and this was not considered for further analysis.

3.2.5.3 *NFATC2* might be associated with differentiation

The finding that *NFATC2* is more highly expressed in less well-differentiated AML, as classified by the FAB classification, is of biological interest. This may reflect findings that NFATs negatively regulate differentiation and the cell cycle in the healthy myeloid compartment (Fric *et al.*, 2012a, Fric *et al.*, 2014). AML M0 has been shown to have a poor prognosis (Amadori *et al.*, 1996), so it could be important to examine the relationship between *NFATC2* expression, FAB classification and survival together. The relationship of survival with FAB classification in the TARGET-AML dataset was not explored due to low numbers of patients in some FAB groups, likely leading to an insufficiently powered statistical test.

However, the FAB classification is now considered to be less prognostic without further cytogenetic information (Walter *et al.*, 2013, Canaani *et al.*, 2017). Additionally, the topology of the haemopoietic hierarchy in AML is more complex than in normal myeloid haemopoiesis and differentiation status is not as 'linear' (Pollyea and Jordan, 2017).

Furthermore, although there were no significant survival differences found in the TCGA or BEAT-AML datasets, the relationship of FAB classification and *NFATC2* expression levels appears to be consistent across these datasets: showing that expression is the lowest in M5 AML. Overall these data present a potential biological and/or clinical significance of *NFATC2* expression in AML patients' BM and warrant further study into this gene's role in AML biology.

3.2.5.4 *NFATC2* expression is variable in AML cell lines

The THP-1 model in which the *KDM4A-PAF1-NFATC2* axis was first described, is a MLL-AF9 infant AML cell line. MLL-AF9 is usually the most common MLL rearrangement found in all groups (Winters and Bernt, 2017); total MLL rearrangements account for less than 3% of adult AML, but 15-20% of paediatric AML (Schoch *et al.*, 2003, Balgobind *et al.*, 2011). In order to investigate whether *NFATC2* is important in MLL-AF9 AML only or in other subtypes it is important to

explore non-MLLr *in vitro* models. Protein expression of *NFATC2* was difficult to detect in some non-MLLr cell lines, such as Kasumi-1 and OCI-AML3. However, no measure of *NFATC2* function has been made in these cases and it could still be functional at a low level. HL-60 had the highest expression of the non-MLLr cell lines examined and may be a more suitable model for study of *NFATC2*.

The study found that transcript variants 3-6 were not well expressed in THP-1 cells. *NFATC2* transcript variants are well-characterised and vary primarily in their lateral TAD domains, which are involved in protein-protein interactions. Shorter protein isoforms may lack specific phosphorylation sites and/or other functional domains (Luo *et al.*, 1996b, Rao *et al.*, 1997a). As such, this may have functional implications when generalising these results to AML patient cells, for which the transcript variants have not been characterised. Furthermore, the absence of the antibody recognition site on variants 7 and 8 means that caution is needed when interpreting any protein-based assay data in this study.

3.2.5.5 The calcium-NFATc2 axis and NFATc2 function in AML

The drug treatment studies performed in THP-1 demonstrate that the nature of calcium signalling and NFATc2 protein structure is highly complex and that the expected results from T cells may not be observed in AML or myeloid cells.

Firstly, in THP-1 ionomycin does not appear to induce nuclear translocation of NFATc2 as expected. However, it could be the case that nuclear translocation of NFATc2 is already at a maximal level, and/or calcium signalling is not a limiting factor to further translocation.

In contrast, when *NFATC2* was overexpressed in THP-1 it resided predominantly in the nucleus. This suggests that, unlike in T cells, the cellular machinery in THP-1 favours dephosphorylation and nuclear import of NFATc2. The balance of phosphorylation, nuclear import and export of NFAT is mediated by a number of signalling pathways, which are not necessarily calcium-driven (Crabtree and Olson, 2002, Sharma *et al.*, 2011). Unlike THP-1, the fractionated protein blot in NOMO-1 shows that NFATc2 resides more equally between fractions. These observations on the balance of cytoplasmic and nuclear NFATc2 are important as they reflect some of the activity of NFATc2-regulatory networks in these cells. However, due

to incomplete fractionation of cellular compartments in some cases, caution should be taken in interpreting these blots.

Co-stimulation with ionomycin and phorbol 12-myristate 13-acetate (PMA) has been shown to induce full NFAT transactivation in the nucleus, downstream of MAPK signalling (García-Rodríguez and Rao, 2000, Okamura *et al.*, 2000, Alam *et al.*, 2018). PMA-induced MAPK activation also leads to recruitment of key NFAT transcriptional partner AP-1 (Macián *et al.*, 2001). In THP-1 the addition of 20 μM PMA to ionomycin was not observed to impact NFATc2 phosphorylation, globally or at ser54, or its translocation to the nucleus.

However, the expected results from ionomycin treatment were not observed under these conditions in Jurkat T cells, either. This suggests that further methodological optimisation of this treatment is necessary. Observation of NFAT dephosphorylation/translocation with ionomycin treatment is published under a range of conditions, which these experiments were designed to best replicate and based on some empirical testing of compound concentrations. Issues may include the concentration of ionomycin, length of stimulation (10 min to 24 hr in the literature) and/or the supplementation of culture media with calcium (García-Rodríguez and Rao, 2000, Okamura *et al.*, 2000, Alam *et al.*, 2018).

Calcium chelation by EGTA did increase the protein size of NFATc2, consistent with rapid re-phosphorylation at 30-60 minutes. Kar *et al*. found that NFATc2 re-phosphorylation and export from the nucleus was relatively slower than for NFATc3, which may explain the observation of phosphorylated NFATc2 in the nucleus upon EGTA treatment, for both THP-1 and Jurkat cells (Kar *et al.*, 2016). Okamura *et al*. proposed a model by which NFATs are present in the nucleus while phosphorylated, but the protein kinetics largely favour export to the cytoplasm in this state (Okamura *et al.*, 2000). The cytoplasmic/nuclear balance of NFATc2 may respond differently to expectations under the stress of EGTA-mediated calcium chelation. These data support the idea that the larger NFATc2 protein observed on an immunoblot represents highly-phosphorylated NFATc2, as observed in the literature, and that NFATc2 phosphorylation is calcium-sensitive. However, the separation of phosphorylation status into cytoplasmic vs. nuclear might not be as clear-cut as expected.

NFATc2 is coupled to calcium 'microdomains' and less dependent on global cellular calcium, and so the kinetics of SOCE and NFATc2 activation is highly nuanced (Kar *et al.*, 2011, Kar *et al.*, 2016). This may underpin the absence of an observed effect of PLC inhibition on NFATc2 activity in THP-1. Small molecule inhibition of PLC can block NFAT-mediated transcription in renal cells (Puri *et al.*, 2004) but these signalling networks may not translate to myeloid or AML cells. Further investigation of the PLC-NFATc2 axis is likely beyond the scope of this study.

The observation that CsA induces a cytoplasmic shuttling of NFATc2 is expected (Aramburu *et al.*, 1998) and provides confidence that NFATc2 is activated downstream of calcineurin signalling in THP-1 cells. This was also observed in Jurkat cells to some extent, as expected, supporting the observations in THP-1. Therefore, this provided grounds to manipulate this pathway in AML cell lines using CsA and other established inhibitors of calcineurin, as a means of assessing NFAT contribution to cell growth and survival.

3.2.5.6 *NFATC2* overexpression as a measure of its function

NFATC2 overexpression increased expansion of THP-1 in liquid culture. NFATc2 regulation of the cell cycle is well-published, but it tends to be a negative regulator of key cycling genes in various cell contexts (Mognol *et al.*, 2016). As such, this result may reveal a novel role for *NFATC2* which should be explored further. However, expression of m*Nfatc2* did not appear to induce this effect.

Murine *Nfatc2* (m*Nfatc2*) shares significant structural homology with h*NFATC2* (Vihma *et al.*, 2008). This vector has been expressed in murine cells and can translocate to the nucleus upon stimulation with ionomycin, in addition to activating the IL-4 promoter (Monticelli and Rao, 2002), but no publications have used this vector in human cells. It is therefore not clear if this m*Nfatc2* protein would be functional in human THP-1 cells, and additionally it is not clear if the m*Nfatc2* was expressed in the nuclear compartment due to challenges in detecting mNfatc2 protein with the antibody used. In conclusion, the phenotype of THP-1 o/e h*NFATC2* did not resemble that of THP-1 o/e mNfatc2, potentially due to fundamental differences in the orthologous proteins and the differing biological machinery of human and mouse cells.

With increased confidence that *NFATC2* has a role to play in AML pathobiology, next the consequence of depletion of *NFATC2* and its function in AML was explored, initially focusing on manipulation of the calcineurin-NFAT axis, which has been validated as functional in the THP-1 model.

4 Results (II): Depletion of *NFATC2* in AML cells *in vitro*

4.1 Introduction

The previous chapter established that *NFATC2* is expressed in the THP-1 cell line model of MLL-AF9 AML and is vulnerable to CsA inhibition of the calcineurin-NFAT axis. The first aim of this chapter was to determine the phenotype of THP-1 cells following inhibition of the calcineurin-NFAT axis, using established compounds, to ascertain whether these cells were dependent on the calcineurin-NFAT signalling axis.

CsA forms a ternary complex with endogenous cyclophilin A and calcineurin, blocking the phosphatase activity of calcineurin on any of its substrates, including NFATs (Huai *et al.*, 2002). The VIVIT peptide blocks the calcineurin-NFAT interaction more specifically, by imitating the PxIxIT binding motif found on each NFAT (Aramburu *et al.*, 1999). The fusion of polyarginine (11R) has made this large peptide more cell-permeable (Noguchi *et al.*, 2004). However, VIVIT-11R is still not specific to NFATc2 and is a large peptide, which may be vulnerable to proteolysis in AML cells and/or it is less permeable than a small molecule. Thirdly, INCA-6 is a small molecule inhibitor which has been shown to block the calcineurin-NFAT interaction specifically *in vitro* and *in vivo*, though the mechanism is not clear (Roehrl *et al.*, 2004, Bretz *et al.*, 2015, Savage *et al.*, 2015). CsA treatment of THP-1 cells is known to inhibit LPS-mediated cytokine transcription (Ma *et al.*, 2007) but the effects of CsA on cellular growth and/or survival are not described. The other inhibitors have not been described in this cell line.

To focus in more specifically on *NFATC2*, THP-1 cells were transduced with lentivirus containing *NFATC2*-targeting shRNA. The aim was to elucidate the phenotype of cells *in vitro* following *NFATC2* transcript depletion, as a means of assessing the function of *NFATC2* in these cells. Analysis of the cell cycle, apoptosis regulation, growth in culture and expression of selected genes were used to determine the existing role(s) of *NFATC2*. shRNA KD can have unintended off-target effects in the cell (Rao *et al.*, 2009) and so it was important to test more than one shRNA construct, to establish whether the observed phenotype was common to *NFATC2* depletion. Additionally, THP-1 o/e m*Nfatc2*, as described in

Chapter 3.2.3., was used as a model to examine if m*Nfatc2* could 'rescue' the phenotype of h*NFATC2* KD. This is a secondary means of assessing shRNA specificity.

This study also assessed AML cells of multiple (cyto)genetic backgrounds, to establish whether *NFATC2* had a specific role in MLL-AF9 AML, or whether its role(s) was different depending on the mutational profile of the cell. To expand beyond THP-1 cells a number of other cell line models were used for *NFATC2* KD and the phenotype assessed as for THP-1. One such model included murine BM cells expressing retroviral MLL-AF9, as described by Somervaille *et al*. (Somervaille and Cleary, 2006), in which shRNA was targeted to endogenous m*Nfatc2*. These data were used to hypothesise further about the specific function(s) of *NFATC2* in AML cells.

4.2 Chapter objectives

1. Determine the viability and phenotype of THP-1 cells after treatment with selected calcineurin-NFAT axis inhibitors.
2. KD *NFATC2* in THP-1 cells and assessment of cell behaviour, in order to assess the function of *NFATC2* in these cells.
3. KD of *NFATC2* in THP-1 o/e m*Nfatc2* to determine if orthologous m*Nfatc2* can rescue any phenotype(s) observed in objective 2.
4. KD of m*Nfatc2* in an established model of MLL-AF9 in murine BM and assessment of cell behaviour, in order to assess the dependency of function of m*Nfatc2* on cell mutational profile.
5. ShRNA KD of *NFATC2* in a variety of selected AML cell lines of differing (cyto)genetic backgrounds, to determine the phenotype and putative function(s) of *NFATC2*, and also to compare with the models used in objectives 2 and 4.

4.3 Results

4.3.1 Inhibition of NFAT family protein activity

THP-1 and Kasumi-1 cells, which express high and low levels of *NFATC2*, respectively, were treated with calcineurin-NFAT inhibitors. THP-1 cells were most sensitive to VIVIT-11R when compared with CsA and INCA-6, as measured by an Alamar Blue cell viability assay (Figure 4-1). The IC_{50} was 5.86 μM for VIVIT-11R and 8.69 μM for CsA, both at 48 hr post-treatment. In contrast Kasumi-1 cells were insensitive to VIVIT-11R or CsA, as the IC_{50} could not be determined in the concentration range tested (Figure 4-2). In summary, VIVIT-11R and CsA had greater potency in THP-1 than Kasumi-1, and for THP-1 VIVIT-11R was the more potent of the 2, with respect to cell viability.

The IC_{50} for INCA-6 in THP-1 cells was 12.23 μM at 48 hr post-treatment. Kasumi-1 cells were found to be sensitive to INCA-6, with an IC_{50} value of 7.91 μM at 48 hr (Figure 4-2C). In fact, the IC_{50} values for INCA-6 treatment were lower for Kasumi-1 than for THP-1 at 24, 48 and 72 hr post-treatment (Table 4-1). So in contrast to VIVIT-11R and CsA, INCA-6 was more potent in Kasumi-1 than in THP-1 cells.

THP-1 cells were treated with each calcineurin-NFAT axis inhibitor at 0.5X, 1.0X and/or 1.5X the estimated IC_{50} value for 24 hr post-treatment (shown in Table 4-2). Note that, while THP-1 cells were not sensitive enough to CsA calculate the IC_{50} 24 hr post-treatment, the estimate based on continuation of the curve was taken for this purpose (10.59 μM).

WCL taken at 24 hr post-treatment were immunoblotted for NFATc2 (Figure 4-3A). This shows that there was markedly slower migration of protein bands following CsA treatment, suggesting an increased protein size of ~5-10 kDa, and a loss of the lower bands, representing the smallest NFATc2 proteins. This size increase could suggest increased global NFATc2 phosphorylation after CsA treatment. Total NFATc2 quantity is also markedly reduced after CsA treatment at 1.0X the estimated IC_{50}, suggesting that CsA leads to reduced transcription, translation or post-translational processing of *NFATC2*/NFATc2.

VIVIT-11R treatment induces an increase in the intensity of the upper NFATc2 band, relative to total NFATc2, as measured by densitometry, though the observed protein size on the blot did not change as observed for CsA (Figure 4-3B&C). This

may reflect that VIVIT-11R treatment leads to increased NFATc2 phosphorylation, in the same manner as observed for calcium chelation by EGTA (see Figures 3-7 and 3-8). The distinction between the changes between CsA and VIVIT-11 are not clear, but it could reflect a more substantial phosphorylation event with CsA treatment compared to VIVIT-11R. In addition, the band size increase observed after CsA treatment is more exaggerated than observed previously in THP-1 (Figure 3-9) or Jurkat cells (Figure 3-10), albeit the 0.5X IC_{50} value used latterly (see Table 4-1) was higher at 5.3 μM, compared with 4.5 μM. This could suggest that the apparent increase in band size in Figure 4-3 is owing more to gel distortion than a real biological effect. Changes to NFATc2 protein quantity or band sizes were not observed 24 hr after treatment with INCA-6.

Treatment of THP-1 with 0.5X the IC_{50} of either CsA or VIVIT-11R (at 24 hr) revealed some changes to NFATc2 on immunoblotting, but minimal impact on cell viability. These concentrations were chosen to generate immunofluorescent images of THP-1 cells 24 hr post-treatment, since lower viability cells would not be expected to stain well. This also provided an opportunity to observe cytoplasmic/nuclear shuttling of NFATc2. After CsA treatment there is a clear reduction of NFATc2 staining in the cell cytoplasm and nucleus, which reflects the global loss of protein quantity observed on the immunoblot.

VIVIT-11R-treated cells show a reduction of NFATc2 staining across the cell. Based on the immunofluorescence observations, it was expected that total NFATc2 quantity (including both phosphorylated and un-phosphorylated protein) would be preserved but the majority translocated to the cytoplasm, due to putatively increased phosphorylation. Therefore, this observation is contradictory to expectations. NFATc2 staining after INCA-6 treatment was unchanged from the vehicle control, regarding subcellular location or signal intensity, which was expected.

A Cyclosporine A

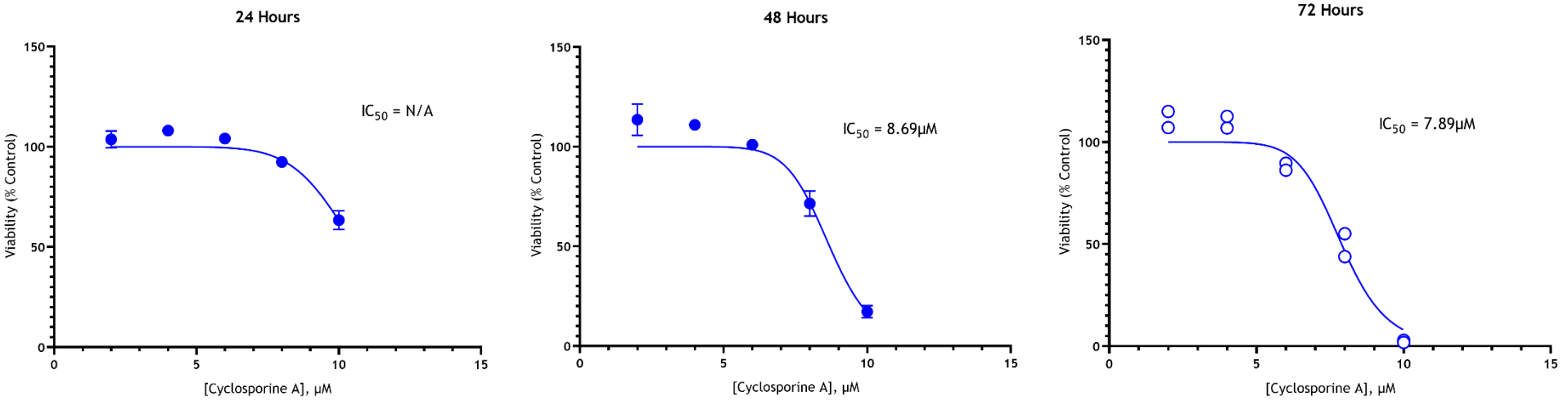

B VIVIT-11R

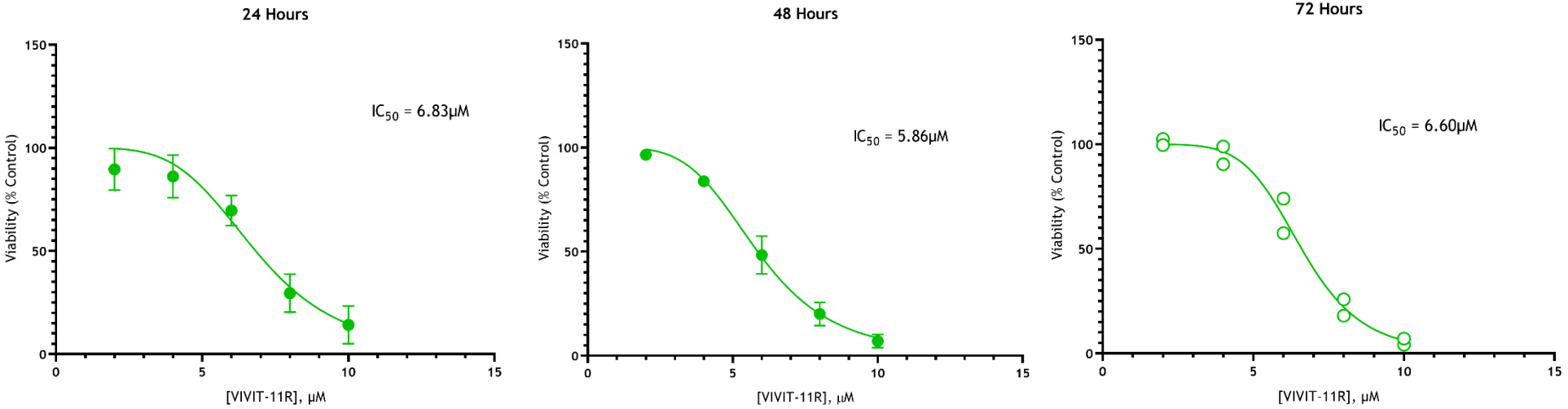

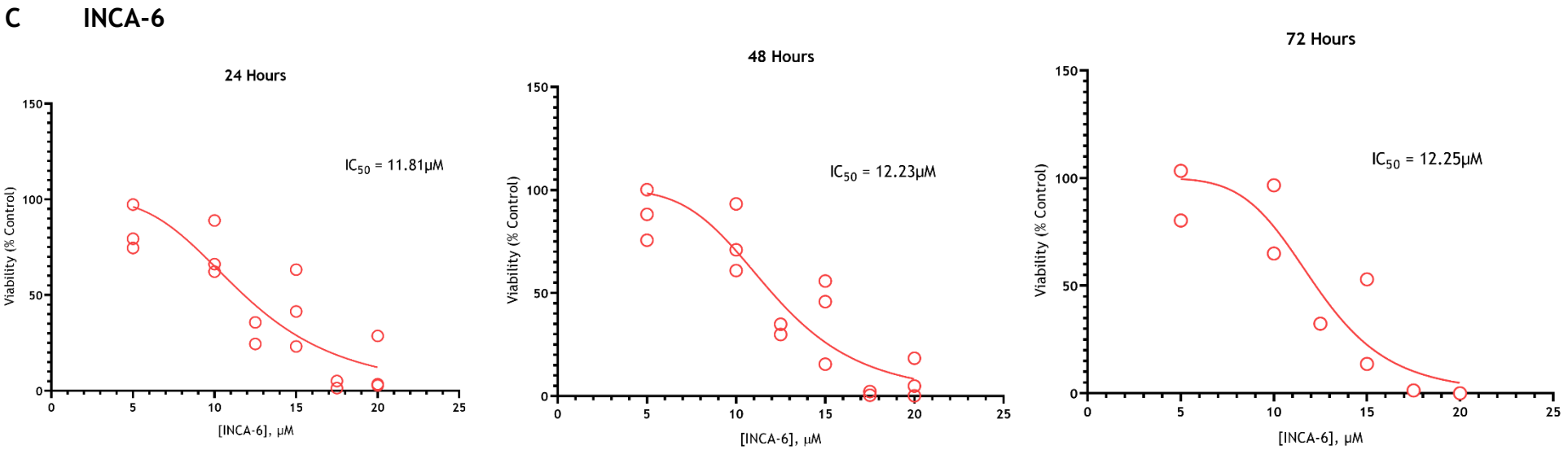

Figure 4-1. THP-1 cells were more sensitive to VIVIT-11R than CsA or INCA-6.
THP-1 cells were treated with either CsA (**A**), VIVIT-11R (**B**) or INCA-6 (**C**), in a range of concentrations, or a vehicle control; n=2 or n=3 biological replicates. Mean (closed circles) ± SEM are shown if n=3, or individual data points (open circles) are shown if n=2-3. All technical replicates in assay n=3. At 24, 48 and 72 hr post-treatment cell suspension was assessed for viability using an Alamar Blue Assay. The graphs show the absorbance measured (at 535_{ex} and 590_{em}) in each sample concentration, as a % of that measured in the vehicle control sample. For each timepoint non-linear regression was used to fit a four-parameter logistic curve to the data, constrained between 0% and 100%. From this the IC_{50} has been estimated and this is shown on each graph. 'N/A' = if IC_{50} was not calculated due to the shape of the curve.

A Cyclosporine A

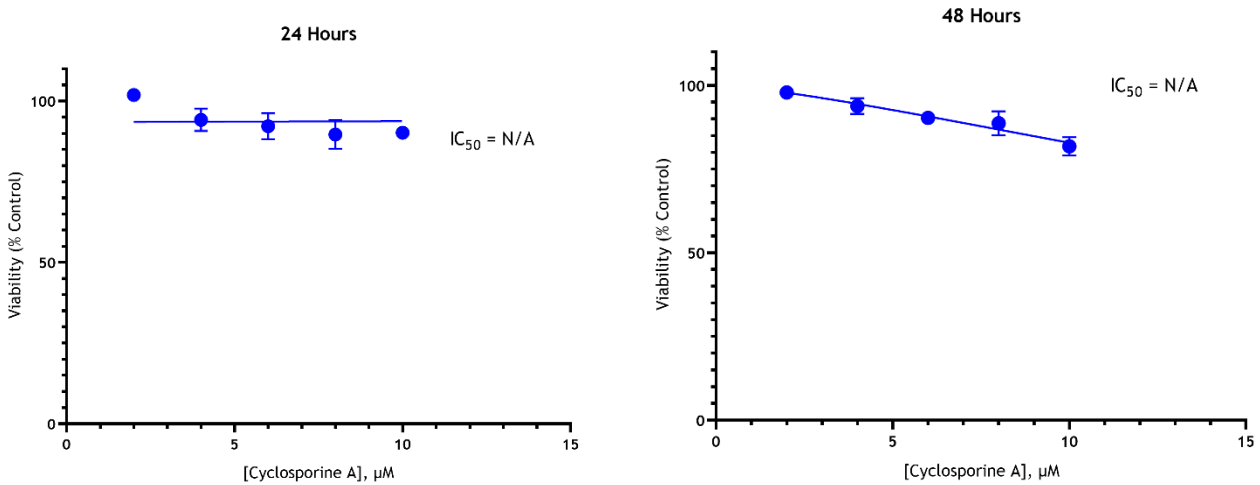

B VIVIT-11R

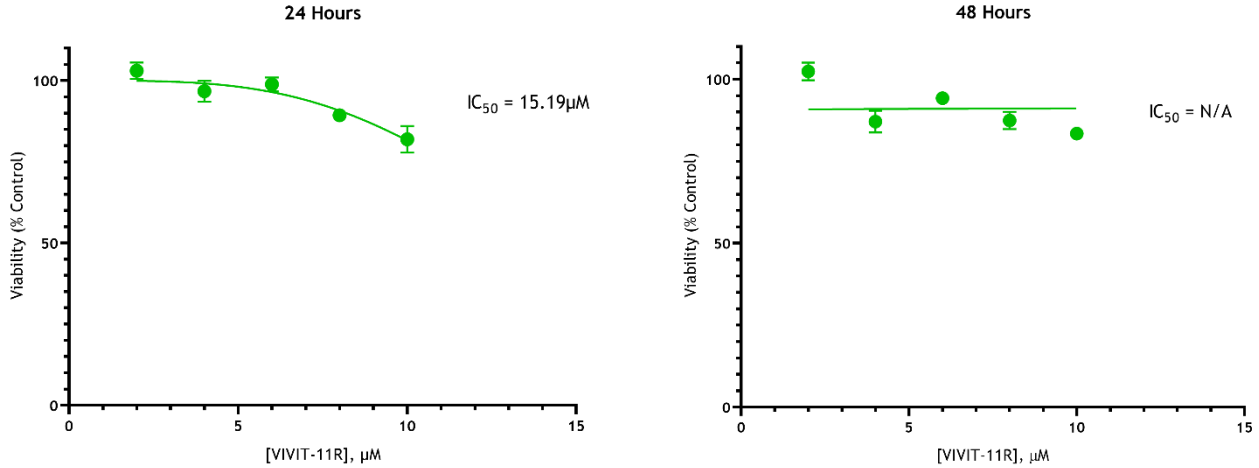

C INCA-6

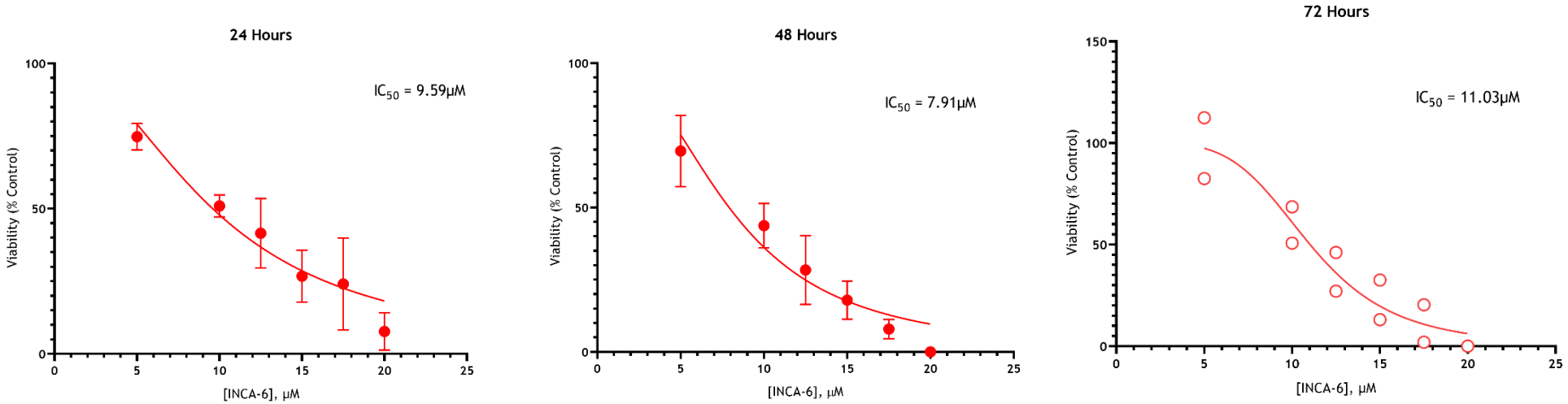

Figure 4-2. Kasumi-1 cells were not sensitive to CsA or VIVIT-11R, but sensitive to INCA-6.
Kasumi-1 cells were treated with either CsA (**A**), VIVIT-11R (**B**) or INCA-6 (**C**), in a range of concentrations, or a vehicle control; n=2 or n=3 biological replicates. Data presented as in Figure 4-1. Mean (closed circles) ± SEM are shown if n=3, or individual data points (open circles) are shown if n=2. All technical replicates in assay n=3.

Inhibitor	Timepoint (Hours)	IC_{50} (Estimated, μM)	
		THP-1	Kasumi-1
Cyclosporine A	24	10.59*	N/A
	48	8.69	N/A
	72	7.89	N/A
VIVIT-11R	24	6.83	15.19
	48	5.86	N/A
	72	6.60	N/A
INCA-6	24	11.81	9.59
	48	12.23	7.91
	72	12.25	11.03

Table 4-1. THP-1 were more sensitive to VIVIT-11R and CsA than Kasumi-1. Viability of THP-1 or Kasumi-1 cells after treatment with either cyclosporine A, VIVIT-11R or INCA-6 was measured by an Alamar Blue Assay, as described in **Figures 4-1** and **4-2.** The IC_{50} values estimated from these regression curves are shown in this table. 'N/A' = IC_{50} could not be determined from the curve fit using the available data.

* THP-1 cells were not sensitive enough to CsA calculate the IC_{50} 24 hr post-treatment, however this was estimated based on continuation of the curve, for the purpose of treating cells for harvest at 24 hr post-treatment.

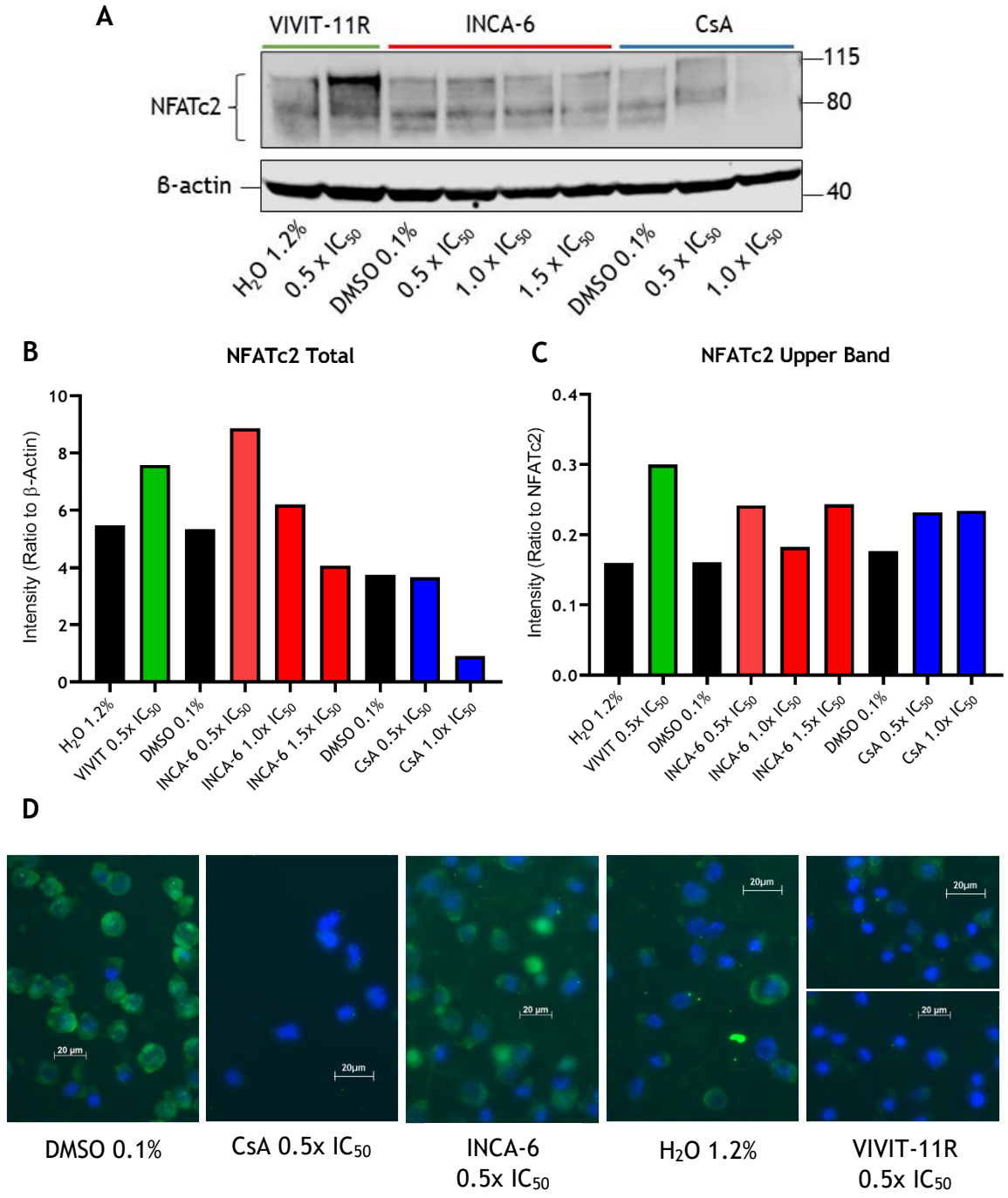

Figure 4-3. CsA treatment of THP-1 cells caused an increase in observed protein size. THP-1 cells were treated with ether VIVIT-11R, cyclosporine A, INCA-6 or a vehicle control, at concentrations determined by the estimated IC_{50} values at 24 hours post-treatment (n=1), shown in Table 4-1. **A:** Whole cell protein lysates from treated THP-1 cells (55µg/well) were immunoblotted with anti-NFATc2 as shown. Anti-β-actin was used as a loading control. Protein size is shown on the right-hand side in kDa. **B,C:** Bar graphs show protein signal intensity as measured by densitometry, each normalised to β-actin. **B** shows the measured intensity of all NFATc2 bands, **C** shows the measured intensity of the highest NFATc2 band only. **D**: Representative immunofluorescence images (n=1) of treated THP-1 cells stained with DAPI and NFATc2/Alexa 488. Scale bars for 20 µm are shown.

THP-1 cells treated with CsA, VIVIT-11R or INCA-6 were assessed for apoptosis using an Annexin V/DAPI assay. Figure 4-4 shows that there was a trend towards increased apoptosis as drug concentrations increase, though none was statistically significant. VIVIT-11R did not alter apoptosis at 0.5X the IC_{50}, but Annexin V^+ cells increased from 6.64% in the vehicle control to 24.81% at 1.0X the IC_{50}. The mean proportion of Annexin V^+ cells after treatment with CsA or INCA-6 at 1.0X the IC_{50} was 58.27% and 40.05%, respectively. The proportion of Annexin V^+ cells increased almost 7-fold with a rising concentration of cytarabine, from 7.09% in the vehicle control to 47.50% at 5 μM.

Assessment of the cell cycle by PI staining revealed that there was a statistically significant accumulation of cells in the G0-G1 phases of the cell cycle after CsA (1.0x IC_{50}) treatment of THP-1 (Figure 4-5A; p=0.0005) with a reduction in S-phase cells (p=0.0407), respective to the vehicle control. Together this suggests cell cycle arrest at the G1/S transition after treatment with CsA.

Treatment with VIVIT-11R resulted in a trend towards increasing cells in the S-phase and a reduction of those in G2-M, but these could not be statistically tested without further replication. The differences in cell cycle phases between the vehicle control and INCA-6 treatment (0.5xIC_{50}) were not significant.

Cells were also treated with cytarabine as a positive control for observation of cell cycle arrest with PI staining. Cytarabine intercalates into leukaemia cell DNA during replication in the S-phase and causes cell cycle arrest (Kufe and Major, 1982). It has also been shown to cause G1/S arrest in THP-1 cells at these concentrations (unpublished data). Here, treatment with cytarabine led to a build-up of cells in the S-phase, which can often indicate an increase in cell proliferation. However, there was also an observed reduction in cells within the G0-G1 and (at the highest concentration) G2-M phases, suggesting there may be arrest at multiple cell cycle checkpoints causing these perturbations. Although dead cells were excluded from analyses, the gating of cell cycle phases may be skewed by the high proportion of apoptotic cells observed after cytarabine treatment, which has also been observed previously in THP-1 cells with cytarabine treatment (unpublished data).

Together these data indicate that CsA and VIVIT-11R inhibit NFATc2 dephosphorylation by calcineurin in THP-1 cells as expected, but that INCA-6 does

not alter NFATc2 global phosphorylation or protein levels. THP-1 cell viability is impeded by CsA and this is driven by a mixed phenotype of apoptosis and G1/S cell cycle arrest. VIVIT-11R impacts THP-1 cell viability by a mix of apoptosis and S/G2 transition arrest, while INCA-6 mainly induces apoptosis. It is unlikely that the effects of INCA-6 are driven through calcineurin-NFATc2 blockade. Kasumi-1 cells are not sensitive to CsA or VIVIT-11R, but are sensitive to INCA-6, although these inhibitors should all act through calcineurin signalling. This reinforces the idea that INCA-6 acts independently of calcineurin-NFAT inhibition.

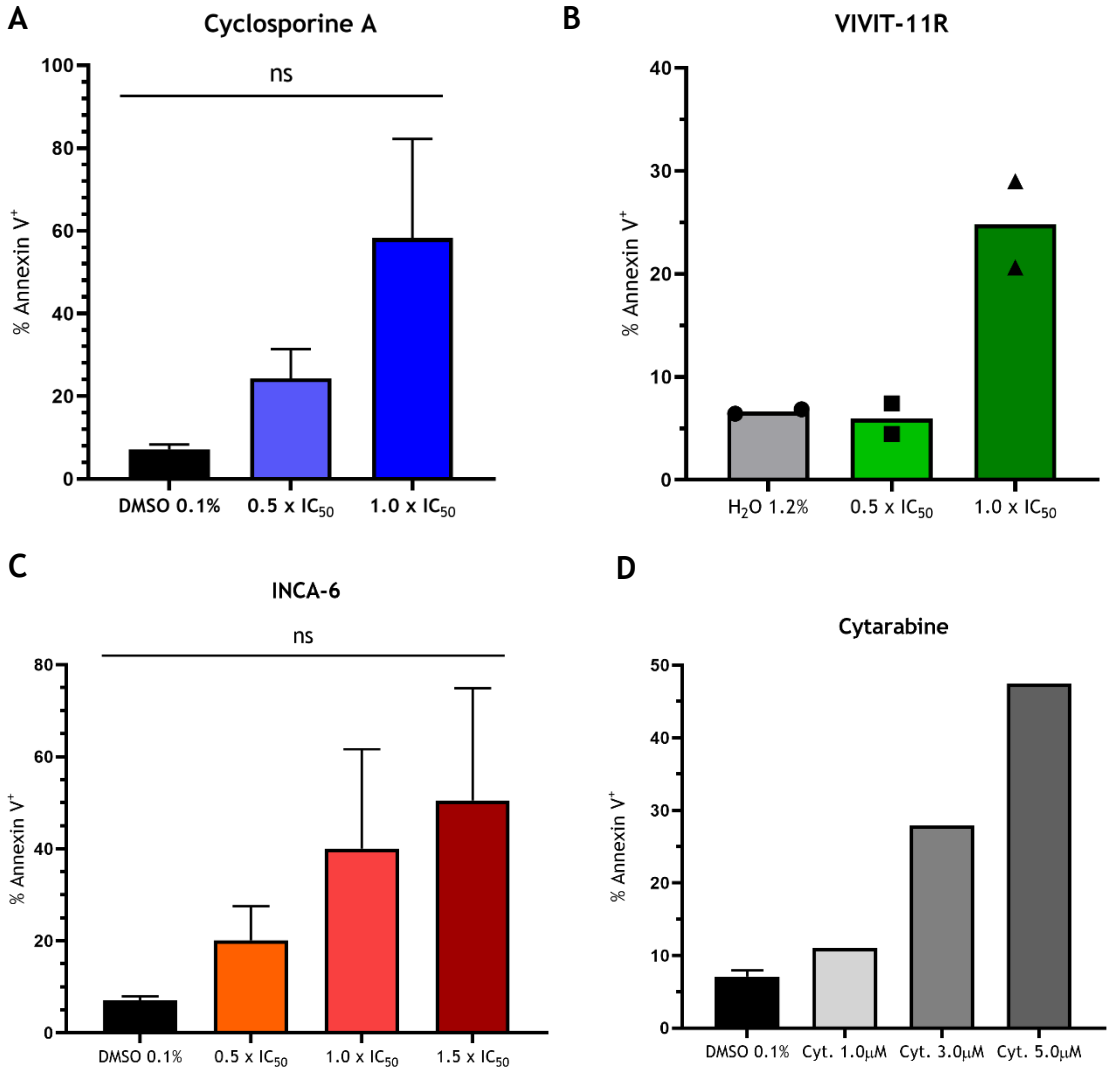

Figure 4-4. Inhibition of calcineurin-NFAT signalling in THP-1 cells led to increased apoptosis. THP-1 cells were treated with inhibitors as previously described. Cells were harvested and stained with Annexin V and DAPI at 48 hrs post-treatment for flow cytometry. Data shown are the mean % of gated cells positive for Annexin V ± SEM for n=3 biological replicates, or individual data points given for n<3. Significance of a difference in means was assessed using a one-way ANOVA, where 'ns' = p>0.05. **A:** Cyclosporine A, n=3. **B:** VIVIT-11R, n=2 biological. **C:** INCA-6, n=3 biological. **D:** Cytarabine, n=1 biological. This was used as a positive control.

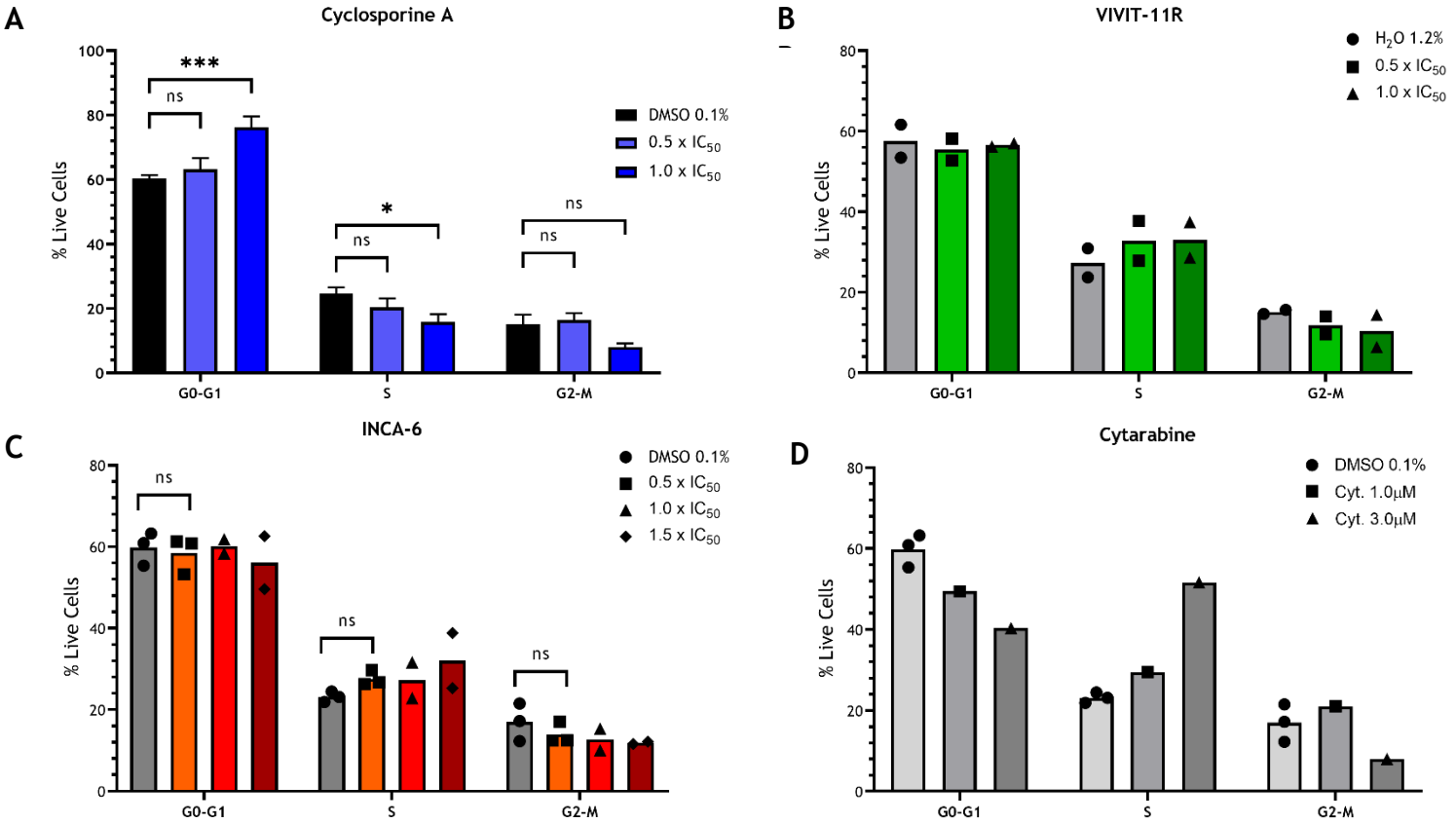

Figure 4-5. Treatment of THP-1 with calcineurin-NFAT inhibitors resulted in G0-G1 phase cell cycle arrest.
THP-1 cells were treated with inhibitors as previously described. Cells were harvested at 48 hr post-treatment and stained with PI for flow cytometry. Cells were gated into the following phases: sub-G0, G0-G1, S and G2-M. The cells in each phase are shown as a % of live cells, meaning cells in sub-G0 were excluded. Data shown are the mean ± SEM for n=3 biological replicates, or individual data points given if n<3. Significance of a difference in means was assessed using a two-way ANOVA or a two-sided unpaired t-test (with correction for multiple testing), where *<0.05, ***<0.001, 'ns' = p>0.05. **A:** Cyclosporine A, n=3 biological. **B:** VIVIT-11R, n=2 biological. **C:** INCA-6, n=2-3 biological as indicated. **D:** Cytarabine, n=1-3 biological as indicated. This is a positive control for cell cycle arrest.

4.3.2 shRNA Knockdown of *NFATC2* in MLL-AF9 AML

In order to assess the function of *NFATC2* more specifically in AML, lentiviral shRNA approach was used to deplete *NFATC2* transcript. Initially 4 shRNA constructs and a scrambled control shRNA were assessed in THP-1 and MOLM-13 cells as models of MLL-AF9 AML. After transduction and puromycin selection, cells were counted in liquid culture as a means of assessing their phenotype following *NFATC2* KD. The concentration required for puromycin selection was determined empirically for every cell line (data in 2.2.8, Figure 2-2) and example data are shown to demonstrate the efficiency of selection in THP-1 and MOLM-13 (Figure 4-6A).

The fold change in MOLM-13 cell count from 24 hr to 72 hr post-puromycin selection was compared to the change in *NFATC2* expression at 48 hr by qRT-PCR (Figure 4-6B) to determine if there was a correlation between these measurements. The R value of -0.6611 was not statistically significant (p=0.3389) and this was not a good means of assessing shRNA construct target specificity, without more data points. Construct sh*NFATC2*-144 was rejected in the study due to its ability to KD *NFATC2* being the smallest.

Cell counts showed that transduction of any *shNFATC2* construct led to a loss of cell expansion in culture. It was observed in THP-1 and MOLM-13 that construct sh*NFATC2*-143 resulted in the lowest expansion of cells in culture, while sh*NFATC2*-145 and sh*NFATC2*-146 showed similar, lesser effects at 72 hr post-selection (Figure 4-6C&D). Constructs -143 and -146 were taken forward as the primary shRNA constructs to assess the range of phenotypes. 72 hr post-puromycin selection was considered the optimal timepoint for phenotypic assessment of changes associated with *NFATC2* KD. THP-1 also had a higher transduction efficiency as demonstrated by puromycin selection (Figure 4-6A) and so this model of MLL-AF9 AML was chosen.

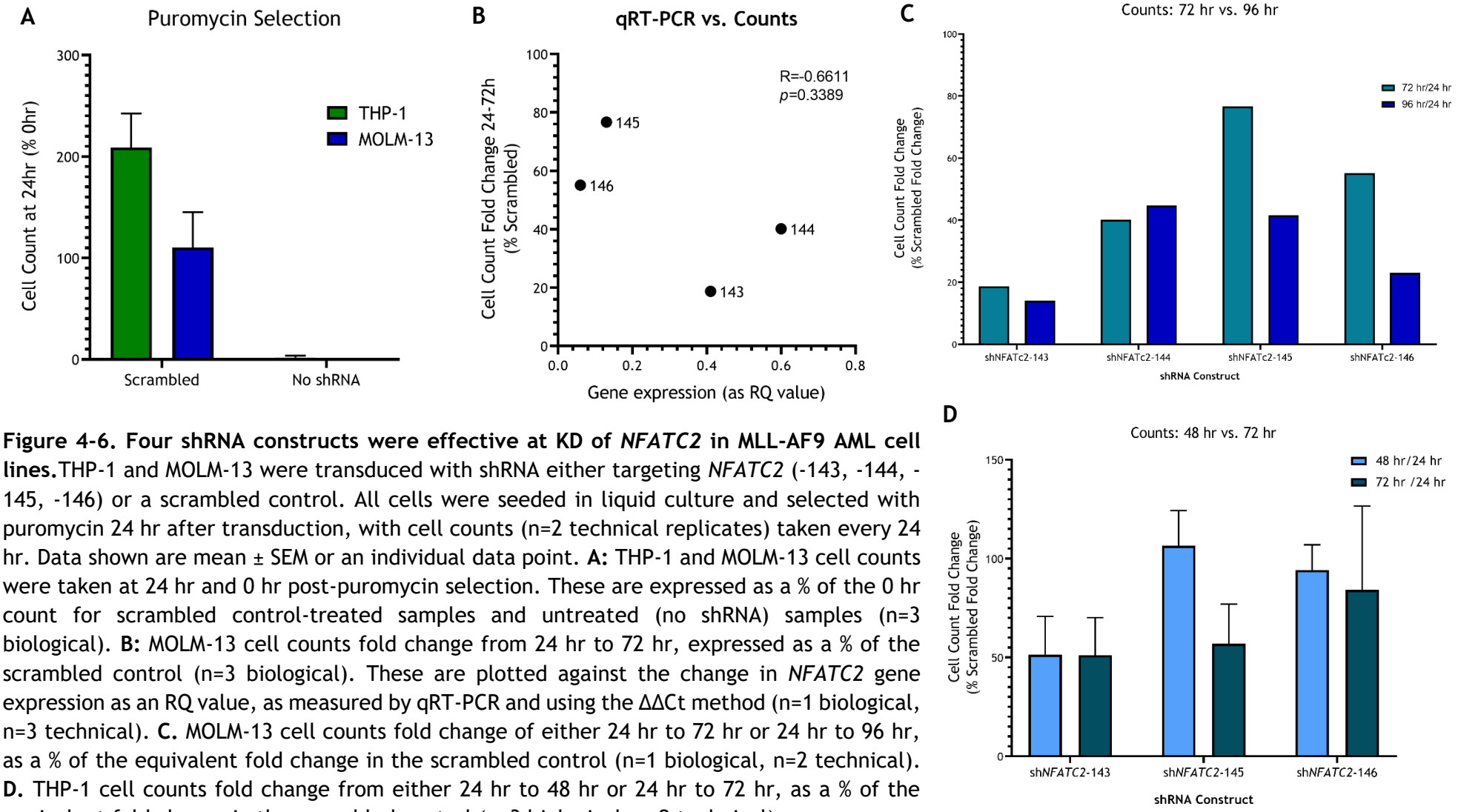

Figure 4-6. Four shRNA constructs were effective at KD of *NFATC2* in MLL-AF9 AML cell lines. THP-1 and MOLM-13 were transduced with shRNA either targeting *NFATC2* (-143, -144, -145, -146) or a scrambled control. All cells were seeded in liquid culture and selected with puromycin 24 hr after transduction, with cell counts (n=2 technical replicates) taken every 24 hr. Data shown are mean ± SEM or an individual data point. **A:** THP-1 and MOLM-13 cell counts were taken at 24 hr and 0 hr post-puromycin selection. These are expressed as a % of the 0 hr count for scrambled control-treated samples and untreated (no shRNA) samples (n=3 biological). **B:** MOLM-13 cell counts fold change from 24 hr to 72 hr, expressed as a % of the scrambled control (n=3 biological). These are plotted against the change in *NFATC2* gene expression as an RQ value, as measured by qRT-PCR and using the ΔΔCt method (n=1 biological, n=3 technical). **C.** MOLM-13 cell counts fold change of either 24 hr to 72 hr or 24 hr to 96 hr, as a % of the equivalent fold change in the scrambled control (n=1 biological, n=2 technical). **D.** THP-1 cell counts fold change from either 24 hr to 48 hr or 24 hr to 72 hr, as a % of the equivalent fold change in the scrambled control (n=3 biological, n=2 technical).

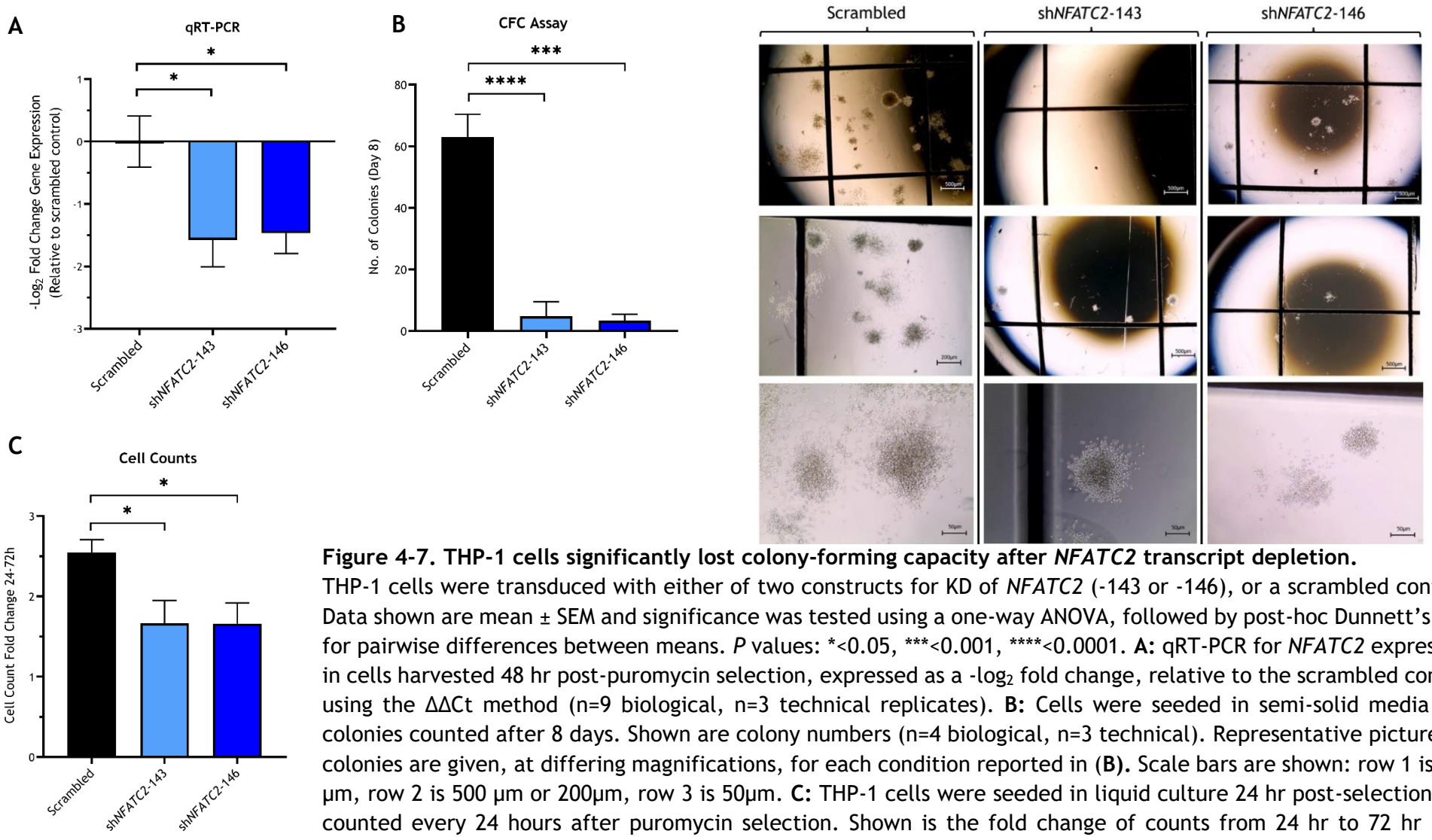

Figure 4-7. THP-1 cells significantly lost colony-forming capacity after *NFATC2* transcript depletion. THP-1 cells were transduced with either of two constructs for KD of *NFATC2* (-143 or -146), or a scrambled control. Data shown are mean ± SEM and significance was tested using a one-way ANOVA, followed by post-hoc Dunnett's test for pairwise differences between means. *P* values: *<0.05, ***<0.001, ****<0.0001. **A:** qRT-PCR for *NFATC2* expression in cells harvested 48 hr post-puromycin selection, expressed as a -$\log_2$ fold change, relative to the scrambled control using the ΔΔCt method (n=9 biological, n=3 technical replicates). **B:** Cells were seeded in semi-solid media and colonies counted after 8 days. Shown are colony numbers (n=4 biological, n=3 technical). Representative pictures of colonies are given, at differing magnifications, for each condition reported in (**B).** Scale bars are shown: row 1 is 500 µm, row 2 is 500 µm or 200µm, row 3 is 50µm. **C:** THP-1 cells were seeded in liquid culture 24 hr post-selection and counted every 24 hours after puromycin selection. Shown is the fold change of counts from 24 hr to 72 hr (n=6 biological, n=2 technical).

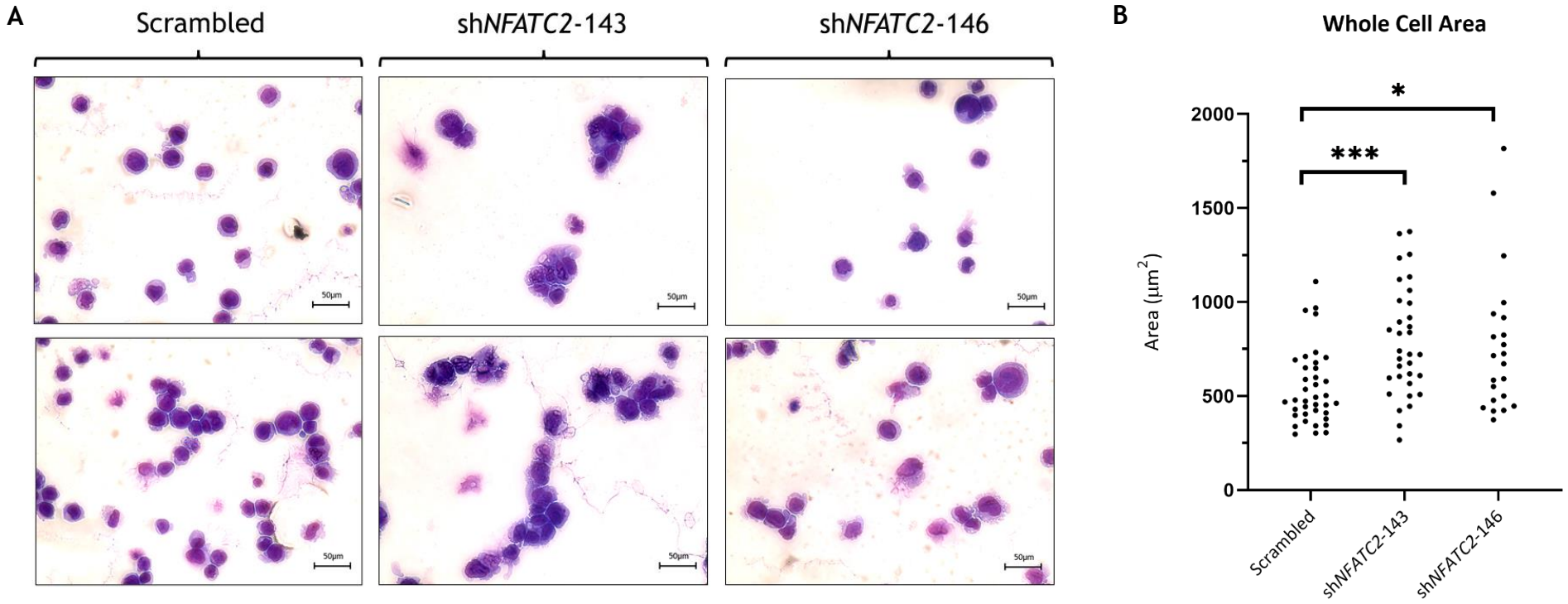

Figure 4-8. THP-1 cells with *NFATC2* KD exhibited an increased cell size.
THP-1 cells were stained with May-Grünwald and Giemsa stains 72 hr post-selection (n=1 biological replicate). **A.** Representative images of stained THP-1 cells for each condition. Scale bar represents 50 µm. **B.** The average cell area was estimated using ImageJ software. Shown are individual data points per cell, for the scrambled control (n=38), shNFATC2-143 (n=33) and shNFATC2-146 (n=22). The difference between conditions was tested using a Kruskal-Wallis H test followed by Dunn's post-hoc test, for pairwise comparison with the scrambled control. *p* values: *<0.05, ***<0.001.
software. Shown are individual data points per cell, for the scrambled control (n=38), shNFATC2-143 (n=33) and shNFATC2-146 (n=22). The difference between conditions was tested using a Kruskal-Wallis H test followed by Dunn's post-hoc test, for pairwise comparison with the scrambled control. *p* values: *<0.05, ***<0.001.

Transduction of THP-1 with two shRNA constructs for *NFATC2* KD led to a statistically significant KD of *NFATC2*, as demonstrated by qRT-PCR (Figure 4-7A). There was a substantial loss of colony-forming capacity in semi-solid media and a loss of expansion in liquid culture, both of which were significantly reduced (Figure 4-7B&C). Cell morphology was most visibly changed after transduction with sh*NFATC2*-143, in which cells were more physically associated together (Figure 4-8). This may indicate the initiation of cell death in these cells, more so than in the other groups. The measured area of cells (using ImageJ) was significantly increased after *NFATC2* KD.

While cell cycle was not significantly changed after *NFATC2* KD, as measured by PI staining (Figure 4-9A), there was a trend towards an increased proportion of cells in the G2-M phases. A CFSE dye tracing assay showed a reduction in cell proliferation in the period 24 hr-72 hr post-selection (Figure 4-9B), though this could not be statistically tested. There was also no significant change in apoptosis across all conditions, as measured by Annexin V and DAPI, however there was an increase in apoptotic cells after treatment with construct -143 (Figure 4-9C).

To investigate the cell cycle further a BrdU incorporation assay was used to assess THP-1 cells in the period 120 hr-144 hr post-selection. This experiment also showed a higher proportion of cells in the G2-M phases, but no change in S phase cells or the G0-G1 phases (Figure 4-9D).

Additionally, expression of selected regulators of the cell cycle was surveyed at a number of timepoints, including 144 hr post-selection (Figure 4-10A). Selected genes included those encoding major cyclins, CDKs and CDC25 isoforms, as well-established regulators of the cell cycle. Upregulation of *CCNA2* and *CCNE2* and downregulation of *CCND1* and *CCND2* were observed. Further qRT-PCR validation revealed that *CCND1* was significantly downregulated at 144 hr post-selection (p= 0.0015 and p=0.0014 for constructs -143 and -146, respectively) and there was a trend towards *CCND2* downregulation, without statistical significance.

These data suggest that there could be arrest of the cell cycle in the G2-M phase after *NFATC2* KD, but this has not been characterised clearly. Downregulation of *CCND1* and *CCND2* may also form part of this mechanism and together these data could explain the loss of colony-forming capacity. The observation that cell cycle gene expression changes most at 144 hr post-selection, but not earlier, suggests

that phenotypic changes are gradual and best observed in longer-term assays. Furthermore, apoptosis is not a consistent feature of *NFATC2* KD in THP-1.

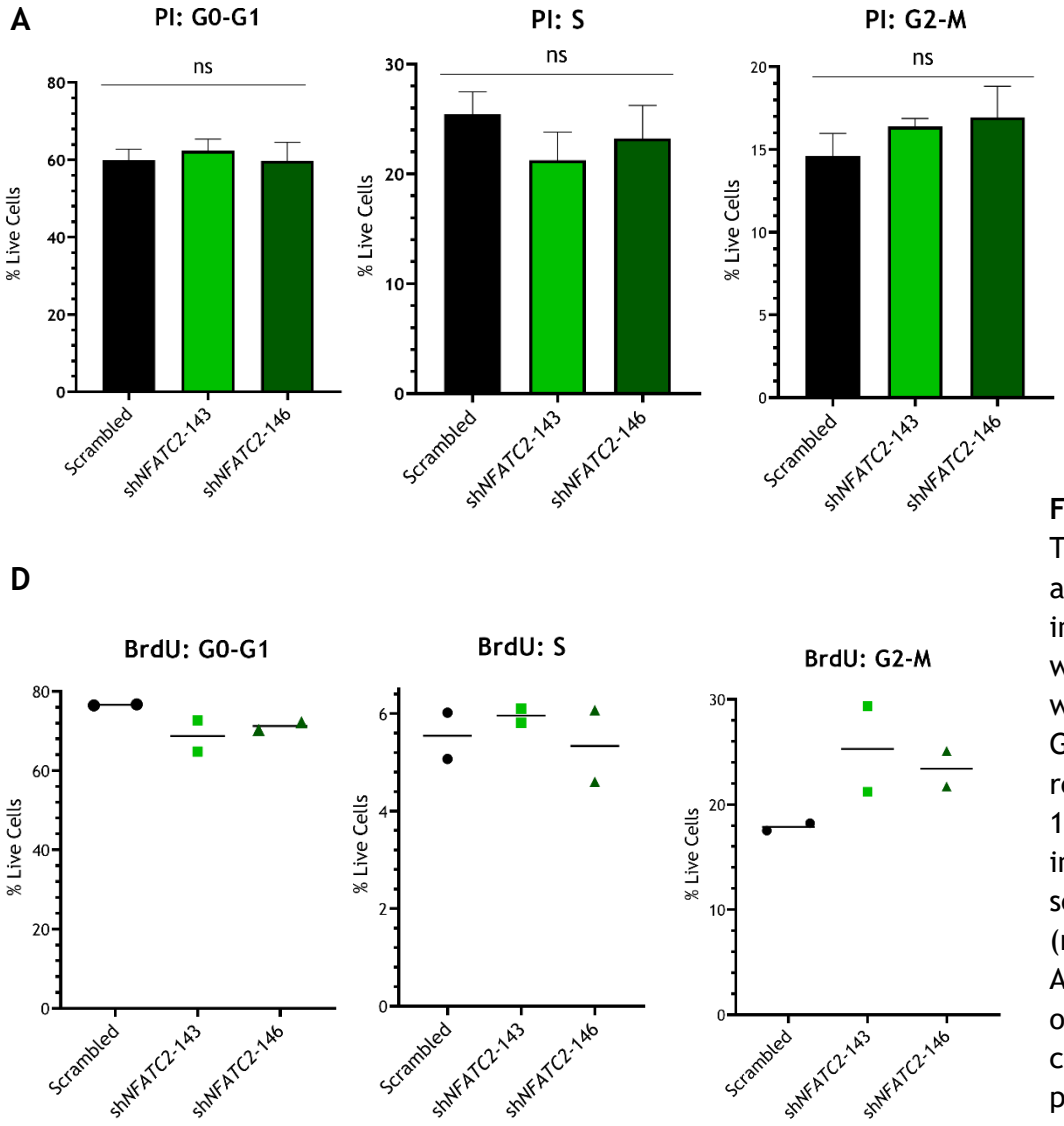

Figure 4-9. THP-1 cell proliferation was reduced after *NFATC2* KD. THP-1 cells were transduced with one of two shRNA for *NFATC2* KD or a scrambled control. Data shown are mean ± SEM or mean with the individual data points when n<3. Significance was tested using a one-way ANOVA for differences between means. 'ns' = p>0.05. **A:** Cells were stained with PI and gated as previously. The % live cells in phases G0-G1, S or G2-M are shown in the panels from left to right, respectively (n=3 biological replicates). **B:** CFSE dye staining of THP-1 cells and tracing by flow cytometry. The geometric mean intensity in the FITC channel was measured at 24 hr and 72hr post-puromycin selection. The graph shows the $\log_2$ fold change from 24 hr to 72 hr (n=2 biological). **C:** Apoptosis was measured in THP-1 cells using an Annexin V/DAPI assay 72 hr post-selection. Shown is the mean ± SEM % of gated cells positive for Annexin V stain, n=6 biological. **D.** THP-1 cells were stained with BrdU/DAPI 144 hr post-selection. Cell cycle phases are expressed as % live cells, as for PI staining (n=2 biological).

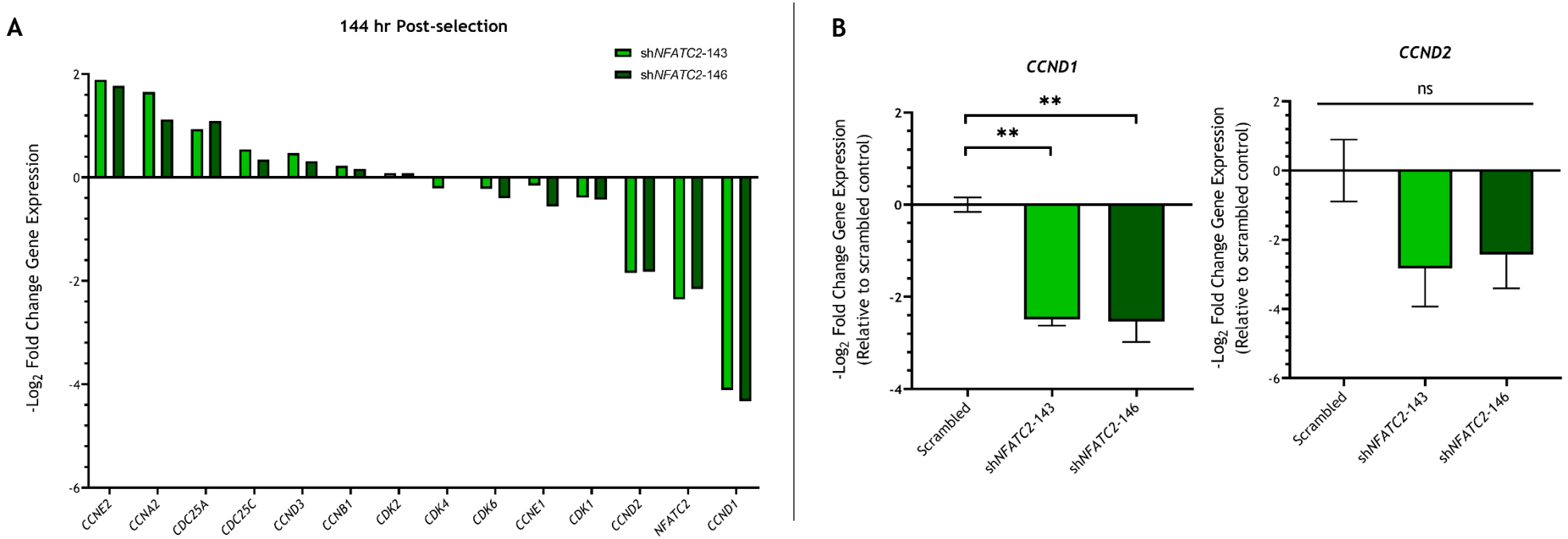

Figure 4-10. *CCND1* was significantly downregulated after *NFATC2* KD in THP-1 cells.

A: THP-1 cells' gene expression of selected cell cycle regulatory genes, in addition to *NFATC2*, were measured at 144 hr post-selection by qRT-PCR. Shown are -$\log_2$ fold changes from the scrambled control, using the ΔΔCt method (n=1 biological, n=3 technical replicates). These are ordered by the average -$\log_2$ fold change, between the pair of shRNA constructs. **B:** THP-1 gene expression of *CCND1* and *CCND2* at 144 hr post-selection is shown as -$\log_2$ fold change from the scrambled control, as measured by qRT-PCR and using the ΔΔCt method (n=3 biological, n=3 technical).

NFATC2 KD led to substantial depletion of NFATc2 protein in the cytoplasmic and nuclear compartments of the cell (Figure 4-11). pNFATc2^{ser54} quantity increased relative to NFATc2 expression, suggesting that phosphorylation at ser54 is maintained at a level of equilibrium in the cell. Alternatively, the binding strength of the pNFATc2^{ser54} antibody is much higher than for NFATc2 and so retains a strong signal, in spite of markedly reduced NFATc2 quantity. pNFATc2^{ser54} was also observed to be predominant in the nucleus (Figure 4-11C).

Known histone targets of KDM4A protein were evaluated to determine if NFATc2 function is important in their regulation. No consistent changes to H3K9me3 or H3K27me3 were observed in THP-1 cells after *NFATC2* KD with any of three shRNA constructs (Figure 4-12A&B). An increase in PARP cleavage was observed, but the magnitude of change was small and not replicated (Figure 4-12C&D). Together with previous data on apoptosis (Figure 4-10C) it is unlikely that this is a major contributor to the observed phenotype. Phosphorylation of H2AX at ser139 was reduced after *NFATC2* KD (Figure 4-12C&D; fold changes from scrambled were 0.646 and 0.670 for constructs -143 and -146, respectively), which could indicate a reduction in DNA double strand breaks (DSBs) in the bulk population.

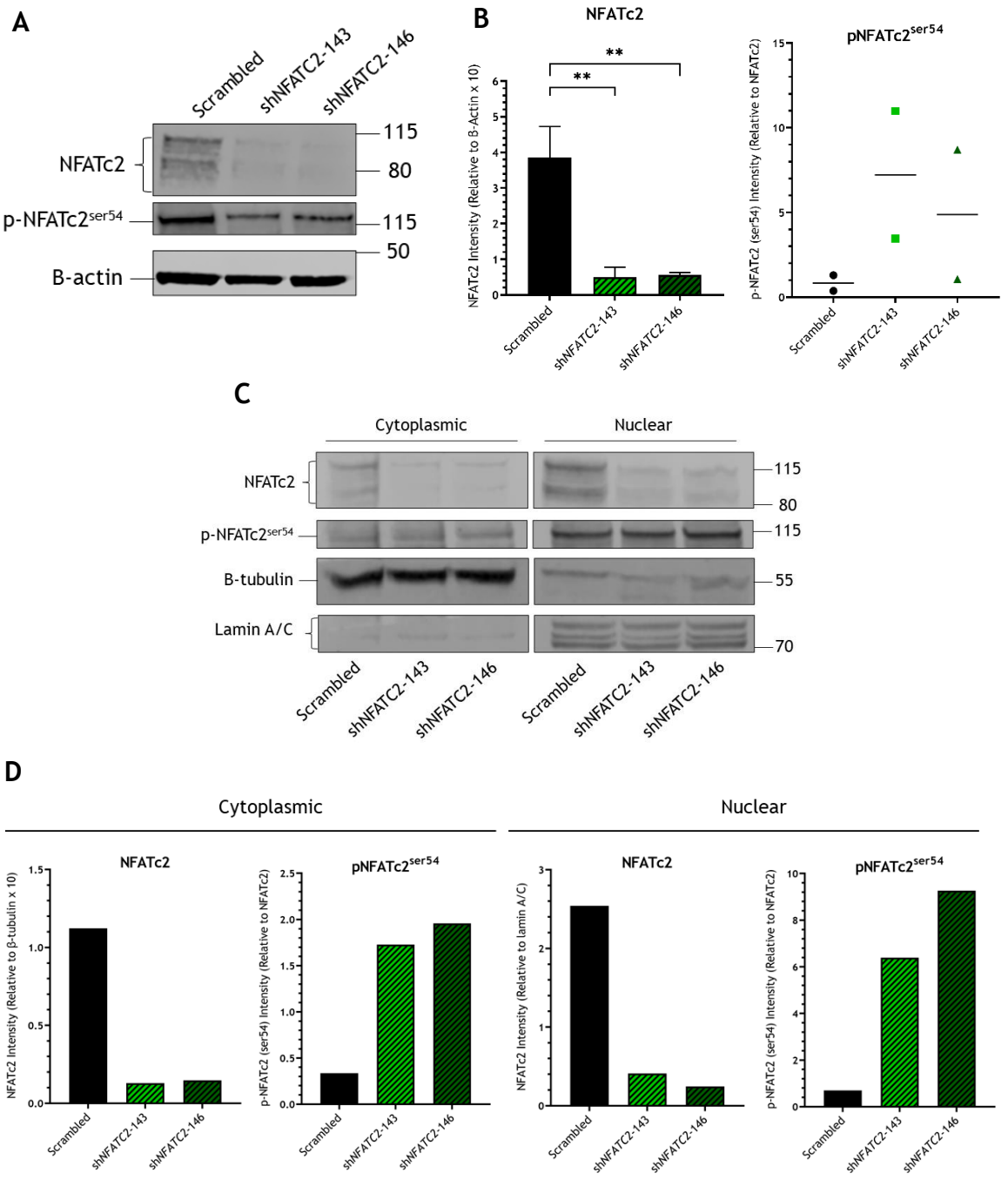

Figure 4-11. KD of *NFATC2* led to depletion of NFATc2 protein in the cytoplasmic and nuclear compartments of THP-1 cells. After *NFATC2* KD THP-1 cells were harvested for either WCL, or fractionated cytoplasmic and nuclear lysates. **A:** 27.5 µg of WCL were loaded and immunoblotted with anti-NFATc2, anti-phospho-NFATc2^{ser54} and anti-ß-actin as a loading control. A size reference is given in kDa on the right-hand side. **B:** Protein was quantified for blots as shown in (**A**) by densitometry. Shown is mean protein intensity ± SEM for NFATc2 (n=3 biological replicates), or as a mean with individual values for p-NFATc2^{ser54} (n=2 biological). Intensity is relative to ß-actin. For NFATc2 the differences in means were calculated by one-way ANOVA followed by post-hoc Dunnett's test for pairwise comparisons; for *p* **<0.01. **C:** 30 µg of fractionated lysates were loaded and immunoblotted with anti-NFATc2, anti-phospho-NFATc2^{ser54}, and anti-ß-tubulin/anti-lamin A/C as loading controls (n=1 biological). **D:** Protein from the blot in (**C**) was quantified by densitometry, for NFATc2 or p-NFATc2^{ser54}. Intensity is relative to either ß-tubulin or lamin A/C for cytoplasmic or nuclear lysates, respectively (n=1 biological).

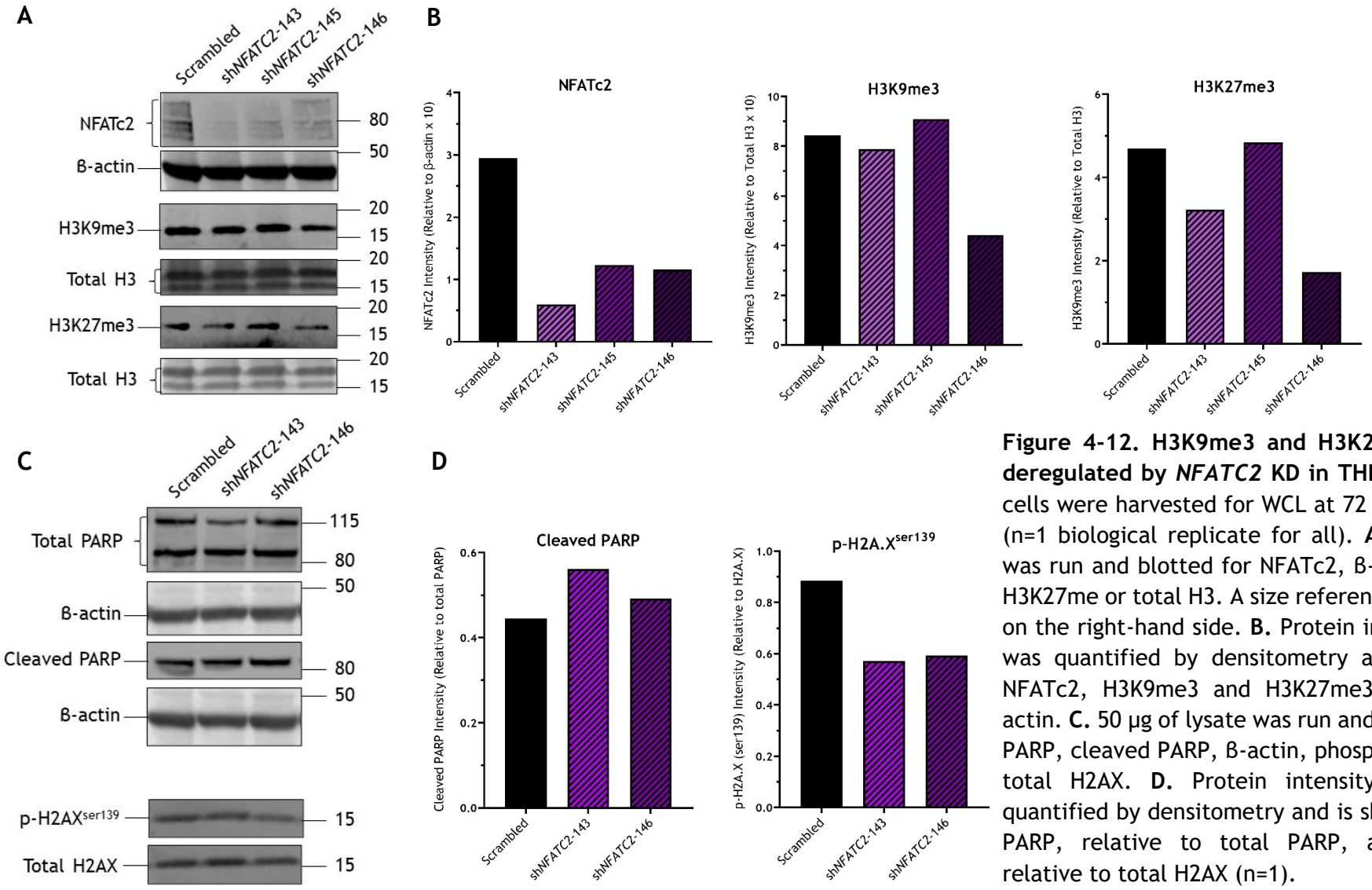

Figure 4-12. H3K9me3 and H3K27me3 were not deregulated by *NFATC2* KD in THP-1 cells. THP-1 cells were harvested for WCL at 72 hr post-selection (n=1 biological replicate for all). **A.** 30µg of lysate was run and blotted for NFATc2, β-actin, H3K9me3, H3K27me or total H3. A size reference in kDa is given on the right-hand side. **B.** Protein intensity from (**A**) was quantified by densitometry and is shown for NFATc2, H3K9me3 and H3K27me3, relative to β-actin. **C.** 50 µg of lysate was run and blotted for total PARP, cleaved PARP, β-actin, phospho-H2AX^{ser139} and total H2AX. **D.** Protein intensity from (**C**) was quantified by densitometry and is shown for cleaved PARP, relative to total PARP, and p-H2AX^{ser139}, relative to total H2AX (n=1).

4.3.3 Rescue of h*NFATC2* KD in THP-1 using m*Nfatc2* expression

m*Nfatc2* was overexpressed in THP-1 cells as shown in Chapter 3.2.3 and used to determine if the phenotype following KD of *NFATC2* could be rescued. Of note, the shRNA constructs used in this chapter did not target the expressed m*Nfatc2* transcript.

KD of *NFATC2* was validated by observing reduced transcript by qRT-PCR and NFATc2 protein on immunoblotting (Figure 4-13A&B). There is a residual level of NFATc2 protein observed in THP-1 o/e m*Nfatc2*, relative to THP-1/empty. This is most likely hNFATc2 due to a lack of antibody specificity for mNfatc2, as discussed in Chapter 3.2.3, which could suggest that m*Nfatc2* overexpression upregulates h*NFATC2* and maintain its expression at a minimal level. However, this was not supported by qRT-PCR data (Figure 4-13A) and so immunoblotting should be explored further, possibly with other hNFATc2-targeting antibodies. *NFATC2* KD did not alter m*Nfatc2* expression (Figure 4-13A), supporting the expectation that these shRNA constructs do not target h*NFATC2*.

Cell expansion in liquid culture was reduced in THP-1/empty after *NFATC2* KD, whereby the fold change in cell counts from 24 hr to 72 hr was 3.21x, 1.82x and 1.78 for the scrambled control, sh*NFATC2*-143 and sh*NFATC2*-146, respectively (Figure 4-13C). This is comparable to *NFATC2* KD in native THP-1, where the count fold changes the 24 hr to 72 hr time window were 2.54x, 1.67x and 1.67x for the scrambled control, sh*NFATC2*-143 and sh*NFATC2*-146 (see Figure 4-7A). In summary, the phenotype of THP-1/empty with *NFATC2* KD is similar to native THP-1 cells, in that there was a loss of cell count expansion in the period after puromycin selection, of a similar magnitude.

However, in o/e m*Nfatc2* THP-1 with *NFATC2* KD, this pattern was not observed (Figure 4-13C). The count fold changes in the 24 hr to 72 hr period after selection were 1.92x, 1.75x and 3.00x for the scrambled, -143 and -146 constructs, respectively. This demonstrates either no change or an increase in the expansion of o/e m*Nfatc2* THP-1 after *NFATC2* KD. However, it was noted that the rate of expansion at baseline (in scrambled control-treated samples) was higher for THP-1/empty compared with o/e m*Nfatc2* THP-1, although this might reflect a difference in the basal growth of these 2 cell lines or their response to the scrambled control. This precludes an accurate comparison of the expansion in

culture between THP-1/empty and THP-1 o/e m*Nfatc2* after *NFATC2* KD compared with the scrambled control. As such, it is not clear if overexpression of m*Nfatc2* was sufficient to truly rescue the loss of expansion in culture observed with *NFATC2* KD in THP-1/empty.

Overexpression of m*Nfatc2* did not rescue the loss of THP-1 colony-forming capacity observed with *NFATC2* KD (Figure 4-13D). More cell growth was observed visually for o/e m*Nfatc2* THP-1 than THP-1/empty with *NFATC2* KD, however most cell clusters were not large enough to be considered colonies (>50 cells).

Cell cycle analysis following *NFATC2* KD in either of THP-1/empty or THP-1 o/e m*Nfatc2* showed no statistically significant differences from scrambled control-treated samples (Figure 4-14A). However, no significant changes in the cell cycle were observed in unmodified THP-1 with *NFATC2* KD also (Figure 4-9A). Further replication is needed to mitigate the high inter-replicate variability observed in these experiments, potentially owing to technical factors, and determine more clearly if there is a true biological effect to be observed. In summary, from these data, there are no changes in the cell cycle following *NFATC2* KD in THP-1 at this timepoint and so later timepoints should be explored. Firstly, to determine if there is a delayed effect of *NFATC2* KD on the cell cycle and secondly, to determine if overexpression of m*Nfatc2* would rescue these effects.

As observed in unmodified THP-1 apoptosis is increased in THP-1/empty after transduction with sh*NFATC2*-143. This was not observed with expression of mNfatc2. Additionally, the level of apoptosis in o/e mNfatc2 THP-1 treated with the scrambled control was 61% of that of THP-1/empty. Together these data suggest that m*Nfatc2* reduces cell apoptosis in THP-1.

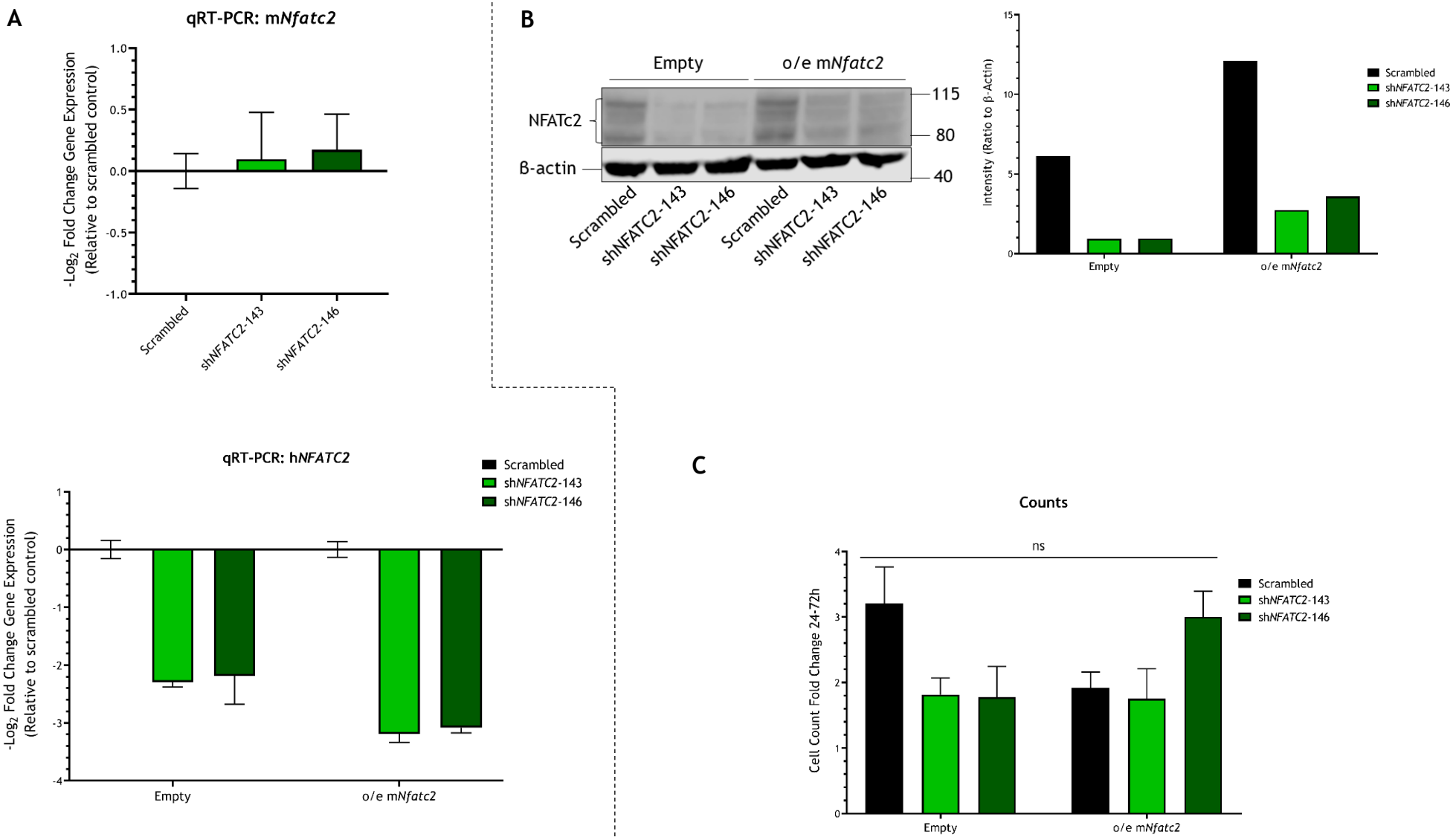
A
qRT-PCR: mNfatc2
-Log2 Fold Change Gene Expression (Relative to scrambled control)
1.0
0.5
0.0
-0.5
-1.0
Scrambled
shNFATC2-143
shNFATC2-146
B
Empty
o/e mNfatc2
NFATc2
ß-actin
115
80
40
Scrambled
shNFATC2-143
shNFATC2-146
Scrambled
shNFATC2-143
shNFATC2-146
Intensity (Ratio to β-Actin)
15
10
5
0
Empty
o/e mNfatc2
Scrambled
shNFATC2-143
shNFATC2-146
qRT-PCR: hNFATC2
-Log2 Fold Change Gene Expression (Relative to scrambled control)
1
0
-1
-2
-3
-4
Empty
o/e mNfatc2
Scrambled
shNFATC2-143
shNFATC2-146
C
Counts
ns
Cell Count Fold Change 24-72h
4
3
2
1
0
Empty
o/e mNfatc2
Scrambled
shNFATC2-143
shNFATC2-146

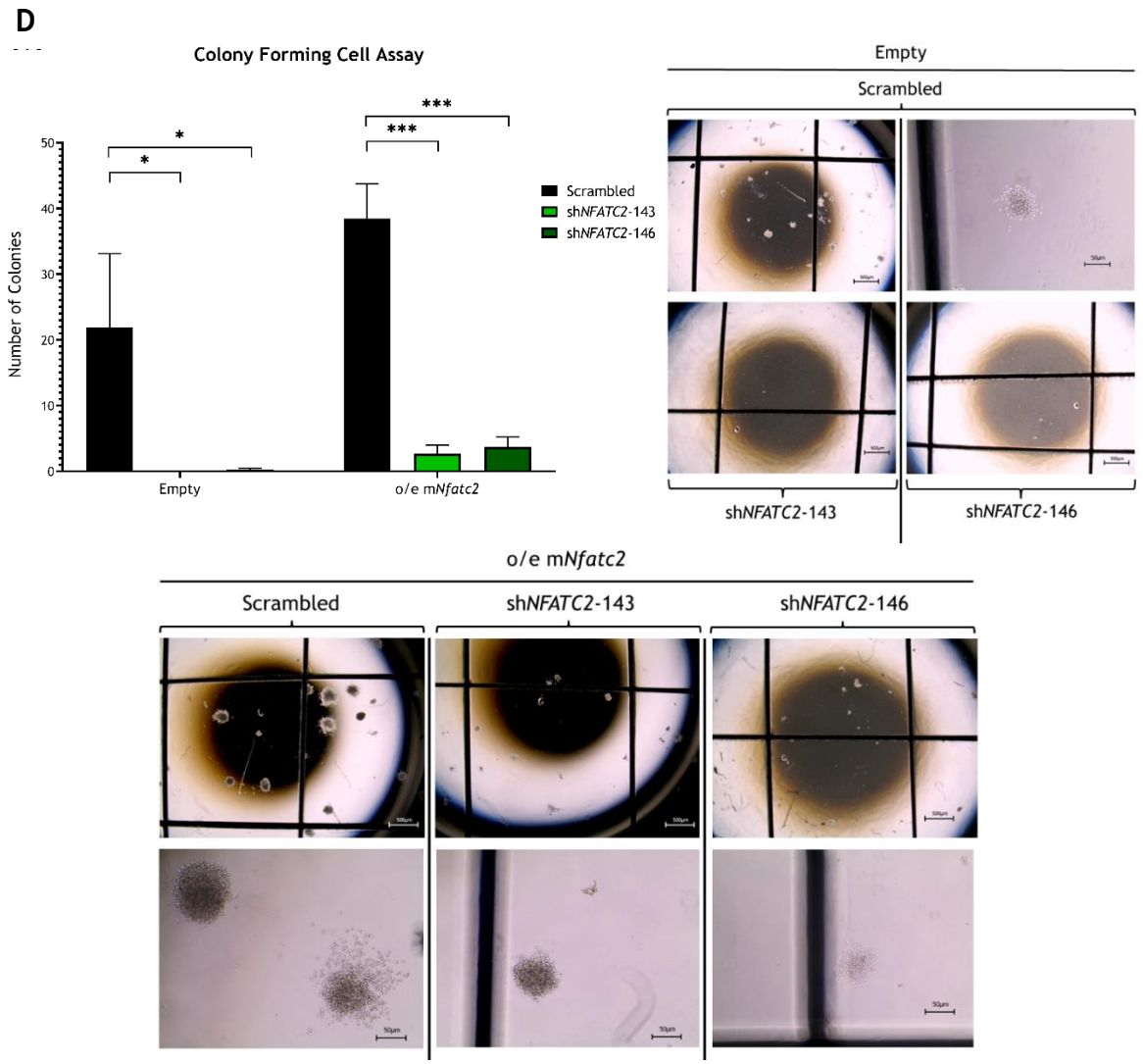

Figure 4-13. Overexpression of m*Nfatc2* in THP-1 cells did not rescue a loss of colony-forming capacity after *NFATC2* KD. THP-1 expressing either m*Nfatc2* or an empty retroviral vector were transduced with either a scrambled control or *NFATC2*-targeting shRNA (-143 or -146). Data shown are mean or an individual data point. A difference in means was tested using a two-way ANOVA, followed by post-hoc Dunnett's test for pairwise differences between KD constructs. *P* values: *<0.05, ***<0.001, 'ns' = *p*>0.05. **A:** qRT-PCR for h*NFATC2* or m*Nfatc2* expression in cells harvested 48 hr post-puromycin selection, expressed as a mean -$\log_2$ fold change ± SD. For THP-1 with empty vector and m*Nfatc2* this was calculated relative to the scrambled control within each cell line, using the ΔΔCt method (n=1 biological, n=3, technical replicates). **B:** 30 µg WCL from cells were run and blotted using anti-NFATc2 and anti-ß-actin. Shown are the blots with the protein size in kDa on the right-hand side, and a bar chart showing the intensity as measured by densitometry (n=1 biological). NFATc2 intensity is expressed relative to ß-actin. **C:** Cells were seeded in liquid culture and counted every 24 hr after puromycin selection. Shown is the mean ± SEM fold change of counts from 24 hr to 72 hr (n=3 biological, n=2 technical). **D:** Cells were seeded in semi-solid media 24 hr post-selection and colonies counted after 10-12 days. Shown are mean colony numbers ± SEM (n=3 biological, n=3 technical) and representative pictures of colonies at differing magnifications, for each condition. Scale bars are shown for 500 µm or 50 µm.

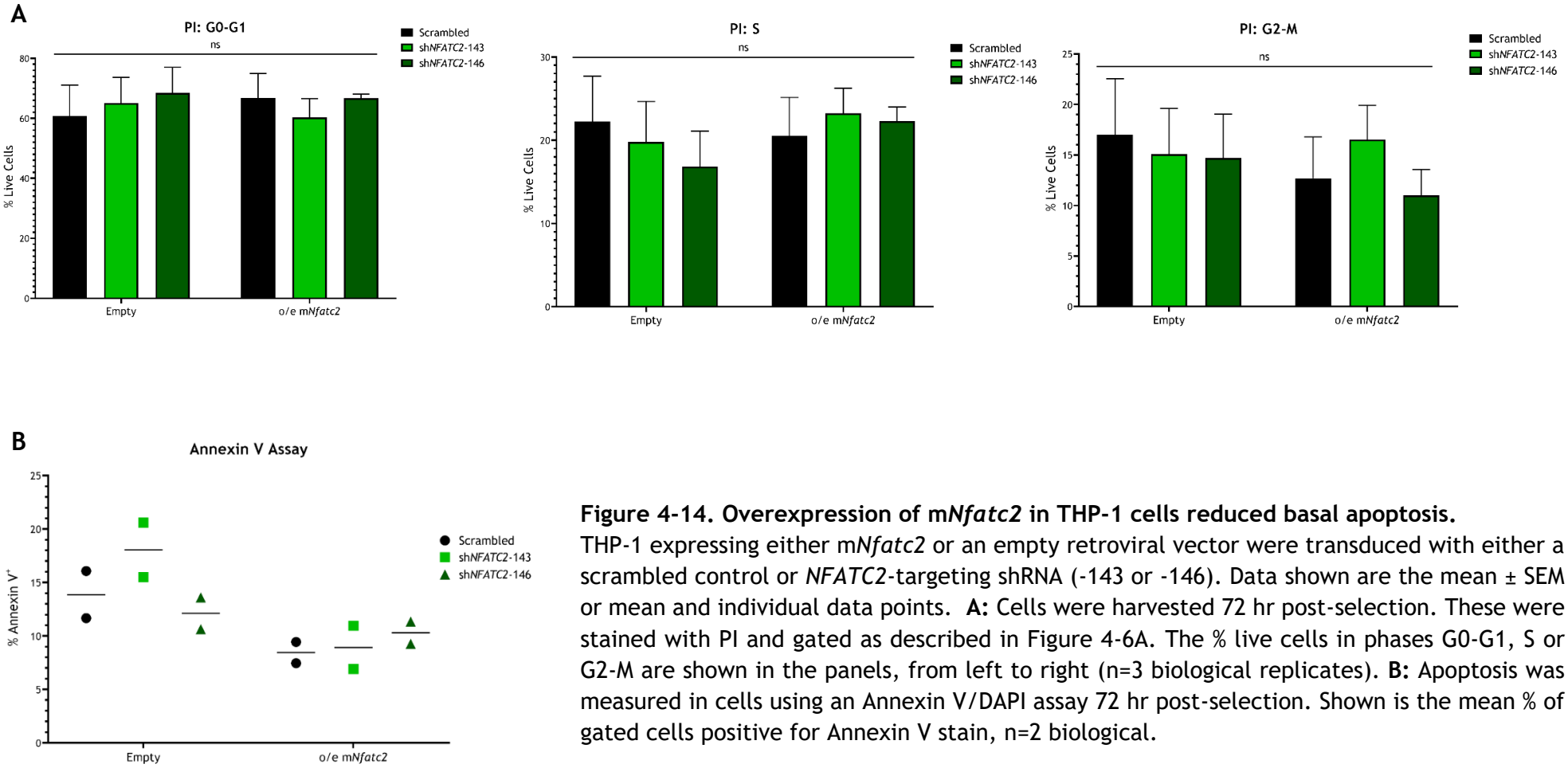

Figure 4-14. Overexpression of m*Nfatc2* in THP-1 cells reduced basal apoptosis.
THP-1 expressing either m*Nfatc2* or an empty retroviral vector were transduced with either a scrambled control or *NFATC2*-targeting shRNA (-143 or -146). Data shown are the mean ± SEM or mean and individual data points. **A:** Cells were harvested 72 hr post-selection. These were stained with PI and gated as described in Figure 4-6A. The % live cells in phases G0-G1, S or G2-M are shown in the panels, from left to right (n=3 biological replicates). **B:** Apoptosis was measured in cells using an Annexin V/DAPI assay 72 hr post-selection. Shown is the mean % of gated cells positive for Annexin V stain, n=2 biological.

4.3.4 KD of m*Nfatc2* in a murine model of MLL-AF9 AML

A model of MLL-AF9 AML was previously established by expressing a retroviral MLL-AF9/GFP construct in CD117-selected murine BM cells. These were compared with unmodified CD117-selected murine BM at baseline ('CD117 BM'; Figure 4-15A&B). On the CD117-selected BM a higher proportion of cells were found to express CD117 in comparison to the MLL-AF9 BM (81.4% and 51.3% of parent population, respectively). The expression of myeloid markers Gr-1 and Mac-1 was also more heterogeneous on CD117 BM.

CD117 BM expanded in culture more when cultured with a cocktail of cytokines (mIL-3, mIL-6, mSCF and mGM-CSF), compared to with mIL-3 alone or with 'X63' media, containing hybridoma-derived mIL-3 (Figure 4-15D). MLL-AF9 BM cells expanded most rapidly when cultured with X63 media alone, suggesting that these are more cytokine independent cells. qRT-PCR revealed that MLL-AF9 BM had a higher expression of known MLL-AF9 targets *Hoxa9* and *Meis1* when compared to CD117 BM, as expected (Figure 4-15E). Expression of *Nfatc2* was slightly increased and there were no observable changes to selected cell cycle gene expression.

KD of murine Nfatc2 in MLL-AF9 BM with either of two shRNA constructs (-356 or -357) led to a loss in colony-forming capacity (Figure 4-16A&B) that was only statistically significant for shNfatc2-356 (p=0.0099). qRT-PCR validated KD of *Nfatc2* transcript but also revealed that *Nfatc1* was depleted, although less than for *Nfatc2* (Figure 4-16C). This may indicate off-target effects of the shRNA or co-regulation of *Nfatc1* by *Nfatc2* in these cells. *Hoxa9* and *Meis1* did not appear to change, but the result was partly obscured by experimental variation.

There was also an increase in apoptosis for construct -356 only (Figure 4-17A; *p*=0.0283). Observation of cell morphology revealed more evidence of chromatin condensation in the nuclei of cells with *Nfatc2* KD, compared to the scrambled control (4-17B). Together this may suggest that *Nfatc2* KD with either construct can lead to apoptosis in MLL-AF9 BM, but perhaps at an earlier stage in the construct -357 condition.

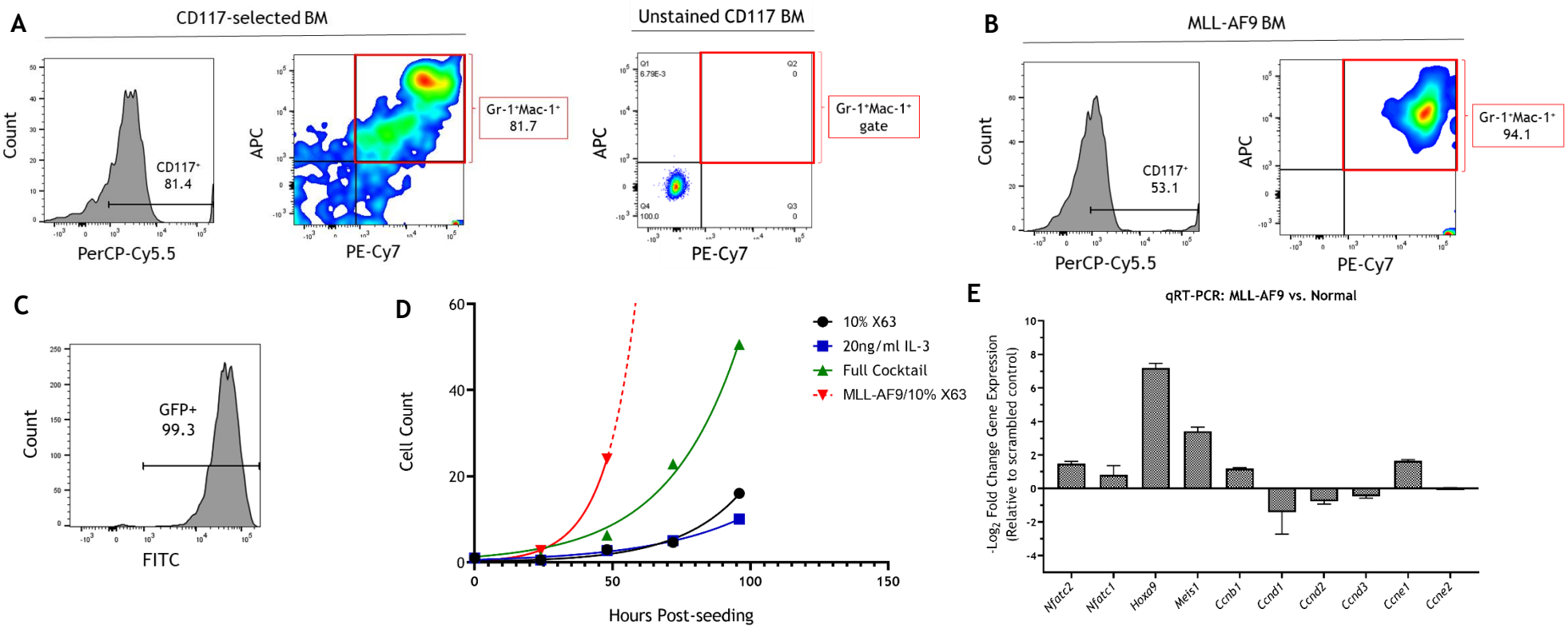

Figure 4-15. Murine BM expressing a retroviral MLL-AF9 construct expressed higher levels of *Hoxa9* and *Meis1* than CD117-selected murine BM. CD117-selected murine BM (**A**) and murine BM expressing a retroviral MLL-AF9/GFP construct (**B**) were immunophenotyped by flow cytometry (n=1 biological replicate). For each, CD117 expression is shown as a histogram (left panel) and expression of Gr-1 and Mac-1 is plotted together (right panel). Two gates are highlighted, showing the Gr-1$^+$Mac-1$^+$ populations. % of the parent population is shown. For CD117 BM an unstained sample is shown. **C:** For the MLL-AF9 BM, GFP expression is shown, as measured in the FITC channel (n=1 biological). **D:** CD117-selected BM cells were cultured with either X63/mIL-3, mIL-3 or a cocktail of mIL-3, mIL-6, mSCF and mGM-CSF. MLL-AF9 BM were cultured with X63/mIL-3. Cell counts were taken every 24 hr and plotted (n=1 biological, n=3 technical). A line of best fit was drawn using non-linear regression, with extrapolation beyond the data for MLL-AF9 BM (shown by dotted line). **E:** qRT-PCR was used to measure selected genes' expression in MLL-AF9 BM, compared with CD117-selected BM, expressed as mean -log$_2$ fold change ± SD (n=3 technical).

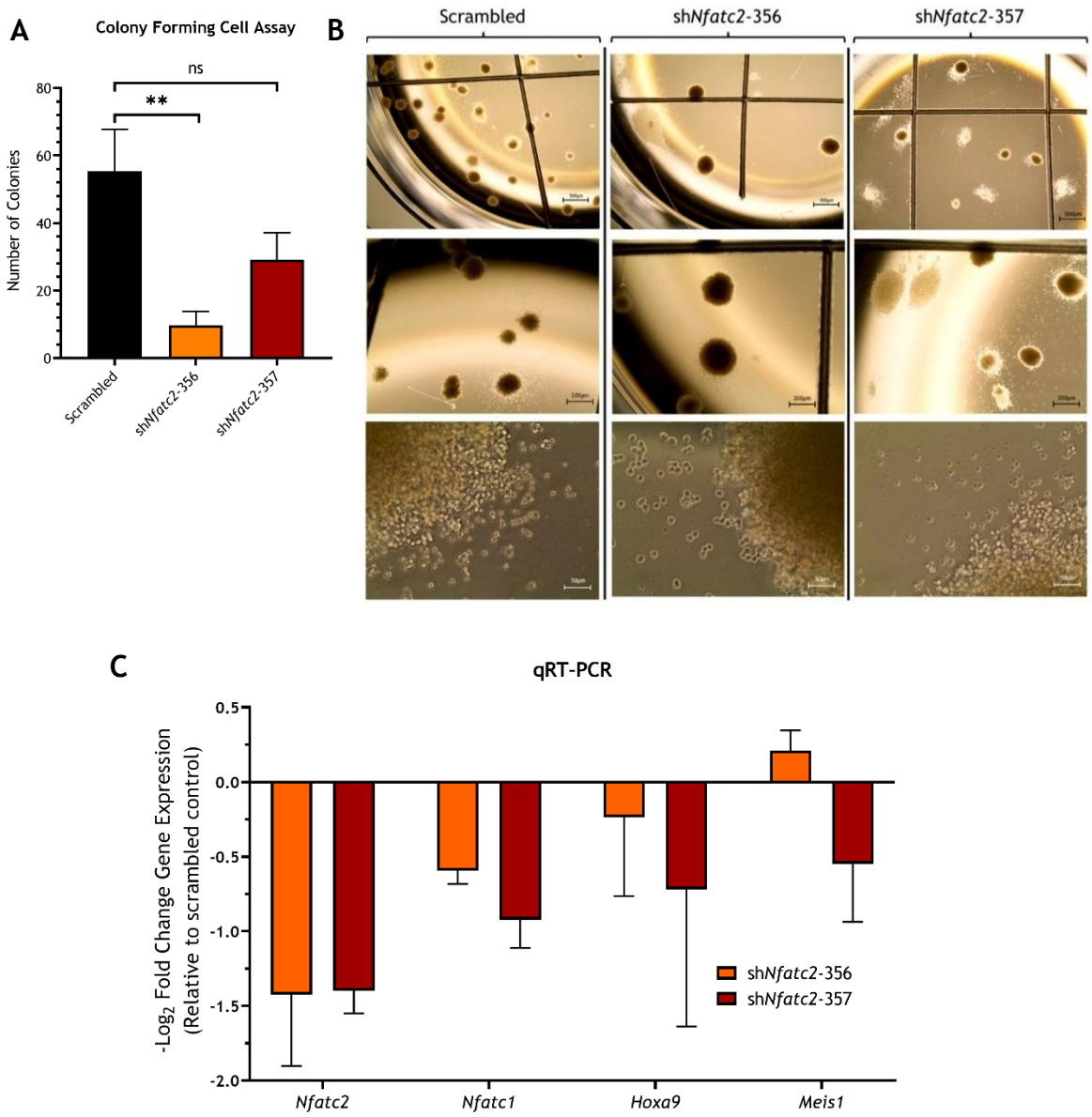

Figure 4-16. KD of m*Nfatc2* in MLL-AF9 murine BM cells caused a reduction in their colony-forming capacity. Murine BM expressing MLL-AF9 were transduced with either of two shRNA targeting m*Nfatc2* (-356 or 357) or a scrambled control. **A:** Transduced BM cells were seeded in semi-solid media 24 hr post-selection and counted after 6-7 days. Shown are mean colony numbers ± SEM. A difference in means was calculated using a one-way ANOVA and post-hoc Dunnett's test for pairwise comparisons. *p* **<0.01, 'ns' = *p*>0.05 (n=3 biological, n=3 technical replicates). **B.** Representative images from colonies in (**A**) are shown at differing magnifications, with scale bars for 500 µm, 200 µm or 50 µm given. **C:** Expression of selected genes was measured in MLL-AF9 BM 48 hr post-puromycin selection by qRT-PCR. Mean -$\log_2$ fold changes ± SD (n=3 technical), relative to the scrambled control, were calculated using the ΔΔCt method.

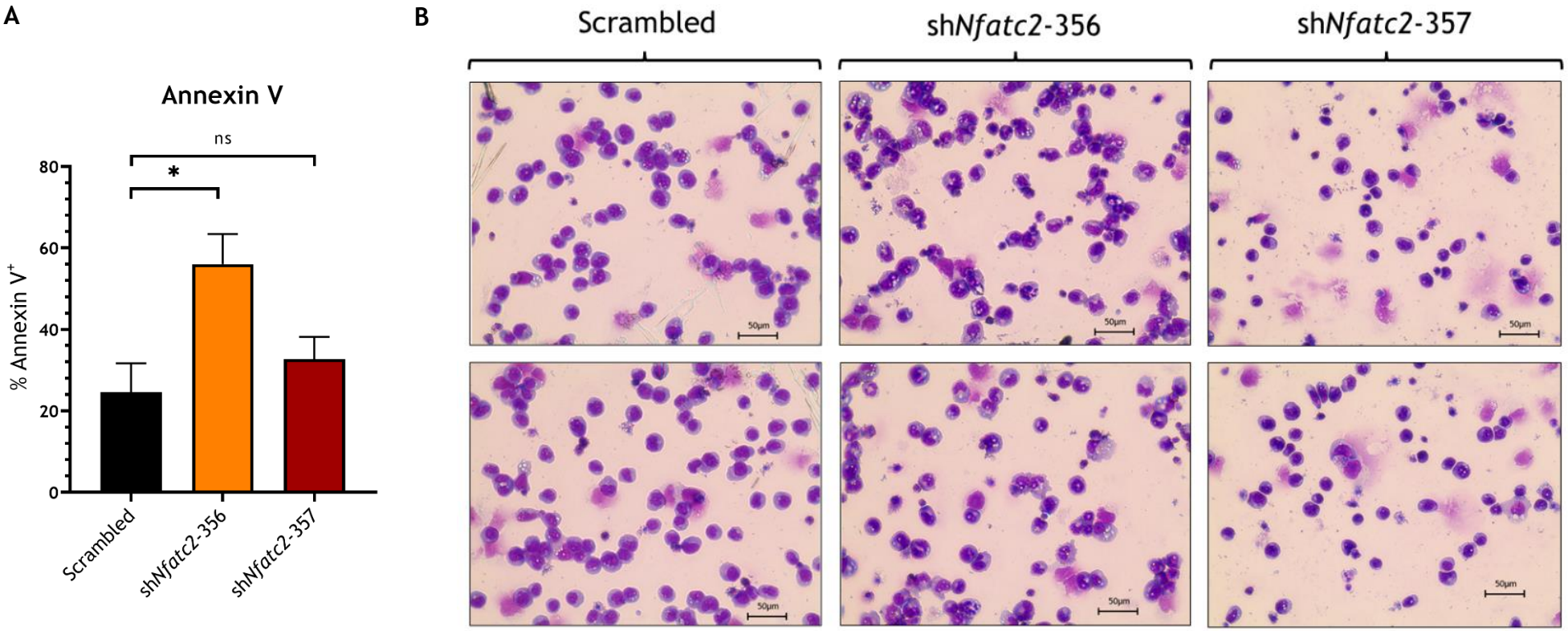

Figure 4-17. There were some signs of apoptosis in MLL-AF9 BM after *Nfatc2* KD.
Murine BM expressing MLL-AF9 were transduced with either of 2 shRNA targeting m*Nfatc2* (-356 or 357) or a scrambled control. A difference in means was calculated using a one-way ANOVA and post-hoc Dunnett's test for pairwise comparisons. *p* *<0.05, 'ns' =*p*>0.05. **A:** Apoptosis was measured in MLL-AF9 BM cells using an Annexin V/DAPI assay 72 hr post-selection. Shown is the mean ± SEM % of gated cells positive for Annexin V stain, n=3 biological replicates. **B:** MLL-AF9 BM cells were stained with May-Grünwald and Giemsa stains (n=1 biological). Representative images of stained cells are shown for each condition. Scale bars are given for 50 µm.

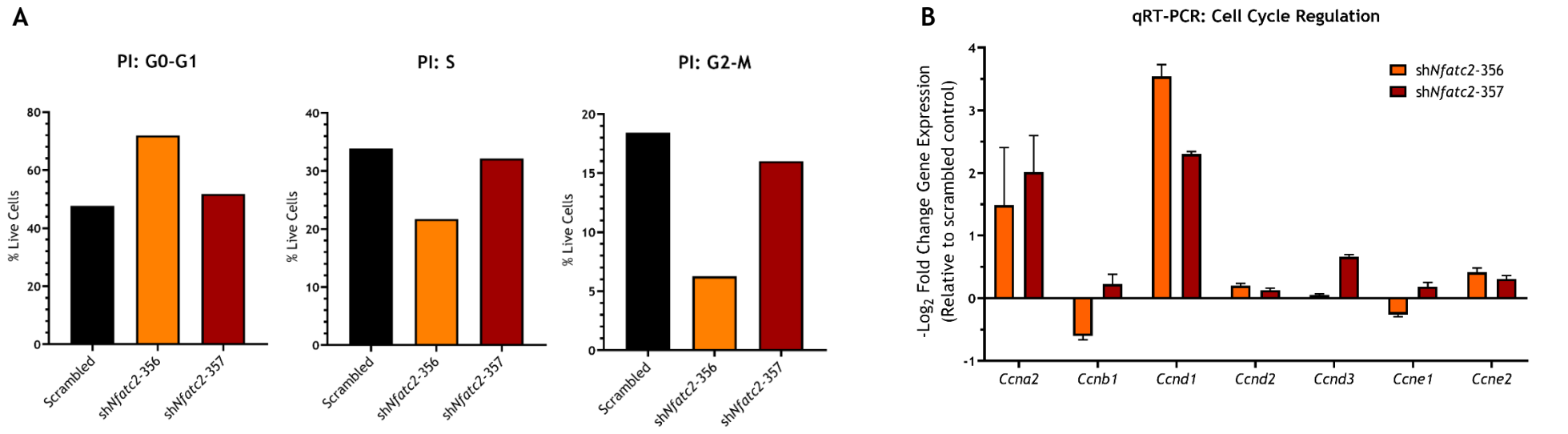

Figure 4-18. KD of m*Nfatc2* in MLL-AF9 murine BM cells caused a marked increase in *Ccnd1* expression.
Murine BM expressing MLL-AF9 were transduced with either of two shRNA targeting m*Nfatc2* (-356 or 357) or a scrambled control. **A:** MLL-AF9 BM cells were stained with PI and gated as described in Figure 4-7A. The % live cells in the phases G0-G1, S or G2-M are shown in the panels clockwise (n=1 biological replicate). **B:** Expression of selected cell cycle genes was measured by qRT-PCR, 48 hr post-puromycin selection. Mean -$\log_2$ fold changes ± SD (n=3 technical), relative to the scrambled control, were calculated using the ΔΔCt method.

There is evidence of reduced cells in the S and G2-M phases of the cell cycle after transduction with sh*Nfatc2*-356, but not -357 (Figure 4-18A). The simultaneous increase of cells in G0-G1 phases with sh*Nfatc2*-356 transduction indicates cell cycle arrest occurs in the G0-G1/S phase transition. Expression of *Ccna2* and *Ccnd1* are markedly increased after *Nfatc2* KD, for both shRNA constructs, while other selected cell cycle regulators are unchanged (Figure 4-18B). The increase in *Ccnd1* is greater in -356 than -357 and so this may be related to the observed cycle arrest, but this is not entirely clear from these data.

Together these data show that *Nfatc2* KD of MLL-AF9 BM cells significantly impairs colony-forming capacity. There are signs of apoptosis, which could be driving this. However, a phenotype of apoptosis and cell cycle arrest is prominent in only one of two shRNA constructs both of which KD m*Nfatc2*, which makes it unclear if these are off-target effects. *Ccna2* and *Ccnd1* are upregulated after *Nfatc2* KD with either construct.

4.3.5 KD of *NFATC2* in other cell line models of AML

To expand the study beyond THP-1 cells and compare the effects of *NFATC2* KD in differing (cyto)genetic backgrounds, a number of cell line models were used for KD of *NFATC2* by shRNA.

4.3.5.1 MLL rearranged AML

NFATC2 KD in MLL-AF9/FLT3^{ITD} MOLM-13 cells was strongest with construct -143 and for both constructs KD was stronger at 72hr post-selection, as opposed to 48hr post-selection (Figure 4-19A). NFATc2 protein depletion was clearly demonstrated by immunoblotting, although basal NFATc2 expression is already low in MOLM-13 (Figure 4-19B). *NFATC2* KD did not lead to a statistically significant reduction in colony-forming capacity, although there was a trend towards reduction (Figure 4-19C). Expansion of cell counts in liquid culture was lower after KD, but only statistically significant for construct -146 (Figure 4-19D).

Overall apoptosis was not significantly increased in MOLM-13 after *NFATC2* KD although a mean increase in annexin V positivity after transduction with sh*NFATC2*-146 was observed, but with high inter-replicate variability (Figure 4-19E). Regarding cell cycle analysis with PI staining, in the context of inter-replicate variability and a lack of sufficient replication for statistical testing, no changes were observed after *NFATC2* KD (Figure 4-19F). Together these data show that MOLM-13 may be dependent on *NFATC2* for colony formation and expansion in culture to some extent, but no firm conclusions can be made from these data alone.

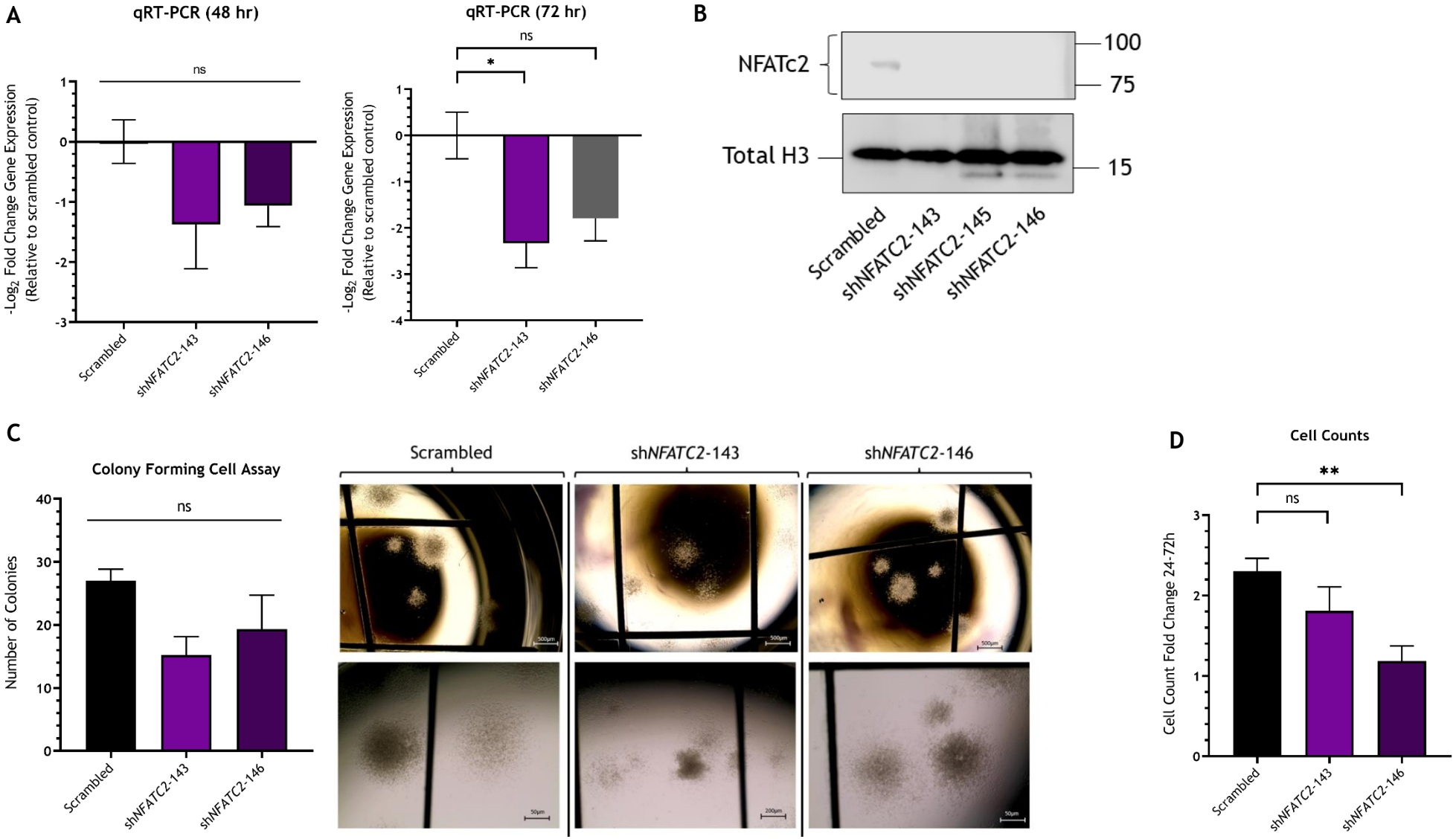
A
qRT-PCR (48 hr)
ns
-Log2 Fold Change Gene Expression
(Relative to scrambled control)
Scrambled
shNFATC2-143
shNFATC2-146
qRT-PCR (72 hr)
ns
*
B
NFATc2
Total H3
100
75
15
Scrambled
shNFATC2-143
shNFATC2-145
shNFATC2-146
C
Colony Forming Cell Assay
ns
Number of Colonies
Scrambled
shNFATC2-143
shNFATC2-146
D
Cell Counts
**
ns
Cell Count Fold Change 24-72h

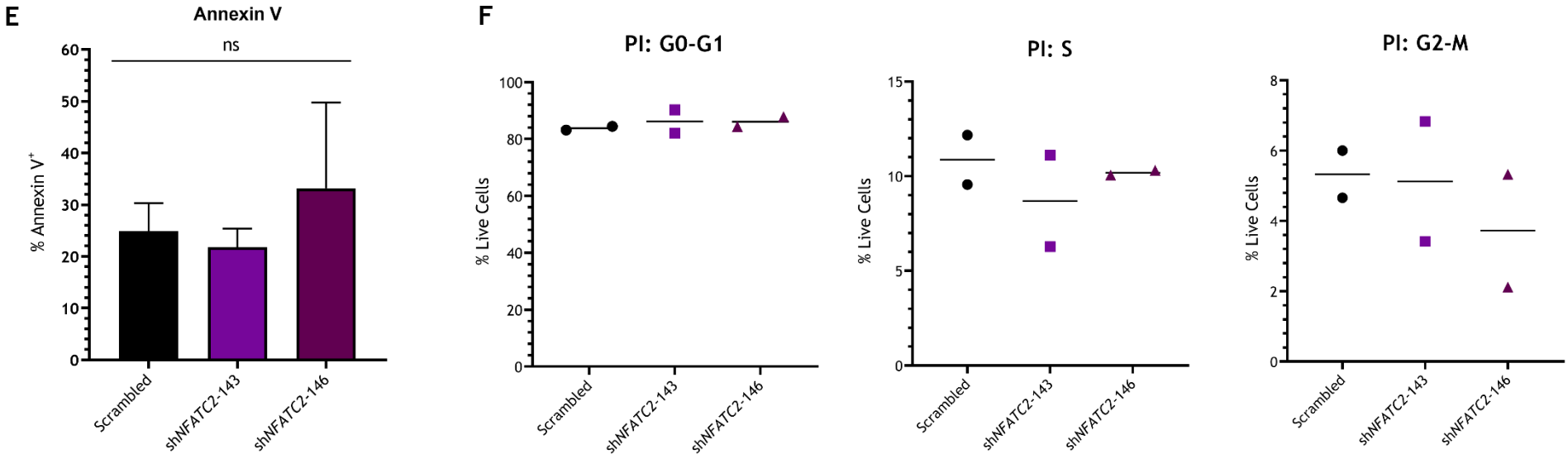

Figure 4-19. KD of *NFATC2* in MOLM-13 did not result in significant changes to colony forming-capacity.
MOLM-13 cells were transduced with either a scrambled control or *NFATC2*-targeting shRNA (-143, -145 or -146). Data shown are mean ± SEM or mean and individual data points. A difference in means was tested using a one-way ANOVA, followed by post-hoc Dunnett's test for pairwise differences. *P* values: *<0.05, **<0.01, 'ns' = *p*>0.05. **A:** qRT-PCR for *NFATC2* expression in cells harvested 48 hr and 72 hr post-puromycin selection, expressed as a $-\log_2$ fold change, relative to the scrambled control using the ΔΔCt method (n=3 biological, n=3 technical replicates). **B:** 26 µg of WCL from MOLM-13 were run and blotted using anti-NFATc2 and anti-total H3. Shown are the blots with the protein size in kDa on the right-hand side (n=1 biological). NFATc2 intensity is expressed relative to total H3. **C:** Cells were seeded in semi-solid media 24 hr post-selection and colonies counted after 8-10 days. Shown are colony numbers (n=3 biological, n=3 technical) and representative pictures of colonies at differing magnifications, for each condition. Scale bars are shown for 500µm or 200µm. **D:** MOLM-13 cells were seeded in liquid culture and counted every 24 hr after puromycin selection. Shown is the fold change of counts from 24 hr to 72 hr (n=7 biological, n=2 technical). **E:** Apoptosis was measured MOLM-13 cells using an Annexin V/DAPI assay 72 hr post-selection. Shown is the mean % of gated cells positive for Annexin V stain, n=4 biological. **F:** MOLM-13 cells were stained with PI and gated as described in Figure 4-7A. The % live cells in phases G0-G1, S or G2-M are shown in the panels, from left to right (n=2 biological).

When transduced with sh*NFATC2*-targeting lentivirus and a scrambled control, MLL-AF4 MV4-11 depletion of *NFATC2* transcript was validated by qRT-PCR (Figure 4-20A). Cells formed significantly fewer colonies after KD of *NFATC2* (Figure 4-20B; p=0.0420 and p=0.0416 for constructs -143 and -146, respectively).

Apoptosis was shown to be similar in each treatment condition, suggesting that this was not a factor in reducing the colony count (Figure 4-20C). PI staining showed a statistically insignificant trend towards reduction in cells in the S and G2-M phases (Figure 4-20D), which requires further replication to validate.

KD of NFATc2 protein was also validated by immunoblotting (Figure 4-20E). NFATc1 protein was detectable, unlike in THP-1 or MOLM-13, and was shown to be unchanged during NFATc2 KD. This reaffirms the assumption that these shRNA are not targeting *NFATC1* and/or suggests that *NFATC1* is not co-regulated by *NFATC2* in these cells.

The MLL-AF9 cell line NOMO-1 was also used to examine the phenotype following *NFATC2* KD. KD was validated at the transcript level by qRT-PCR (Figure 4-21A) and at the protein level by immunoblotting (Figure 4-21B). These cells did not form discrete colonies in semi-solid media and so could not be counted accurately. However, images from these assays show that there is a marked loss of cell growth in the media after *NFATC2* KD (Figure 4-21C). Cell counts in liquid culture were reduced after transduction with sh*NFATC2*-143 but not -146, and changes were not statistically significant (Figure 4-21D).

PI staining suggests minimal changes to the cell cycle in NOMO-1 after *NFATC2* KD (Figure 4-20E). Apoptosis is marginally increased for construct -143 only (Figure 4-20F). Together these results show a trend towards increased apoptosis and cell cycle arrest for construct -143, but not -146, contributing to a loss of expansion in liquid culture. Replication is required to validate these changes.

These data in MLLr cell lines shows that MLL-AF9 and MLL-AF4 cells are sensitive to *NFATC2* KD, leading to a loss of colony formation, but to differing extents. The cellular events leading to this are not clear and may involve contributing elements of apoptosis and cell cycle arrest. Further characterisation is needed to offer firm conclusions.

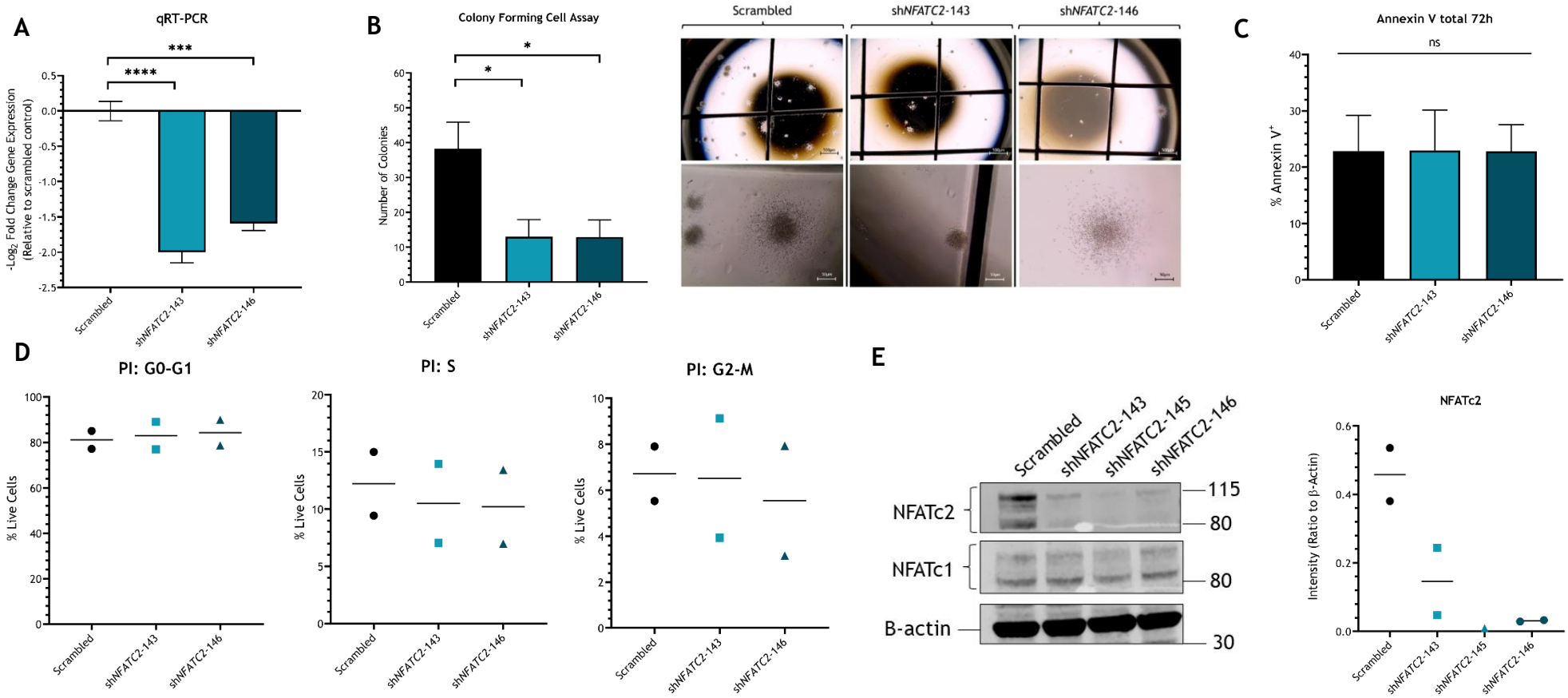

Figure 4-20. MV4-11 with *NFATC2* KD formed fewer colonies in semi-solid media.

MV4-11 were transduced with either a scrambled control or *NFATC2*-targeting shRNA (-143, -145 or -146). All figures are as for MOLM-13 in Figure 4-19. unless otherwise stated. Data are mean ± SEM, or mean and individual data points. *P* values: *<0.05, ***<0.001, ****<0.0001, 'ns' = p>0.05. **A:** qRT-PCR for *NFATC2* expression in cells harvested 48 hr post selection, relative to the scrambled control using the ΔΔCt method (n=3 biological, n=3 technical replicates). **B:** Cells were seeded in semi-solid media at 24 hr post-selection and colonies counted after 8-9 days (n=3 biological, n=3 technical). **C:** Annexin V/DAPI assay 72 hr post-selection (n=4 biological). **D:** Cells stained with PI, 72 hr post-selection (n=2 biological). **E:** 30 µg WCL from MV4-11 was blotted using anti-NFATc2, anti-NFATc1 and anti-ß-actin. NFATc2 intensity is expressed relative to ß-actin (n=2 biological).

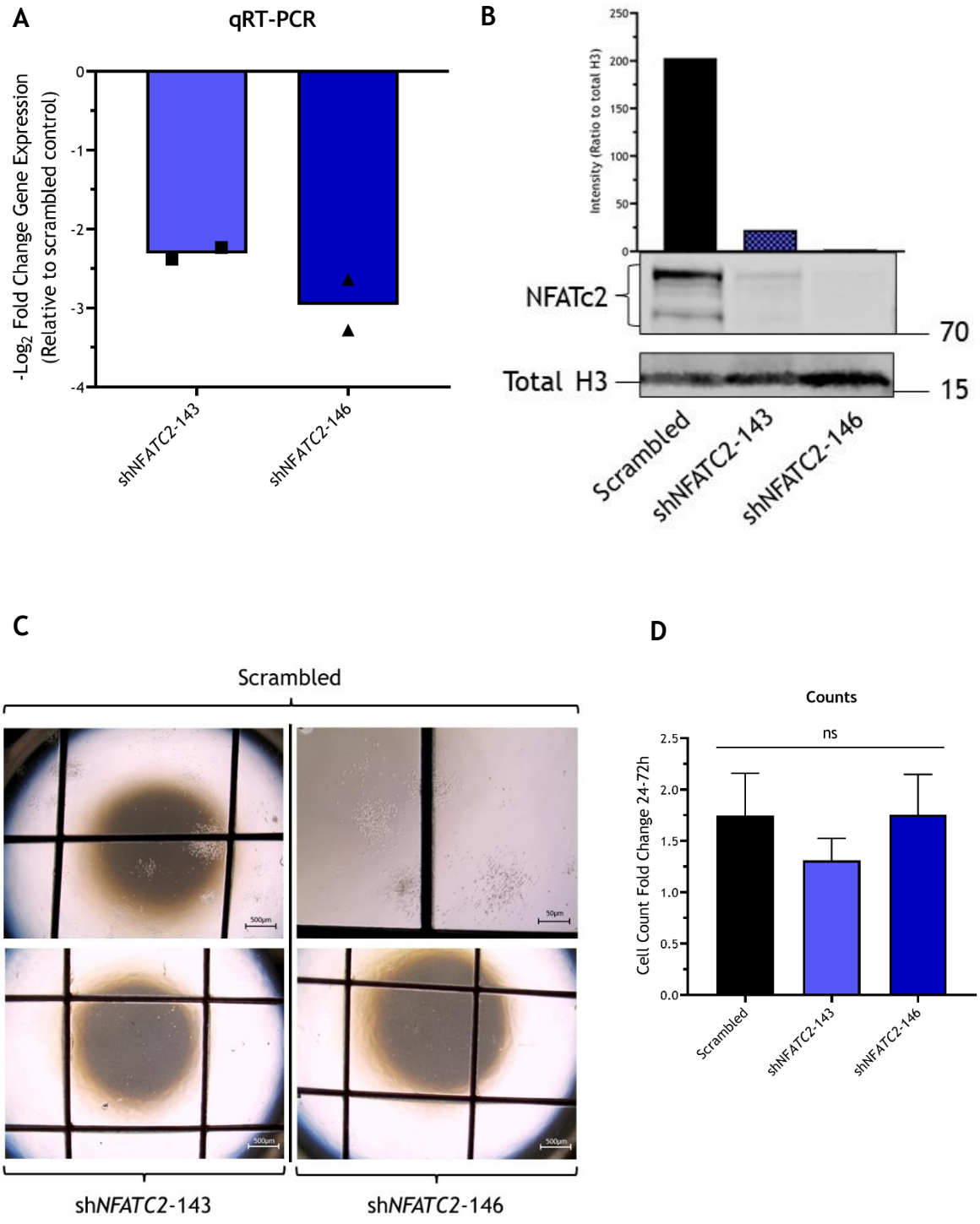
A
qRT-PCR
-Log2 Fold Change Gene Expression
(Relative to scrambled control)
0
-1
-2
-3
-4
shNFATC2-143
shNFATC2-146
B
Intensity (Ratio to total H3)
250
200
150
100
50
0
NFATc2
70
Total H3
15
Scrambled
shNFATC2-143
shNFATC2-146
C
Scrambled
500µm
50µm
500µm
500µm
shNFATC2-143
shNFATC2-146
D
Counts
ns
Cell Count Fold Change 24-72h
2.5
2.0
1.5
1.0
0.5
0.0
Scrambled
shNFATC2-143
shNFATC2-146

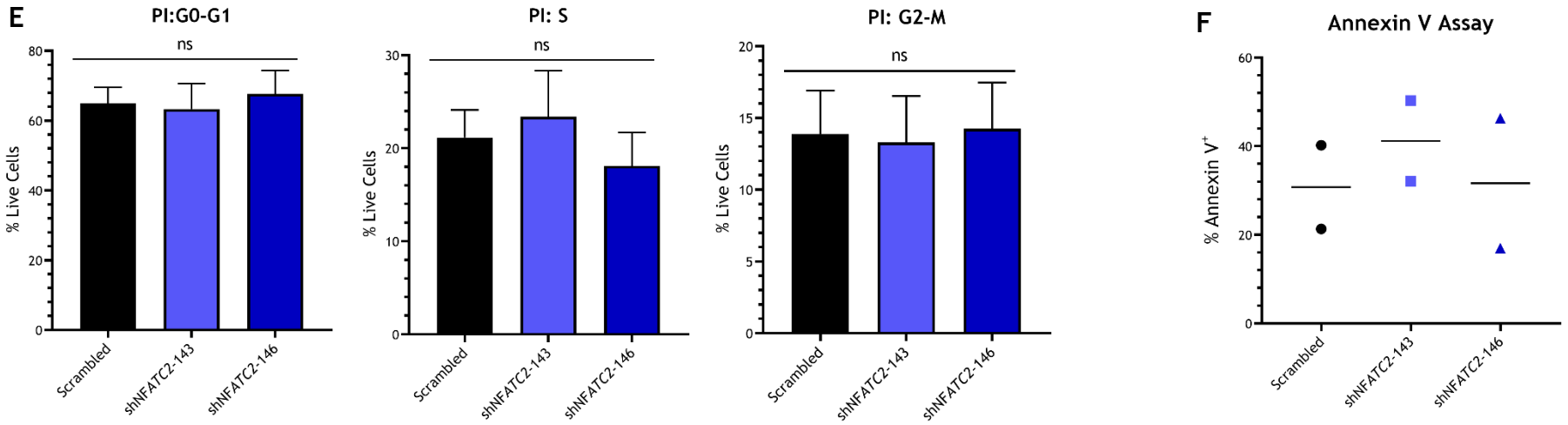

Figure 4-21. NOMO-1 with *NFATC2* KD did not grow in semi-solid media.
NOMO-1 were transduced with a scrambled control or *NFATC2*-targeting shRNA. All figures are as presented as in Figure 4-19 unless otherwise stated. Data shown are mean ± SEM, or mean and individual data points. 'ns' = $p>0.05$. **A:** qRT-PCR for *NFATC2* expression in cells harvested 48hr post selection, relative to the scrambled control using the ΔΔCt method (n=2 biological, n=3 technical replicates). **B:** 35µg of WCL from NOMO-1 was run and blotted using anti-NFATc2 and total H3. NFATc2 intensity is expressed relative to total H3 (n=1 biological). **C:** Cells were seeded in semi-solid media and representative images (n=2 biological) taken after 12-14 days. **D:** Cells were seeded in liquid culture and counted every 24 hr. Shown is the fold change in counts from 24 hr to 72 hr (n=3 biological, n=2 technical). **E.** NOMO-1 cells stained with PI (n=3 biological). **F.** Annexin V/DAPI assay 72 hr post-selection (n=2 biological).

4.3.5.2 Non-MLLr AML

NFATC2 KD in non-MLLr HL-60 cells (amplified *MYC* and *NRAS*, *TP53*^{del}) was shown by a depletion of NFATc2 protein, using an immunoblot (Figure 4-22A). HL-60 were also sensitive to *NFATC2* KD, as cells significantly lost colony-forming capacity (Figure 4-22B; p=0.0280 and p=0.0327 for constructs -143 and -146, respectively) and expanded less in liquid culture (Figure 4-22C) with KD.

PI stain data showed a reduction of cells in the S phase, and an increase in the G0-G1 phases, though none was statistically significant (Figure 4-20D). Together these data could suggest a mild level of G1/S phase transition arrest. Apoptosis was markedly increased after *NFATC2* KD (Figure 4-20E; fold changes of 2.08 and 2.16), suggesting that this is a significant contributor to the loss of colony-forming capacity and expansion in culture. Further replication is required to confirm these data.

OCI-AML3 cells (*NPM1*^{mut}, *DNMT3a*^{mut}, *NRAS*^{mut}) do not express detectable *NFATC2* transcript as demonstrated in Chapter 3.2.2. *NFATC2* KD was carried out to determine if even low levels of transcript/protein would be functional in these cells. KD does show a modest reduction in OCI-AML3 colony formation, but not in cell expansion in liquid culture (Figure 4-23A&B). Transduction with construct -146 leads to an increase in cell expansion. KD of transcript or protein were not validated at this stage due to their poor expression in these cells.

There was an increase in apoptosis after transduction with either construct, most markedly for construct -143 (Figure 4-23C). This was not entirely consistent with the insignificant changes observed in colony formation, but the inter-replicate variability in these experiments was high and further replication is required to perform statistical testing. There were minimal changes to the cell cycle in OCI-AML3 after *NFATC2* KD (Figure 4-23D). This suggests that apoptosis follows *NFATC2* KD in OCI-AML3 cells, but validation of the *NFATC2* KD is required to make this conclusion with confidence.

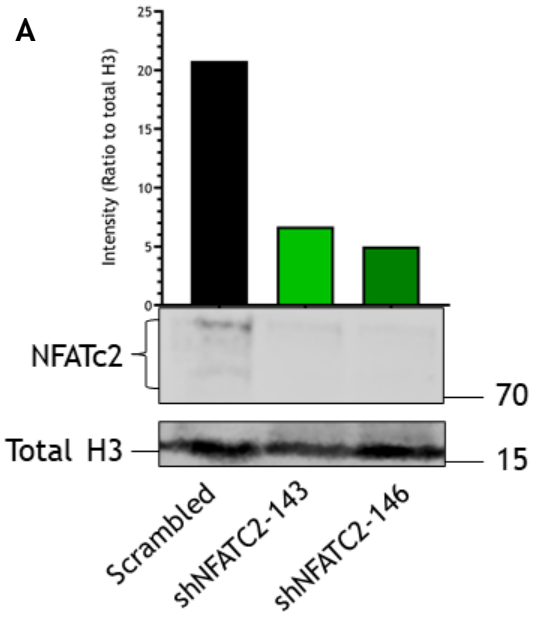
A
Intensity (Ratio to total H3)
25
20
15
10
5
0
NFATc2
70
Total H3
15
Scrambled
shNFATC2-143
shNFATC2-146

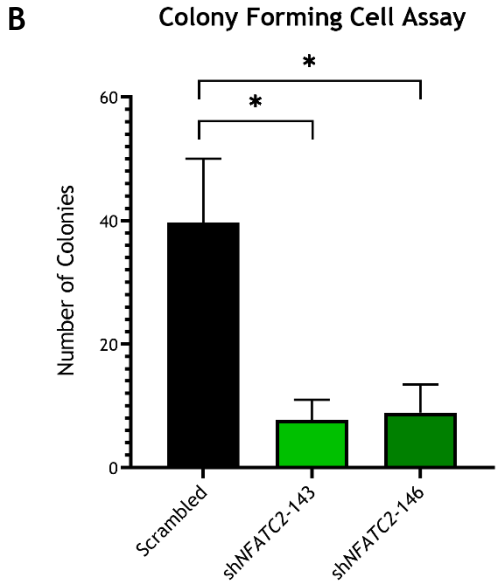
B
Colony Forming Cell Assay
Number of Colonies
60
40
20
0
*
*
Scrambled
shNFATC2-143
shNFATC2-146

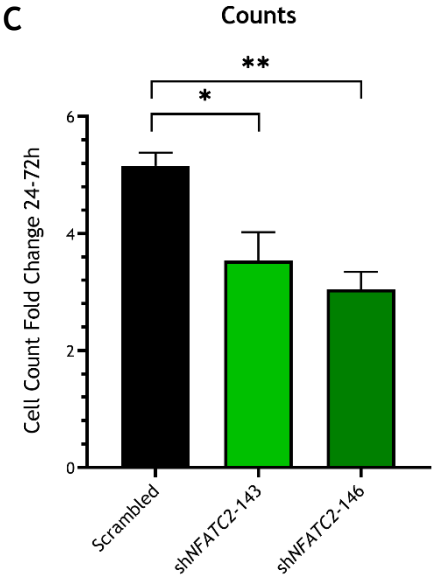
C
Counts
Cell Count Fold Change 24-72h
6
4
2
0
**
*
Scrambled
shNFATC2-143
shNFATC2-146

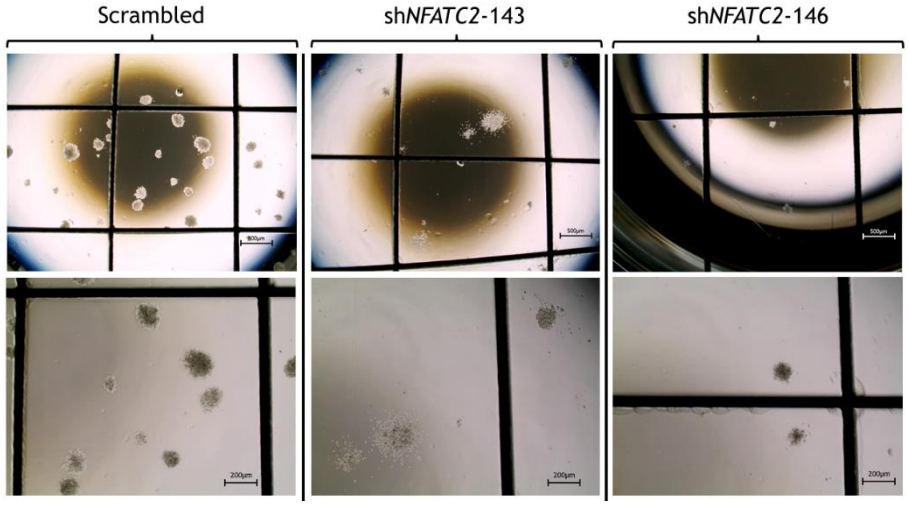
Scrambled
shNFATC2-143
shNFATC2-146

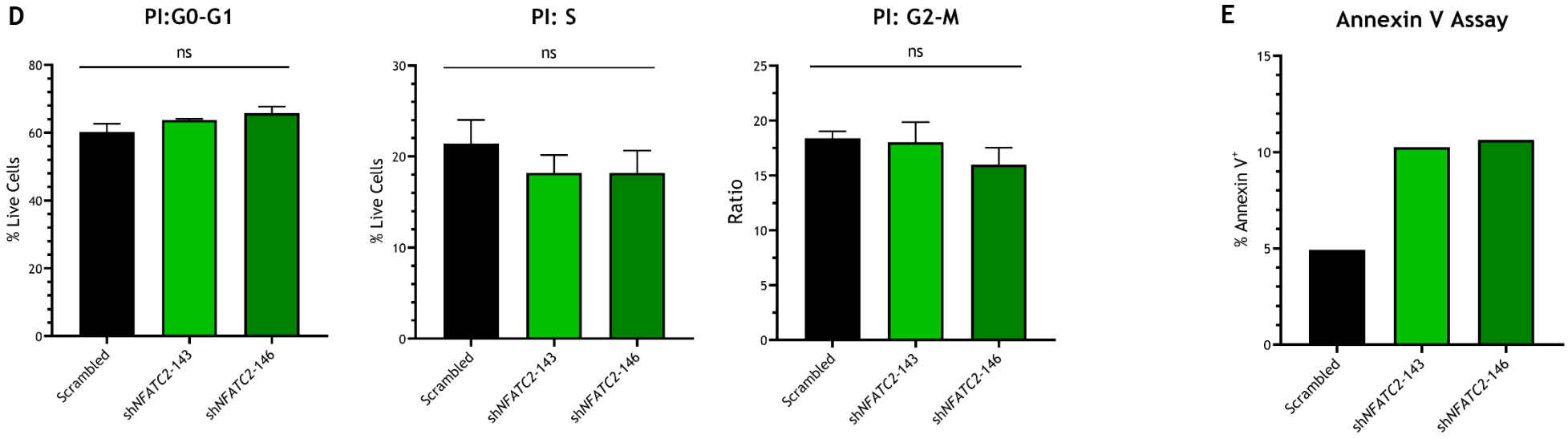

Figure 4-22. HL-60 cells with *NFATC2* KD had reduced colony-forming capacity and show increased apoptosis.
HL-60 were transduced with a scrambled control or *NFATC2*-targeting shRNA. All figures are as presented as in Figure 4-19 unless otherwise stated. Data shown are mean ± SEM or the individual data point (for n=1 biological replicate). *p* values: *<0.05, **<0.01, 'ns' = *p*>0.05. **A:** 35 µg of WCL from HL-60 was run and blotted using anti-NFATc2 and total H3. NFATc2 intensity is expressed relative to total H3 (n=1 biological). **B:** Cells were seeded in semi-solid media at 24 hr post-selection and colonies counted after 7-8 days (n=3 biological, n=3 technical). Representative images are shown below. **C:** Cells were seeded in liquid culture and counted every 24 hr. Shown is the cell count fold change from 24 hr to 72 hr (n=3 biological n=2 technical). **D:** HL-60 cells harvested 72 hr post-selection and stained with PI (n=3 biological). **E.** Annexin V/DAPI assay 72 hr post-selection (n=2 biological).

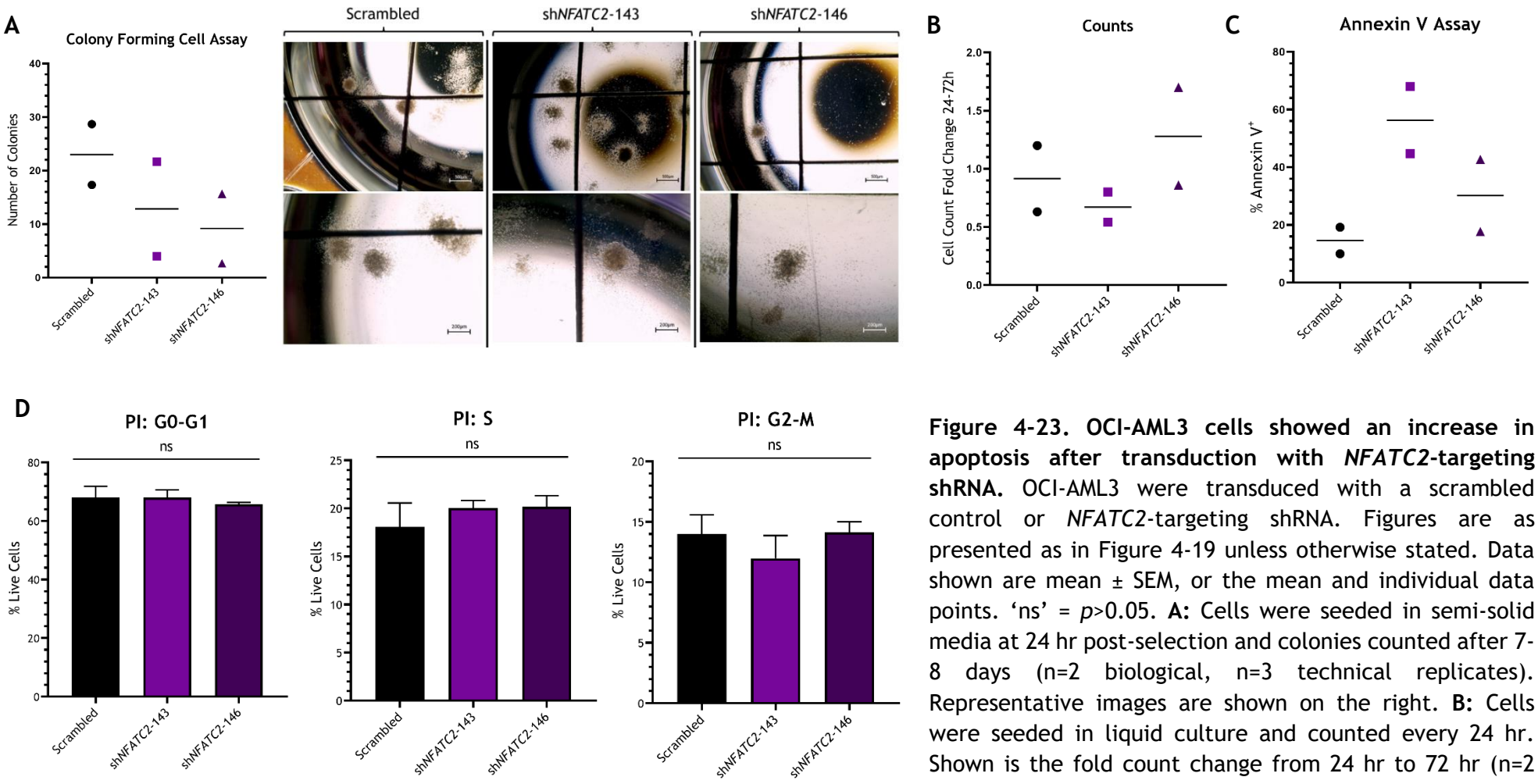

Figure 4-23. OCI-AML3 cells showed an increase in apoptosis after transduction with *NFATC2*-targeting shRNA. OCI-AML3 were transduced with a scrambled control or *NFATC2*-targeting shRNA. Figures are as presented as in Figure 4-19 unless otherwise stated. Data shown are mean ± SEM, or the mean and individual data points. 'ns' = $p>0.05$. **A:** Cells were seeded in semi-solid media at 24 hr post-selection and colonies counted after 7-8 days (n=2 biological, n=3 technical replicates). Representative images are shown on the right. **B:** Cells were seeded in liquid culture and counted every 24 hr. Shown is the fold count change from 24 hr to 72 hr (n=2 biological, n=2 technical). **C:** Annexin V/DAPI assay 72 hr post-selection (n=2 biological). **D:** Cells harvested 72 hr post-selection, stained with PI (n=3 biological).

Finally, Kasumi-1 cells (AML1-ETO, *TP53*^{mut}) were transduced with shRNA for *NFATC2* KD. These cells express low levels of *NFATC2* but it is detectable by qRT-PCR. Kasumi-1 cells did not readily form colonies and so this was not assessed. KD of *NFATC2* was validated by qRT-PCR (Figure 4-24A). Apoptosis was not markedly changed after KD (Figure 4-24B) however there was a statistically significant reduction in cells in the S phase (p=0.0016 and p=0.0040 for constructs -143 and -146, respectively), and a marginal increase of those in the G0-G1 phases of the cell cycle (Figure 4-24C) Overall these data suggest that there is cell cycle arrest at the G0-G1/S phase transition after *NFATC2* KD in Kasumi-1 cells.

Together these results show that a number of non-MLLr cell lines of varying (cyto)genetic backgrounds are responsive to *NFATC2* KD, including those with low expression of the gene. The cellular response to *NFATC2* depletion is, however, different in each. While HL-60 and OCI-AML3 tend to become more apoptotic after KD Kasumi-1 cells demonstrate G0-G1/S phase cell cycle arrest.

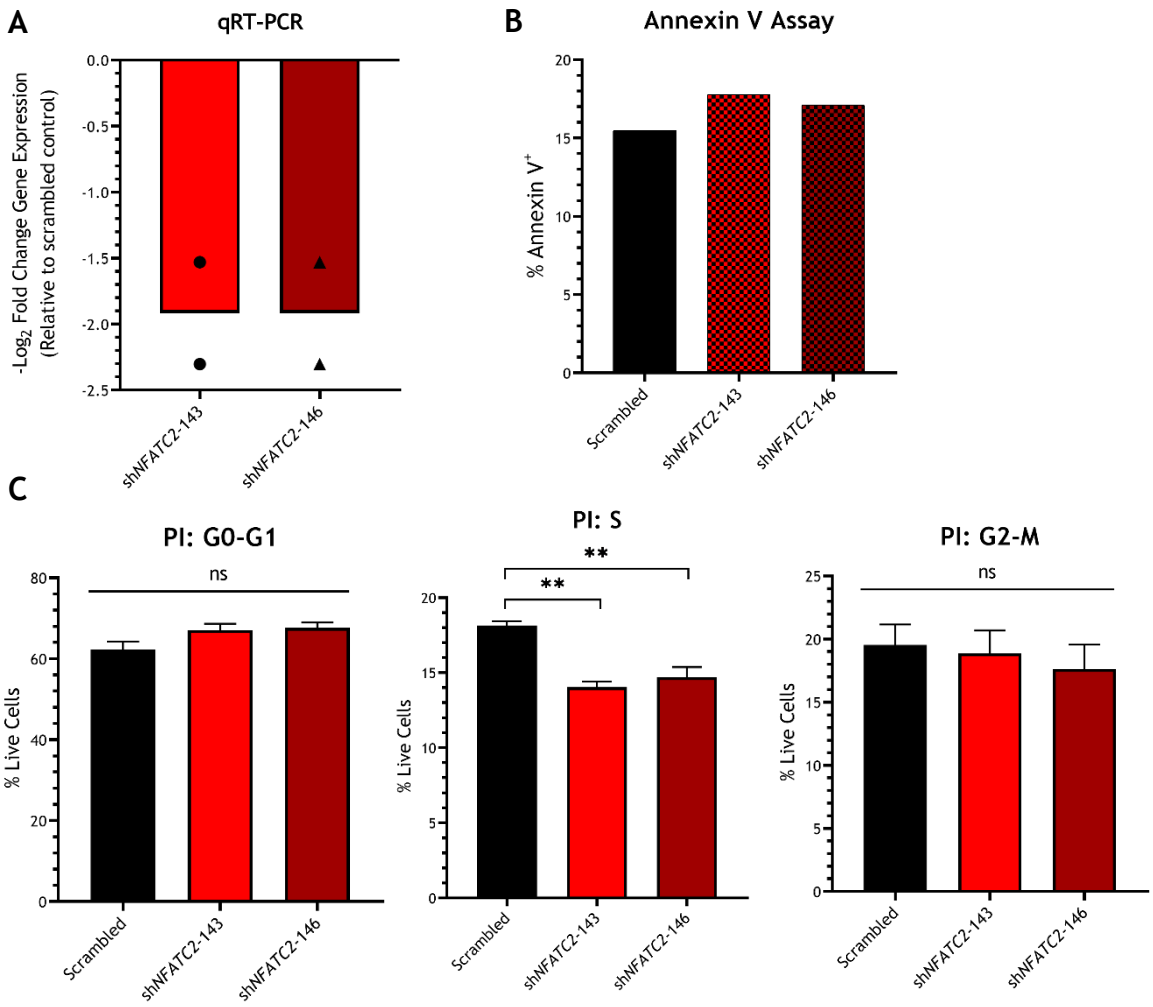

Figure 4-24. Kasumi-1 showed G1/S phase cell cycle arrest after *NFATC2* KD. Kasumi-1 cells were transduced with a scrambled control or *NFATC2*-targeting shRNA. All figures are as presented as in Figure 4-19 unless otherwise stated. Data shown are mean ± SD or the mean ± individual data point(s). *p* values: **<0.01, 'ns' = *p*>0.05. **A.** qRT-PCR for *NFATC2* expression in cells harvested 48 hr post selection (n=2 biological, n=3 technical replicates). **B.** Annexin V/DAPI assay 72 hr post-selection (n=1 biological). **C.** Kasumi-1 cells harvested 72 hr post-selection and stained with PI (n=3 biological).

4.4 Discussion

The methods utilised in this chapter focused on key elements of the phenotype of AML cell lines after depletion of NFATc2 function or *NFATC2*/*Nfatc2* transcript. CFC assays were used to measure the clonogenic properties of cells and revealed that, across 8 cell types of diverse (cyto)genetic backgrounds, 6 formed quantifiable colonies. In all cases colony-forming capacity was reduced after *NFATC2*/*Nfatc2* KD, mostly with statistical significance. Measures of the cell cycle – including PI staining, BrdU staining and CFSE dye tracing – revealed that some cell lines underwent G1/S or G2/M phase arrest after *NFATC2*/*Nfatc2* KD, but usually below statistical significance thresholds. Similarly, a subset of cell lines exhibited enhanced apoptosis after KD. In addition, inhibition of calcineurin-NFAT signalling led to a combination of cell cycle arrest and apoptosis in THP-1 cells. Overall, it was not immediately clear how the changes observed following NFAT or NFATc2/*NFATC2* depletion were related with the mutational or molecular profile of the individual cell types. These are discussed in further detail below.

4.4.1 THP-1 cells, but not Kasumi-1, were sensitive to inhibition of the calcineurin-NFAT axis

The first part of this chapter focused on the inhibition of calcineurin-NFAT signalling using established inhibitors, as an indirect means of examining cells' dependence on *NFATC2*. The data in THP-1 cells show a loss of cell viability after treatment with any of these compounds, which suggests that these cells are dependent on calcineurin-NFAT signalling. There was evidence that CsA and VIVIT-11R could block dephosphorylation of NFATc2 and reduce the expression or availability of NFATc2 protein itself. NFATs are known to self-regulate their expression in T cells (Chuvpilo *et al.*, 2002, Serfling *et al.*, 2006, Shin *et al.*, 2019), so this suggests similar feedback loops exist within THP-1 cells. INCA-6 did not induce these effects, which might suggest its effects on viability are not mediated through NFATc2.

CsA treatment induced a marked apoptotic response and there was some evidence of an accumulation of cells in the G1 phase, which could indicate a trend towards G1/S arrest. VIVIT-11R induced apoptosis and the changes in the cell cycle were difficult to assess, in the absence of further replication. Together, this suggests

that NFAT functional inhibition leads to apoptosis. NFATs have been attributed various roles in the regulation of apoptosis and the cell cycle (Mognol *et al.*, 2016), and here the phenotype may reflect the function(s) of NFATc1-4 individually, or a combination of multiple. There is some known functional redundancy between different NFATs - as reported in KO mouse models (Crabtree and Olson, 2002), which could mean that the phenotype observed was demonstrable only after inhibiting multiple NFAT proteins. Additionally, calcineurin has been shown to directly downregulate CDK4 activity by phosphorylation and the evidence of S/G1 phase arrest is consistent with this phenotype (Baksh *et al.*, 2000).

Interestingly, the IC_{50} values for VIVIT-11R and INCA-6 in THP-1 did not change substantially between 24 hr, 48 hr and 72 hr. Further experimentation to determine the reversibility of these drugs' binding – for example, by washing the drug out from the cells' media and measuring cell recovery – may provide information as to why their effects on these cells are consistent over this 72 hr period. Another unknown factor is the half-life of the drugs in these *in vitro* conditions, which would be a key factor if the drugs bind their targets reversibly.

Kasumi-1 cells' lack of sensitivity to CsA or VIVIT-11R supports a number of conclusions. Firstly, that calcineurin-NFAT signalling is not essential for these cells' growth and/or survival. Given that these inhibitors were demonstrated to inhibit NFATc2 effectively in THP-1 cells, this finding likely reflects a difference between THP-1 and Kasumi-1 in their dependence on NFAT function, and not on inhibitor activity. Logically, this would imply that Kasumi-1 are not dependent on isolated NFATc2 protein function either, however NFAT signalling is multi-dimensional and this may not be the case. It may also be the case that Kasumi-1 cells are low expressors of *NFATC1, NFATC3* and *NFATC4* - the latter of which is expected in myeloid cells - but these were not measured in this study.

Finally, the finding that Kasumi-1 cells were sensitive to INCA-6 but not to CsA or VIVIT-11R indicates that its effect on viability was not a result of calcineurin-NFAT inhibition. Blockade of dephosphorylation was not demonstrated in THP-1 cells with INCA-6 treatment and so, together, these data suggest that INCA-6 is not selective for the calcineurin-NFAT interaction specifically, in these cells and at the concentrations used.

4.4.2 shRNA KD of *NFATC2* in THP-1 cells led to a loss of colony-forming capacity, *CCND1* downregulation and evidence of cell cycle arrest

To focus more specifically on *NFATC2* function, a lentiviral shRNA approach was used in AML cell lines. The magnitude of transcript depletion could not be correlated with cell count changes for 4 shRNA constructs in MOLM-13; a strategy similar to that used previously (Harris *et al.*, 2012) to select more on-target shRNA. 3 candidate shRNA were initially taken forward based on their ability to deplete *NFATC2* and demonstrate a measurable effect on cells at 72hr post-puromycin selection.

NFATC2 depletion in THP-1 cells led to a dramatic loss of colony formation and a milder, but significant, loss of expansion in liquid culture. Colony-forming assays are a sensitive method of assessing single cells' ability to proliferate, with minimal interaction with other cells (Puck and Marcus, 1956). This result could reflect an increase in cell death (by apoptosis or necrosis), a reduction in proliferation, or both. It is also possible that the cells have differentiated into non-dividing effector cells; THP-1 cells can be readily differentiated from monocytes into macrophages *in vitro* (Starr *et al.*, 2018). However, changes in morphology were not observed microscopically in slide preparations, colonies or macroscopically in liquid culture.

An increase in apoptosis was observed after transduction of sh*NFATC2*-143, by an increase in Annexin V binding and a modest increase in PARP cleavage; both of which are hallmarks of cell apoptosis (Mullen, 2004). RNA interference can induce off-target effects, through a number of known mechanisms (Rao *et al.*, 2009), so caution must be taken when interpreting this finding in only one of two constructs. It is possible that there is a threshold-dependent induction of apoptosis upon *NFATC2* depletion, however the qRT-PCR results show a similar level of KD between constructs -143 and -146. *NFATC2* gene KO using such a system as CRISPR/Cas9 would mitigate this issue and would serve as a useful follow-up method here. Additionally, further apoptosis assays (such as a TUNEL assay) could be used to complement existing methods (Mullen, 2004).

Cell proliferation was reduced as measured by CFSE proliferation tracing, but the magnitude of this change from 24 to 72 hr post-selection does not fully explain

the greater change in cell counts within same period, which could indicate that increased cell death is a contributing factor. Since proliferation dye tracing only accounts for changes in cells which are alive at the experiment end it is difficult to compare these magnitudes of change with cell counts, which take account of cell death.

However, the near total loss of colony formation at 8 days (192 hr) post-selection with *NFATC2* KD is a dramatic change which seems unlikely to be accounted for by these modest changes in CFSE dilution at 72 hr. It is possible that the selected 72 hr timepoint post-selection is too soon after *NFATC2* KD to observe extensive changes in cell behaviour. Colony formation is dependent on sufficient growth of single cells to become macroscopic colonies, which is a later observation and unlikely to occur within 72 hr, even in untreated THP-1 cells. *CCND1* and *CCND2* were downregulated minimally prior to 144 hr post-selection, supporting the hypothesis that the effects of *NFATC2* KD are gradually cumulative events in THP-1 cells.

Cell cycle data show modest changes, from which conclusions cannot be accurately drawn, and this may reflect the prematurity of the 72 hr timepoint. Examination of cell cycle changes at later timepoints may provide insight into the mechanism driving the loss of colony formation over the course of the colony-forming assay time period.

The primary observable change is a trend towards accumulating G2-M phase THP-1 cells after *NFATC2* KD. The G2/M transition is regulated by p53, which can induce arrest via suppression of *CCNB1* (encoding cyclin B1), usually in response to DNA damage (Taylor and Stark, 2001). However, THP-1 cells carry a functionally deleterious *TP53* sequence deletion, which might lead to an absent or weakened G2/M checkpoint in these cells. p53-independent mechanisms of G2/M arrest have been described in mammalian cells, driven by ATM and ATR kinases' response to DNA damage (Taylor and Stark, 2001, Schnerch *et al.*, 2012).

DNA damage can be measured by γH2AX (pH2AX ser139) which has been shown to correlate with DSBs in AML cells. Additionally, chemical induction of DNA damage can be used to demonstrate AML cells' stringency of control at the G2/M checkpoint; whereby a lower level of γH2AX would suggest a more successful block of cells with DSBs from entering mitosis (Didier *et al.*, 2008). The observation in

THP-1 cells was that phosphorylation of H2AX at ser139 was reduced after *NFATC2* KD. Therefore, *NFATC2* KD may restore some of the function of the G2/M checkpoint, which is otherwise weakened in the presence of mutated *TP53*, thus inducing G2/M arrest. This could imply a role for *NFATC2* in the repression of G2/M arrest, possibly through p53-independent mechanisms.

CCND1 and *CCND2* were downregulated after *NFATC2* KD. Cyclin D isoforms are usually described as regulators of the G1/S phase transition, during which they bind CDK4 or CDK6 to release Rb-mediated E2F suppression of S-phase entry. Cyclin D1-3 also have functions unrelated to the cell cycle (Dai *et al.*, 2019). Downregulation of cyclins D1/D2 after *NFATC2* KD does not seem consistent with G2/M arrest. However, cyclin D1 has been reported to peak in both G1 and G2 phases in fibroblasts (Yang *et al.*, 2006), which could imply it has less well-characterised functions in the G2/M transition.

Consider also that induction of cyclin D1 in the G2 phase has been shown to be dependent on Ras activity (Hitomi and Stacey, 1999). The significance of this is that THP-1 cells carry an activating G12D mutation of *NRAS*, which is known to cooperate with MLL-AF9 in leukaemogenesis (Shi *et al.*, 2013). It could be hypothesised that elevated cyclin D in the G2 phase, downstream of $NRAS^{G12D}$, is part of the mechanism which enables aberrant self-renewal in THP-1 cells. *NFATC2* could be involved in the maintenance of this axis, or other regulatory elements, but it is not clear from these data alone. Furthermore, $TP53^{mut}$ and $NRAS^{G12D}$ can cooperate in AML induction (Zuber *et al.*, 2009, Vainchenker and Plo, 2017) and so the interplay of these mutational features in the regulation of the cell cycle is likely to be highly complex, in THP-1 cells.

Contrast these findings with known roles of *NFATC2* in the cell cycle. In T cells NFATc2 can recruit HDAC1 to the *CDK4* promoter in order to downregulate its expression and facilitate cells' exit from the cell cycle (Baksh *et al.*, 2002). In pancreatic cancer NFATc2 has been shown to upregulate *CDK6* and promote cell growth, under the control of GSK3β (Baumgart *et al.*, 2016). In connective tissue NFATc1, but not NFATc2, can upregulate cyclin D1; here, NFATc2 is thought to be more suppressive of the cell cycle (Karpurapu *et al.*, 2010). Clearly the cellular context and other transcriptional networks are important in defining NFAT function.

4.4.3 Overexpression of m*Nfatc2* rescued the loss of cell expansion in culture after h*NFATC2* KD in THP-1 cells

The effects of *NFATC2* KD on colony formation were not reversed by m*Nfatc2* expression, although some growth below the colony size threshold was observed by eye. The loss of expansion in liquid cultures was rescued, however, so together the data suggest that m*Nfatc2* partially compensated h*NFATC2* function in this initial period following KD.

There was a rescue of the increase in apoptosis caused by construct -143, which suggests that is an on-target effect of *NFATC2* KD. Constructs -143 and -146 differ in that -146 does not target transcript variants 3-6, however these were shown to be poorly expressed in THP-1 in Chapter 3.2.2. The level of *NFATC2* depletion (using qRT-PCR primers targeting all known variants) is equivalent between constructs in these experiments. However, if variants 3-6 are functional at even low levels of expression in THP-1, it may be the case that pan-*NFATC2* KD by construct -143 induces a more apoptotic phenotype than selective KD of variants 1, 2, 7 and 8 by construct -146.

There were limited observable changes in the cell cycle after *NFATC2* KD, with either empty vector or m*Nfatc2* expression. This may not be surprising, since minimal changes were observed in unmodified THP-1 at this timepoint. An effect at later timepoints should be measured in unmodified THP-1 first, before attempting to rescue this effect. If there is evidence of a cell cycle arrest at these later points, it appears from expansion and colony-forming data that rescue of the driving mechanism by m*Nfatc2* is unlikely.

Orthologous h*NFATC2* and m*Nfatc2* share high structural homology, although some mouse transcript variants are missing key rel-homology domain components (Vihma *et al.*, 2008). The m*Nfatc2* isoform transcribed from the vector used is the full-length isoform C (Luo *et al.*, 1996a, Monticelli and Rao, 2002), which is one of the shorter variants and may have altered DNA-binding and/or partner interaction properties. Additionally, protein detected in o/e m*Nfatc2* THP-1 by immunoblotting – which was not confirmed to be mNfatc2, as opposed to hNFATc2 – was demonstrably predominantly in the cytoplasm (Chapter 3.2.3). Its subcellular location may reflect its inability to translocate effectively into the nucleus due to structural differences and a failure of recognition by enzymatic

regulators. Together, these variations between hNFATc2 and mNfatc2 could explain the limited ability of mNfatc2 to rescue h*NFATC2* KD.

4.4.4 MLL-AF9-driven murine BM cells with *Nfatc2* KD displayed signs of apoptosis, cell cycle arrest and *Ccnd1* upregulation

The expression of MLL-AF9 in murine BM cells conferred enhanced self-renewal and leukaemogenic potential when originally generated and studied *in vivo* by Somervaille *et al.* (Somervaille and Cleary, 2006). The reported surface expression of CD117, Gr-1 and Mac-1 in splenocytes in this study was similar to that measured and reported here in Figure 4-15B. Additionally, a high proportion of LSCs was reported previously in these cells, and so this provided a model more reflective of primary AML than an AML cell line, albeit in mouse.

In contrast, CD117-selected BM cells displayed a higher proportion of CD117 and more heterogeneous expression of myeloid markers Gr-1/Mac-1. Upregulation of MLL-AF9 target Homeobox genes *Hoxa9* and *Meis1* in the MLL-AF9 BM, as compared to the $CD117^+$ BM, confirmed the expected activity of MLL-AF9 (Zhu *et al.*, 2016). The upregulation of *Nfatc1* and *Nfatc2* was of too small a magnitude to determine significance, and similarly minimal changes were observed in selected cyclin genes. MLL-AF9 AML cells were shown to be dependent on CDK6-mediated differentiation block (Placke *et al.*, 2014) and cyclin D is a key partner of CDK6 in cell cycle regulation. *CCND1* expression is not necessarily upregulated in MLLr AML but it is predictive of patient outcome (Chen *et al.*, 2019). Together with *CCND1* downregulation in THP-1 cells after *NFATC2* KD, this was a gene of interest in these cells.

The loss of colony-forming capacity in MLL-AF9 BM after *Nfatc2* KD seemed to be driven largely by apoptosis, though early signs of G1/S cell cycle arrest was observed after transduction with construct -356. As this was not consistent between constructs, few conclusions can be made at this stage. Surprisingly the expression of *Ccna2* and *Ccnd1* were markedly upregulated, the latter of which being the opposite of that observed in THP-1. *CCND1* upregulation is a known inducer of apoptosis in a number of cell types, sometimes through CDK4 binding, though the magnitude of change and cellular context can influence its precise role (Han *et al.*, 1999). Furthermore, p53 can induce cyclin D-mediated apoptosis (Chen *et al.*, 1995). If there is indeed a G1/S phase transition arrest after

transduction of construct -356 by KD of *Nfatc2,* this is also consistent with the known functions of cyclin D, via CDK6 (Han *et al.*, 1999).

Cyclin A has also been attributed roles in apoptosis, in complexes with either of its canonical binding partners CDK1 or CDK2, or also in cooperation with *MYC*. Its function may also be dependent on its subcellular localisation (Borgne and Golsteyn, 2003, Zuryn *et al.*, 2007). The Cyclin A2 promoter has been demonstrated as a strong NFATc2 binding site in T cells, where it acts putatively as a tumour suppressor (Carvalho *et al.*, 2007). This seems to contrast with this current model, where the absence of *Nfatc2* was suppressive of tumour growth. Finally, *Hoxa9* and *Meis1* expression were not significantly affected by *Nfatc2* KD, suggesting that MLL-AF9-driven self-renewal pathways may not be affected by *Nfatc2*.

It is important to acknowledge the potential for divergent signalling between human and murine cells when making any direct comparisons. However, some parallels between THP-1 cells and MLL-AF9 BM cells might be useful in elucidating the role(s) of *NFATC2*/*Nfatc2* in MLL-AF9 AML. The phenotypes are somewhat distinct: where THP-1 cells exhibited G2/M arrest and apoptosis, MLL-AF9 BM showed G1/S arrest and apoptosis. Morphologically, cell death was more of a feature in MLL-AF9 BM. Upregulation of *CCNA2*/*Ccna2* was observed in THP-1/MLL-AF9 BM after *NFATC2*/*Nfatc2* KD, but *CCND1*/*Ccnd1* deregulation was opposing.

The differing mutational profiles may be a contributor to these differences. Given the known interactions of p53 and cyclin D, the presence of $TP53^{mut}$ in THP-1 may have an impact on the regulation of cyclin D and/or its function. The same may be said for $NRAS^{G12D}$. Still, from these data, the role of *NFATC2*/*Nfatc2* in these complex cellular environments is not clear, but it may interact with or co-regulate targets of p53, for example. However, the phenotype after *NFATC2*/*Nfatc2* KD is different in each, which suggests that the MLL-AF9 oncogene is less relevant, or that the targets/function of MLL-AF9 changes in the context of other oncogenes. Finally, the observed changes to apoptosis and the cell cycle are modest in both of these models and should be interpreted carefully.

4.4.5 AML cell lines of varying (cyto)genetic background were sensitive to *NFATC2* KD in CFC assays

Cell lines of varying (cyto)genetic backgrounds were used to provide a wider context for *NFATC2* function in AML. There are a number of MLLr AML cell lines which co-express other oncogenes, including $FLT3^{ITD}$ MLL-AF9 MOLM-13 cells. KD of *NFATC2* in MOLM-13 led to a modest reduction in colony formation and cell expansion in culture, with minimal changes observed to the cell cycle. It is possible that these cells are not as vulnerable to *NFATC2* KD as THP-1 cells due to signalling driven by $FLT3^{ITD}$. In contrast, MOLM-13 was compared to $FLT3^{ITD}$ MLL-AF4 MV4-11 cells, in which *NFATC2* KD did have a substantial impact on colony forming capacity. Changes to the cell cycle were modest at best, with some indication of G1/S arrest, but further characterisation required.

$FLT3^{ITD}$ upregulates proliferation and self-renewal through aberrant recruitment of cyclin D3, Pim-1 and c-Myc, via STAT5, through which it can deregulate CDK2, CDK4 and CDK6 activity (Li *et al.*, 2007). p27 has also been described as a key regulator of these pathways in $FLT3^{ITD}$ AML (Iris *et al.*, 2017). One study in myeloid tissue showed that NFATs act downstream of normal FLT3 (Fric *et al.*, 2014), while another demonstrated cooperativity of $FLT3^{ITD}$ and *NFATC1* in AML development (Solovey *et al.*, 2019).

It seems likely that, if a relationship does exist in these cells, *NFATC2* would act downstream of $FLT3^{ITD}$ at the nuclear level. The differences in the responses of MOLM-13 and MV4-11 to *NFATC2* KD suggest either that $FLT3^{ITD}$ is not a driver of *NFATC2*-mediated signalling, or that MV4-11 harbours a distinct molecular landscape, possibly due the presence of MLL-AF4, as opposed to MLL-AF9. Additionally, MOLM-13 and MV4-11 express heterozygous and homozygous $FLT3^{ITD}$ alleles, respectively. There is some evidence to demonstrate that loss of the $FLT3^{WT}$ allele is sufficient to induce more aggressive disease, so the contribution of this to these cells could be important to downstream signalling (Li *et al.*, 2011b).

Co-expression of MLL-AF9, or some other MLL fusion genes, with $FLT3^{ITD}$ is sufficient to induce penetrant AML *in vivo* (Ono *et al.*, 2005, Stubbs *et al.*, 2008), although the co-occurrence of MLLr and $FLT3^{ITD}$ in patients is relatively uncommon (Steudel *et al.*, 2003, Balgobind *et al.*, 2011). MLL-AF9 and MLL-AF4 have distinct transcriptional targets, although there is a degree of overlap, as found in AML cell

lines (Prange *et al.*, 2017). Interestingly, this study by Prange *et al.* found *NFATC2* to be a target of WT MLL, but not MLL-AF4 or MLL-AF9 in these cell lines.

The data from MLL-AF9 *TP53*^{mut} *KRAS*^{mut} NOMO-1 cells are more limited but do suggest a loss of growth in semi-solid media (although colonies were not formed). Together these data suggest that a number of MLLr AML cell lines are vulnerable to *NFATC2* KD, to differing degrees. This suggests that *NFATC2* is responsible for maintaining specific oncogenic transcriptional programs in these cells, but the contributions of individual mutations are not clear without investigating the mechanisms further. The role(s) of *NFATC2* may also be distinct in each, depending on the cellular context.

Evaluation of *NFATC2* KD in non-MLLr cell lines was essential to investigate this further. HL-60 cells carry a number of oncogenic properties, including amplified *MYC*, *TP53*^{del} and *NRAS*^{mut}. Unlike other cell lines, a marked increase in apoptosis was observed in HL-60 cells after *NFATC2* KD. *NPM1*^{mut} *DNMT3a*^{mut} *NRAS*^{mut} OCI-AML3 cells also became more apoptotic after *NFATC2* KD, which was surprising as *NFATC2* was barely detectable. This would require validation of KD with a more sensitive technique (or a higher quantity of cDNA), but if a true result then this suggests that *NFATC2* can maintain the function of AML cells even at low levels.

Finally, Kasumi-1 (which expresses an AML1-ETO fusion and *TP53*^{mut}) was the only cell line to exhibit statistically significant reduction of S-phase cells, indicating G1/S arrest after *NFATC2* KD. Apoptosis was not observed to change substantially either.

A summary of the observed phenotypes is shown in Table 4-2. THP-1 cells were the only cell line to show signs of G2/M arrest after *NFATC2* KD. Most of the observed phenotypes demonstrated only trends towards increased apoptosis or cell cycle arrest, few were statistically significant. Further exploration of the cell cycle and apoptosis regulators identified in these pathways is required to make further conclusions on the mechanism of *NFATC2*-driven oncogenesis.

Cells	Key Mutations	Colony Formation Capacity	Phenotype Summary	
			Cell Cycle	Apoptosis
THP-1	MLL-AF9; $NRAS^{mut}$; $TP53^{mut}$	Reduced**	G2/M arrest	Increased (-143 only)
MOLM-13	$FLT3^{ITD}$ (heterozygous); MLL-AF9	Reduced	Unchanged	Increased (-146 only)
NOMO-1	MLL-AF9; $TP53^{mut}$; $KRAS^{mut}$	N/A	Unchanged	Unchanged
MLL-AF9 Murine BM	MLL-AF9	Reduced*	G1/S arrest (-356 only)	Increased (-356 only)
MV4-11	$FLT3^{ITD}$ (homozygous); MLL-AF4	Reduced**	G1/S arrest	Unchanged
HL-60	Amplified MYC and NRAS; $TP53^{del}$; $NRAS^{mut}$	Reduced**	G1/S arrest	Increased
OCI-AML3	$NPM1^{mut}$; $DNMT3a^{mut}$; $NRAS^{mut}$	Reduced	Unchanged	Increased
Kasumi-1	AML1-ETO; $TP53^{mut}$	N/A	G1/S arrest**	Unchanged

Table 4-2. Summary of observed phenotypes in AML cell lines after *NFATC2* KD.
Shown are the key mutations discussed in each cell line and a summary statement for changes observed in each of: colony-forming assays, cell cycle assays and apoptosis assays. ** if $p<0.05$ for any pairwise statistical t-test between the scrambled control and both of two sh*NFATC2* constructs; * if $p<0.05$ for 1 of 2 constructs.

5 Results (III) Sequencing-based approaches to determine the activity and function of *NFATC2* in AML

5.1 Introduction

To characterise better the transcriptomic effects of *NFATC2* KD, RNA-Seq was undertaken using THP-1 cells with *NFATC2* KD. RNA-Seq is an established method of quantifying global transcriptomic changes with greater coverage than a microarray and using mRNA enrichment. Short-read sequencing is highly established using Illumina platforms, for example, although some biases can be introduced when aligning short reads to human transcripts (Wang *et al.*, 2009b, Stark *et al.*, 2019). While single cell RNA-Seq methods have often superseded bulk sequencing in the pursuit of rare cell populations and surveying cell-cell heterogeneity, the application of bulk methods seems most appropriate in the context of a homogenous cell line.

Reconstructing putative gene networks from transcriptomic data is a multi-dimensional process with various methods available. These may include correlation or Bayesian-based approaches, gene clustering and topology-based approaches to determine gene-gene relationships (Wang and Huang, 2014). TF binding data from ChIP-Seq can also provide direct genomic binding sites and be integrated with RNA-Seq. Integration of RNA-Seq and ChIP-Seq data can provide some insight into TF dynamics, however improvement on the available tools is required to enhance the quality of statistical inference possible from these data (Angelini and Costa, 2014).

ChIP-Seq for NFATc2 has been performed in murine dendritic cells, where it was thought to regulate anti-microbial responses. ChIP-Seq identified a number of direct cytokine binding targets and also that NFATc2 bound at sites with reduced H3K4me3, suggesting an epigenetic interaction (Yu *et al.*, 2014). In this study, ChIP-Seq was used in THP-1 cells to identify novel NFATc2 binding sites which are relevant to AML pathology. Analysis of ChIP-Seq binding sites may also shed light on NFATc2 DNA binding motifs in THP-1 cells: in other cell types the 'GGAA(A)' NFAT motif has been well-described (Badran *et al.*, 2002).

Key genes which were identified by combined analyses of RNA-Seq and ChIP-Seq data, which were investigated further in other cell line models of AML. Finally,

open-source patient data was revisited to determine if the putative targets of *NFATC2* or NFATc2 protein would have an impact on survival outcomes, as was shown for the expression of *NFATC2* itself in the TARGET-AML dataset.

5.2 Chapter objectives

1. Determine gene expression regulation by *NFATC2* in THP-1 cells using RNA-Seq analysis of *NFATC2* KD and m*Nfatc2*/h*NFATC2* overexpression cells.
2. Examine if putative regulated genes are also deregulated in AML cells of differing (cyto)genetic backgrounds after *NFATC2* KD.
3. Determine genomic binding loci of NFATc2 protein in THP-1 cells and elucidate any consensus binding sequence(s) using ChIP-Seq.
4. Integrate ChIP-Seq and RNA-Seq data to identify genes most likely to be regulated by NFATc2, either directly or indirectly, in THP-1 cells.
5. Use functional analyses of targets identified by sequencing approaches to hypothesise regulatory function(s) for *NFATC2* in THP-1 and/or other AML cell lines.
6. Examine the expression of genes identified in objective 4, in open-source patient data, to determine if they have any relationship with patient outcomes.

5.3 Results

5.3.1 *NFATC2* KD leads to global transcriptomic changes in THP-1

5.3.1.1 Gene expression changes were not concordant between experimental replicates

THP-1 cells were transduced with either a scrambled control or either of 2 sh*NFATC2* constructs and then selected for transgene expression using puromycin at 24 hr post-transduction, as described previously. RNA was harvested from these cells 24 hr post-puromycin treatment, confirming selection, and cDNA libraries constructed for sequencing. This timepoint was selected to measure the earliest targets of *NFATC2* KD, while preserving maximum number of live cells to maintain RNA quality. Raw RNA-Seq data were subject to QC steps which are summarised in (2.2.13) and some of these data are given in the Appendices (Section 9.2).

All genes with a mean expression level of FPKM≥1.0 were identified in the data and classed as being 'expressed' in those cells. 9344 genes were commonly expressed between all 3 conditions (Figure 5-1), which is 92.0% of all genes expressed across conditions.

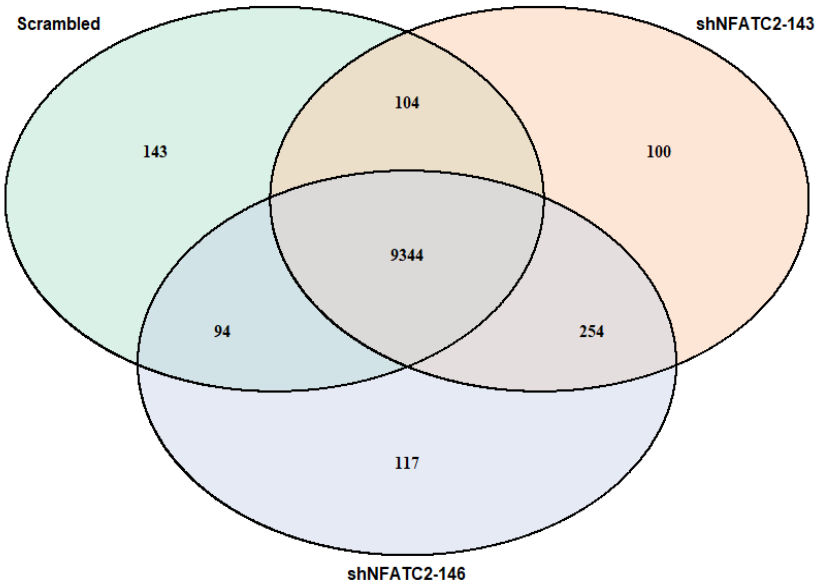

Figure 5-1. The majority of expressed genes were common to all conditions.
Mean FPKM ≥1.0 values were filtered from the total data per condition and the remaining 'expressed' Ensembl gene IDs were overlapped between conditions. Here they are shown as a Venn diagram. The number of Ensembl IDs overlapping between each set of conditions is shown on the diagram (n=3 per condition).

Principal component analysis (PCA) of the FPKM expression (if FPKM ≠ 0) values did not show distinct grouping of experimental conditions across all 3 replicates (Figure 5-2). Data for replicates 2 and 3 were spatially adjacent within each condition, but not well separated between conditions, indicating similarity of variance between their expression profiles. The data for replicate 1 were more distinct and did not cluster with replicates 2-3. These results indicate more similarity in gene expression across replicates 2-3, but not replicate 1. Additionally, 2 components accounted for 86.3% of variation in the data.

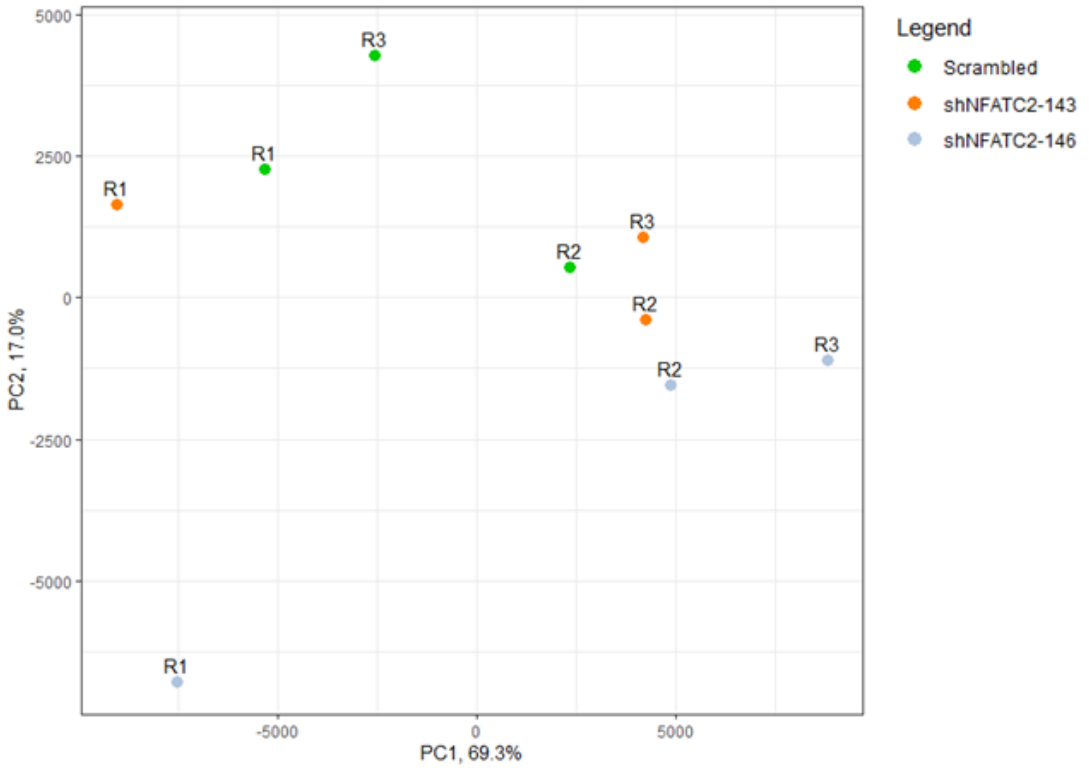

Figure 5-2. RNA-Seq experimental conditions can be grouped by principal components from replicates 2-3, but not replicate 1. PCA plot in 2D shows the spatial distribution of principal components PC1 and PC2 (± PC3) generated from RNA-Seq FPKM values, excluding FPKM values of 0 (n=15,634). Samples are coloured by experimental condition (see legend) and replicate number indicated per data point. The axes show the principal component plotted and the % of variance explained by this component.

5.3.1.2 *NFATC2* KD in THP-1 resulted in the statistically significant deregulation of several genes

Differential expression analysis between either sh*NFATC2* construct condition and the scrambled control (24 hr post-selection) was carried out using DESeq2, which utilises unfiltered read counts from the whole dataset.

Initial examination of the data show that *NFATC2* was significantly downregulated by either sh*NFATC2* construct, while neither *NFATC1* or *NFATC3* were affected, as expected (Figure 5-3). *KDM4A* and *PAF1*, which are putatively upstream of *NFATC2*, were not deregulated after *NFATC2* KD.

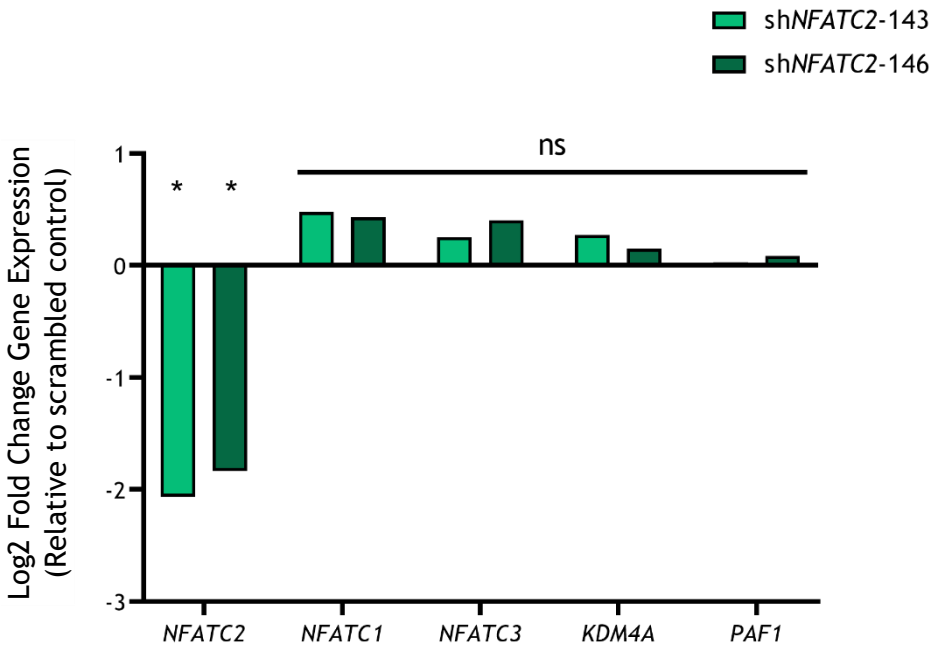

Figure 5-3. *NFATC2* was downregulated after transduction of both sh*NFATC2* constructs, but not *NFATc1* or *NFATc3*. Log_2 fold changes between the scrambled control and either of sh*NFATC2*-143 or sh*NFATC2*-146 were taken from the results of DESeq2 analysis (n=3 biological replicates). Shown are selected genes relating to the *NFAT* family and the *KDM4A-PAF1-NFATC2* axis. Adjusted *p* values, for a difference in mean expression, were taken from the DESeq2 analysis, where *<0.05 and 'ns' = not significant.

Volcano plots (Figure 5-4) show a wide distribution of log_2fold changes and $-log_{10}$ adjusted p values/FDR (denoted padj) for expression changes between the scrambled control and constructs -143 or -146. Statistically significant genes were classed as those with both padj of <1.0 ($-log_{10}$padj >1.0) and log_2 fold changes of either ≥1.0 or ≤-1.0, representing a doubling or halving. KD with construct -143 resulted in 43 upregulated and 87 downregulated genes which met this threshold, while KD with construct -146 led to 41 upregulated and 32 downregulated genes.

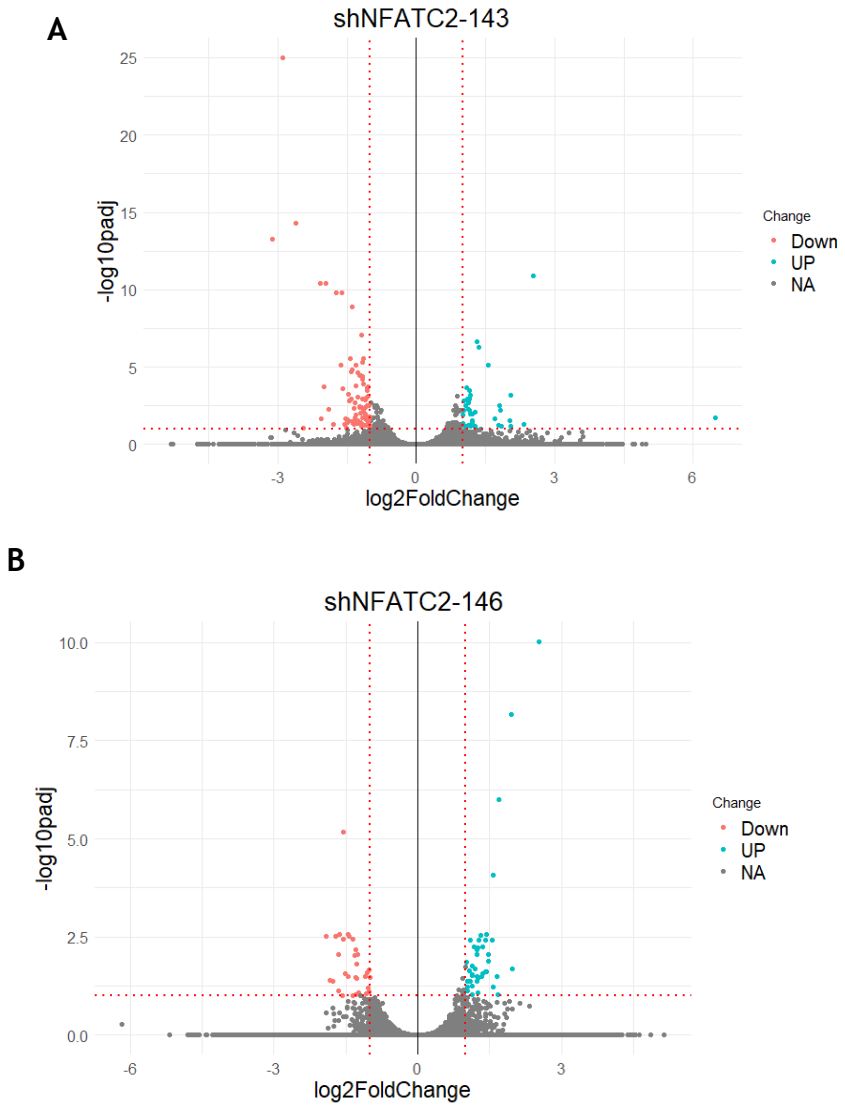

Figure 5-4. *NFATC2* KD in THP-1 resulted in the statistically significant deregulation of several genes. Volcano plots show the log_2 fold changes in expression, as compared to the scrambled control as calculated by DESeq2, for each shRNA construct: -143 (**A**) and -146 (**B**). On the y-axis are the $-log_{10}$ adjusted *p*-values (-log10padj) for each fold change. Horizontal red dotted line highlight thresholds for adjusted *p* values <0.1 ($-log_{10}$ adjusted p values >1.0) and vertical dotted lines the log_2 fold changes ≥1.0 (up-regulated) or ≤-1.0 (downregulated). Data at extremes of these thresholds are coloured either red for downregulated genes, or blue for upregulated genes. 23,828 and 23,854 genes were included for the comparison with construct -143 or -146, respectively.

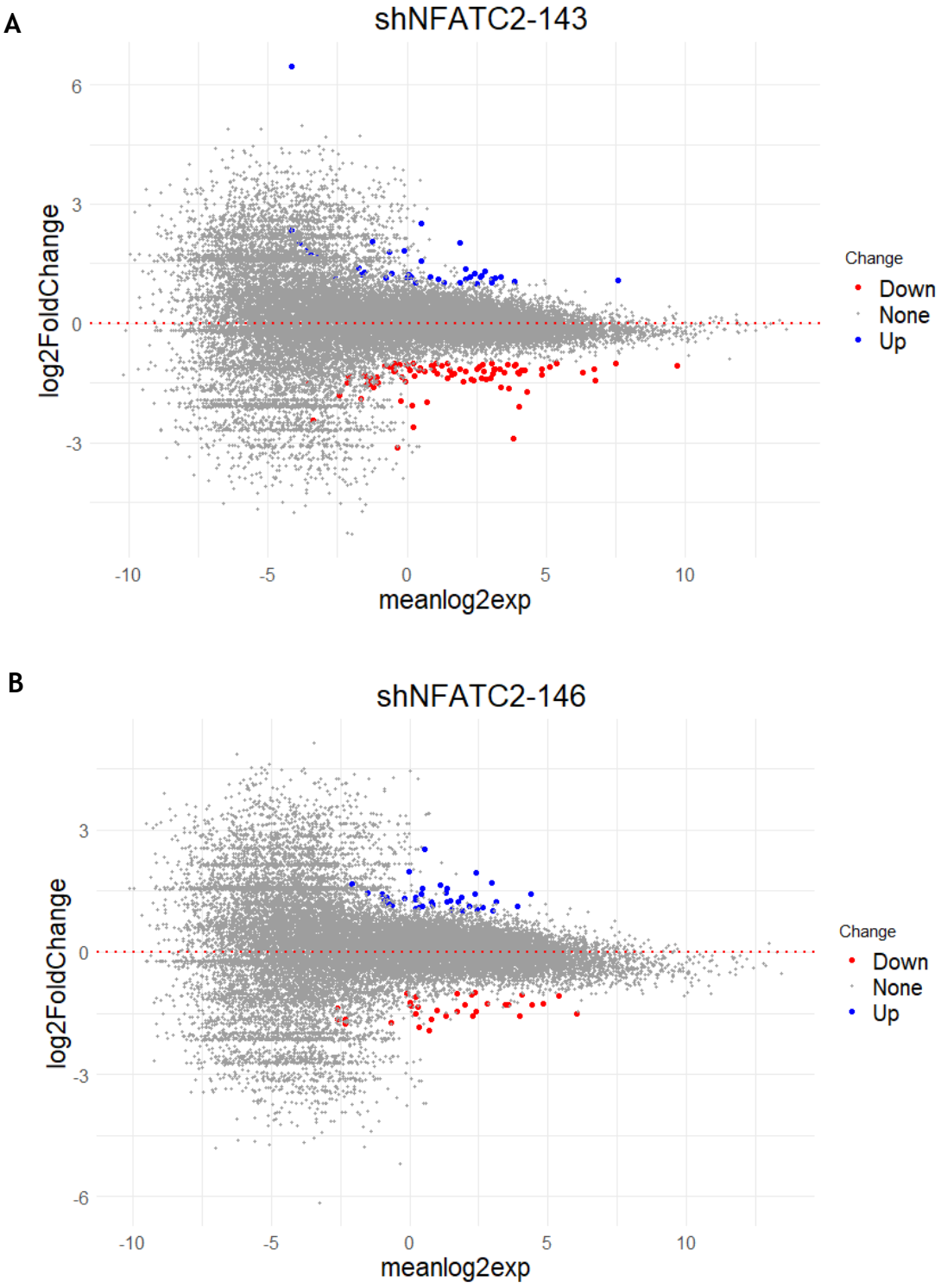

Figure 5-5. Genes significantly deregulated by *NFATC2* KD in THP-1 had a range of expression levels across the samples. Scatterplots showing the mean $\log_2$ expression (meanlog2exp) of each gene across conditions (per pairwise comparison), as FPKM, plotted against the $\log_2$ Fold Change between the pair of conditions. Comparisons shown are the scrambled control vs. either (**A**) construct -143 or (**B**) -146. Highlighted are changes deemed as significant by an adjusted *p* value of <0.1 and a $\log_2$ Fold Change of either ≤-1.0 (down regulated in red) or ≥1.0 (upregulated in blue). Red dotted line demarcates a $\log_2$ fold change of 0.

Distribution plots (Figure 5-5) show that in both comparisons (scrambled control vs. either construct -143 or -146), genes with a mean log_2FPKM<0 (FPKM<1.0) tended to show a larger magnitude of log_2 fold changes between conditions. A majority of changes determined as significant were in genes with expression values above above log_2 0. This indicates that changes observed are more likely to be meaningful and less likely to be the result of background noise.

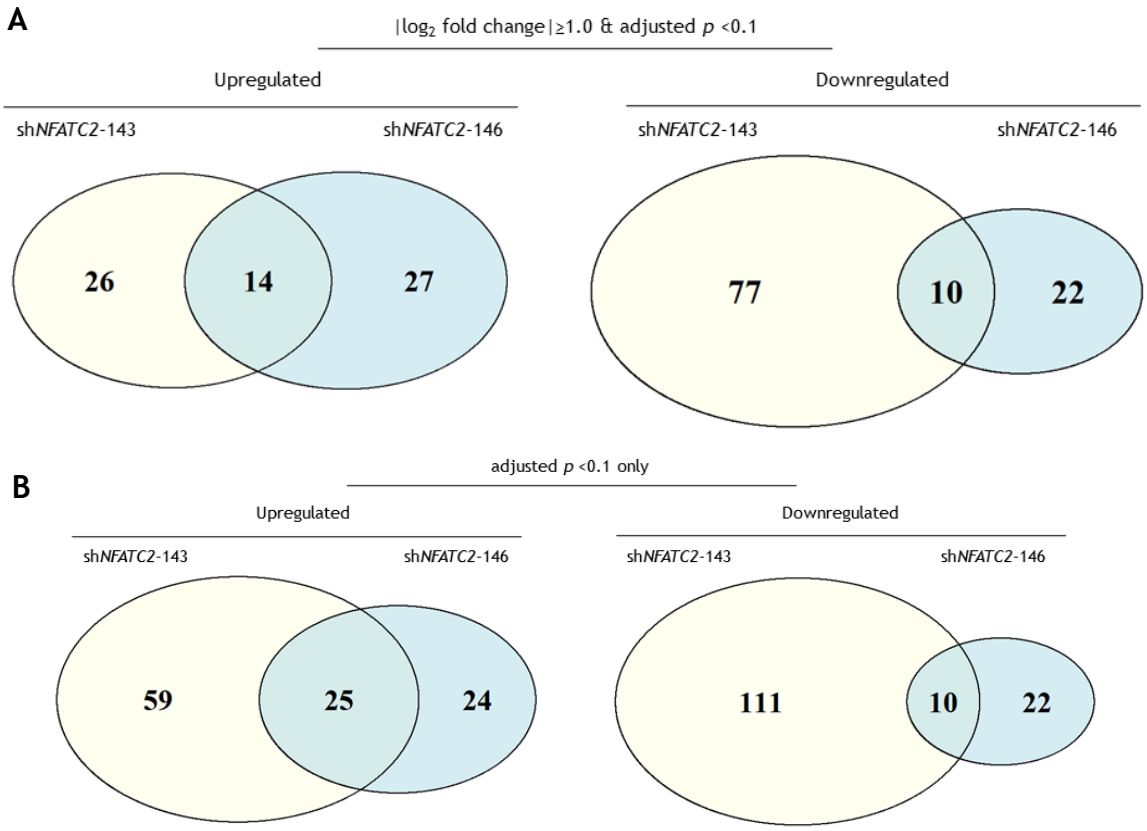

Figure 5-6. More genes were downregulated by sh*NFATC2*-143 than sh*NFATC2*-146 in THP-1 cells. The Venn diagrams show overlaps between differentially expressed genes between the scrambled control and either construct -143 (in yellow on the left) or -146 (in blue on the right). Two different thresholds for significance were applied. **A:** Genes with log_2 fold change either ≤-1.0 or ≥1.0 and adjusted *p* <0.1. **B**: Genes with adjusted *p* <0.1 only were examined in order to include a larger number of genes as 'significant'.

The identified deregulated genes between KD by constructs -143 or -146 and the control were overlapped, using defined significance thresholds (Figure 5-6A). In total 14 and 10 genes were upregulated and downregulated, respectively, in common to both constructs. Transduction of sh*NFATC2*-146 led to deregulation of 49 unique genes in either direction, compared to 103 with sh*NFATC2*-143.

A lower threshold was then applied to define more genes as significant for downstream analyses; only a cut-off of adjusted p<0.1 was applied (Figure 5-6B). Using this threshold log_2 fold changes of upregulated genes ranged from 0.65 to 6.47 for construct -143, and 0.82 to 2.53 for construct 146. Log_2 fold changes of downregulated genes ranged from -3.11 to -0.62, and -1.92 to -1.00, for constructs -143 and -146, respectively. From these observations, the magnitude of changes was of a larger range after KD using construct -143, compared to construct -146.

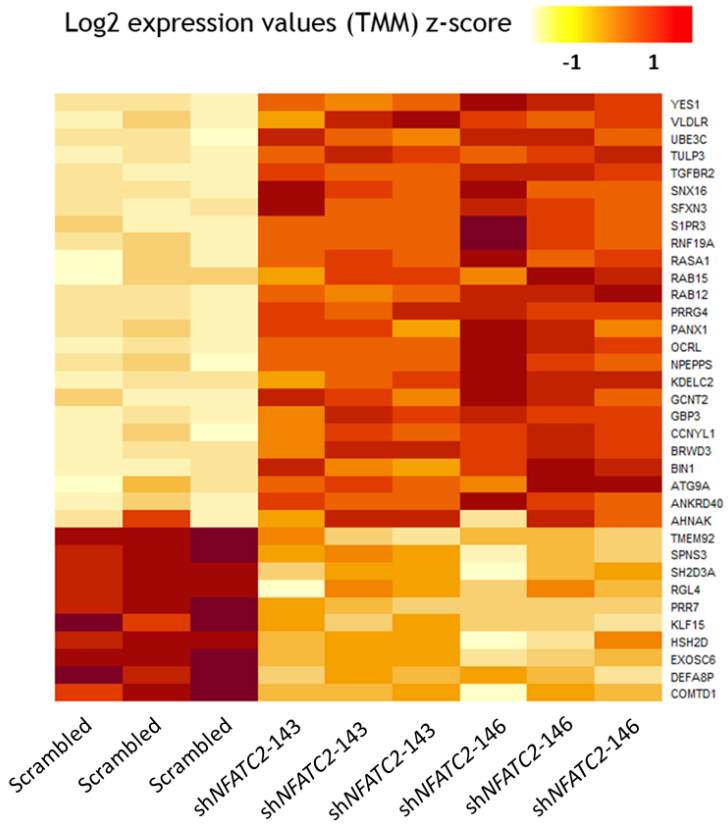

Figure 5-7. Thirty-five genes were significantly deregulated after *NFATC2* KD in THP-1. Heatmap showing the 35 genes (25 upregulated; 10 downregulated) which were deregulated by both constructs -143 and -146, compared to the scrambled control, in THP-1. This is using the less stringent threshold of adjusted p<0.1. Shown are the log_2 TMM expression values, normalised as a Z-score, per condition and gene. The gene names are identified on the right-hand side.

The significance threshold of adjusted p<0.1, without limits on the log_2 fold change of expression, was used to select out genes for subsequent validation. Those changes which met this threshold following KD with both constructs, as highlighted in Figure 5-6B are shown as a heatmap in Figure 5-7. Twenty-five genes were upregulated and 10 genes were downregulated, common to both shRNA constructs.

5.3.1.3 *NFATC2* KD led to deregulation of cytoskeleton regulation, and targets of *MYC* and *STK33*

Gene Symbol	Chromosome	Protein type/function summary	Adjusted p value	
			-143	-146
YES1	18	Non-receptor tyrosine kinase	5.42x1s0^{-7}	6.80x10^{-9}
VLDLR	9	Lipoprotein receptor and transporter	0.043	0.036
UBE3C	7	Ubiquitin protein ligase	0.003	0.017
TULP3	12	Negative regulator of Shh signalling	1.22x10^{-11}	9.41x10^{-11}
TGFBR2	3	Transmembrane serine/threonine kinase	0.006	0.014
SNX16	8	Intracellular trafficking	7.56x10^{-6}	0.004
SFXN3	10	Putative iron transporter	0.006	0.018
S1PR3	9	Lysosphingolipid receptor	0.011	0.041
RNF19A	8	Ubiquitin protein ligase	0.007	0.032
RASA1	5	Inhibitory regulator of Ras-cAMP pathway	0.012	0.044
RAB15	14	RAS oncogene family	0.071	0.036
RAB12	18	Intracellular membrane trafficking	0.001	8.22x10^{-5}
PRRG4	11	-	0.003	0.071
PANX1	11	Calcium channel	0.084	0.074
OCRL	X	Lysosomal membrane trafficking	2.20x10^{-7}	9.83x10^{-7}
NPEPPS	17	Proteolysis: cell growth and activity	0.076	0.093
KDELC2	3	-	0.078	0.004
GCNT2	6	Enzyme for branching aminoglycans	0.011	0.009
GBP3	1	Antiviral responses	0.006	0.004
CCNYL1	2	Cyclin family	0.006	0.007
BRWD3	X	Cell morphology and cytoskeleton organisation	0.006	0.006
BIN1	2	Endocytosis and (putative) tumour suppressor	0.057	0.003
ATG9A	2	Autophagy and vacuole transport	0.010	0.024
ANKRD40	17	-	2.00x10^{-4}	0.009
AHNAK	11	(Putative) differentiation	0.006	0.020

Table 5-1. Genes upregulated after *NFATC2* KD in THP-1 cells have a range of cellular functions. The table lists each of the genes upregulated by *NFATC2* with both constructs -143 and -146, adjusted p<0.1. The chromosome location is given for each. A summary statement of the known function of each gene-associated protein is shown, as given by the STRING database. '-' if no function is given here. The adjusted p value for the change in each by either construct sh*NFATC2*-143 or sh*NFATC2*-146 is also given.

Gene Symbol	Chromosome	Gene Function	Adjusted *p* value	
			-143	-146
TMEM92	17	-	0.002	0.004
SPNS3	17	Sphingolipid transport	0.019	0.003
SH2D3A	19	(Putative) JNK activation	0.019	0.075
RGL4	22	-	0.052	0.044
PRR7	5	Messenger and interacts with JUN	8.42×10^{-4}	0.003
KLF15	3	Transcriptional regulator	0.037	0.003
HSH2D	19	(Putative) regulator of apoptosis	0.001	0.028
EXOSC6	16	RNA processing and degradation	5.76×10^{-5}	6.57×10^{-6}
DEFA8P	8	*Pseudogene: no protein*	0.004	0.035
COMTD1	10	-	0.004	0.091

Table 5-2. Genes downregulated after *NFATC2* KD in THP-1 have a range of cellular functions. The table lists each of the genes downregulated by *NFATC2* with both constructs -143 and -146, adjusted $p<0.1$. '-' if no function is given or 'pseudogene' is stated if no known protein is transcribed from the gene.

To derive functional meaning from the deregulated genes identified after *NFATC2* KD a number of databases and pathway-based analyses were used. The chromosomal location and function of each gene was examined using the STRING database and are listed in Tables 5-1 and 5-2 for upregulated and downregulated genes, respectively.

Furthermore, RNA-Seq data were obtained from THP-1 with *KDM4A* KD in a previous study (data generated by Dr. Matthew Massett). In this latter study, *KDM4A* was knocked down using 2 shRNA constructs. The genes deregulated by *NFATC2* KD were compared to the $\log_2$ fold changes and significance values in the *KDM4A* KD dataset; these results are shown in the Appendices, (Section 9.4, Table A-4). Of the 35 *NFATC2*-deregulated genes, 13 were also deregulated by *KDM4A* with statistical significance (FDR<0.1) and in the same direction of change as for *NFATC2* KD. More specifically, this was 12 upregulated and 1 downregulate gene(s). These 13 genes could be targets of the *KDM4A-NFATC2* axis, and therefore contribute to the mechanism of *KDM4A* oncogenic activity.

The STRING database was also used to evaluate known protein-protein interactions in these 35 deregulated genes. This tool provides a score which estimates the probability of any predicted interaction having occurred between any random pair of proteins. Three pairs of interactions were found, shown in Figure 5-8, between *VLDLR*/*BIN1*, *YES1*/*RASA1* and *TULP3*/*OCRL*. The first pair is described together in a number of abstracts relating to Alzheimer's Disease pathobiology. The *YES1*/*RASA1* pair is described together in a number of cellular pathways in humans. Since this score is >0.7 it would be considered as a high confidence interaction (von Mering *et al.*, 2005). Thirdly, the *TULP3*/*OCRL* pair is described in phosphatidylinositol metabolism in humans. The overall enrichment *p* value is 0.442, indicating that there were not any more protein-protein interactions in this group of 34 proteins than would be expected.

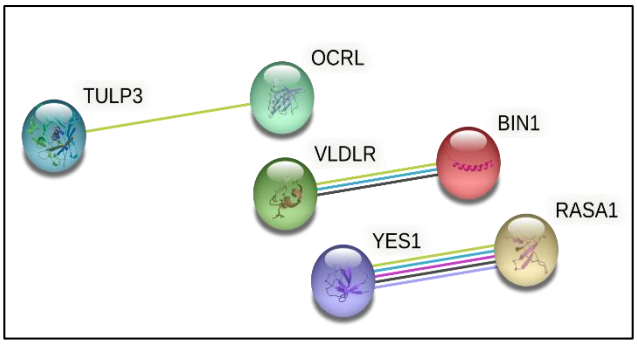

Interaction	STRING: Combined score
VLDLR – BIN1	0.643
YES1 – RASA1	0.931
TULP3-OCRL	0.428

Figure 5-8. Of the genes deregulated by *NFATC2* KD in THP-1, 3 pairs of protein interactions are known to exist in humans. Thirty four of the 35 genes described previously were entered into the STRING database (*DEFA8P*, a pseudogene, was excluded). Known protein-protein interactions, as described in the literature and from co-expression/biochemical data, are shown visually. The coloured lines represent the differing types of source from which known interactions are described. Below the diagram the STRING combined score is given, which estimates the probability of a true pairwise association.

Functional annotation of genes deregulated by *NFATC2* (Figure 5-9) showed that genes annotated as 'Membrane' were enriched in the upregulated gene set, relative to the background; (64.0% vs. 31.9%, respectively). Only 20.0% of downregulated genes were annotated as 'Membrane'. While 9.5% of background genes were annotated with 'Transport', 28.0% of those upregulated had this annotation. Downregulated genes were similar to the background, with 10.0% having the 'Transport' annotation.

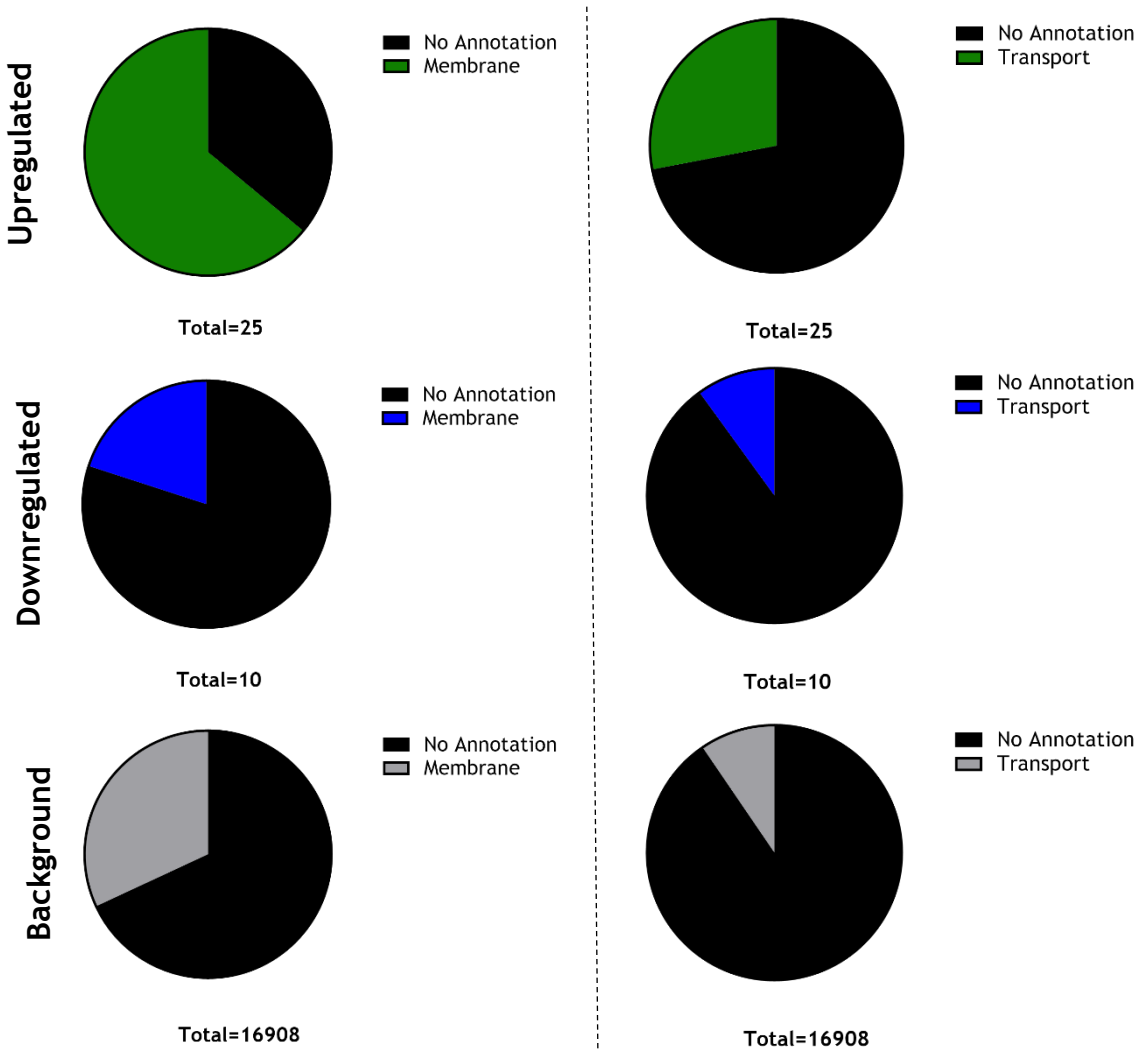

Figure 5-9. Genes encoding membrane and/or transport proteins are over-represented in those upregulated after *NFATC2* KD. Annotations associated with each gene were obtained from the DAVID Bioinformatics Resources website, using the functional annotation tool. Genes with 'membrane' or 'transport' as an annotation were quantified. Shown are groups for upregulated genes and downregulated genes with adjusted $p<0.1$ (green and blue, respectively) and recognised gene IDs from the whole dataset as background (grey). The total number of genes included in each chart is shown.

Pathway analysis of the top 35 significant genes using either the Reactome platform or the PANTHER database did not highlight any pathways which were significantly enriched (FDR<0.1). SPIA was used as an alternative pathway analysis tool, which considers the log_2fold change of individual genes and incorporates topological features. The top 1000 differential genes per sh*NFATC2* construct, as ordered by adjust *p* values, were used as an input to provide greater power. Of the top 1000, 91 and 71 gene IDs could not be mapped to a gene symbol for the analyses of constructs -143 and -146, respectively. Of those remaining, 314 gene IDs were common to both constructs.

Three pathways were found to be significantly deregulated using both of construct -143 or -146 using the SPIA platform, of which 2 pathways were discounted due to a distinct lack of biological relevance to haemopoietic cells. The most significant result for both constructs was 'Regulation of the actin cytoskeleton' (Figure 5-10A). This pathway included 18 and 17 deregulated genes per construct -143 and -146, respectively (Figure 5-10B), of which 9 overlapped between the constructs. The diagram in Figure 5-11 shows the pathway described (diagram from the KEGG database) and the relationship of these deregulated genes to one another. Indicated are the genes deregulated by *NFATC2*. The group of integrin genes (labelled '*ITG*') contained a number of affected genes, while numerous downstream elements of the pathway were also affected.

A

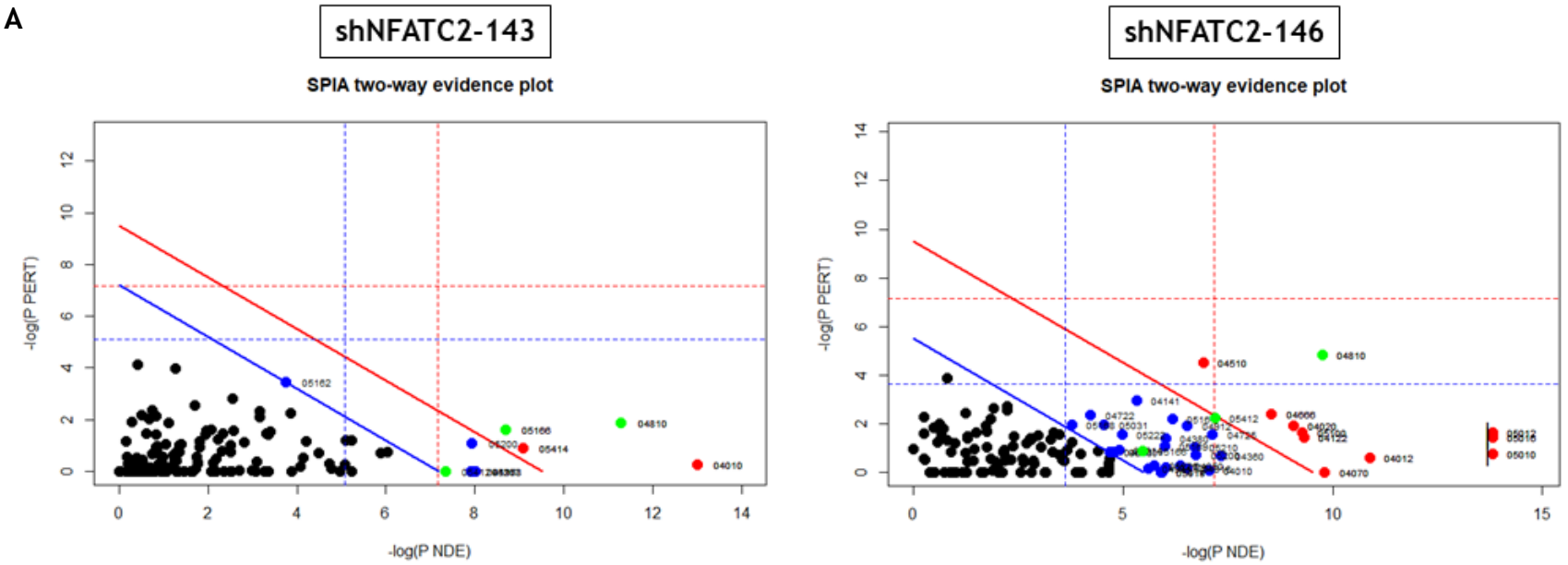

B

Name	Pathway size	KD Construct	NDE	tA	pGFDR	pGFWER	Status
Regulation of actin cytoskeleton	213	143	18	12.91	0.0018	0.0035	Activated
		146	17	25.65	0.0002	0.0009	Activated

Figure 5-10. Cytoskeleton pathway genes were enriched in THP-1 cells with *NFATC2* KD, as found using the SPIA platform.
The top 1000 significant differential genes (adjusted p <0.1) input for SPIA, for each of the *shNFATC2* constructs. **A:** Individual pathways per data point are shown. The data are the significance value for 'over-representation' (-log(P NDE)) and 'perturbation' (-log(P PERT)). Oblique lines represent a combined p value threshold set at 5%, either with FDR correction (blue line) or Bonferroni correction, to become a FWER value (red line). Data which are above any threshold are coloured. Pathways identified as significant by either threshold for both constructs are highlighted green. **B:** The most significant pathway for both sh*NFATC2* constructs are shown with the pathway size, the differential genes over-represented (NDE), the accumulated 'perturbation' of the pathway (tA), and significance values for FDR and FWER, enumerated. The pathway direction of change is shown under 'Status'.

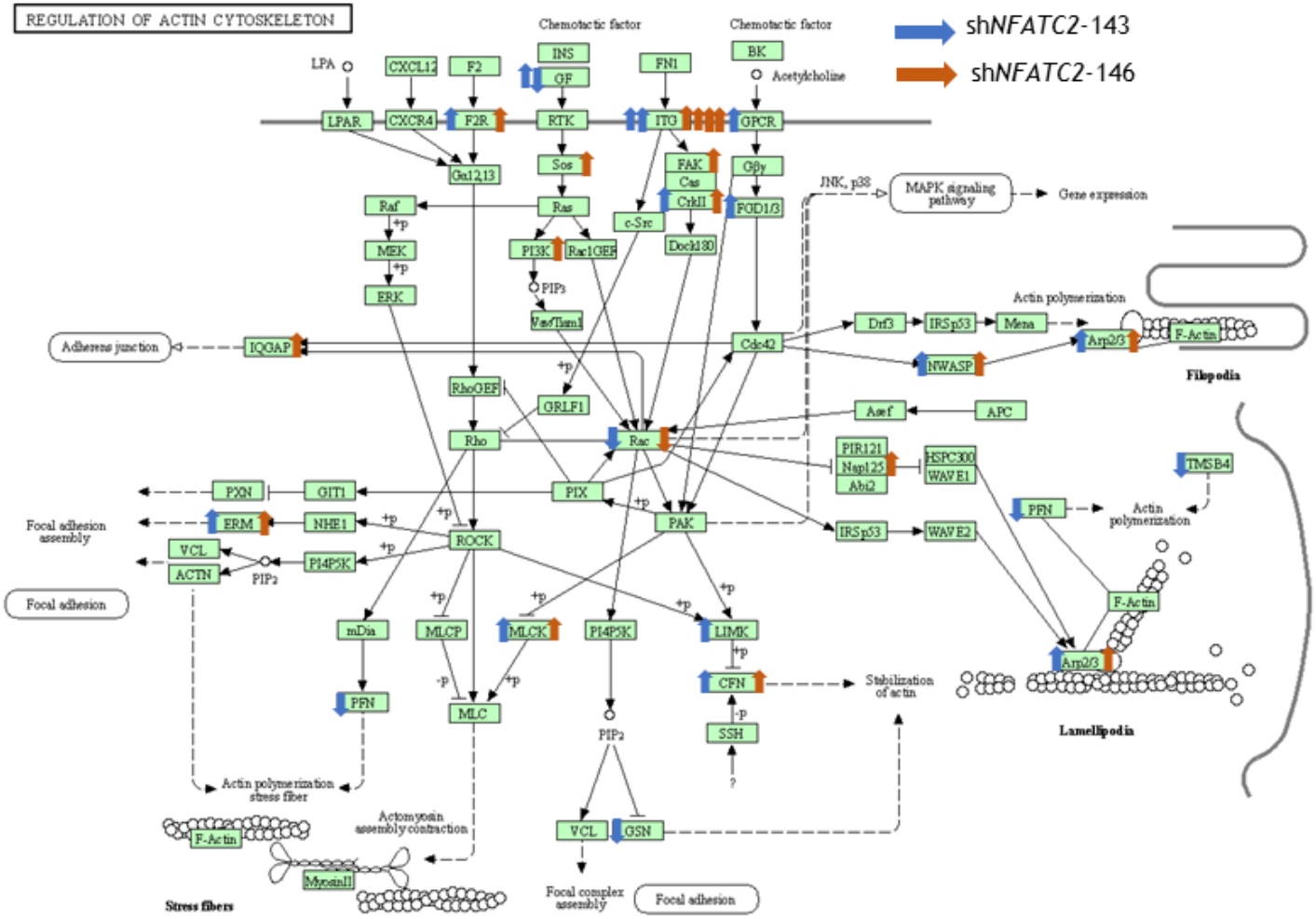

Figure 5-11. The 'regulation of actin cytoskeleton' KEGG pathway was perturbed at multiple levels following *NFATC2* KD in THP-1 cells.
This plot details the 'Regulation of actin cytoskeleton' pathway as described in the SPIA platform. Each green box labels a group of related genes, rather than individual genes. The arrows indicate whether a gene within each group was up- or downregulated in the sh*NFATC2* condition, per construct -143 and -146, relative to the scrambled control (in the top 1000 genes with adjusted p<0.1). Each arrow represents one gene within the group.

Next, GSEA was used as a means of finding functionally relevant patterns of change across the whole RNA-Seq dataset.

Group	Direction of differential enrichment	Pathway	sh*NFATC2*-143		sh*NFATC2*-146	
			NES	FWER *p* value	NES	FWER *p* value
C2: curated	Scrambled	REACTOME_EUKARYOTIC_TRANSLATION_ELONGATION	-2.59	<0.001	-3.12	<0.001
C2: curated	Scrambled	KEGG_RIBOSOME	-2.57	<0.001	-3.07	<0.001
C2: curated	Scrambled	REACTOME_TRANSLATION	-2.54	<0.001	-3.02	<0.001
C5: ontology	Scrambled	GO_STRUCTURAL_CONSTITUENT_OF_RIBOSOME	-2.89	<0.001	-3.28	<0.001
C5: ontology	Scrambled	GO_RIBOSOMAL_SUBUNIT	-2.81	<0.001	-3.27	<0.001
C6: oncogenic	Scrambled	MYC_UP.V1_UP	-2.15	<0.001	-2.19	<0.001
C6: oncogenic	Scrambled	STK33_DN	-2.03	0.001	-1.80	0.037
C6: oncogenic	sh*NFATC2*	STK33_UP	2.91	<0.001	3.22	<0.001

Table 5-3. Oncogenic pathways containing targets of *MYC* and *STK33* were enriched in the deregulated genes resulting from *NFATC2* KD.
GSEA applied to normalised read counts (filtered for read counts >10; 14, 238 genes) from the scrambled control and either of construct -143 or -146 was used to identify MSigDB pathways enriched in the data. Shown are the group in which each pathway was identified, as classified by MSigDB, the direction of differential enrichment (whether the enrichment was found when comparing in the direction of scrambled vs. sh*NFATC2* or sh*NFATC2* vs. scrambled) and the pathway name. Shown are the NES, detailing the magnitude of change and the FWER *p* value. Only pathways which were enriched for both constructs sh*NFATC2*-143 and -146 were included, providing FWER $p<0.1$.

Group	Direction of change	Pathway	shNFATC2-143		shNFATC2-146	
			NES	FWER p value	NES	FWER p value
Hallmark	Scrambled	HALLMARK_MYC_TARGETS_V1	2.69	<0.001	2.68	<0.001
Hallmark	Scrambled	HALLMARK_MYC_TARGETS_V2	2.17	<0.001	2.13	0.001
Hallmark	Scrambled	HALLMARK_OXIDATIVE_PHOSPHORYLATION	2.11	0.002	2.49	<0.001
Hallmark	Scrambled	HALLMARK_DNA_REPAIR	1.67	0.065	1.94	0.005
Hallmark	Scrambled	HALLMARK_INFLAMMATORY_RESPONSE	-2.03	<0.001	-2.49	<0.001
Hallmark	Scrambled	HALLMARK_IL6_JAK_STAT3_SIGNALING	-1.77	0.015	-2.31	<0.001

Table 5-4. Genes involved in the regulation of DNA repair and the inflammatory response are deregulated after *NFATC2* KD in THP-1.
GSEA results from MSigDB Hallmark group pathways are shown as for other pathway groups in Table 5-3.

GSEA was performed using normalised read counts, excluding values <10 to increase statistical power. The analyses collapsed Ensembl gene IDs which overlapped and so 13,518 or 13,563 gene IDs were used in the analysis of sh*NFATC2*-143 or sh*NFATC2*-146 KD, respectively.

GSEA identified a considerable number of pathways enriched in the data with FWER<0.1 and in both constructs. Selected pathways included those relating to ribosomal function, translation or targets of STK33 (Tables 5-3 and 5-4). In addition to pathways shown, GSEA also found STK33_NOMO_DN and STK33_SKM_DN were downregulated with *NFATC2* KD, while STK33_NOMO_UP and STK33_SKM_UP were upregulated with both sh*NFATC2* treatment conditions. This shows that targets of *NFATC2* were deregulated in the same direction as the changes in these STK33 datasets.

Analyses of MSigDB Oncogenic and Hallmark pathways identified multiple pathways containing targets of *MYC* to be downregulated after *NFATC2* KD (Tables 5-3 and 5-4). Other Hallmark pathways identified were involved in DNA repair, targets of E2F and the G2-M cell cycle checkpoint, however the latter two pathways were only found to be statistically significant (FWER<0.1) in samples treated with 1 of 2 shRNA constructs.

GSEA enrichment plots for individual analyses are shown for pathways relating to *MYC* and *STK33* (Figure 5-12), which illustrate the findings described above.

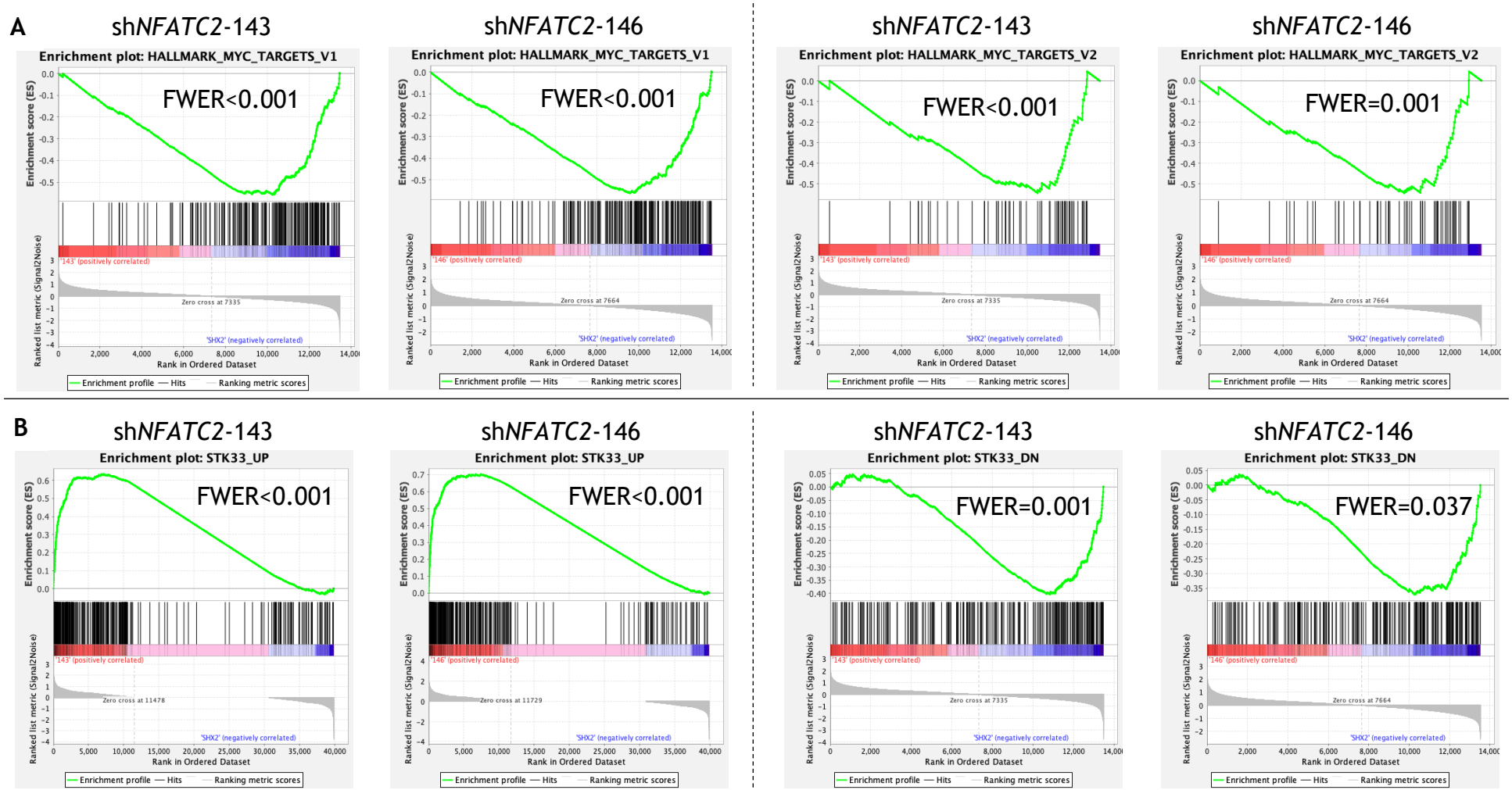

Figure 5-12. GSEA showed that targets of *MYC* and *STK33* were downregulated after *NFATC2* KD in THP-1 cells.
Shown are individual GSEA plots for selected pathways identified to be statistically significant (FWER<0.1), using the gene set derived from THP-1 with *NFATC2* KD. Each plot is for the differential gene expression between the scrambled control and either sh*NFATC2*-143 (left) or sh*NFATC2*-146 (right), as shown. **A:** pathways involving targets of *MYC*. **B:** pathways involving targets of *STK33*. FWER *p* values are shown on each.

5.3.2 Validation of RNA-Seq data

5.3.2.1 Multiplexed qRT-PCR-based validation of significant genes

The Fluidigm BioMark™ system was used to validate genes putatively deregulated by *NFATC2* KD in MLL-AF9 AML. These were tested in: an independent culture of THP-1 with *NFATC2* KD; MOLM-13 with *NFATC2* KD; THP-1 overexpressing m*Nfatc2*, h*NFATC2* or an empty vector; MOLM-13 overexpressing m*Nfatc2*, h*NFATC2* or an empty vector; or THP-1 either overexpressing m*Nfatc2* or an empty vector, both with KD of h*NFATC2*. A later timepoint of 48 hr post-selection was selected to determine if gene deregulation was maintained longer than 24hr, or to determine if some genes became more dysregulated than at 24 hr.

The selected 35-gene list was expanded to include genes which were deregulated after transduction with only 1 of 2 sh*NFATC2* constructs at 24 hr post-selection. This was to account for potential differences in the degree of specific genes' deregulation by the 2 shRNA constructs at 24 hr post-selection. It was hypothesised that at 48 hr the changes in some genes' expression may have become more congruent between the 2 shRNA.

In the original RNA-Seq data, 3.7X as many genes were deregulated by sh*NFATC2*-143 transduction alone, compared to sh*NFATC2*-146 alone (as shown in Figure 5-8B), and so the proportions of genes were selected from each to approximately reflect this. Genes were selected in order of statistical significance.

Additionally, selected genes which contributed to the 'leading edge' subset of either the *MYC*- or *STK33*-related gene sets (from GSEA) were included. Note that due to the nature of GSEA, which selects patterns of change as opposed to individually significant genes, some of these genes' individual significance values were above the significance threshold in the original RNA-Seq data. In total, a balance of genes was selected to allow expression quantification in 1 plate. All new genes added are highlighted in Table 5-5.

Selected cell cycle genes' expression was also quantified using multiplexed PCR - *CCNA2*, *CCNB1*, *CCNC*, *CCND1*, *CCND2*, *CCNE1* and *CCNE2* – aiming to cover the main cyclin-coding genes. Finally, *NFATC1-3*, *KDM4A* and *PAF1* were quantified. The final list of 82 genes consisted of 48 new genes and 34 genes from the original list (excluding pseudogene *DEFA8P*).

Gene symbol	Inclusion group	sh*NFATC2*-143		sh*NFATC2*-146	
		Log_2 fold change	Adjusted *p* value	Log_2 fold change	Adjusted *p* value
SHISA5	sh*NFATC2*-143 only	-2.90	$9.63x10^{-26}$	-0.26	0.930
ETFRF1	sh*NFATC2*-143 only	-2.62	$4.85x10^{-15}$	0.25	0.962
PPP1R14C	sh*NFATC2*-143 only	-3.11	$5.71x10^{-14}$	0.16	0.975
DGUOK	sh*NFATC2*-143 only	-2.08	$3.65x10^{-11}$	-0.53	0.765
ELL2	sh*NFATC2*-143 only	-1.96	$3.65x10^{-11}$	-0.43	0.860
ADGRE5	sh*NFATC2*-143 only	-1.61	$1.48x10^{-10}$	0.49	0.838
LMO2	sh*NFATC2*-143 only	-1.74	$1.48x10^{-10}$	0.13	0.977
PIGW	sh*NFATC2*-143 only	-1.39	$1.27x10^{-09}$	-0.28	0.947
CUL4A	sh*NFATC2*-143 only	-1.19	$8.24x10^{-08}$	-0.02	0.997
FAM192A	sh*NFATC2*-143 only	-1.15	$2.82x10^{-06}$	-0.25	0.925
H2AFX	sh*NFATC2*-143 only	-1.43	$3.00x10^{-06}$	-0.64	0.814
BZW2	sh*NFATC2*-143 only	-1.16	$5.20x10^{-06}$	-0.34	0.920
RAC3	sh*NFATC2*-143 only	-1.63	$7.30x10^{-06}$	-1.22	0.287
STAT5B	sh*NFATC2*-143 only	-1.30	$7.72x10^{-06}$	-0.16	0.964
MAGEF1	sh*NFATC2*-143 only	-1.39	$1.52x10^{-05}$	-0.68	0.528
FAM216A	sh*NFATC2*-143 only	-1.41	$1.86x10^{-05}$	-0.60	0.756
SLC25A22	sh*NFATC2*-143 only	-1.26	$2.17x10^{-05}$	0.10	0.986
ADGRG5	sh*NFATC2*-143 only	-1.21	$3.47x10^{-05}$	-0.41	0.838
CTPS1	sh*NFATC2*-143 only	-1.23	$3.47x10^{-05}$	0.09	0.982
RRM2	sh*NFATC2*-143 only	-1.18	$4.01x10^{-05}$	0.28	0.930
MCU	sh*NFATC2*-143 only	-0.62	0.077	0.00	1.000
SLC16A9	sh*NFATC2*-143 only	0.78	0.088	0.52	0.847
CLCN3	sh*NFATC2*-143 only	0.70	0.084	0.79	0.267
HPDL	sh*NFATC2*-143 only/*STK33* pathway	-0.76	0.066	-1.00	0.307
ALOX5	sh*NFATC2*-143 only/*STK33* pathway	-1.32	0.030	-1.01	0.557
CDKN1A	sh*NFATC2*-146 only	0.47	0.859	1.43	0.003
SVIP	sh*NFATC2*-146 only	-0.24	0.922	-1.64	0.003
CALHM6	sh*NFATC2*-146 only	-0.55	0.861	-1.92	0.003

PTK2	sh*NFATC2*-146 only	0.77	0.715	1.58	0.060
ADAM9	sh*NFATC2*-146 only	0.94	0.180	1.47	0.013
KLRG2	sh*NFATC2*-146 only/*STK33* pathway	-1.03	0.246	-1.23	0.083
CD3EAP	*MYC* pathway	-1.05	0.211	-0.50	0.767
VDAC1	*MYC* pathway	-0.49	0.486	-0.80	0.219
EEF1E1	*MYC* pathway	-0.67	0.545	-0.60	0.794
ISOC2	*MYC* pathway	-0.46	0.688	-0.65	0.423
PRR3	*MYC* pathway	-0.56	0.243	-0.52	0.657
MYC	*MYC* pathway	0.03	0.986	-0.15	0.977
CCNA2	Cyclin-coding	-0.09	0.951	-0.39	0.895
CCNB1	Cyclin-coding	-0.16	0.937	0.08	0.986
CCNC	Cyclin-coding	0.07	0.973	0.08	0.990
CCND1	Cyclin-coding	0.27	0.944	0.87	0.794
CCND2	Cyclin-coding	-0.97	0.660	-0.52	0.930
CCNE1	Cyclin-coding	-0.51	0.433	-0.06	0.989
CCNE2	Cyclin-coding	0.56	0.754	0.80	0.611
KDM4A	*NFATC2*-related	0.27	0.921	0.15	0.981
NFATC1	*NFATC2*-related	0.48	0.838	0.43	0.930
NFATC3	*NFATC2*-related	0.25	0.914	0.40	0.865
NFATC2	*NFATC2*-related	-2.07	0.021	-1.84	0.040

Table 5-5. Additional genes were added to the significance list for validation by qRT-PCR. The table lists 48 selected genes which were added and their grouping, or, the reason why they were selected from the RNA-Seq data. The $\log_2$ fold changes between either construct -143 or -146 and the scrambled control are shown, with the associated adjusted *p* value. Adjusted *p* values <0.1 are shaded in colour.

Of the 48 genes input to the multiplexed qRT-PCR, 17 were excluded due to poor expression or unsuccessful amplification in any replicates, leaving 65 genes for analysis. Firstly, in an independent set of THP-1 cells, 22 genes were found to be differentially expressed after *NFATC2* KD with either construct -143 or -146 (adjusted p<0.1). A heatmap of the results of the multiplexed qRT-PCR are shown in Figure 5-13 (n=3).

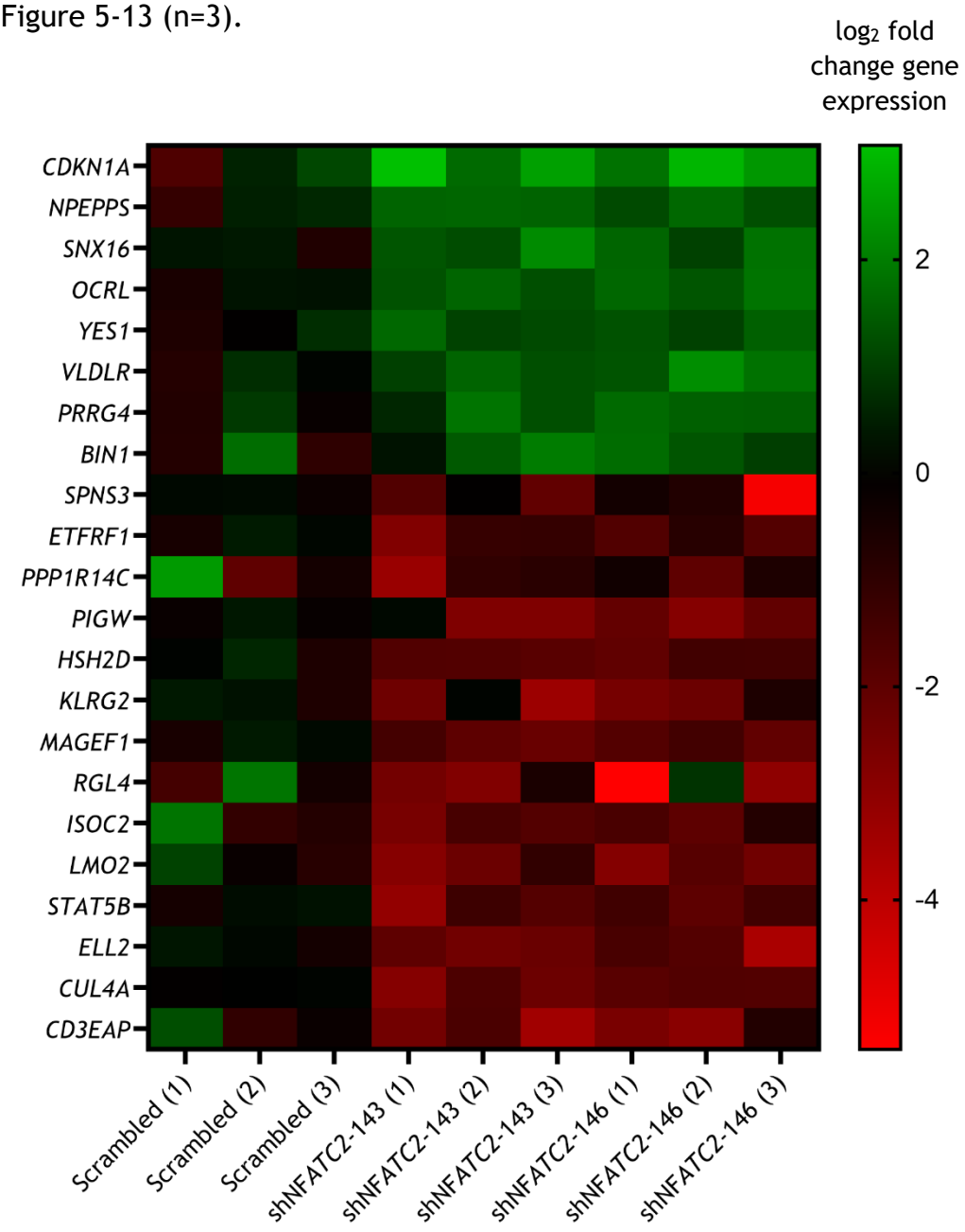

Figure 5-13. Twenty-two genes were significantly deregulated after *NFATC2* KD in THP-1 cells, in a validation set. The heatmap presents the $\log_2$ fold changes of the scrambled control compared to either sh*NFATC2*-143 or sh*NFATC2*-146, determined by multiplexed qRT-PCR using the ΔΔCt method for quantification with replicate pooling (n=3 biological, n=1 technical replicates). Each replicate is shown and the reference scale is given on the right hand side. Only genes with an FDR q value <0.1 for a difference in means with both constructs are shown. Significance was calculated using a two-way ANOVA and post-hoc pairwise tests, corrected for multiple testing.

Of these genes, 8 were significantly upregulated and 14 were downregulated. All of these changed in the expected direction, based on the results after *NFATC2* KD with at least 1 of the sh*NFATC2* constructs in the original RNA-Seq dataset. Interestingly none of the gene subset measured by multiplexed qRT-PCR was significantly deregulated in MOLM-13 with *NFATC2* KD (n=3; data not shown).

To validate the results of GSEA on the original RNA-Seq data the results from the multiplexed qRT-PCR were used in a pre-ranked GSEA analysis. This analysis used all 65 genes tested and their $\log_2$ fold changes, without filtering *p* (Figure 5-16).

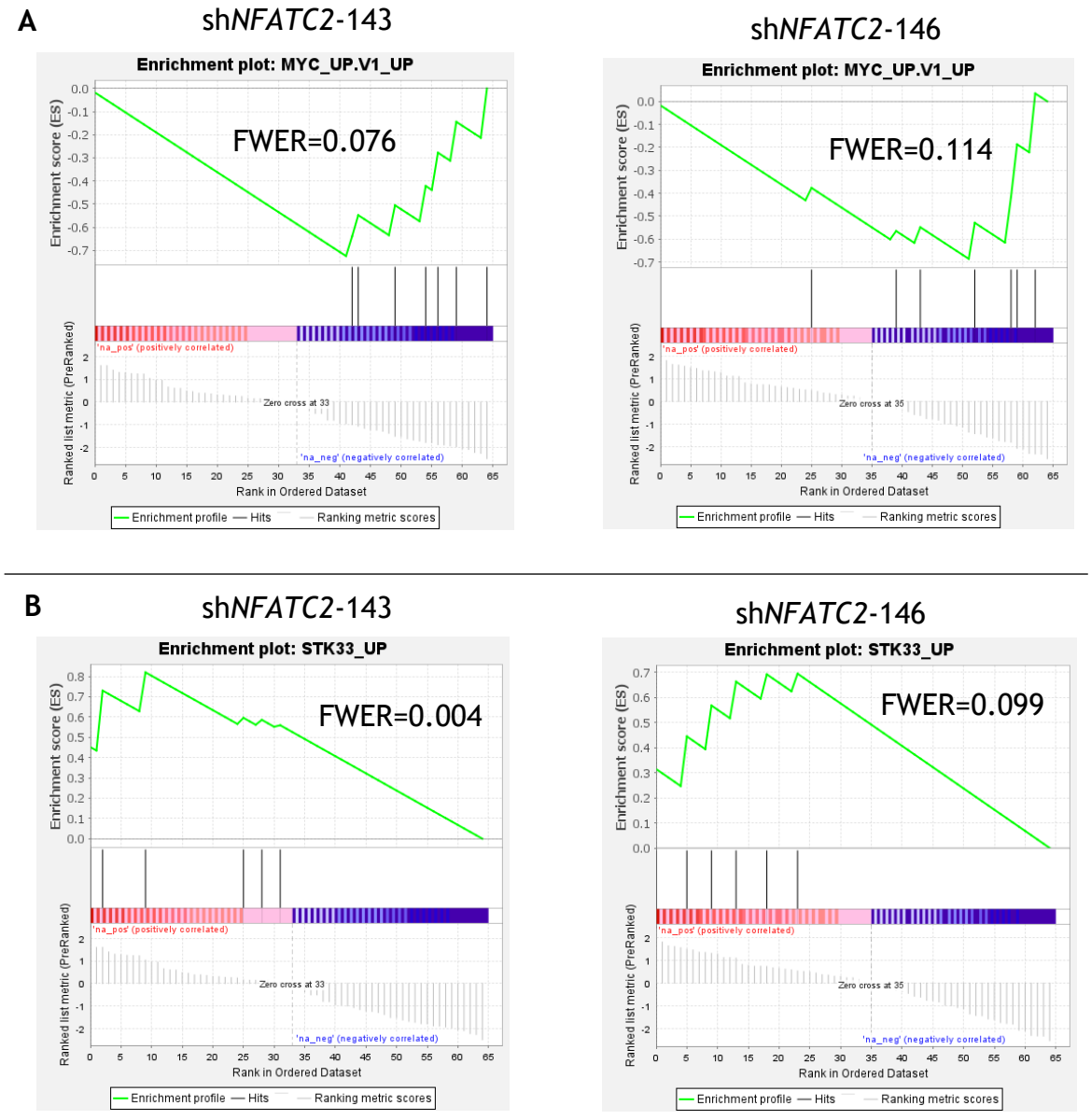

Figure 5-14. Targets of *STK33* were validated as being enriched within genes deregulated by *NFATC2* KD in an independent culture of THP-1 cells. Shown are data from a pre-ranked GSEA analysis using 68 selected genes' expression, after *NFATC2* KD in THP-1. Plots presented in Figure 5-14. **A:** pathways involving **A:** targets of *MYC*; **B:** targets of *STK33*. FWER *p* values are shown.

Using the validation data GSEA found the C6: oncogenic group pathway 'MYC_UP.V1_UP' to be negatively correlated with *NFATC2* KD (Figure 5-14A), as found for the original data. Using the FWER this was not statistically significant for sh*NFATC2*-146. However, given that the input data are small, the less conservative 'FDR *q* value' parameter is also valid; in which case FDR=0.039 and *q*=0.067 for constructs -143 and -146, respectively. 'STK33_UP' was found to positively correlate with the gene subsets in the sh*NFATC2*-143 and sh*NFATC2*-146 groups, with statistical significance (using FWER). For each of the *MYC* and *STK33* pathways in these analyses, 2/7 and 2/6 of the genes included were found to be statistically significant as individual genes (adjusted *p* <0.1), by qRT-PCR.

Next, THP-1 overexpressing either m*Nfatc2* or h*NFATC2* were compared to an empty vector at baseline. These cells showed deregulated expression of 11 genes in both cases (FDR *q* value <0.1). A further 6 genes were significantly deregulated with h*NFATC2* overexpression alone, giving a total of 17 genes of interest. Of these genes, 8 overlapped with those which were deregulated after *NFATC2* KD in THP-1 (Figure 5-15), reinforcing confidence that these are targets of *NFATC2*.

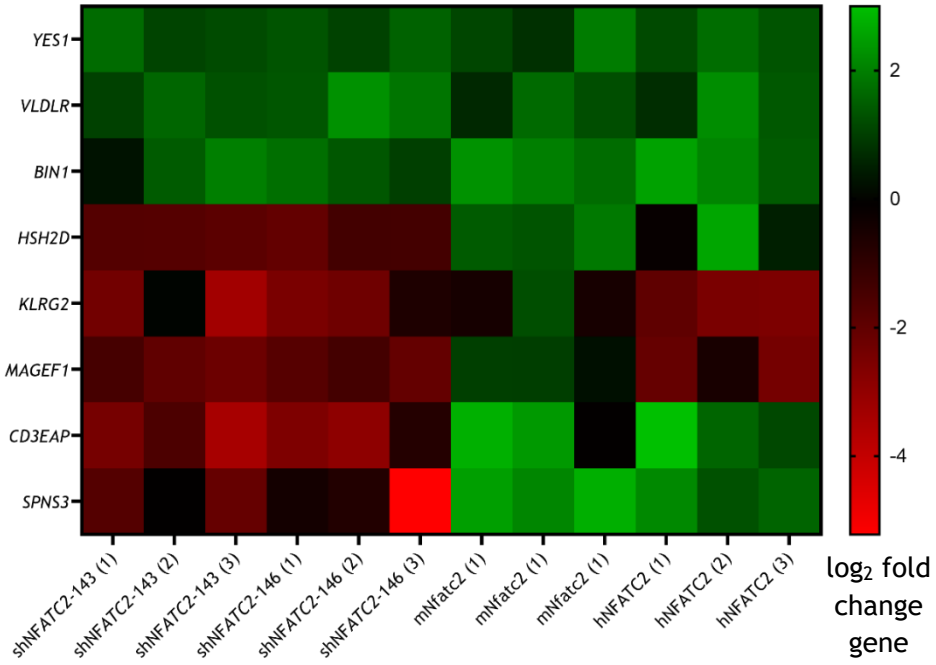

Figure 5-15. The expression of 8 genes was deregulated after either *NFATC2* KD or h*NFATC2* overexpression in THP-1. Heatmap of individual replicates' data from the Fluidigm® platform multiplexed qRT-PCR (n=3 biological, n=1 technical replicates), for genes which were significantly deregulated (*q* value<0.1) relative to their respective control shown here as the $\log_2$ fold change relative to either the scrambled control, for sh*NFATC2* constructs -143 or -146, or the empty vector, for overexpression constructs for m*Nfatc2* or h*NFATC2*. The data for the scrambled control distance from the mean was omitted for visual clarity. Note that data for *NFATC2* KD are derived from the same experiment as in Figure 5-13.

Both KD or overexpression of h*NFATC2* in THP-1 led to the significant upregulation of 3 genes in THP-1 cells: *YES1*, *VLDLR* and *BIN1*. Similarly, *KLRG2* and *MAGEF1* were downregulated with either KD or overexpression conditions. In contrast, *HSH2D*, *CD3EAP* and *SPNS3* were downregulated upon *NFATC2* KD and upregulated with h*NFATC2* overexpression. Four of 6 genes which were upregulated by h*NFATC2* overexpression were also upregulated with statistical significance following m*Nfatc2* overexpression.

Significance tests were used to determine whether m*Nfatc2* overexpression in THP-1 was sufficient to rescue any gene deregulation observed with *NFATC2* KD alone. None of this subset of genes was observed to be deregulated differentially after *NFATC2* KD in either THP-1 o/e empty or THP-1 o/e m*Nfatc2*.

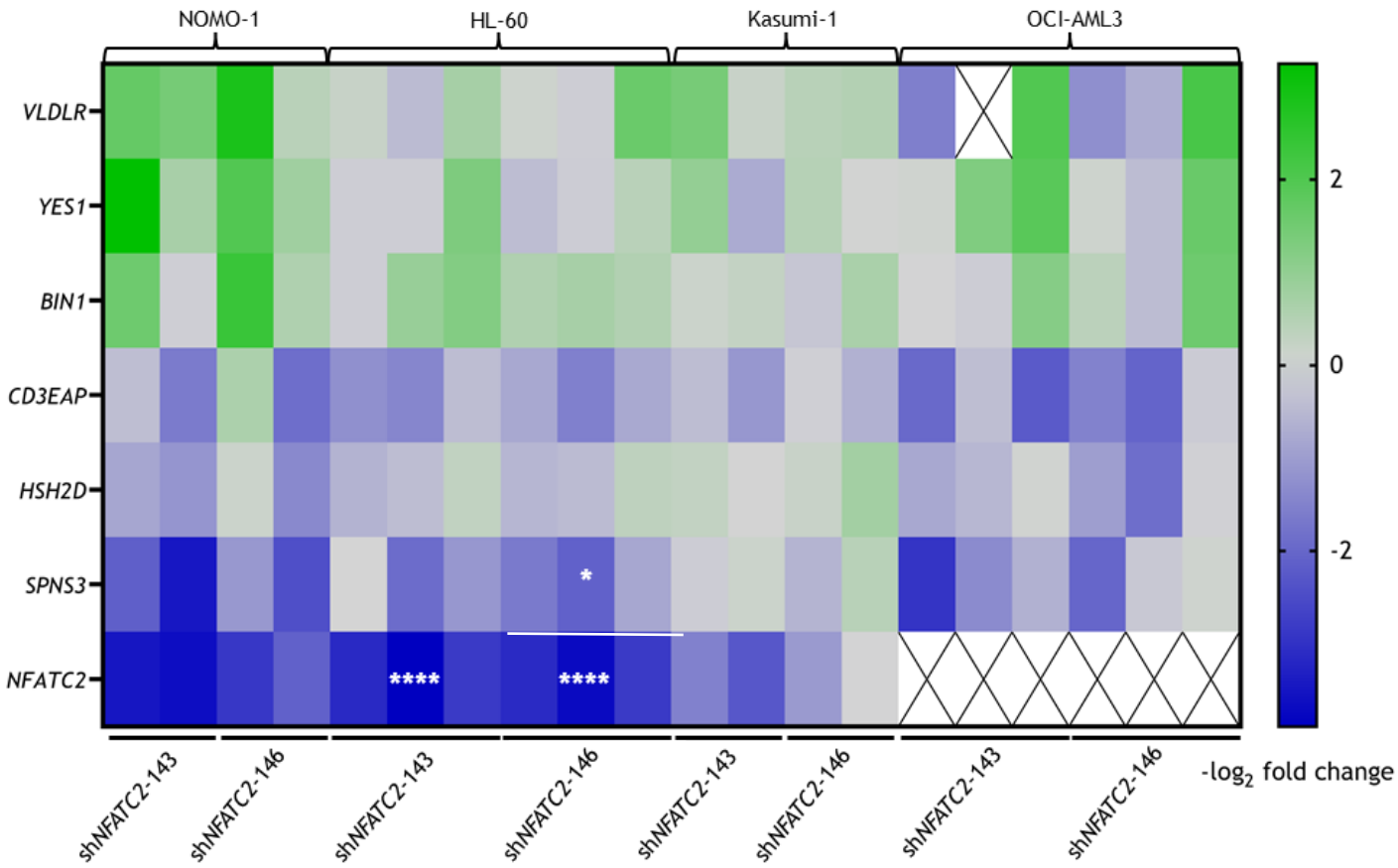

Figure 5-16. Putative targets of *NFATC2* in THP-1 were deregulated in a broadly similar pattern in AML cell lines other than THP-1.
The heatmap shows -$\log_2$ fold changes between cell lines transduced with a scrambled control and either sh*NFATC2* construct -143 or -146. These data are derived from qRT-PCR and using the ΔΔCt method (n=2-3 biological replicates as shown, n=3 technical replicates). Data from the scrambled control are omitted for visual clarity. The cell line is indicated at the top and experimental condition at the bottom. Gene names are on the left and the scale bar is on the right. Two-way ANOVA was conducted within each cell line and the result of post-hoc pairwise comparisons is shown, for adjusted p >0.05. *<0.05, ****<0.0001. Undetectable genes are indicated by crosses.

A total of 6 genes – *YES1*, *VLDLR*, *BIN1*, *HSH2D*, *CD3EAP* and *SPNS3* – were analysed for expression changes in other AML cell lines after *NFATC2* KD (Figure 5-16). In MLL-AF9 NOMO-1, *VLDLR* and *YES1* were the most upregulated, and *SPNS3* the most downregulated (excluding *NFATC2*), which follows the direction of trends observed in THP-1 cells. *CD3EAP* and *SPNS3* were most strongly downregulated in HL-60 and no gene's expression was increased by more than 0.67X (log_2 fold change). *SPNS3* downregulation after sh*NFATC2*-146 transduction was the only statistically significant change (p=0.128) in HL-60, other than *NFATC2*. All gene expression changes in Kasumi-1 were within -1.0 to 1.0 log_2fold change from the scrambled control, other than *NFATC2*. Finally, OCI-AML3 showed downregulation of *CD3EAP* and *SPNS3* but no changes were statistically significant.

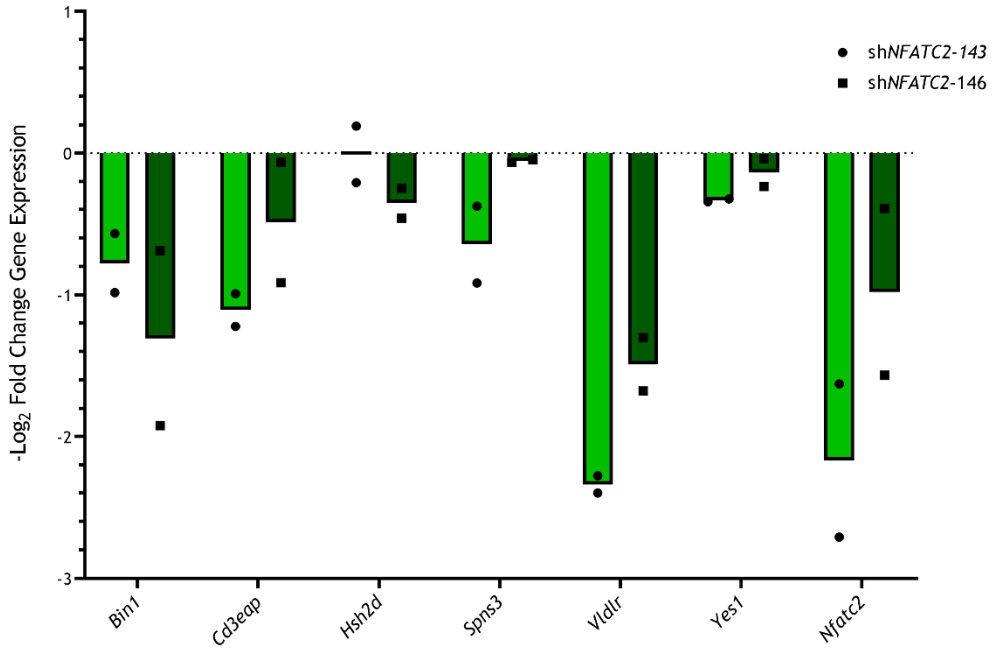

Figure 5-17. *Vldlr* was downregulated after *Nfatc2* KD in MLL-AF9-driven murine BM. Expression of selected genes was measured in MLL-AF9 murine BM after m*Nfatc2* KD, using either construct sh*Nfatc2*-356 or sh*Nfatc2*-357, using qRT-PCR. Shown are -log_2 fold changes in gene expression relative to the scrambled shRNA, using the ΔΔCt method. Individual replicates' values are given (n=2 biological, n=3 technical replicates), the bar represents the mean.

The expression of mouse orthologs of these 6 genes was also measured in the MLL-AF9 murine BM model after *Nfatc2* KD using either sh*Nfatc2*-356 or sh*Nfatc2*-357, relative to the scrambled control (Figure 5-17). All genes showed a trend towards downregulation after KD, to differing extents. Aside from *Nfatc2* itself, *Vldlr* and *Bin1* displayed the highest level of downregulation of the genes tested, opposing the effects observed in THP-1 for the human orthologs *VLDLR* and *BIN1*.

5.3.2.2 c-Myc expression is not downstream of NFATc2

Next, the relationship between *MYC* and *NFATC2* in THP-1 cells was examined more directly using gene and protein expression.

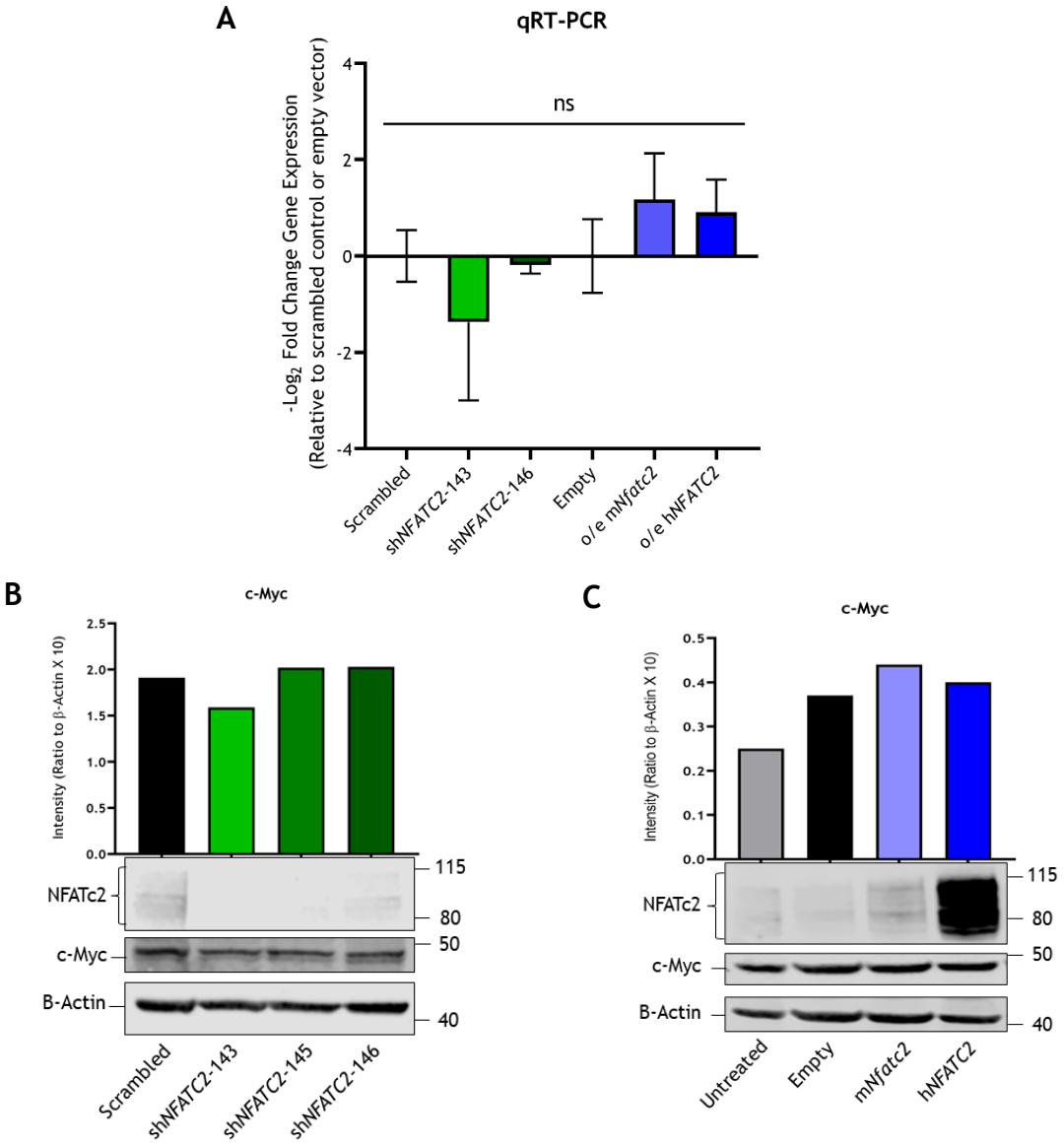

Figure 5-18. Overexpression of *NFATC2* marginally increased *MYC* expression.
A: *MYC* expression changes, in THP-1 with either *NFATC2* KD or *NFATC2* o/e, were measured by multiplexed qRT-PCR. -$\log_2$ fold changes are in cells after transduction with either sh*NFATC2* construct -143 or -146 relative to the scrambled control; or expressing either o/e m*Nfatc2* or o/e h*NFATC2* relative to the empty vector. This was calculated using the ΔΔCt method (n=3 biological, n=3 technical replicates). A one-way ANOVA was used to test differences in means ('ns' = not significant). **B:** 40 µg WCL from THP-1 72 hr after transduction by either of the shRNA constructs -143, -145 or -146, or the scrambled control, were immunoblotted with anti-NFATc2, anti-c-Myc and ß-actin. The protein size in kDa is given on the right-hand side. The bar chart represents the quantification by densitometry, relative to ß-actin (n=1 biological). **C:** 22µg WCL from either untreated THP-1, THP-1 with an empty vector, THP-1 o/e m*Nfatc2* or THP-1 o/e h*NFATC2* were immunoblotted with anti-NFATc2, anti-c-Myc and ß-actin. (n=1 biological).

Expression of *MYC*/c-Myc appears unchanged after *NFATC2* KD in THP-1(Figure 5-18A&B). Overexpression of either m*Nfatc2* or h*NFATC2* in THP-1 marginally increased gene expression of *MYC* but these changes were found not to be statistically significant (Figure 5-18A; overall ANOVA p=0.0546). Immunoblotting shows a very marginal increase in c-Myc protein, relative to ß-actin, when m*Nfatc2* or h*NFATC2* are overexpressed (Figure 5-18C). In summary *MYC*/c-Myc expression, at the transcript or protein level respectively, is not affected by *NFATC2* expression in THP-1 cells.

5.3.2.3 Investigating *STK33-NFATC2* interplay in THP-1 cells

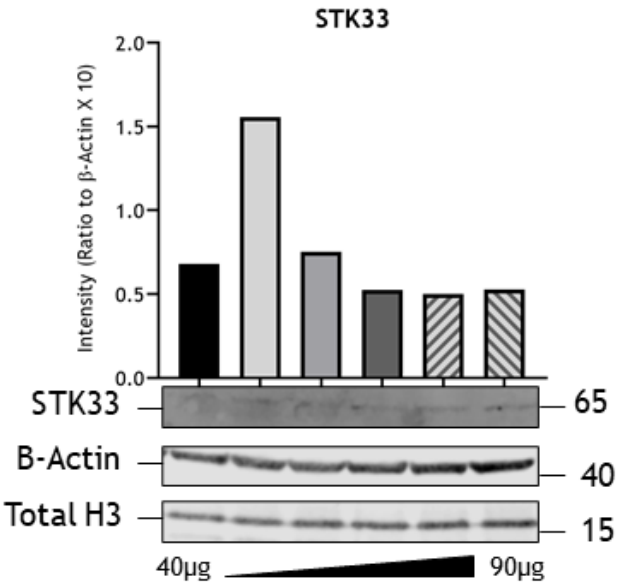

Figure 5-19. STK33 protein was not clearly visualised in THP-1 cell lysate.
WCL from THP-1 was loaded at quantities in the range 40-90µg and immunoblotted for STK33, ß-actin and total H3. Protein size is shown on the right-hand side in kDa and STK33 protein was quantified by densitometry, relative to ß-actin, as shown above the blot (n=1 biological replicate).

STK33 protein was visibly expressed in THP-1, as measured in up to 90 µg of WCL (Figure 5-19), though the bands were not clearly visualised in this immunoblot. This may be a result of inadequate antibody optimisation, leading to high background and/or poor signal. The antibody signal did not change considerably across differing quantities of WCL loaded, suggesting that further antibody optimisation was required. As such, it is difficult to make conclusions on STK33 protein expression in THP-1 from these data alone.

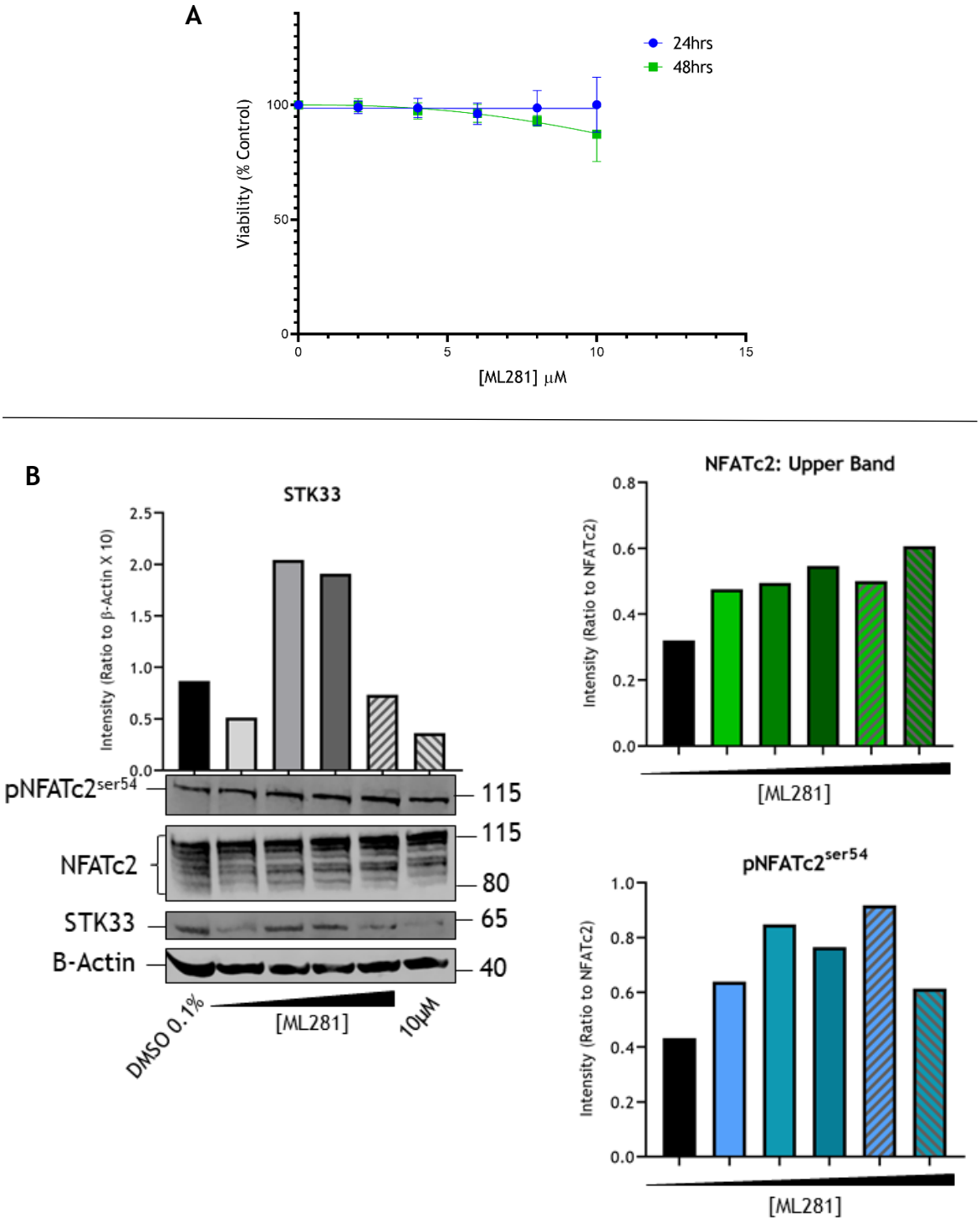

Figure 5-20. STK33 kinase inhibitor ML281 did not affect THP-1 cell viability.
THP-1 cells were treated with ML281 in a range of concentrations from 0-10 µM, for up to 48 hr. **A:** Alamar Blue viability assay was performed on cell suspensions at 24 hr and 48 hr. The absorbance is presented as % of the 0.1% (v/v) DMSO control (n=3 biological, n=2 technical replicates). **B:** 40 µg WCL harvested from THP-1 cells after 24hr of ML281 treatment was immunoblotted for NFATc2, pNFATc2^{ser54}, STK33 and ß-actin. Shown are protein sizes on the right-hand side, in kDa, and quantification by densitometry in the bar graph. STK33 is relative to ß-actin and the NFATc2 upper band or pNFATc2^{ser54} are relative to total NFATc2 (n=1 biological).

The STK33 kinase inhibitor, ML281 was used to determine the dependence of THP-1 on STK33 activity and also test whether STK33 kinase activity acts upstream of NFATc2, or alters its phosphorylation status. ML281 binds to STK33 and inhibits its serine/threonine kinase activity, with high potency and reasonably high specificity (Weïwer *et al.*, 2012).

ML281 did not have any effect on the viability of THP-1 cells up to 10 μM in concentration after 24hr (Figure 5-20A). After 48hr a marginal drop in viability was observed at 10 μM, to 87.2% of the viability in the vehicle control. Immunoblotting showed that STK33 protein quantity changed unpredictably in response to ML281 treatment, with no clear trend with the drug concentration.

There was no change in NFATc2 size, which may have signified protein phosphorylation (Figure 5-20B). However, the uppermost band of NFATc2 did increase in intensity across the rising concentration of ML281, as did pNFATc2^{ser54}, suggesting that phosphorylation of NFATc2 did increase. It is not known whether STK33 kinase activity targets NFATc2, but it may be surprising that STK33 kinase inhibition led to NFATc2 phosphorylation, if NFATc2 were a substrate. Specific inhibition of STK33 by ML281 was not validated due to a lack of available phospho-antibodies. Finally, the effect(s) of *NFATC2* KD or *NFATC2* overexpression on STK33 were not assessed due to challenges in detecting STK33 protein at lower concentrations of protein lysate.

5.3.3 ChIP-Seq to determine NFATc2 binding sites in THP-1 cells

NFATc2-bound chromatin was precipitated for sequencing in THP-1 cells and compared against input DNA. The methods for data QC and the QC data are shown in the Appendices (Section 9.3). In total, 131 peak regions were identified in DNA precipitated by NFATc2 pull-down compared to input DNA.

In the 2D PCA plot shown, the input DNA samples were more similar to one another, when described using principal components 1 and 2 (Figure 5-21A). In contrast, NFATc2 IP replicates were distinct from the input control, but also not similar to one another. Replicates 1 and 3 were most similar to each other in 1 dimension with component 1 alone, while 2 and 3 were similar using only component 2; but both components together did not group these replicates proximally. Together these 2 principal components described 82% of the variation in the data. These findings are also shown in the correlation heatmap (Figure 5-21B), where the input samples clustered together but the individual NFATc2 IP replicates were not found to cluster.

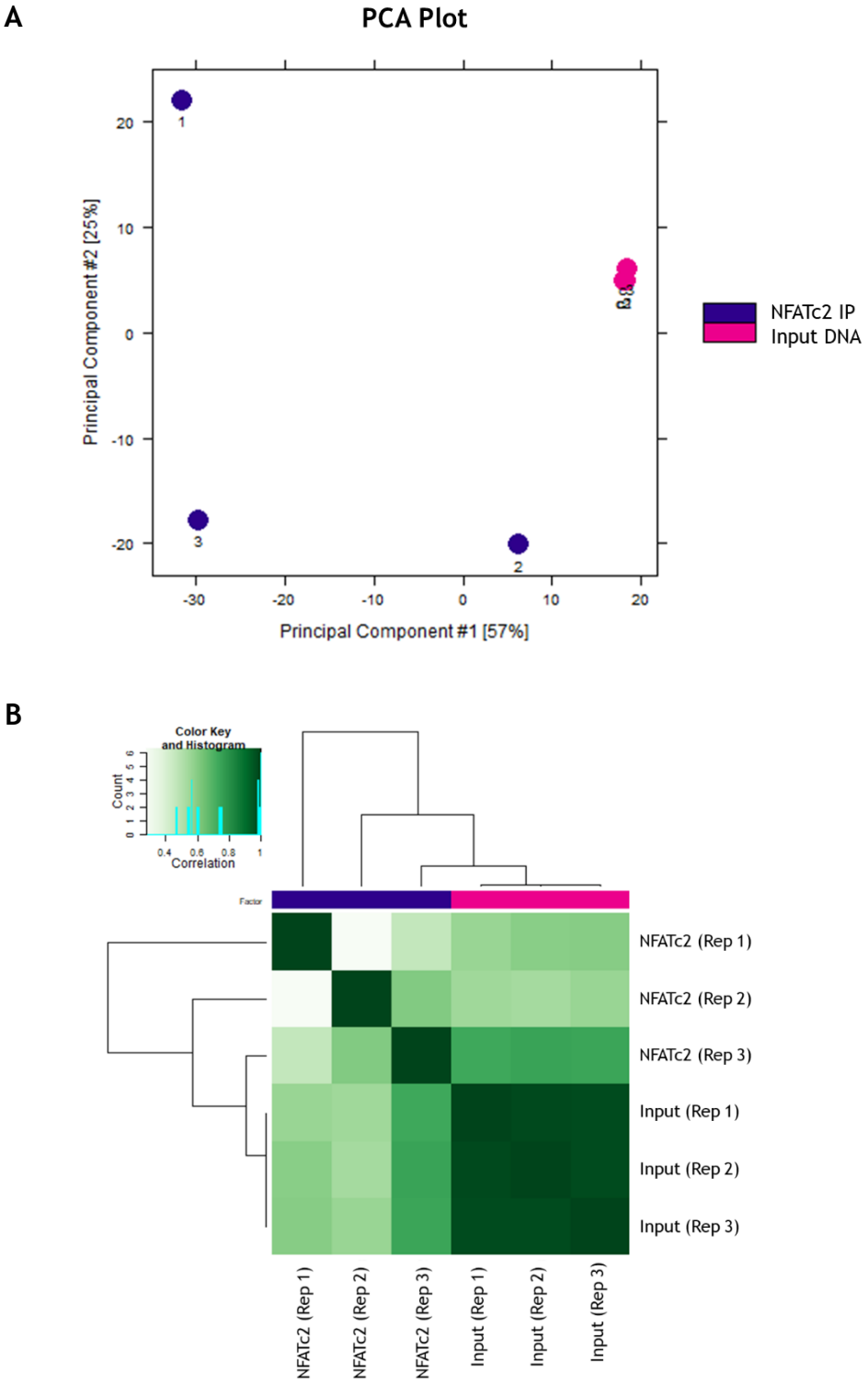

Figure 5-21. DNA with NFATc2 pull-down showed a distinct global pattern of peak scores from unselected input DNA, but replicates were not clustered. A: The PCA plot shows the principal components produced by the *ChIPQC* package. One data point is shown per replicate, where NFATc2 IP replicates are labelled '1', '2', '3', and control input DNA replicates 'c1', 'c2', 'c3'. The colours are indicated in the right-hand side legend. The % of variance accounted for by each principal component (1 and 2) are shown in the x- and y-axis labels, respectively. **B:** A correlation heatmap produced by *ChIPQC*. This shows the correlation between individual sample replicates. A key is shown in the top left corner, which includes a histogram for individual correlation coefficients in the samples.

5.3.3.1 ChIP-Seq: NFATc2 IP enrichment data

The 131 peak regions called by MACS2 were mapped to 104 unique genes (via Ensembl). The distribution of these in the genome is shown in Figure 5-22.

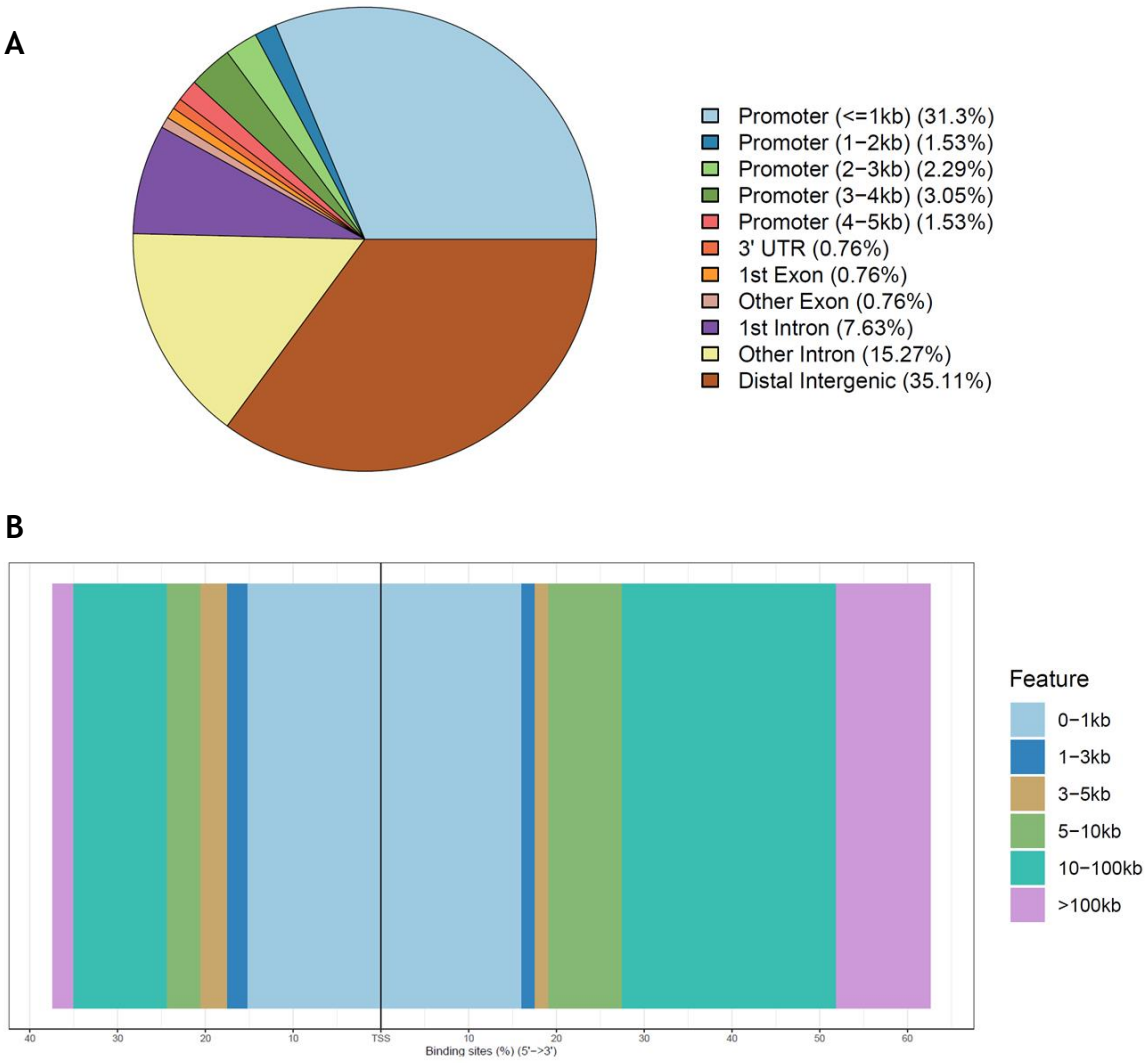

Figure 5-22. Over 1 in 3 peaks called for NFATc2 binding in THP-1 are within 3 kb of a transcription start site (TSS). Plots produced by the *ChIPseeker* package show the distribution of *MACS2* peaks relative to genomic features. **A:** Pie chart shows the % of total peaks in each genomic region. **B:** A graphic view showing the bi-directional distribution of peaks, relative to the TSS. A size reference is given on the right-hand side in kb.

This plot shows that over 30.0% of peaks are within 1 kb of the TSS, while 39.7% were within promoter regions, when 'promoter' is defined as 5kb either side of the TSS. Figure 5-22B shows that beyond 5 kb from the TSS the majority of binding sites are at the 3' side. Of all peaks, 35.11% were in distal intergenic regions.

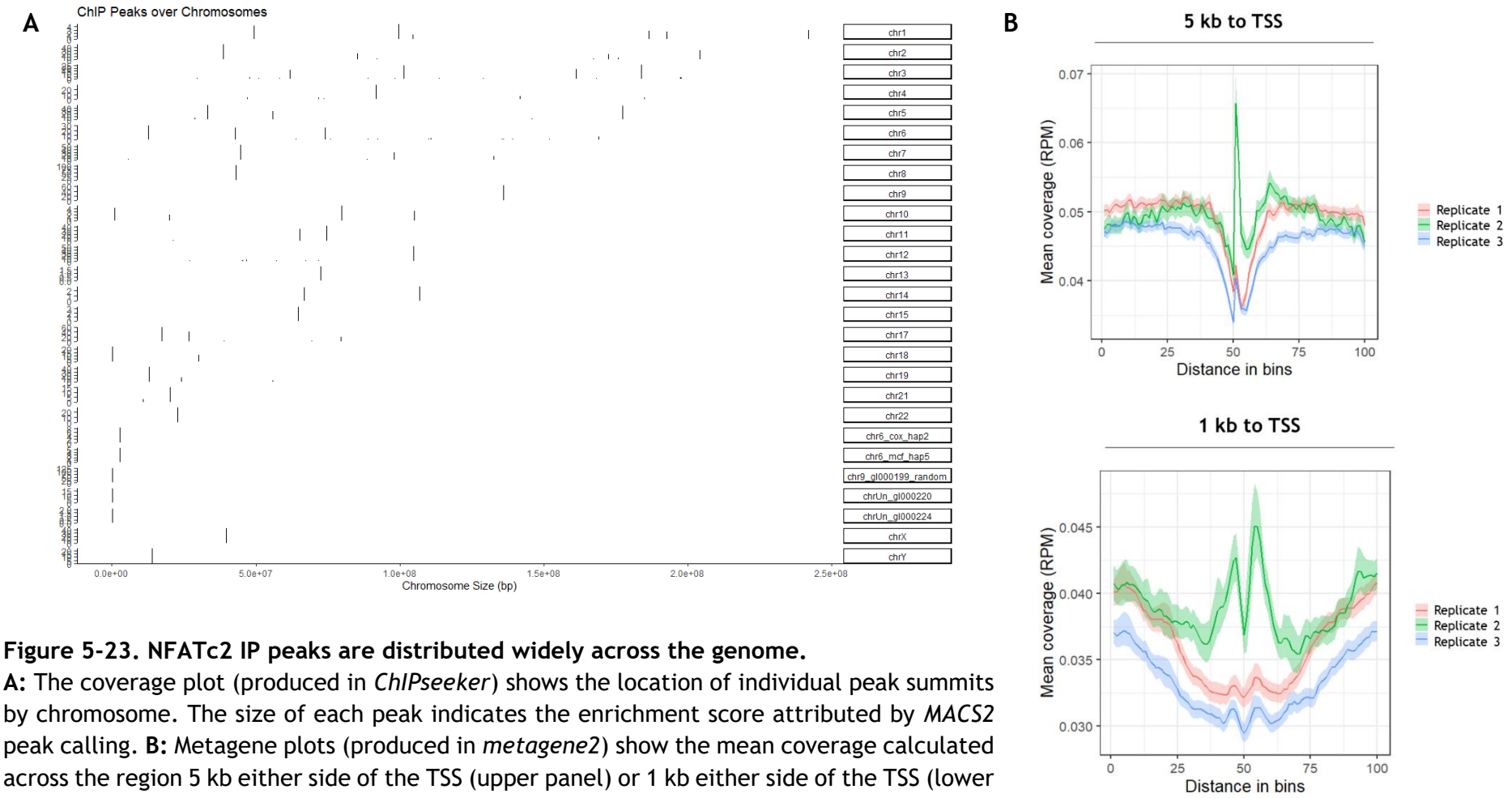

Figure 5-23. NFATc2 IP peaks are distributed widely across the genome.
A: The coverage plot (produced in *ChIPseeker*) shows the location of individual peak summits by chromosome. The size of each peak indicates the enrichment score attributed by *MACS2* peak calling. **B:** Metagene plots (produced in *metagene2*) show the mean coverage calculated across the region 5 kb either side of the TSS (upper panel) or 1 kb either side of the TSS (lower panel). Shown is the coverage distribution for each individual replicate, as highlighted on the right-hand side.

Figure 5-23A shows that *MACS2* peaks are well-distributed across the genome and do not appear to be clustered at any particular locus. Metagene plots (Figure 5-23B) show a gradual reduction in coverage moving towards the TSS and a distinct peak at either side of the TSS. This is more pronounced when viewed in the region of TSS±5000 bases. Additionally, replicate 2 shows clear peaks around the TSS, while the peaks replicates 1 and 3 are considerably smaller, indicating a lower signal in these replicates. The peaks appear to be slightly larger at the 3' side of the TSS, indicating that binding sites were more prevalent here. This reinforces observations made from the *ChIPseeker* plots in Figure 5-22B.

A

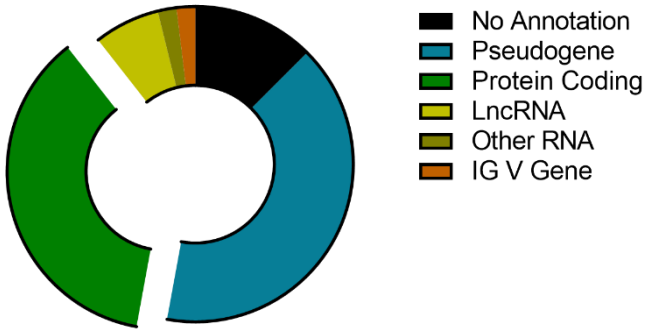

B

Gene Symbol	Region	Chr.	Score	Gene Summary
MALAT1	Promoter (≤1 kb)	11	345	-
ACTG1	Promoter (≤1 kb)	17	202	Cytoplasmic actin
TMSB10	Promoter (≤1 kb)	2	187	Cytoskeleton organisation
CHCHD3	Exon (1 of 3)	7	154	Mitochondrial protein
SMOC2	Intron (7 of 12)	6	59	Calcium-binding protein
RPS24	Promoter (≤1 kb)	10	49	40S ribosomal protein
BEND5	Intron (6 of 13)	1	43	Transcriptional repressor
STOX2	Intron (1 of 1)	4	42	-
RPL28	Promoter (≤1 kb)	19	39	60S ribosomal protein
METTL24	Intron (1 of 4)	6	35	Methyltransferase-like

Figure 5-24. Over 1 in 3 putative NFATc2 binding sites are associated with protein-coding genes. A: The Ensembl database was used to classify gene IDs, with which each NFATc2 IP peak was associated. These are presented as proportions, with a legend on the right-hand side. **B:** The top 10 protein-coding genes with which peaks were associated, as ranked by *MACS2* enrichment score, were annotated in a table. The 'score' is the enrichment score. The gene summary was derived from the STRING database description per protein. '-' indicates a summary was not available.

Figure 5-24A shows that of the 104 genes associated with peaks, 38 were protein-coding and 42 were pseudogenes. The top 10 protein-coding genes are summarised in Figure 5-24B, which have a number of known functions, including in the ribosome, mitochondria and cytoskeleton structures. GSEA was used to identify the enrichment of any known pathways within the top 131 Ensembl gene IDs highlighted by the peak calls.

A

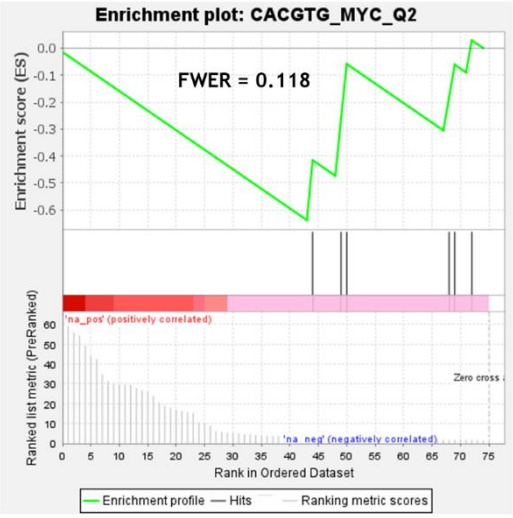

B

Rank in gene set (n=131)	Gene symbol
44	ADAMTS3
49	IQCG
50	TCERG1
68	RPL30
69	MYB
72	ATL2

Figure 5-25. Myc consensus binding sequence CACGTG was enriched in NFATc2 ChIP DNA. A pre-ranked GSEA analysis was conducted using 131 Ensembl gene IDs identified by *MACS2* peak calls. **A:** The GSEA plot is shown with the FWER statistic given. **B:** The genes contributing to the signature in **A** are listed, with their rank in the dataset contributing to the enrichment score.

No pathways were found to be enriched with FWER<0.1 using selected gene sets from the MSigDB collection. However, 'CACGTG_MYC_Q2' was found negatively enriched (NES=-1.52) in the uploaded data and narrowly missed the significance threshold (FWER=0.118; Figure 5-25A). Six contributing genes are shown in Figure 5-25B, all of which are protein-coding.

Motif number	Motif sequence	*E*-value	Similar motifs
1		$3.0x10^{-53}$	-
2	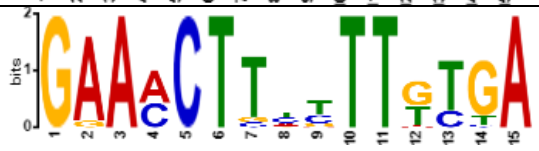	$2.1x10^{-52}$	NFATC1_full_1 - human
3		$6.3x10^{-41}$	-
4		$6.4x10^{-38}$	-
5		$5.1x10^{-23}$	-
6	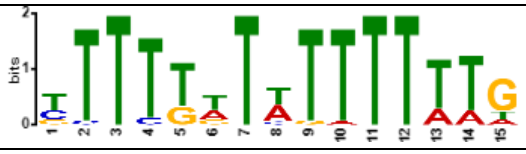	$5.3x0^{-22}$	MA1125.1 (ZNF384) - human

Table 5-6. A known NFATc1 binding motif was identified as being similar to one DNA motif bound by NFATc2 in THP-1 cells. MEME-ChIP identified DNA motifs which were enriched in the sequences containing *MACS2* peaks after NFATc2 IP; six of these motifs are shown here, as taken from the platform. The *E*-value is shown. Similar motifs were identified by the attached Tomtom motif comparison tool.

In total, 138 DNA sequences (131 annotated peaks, plus the 7 non-annotated sequences identified by *MACS2*) were parsed and uploaded to the MEME-ChIP platform for motif discovery. Six of the top DNA motifs identified (*E*-value<0.05) are shown in Table 5-6. The Tomtom comparison tool identified two similar known motifs from humans; 'NFATC1_full_1' (p=0.0005, e=0.9810) from the 'Jolma' database (Jolma *et al.*, 2013) and 'MA1125.1 (ZNF384)' (p=0.0001, e=0.0701) from the JASPAR database.

5.3.3.2 Comparison of RNA-Seq and ChIP-Seq data in THP-1 cells

Genes from the peaks identified after NFATc2 ChIP-Seq (82 had available gene symbols to compare) were overlapped with the top 1000 most significant genes identified in RNA-Seq, for constructs -143 and -146 separately. Only two ChIP-Seq genes overlapped with sh*NFATC2*-143 genes, and five genes with sh*NFATC2*-146 genes, which are described in Table 5-10.

Gene symbol	sh*NFATC2*-143		sh*NFATC2*-146	
	Log2 fold change	Adjusted p value	Log2 fold change	Adjusted p value
STOX2	1.55	0.235	1.41	0.333
SLC38A1	-0.53	0.218	-0.38	0.851
RPS24	-0.34	0.893	-0.74	0.528
BEND5	-0.38	0.908	-1.13	0.557
RPL28	-0.17	0.940	-0.60	0.587
NT5C2	0.59	0.634	0.67	0.611

Table 5-7. Few NFATc2-bound genes were deregulated by *NFATC2* KD in THP-1 cells. The table shows the six genes which were enriched in NFATc2 ChIP-Seq DNA and present in the top 1000 most significant genes after *NFATC2* KD in THP-1 cells. Given are the $\log_2$ fold changes in expression and adjusted *p* values from the RNA-Seq, per shRNA construct (n=3 biological replicates). For the shRNA construct condition in which the gene was identified in the top 1000 a green highlight has been used.

STOX2 was identified as the most significantly deregulated by *NFATC2* KD in THP-1, as a subset of the putative NFATc2-bound genes. However, KD with neither of the shRNA constructs was statistically significant (adjusted p=0.235, p=0.333, for constructs -143 and 146, respectively). The remaining 5 genes appeared most significantly downregulated in 1 of the 2 constructs, but the significance was low in the other. Log_2 fold changes were in the same direction between both constructs for all 6 genes.

5.3.4 Investigating novel targets of *NFATC2* in patient datasets

From the RNA-Seq and ChIP-Seq data analyses, 49 genes of interest were selected aiming to cover those with the highest statistical and biological significance (e.g. *MYC* and *STK33*). The correlation between gene expression and patient survival in the TARGET-AML cohort was examined by dividing patients into 2 groups based on the BM expression per gene, around the median expression value (n=119 patients).

Stratification of patients by gene expression was found to impact overall survival when using 13 of the 49 individual genes, with a statistically significant difference between the 2 patient groups (log-rank test $p<0.05$; Figure 5-26). Additionally, for every gene the 50% of patients with the higher expression had a lower median overall survival. *MYC* and *STK33* expression did not impact on patient survival in this cohort.

Correlation analysis revealed that a subset of genes clustered together well when looking at those with the highest impact on survival (Figure 5-27A). Those genes included *RASA1*, *OCRL*, *GBP3*, *NPEPPS* and *BRWD3*. When expanding the analysis to all 49 genes of interest, plus *NFATC2*, these genes form a larger cluster with several others (Figure 5-27B). This could suggest a common mechanism to these genes which has an impact on AML pathogenesis and survival. *NFATC2* clustered with *SNX16* and *YES1* in the first analysis (Figure 5-27A).

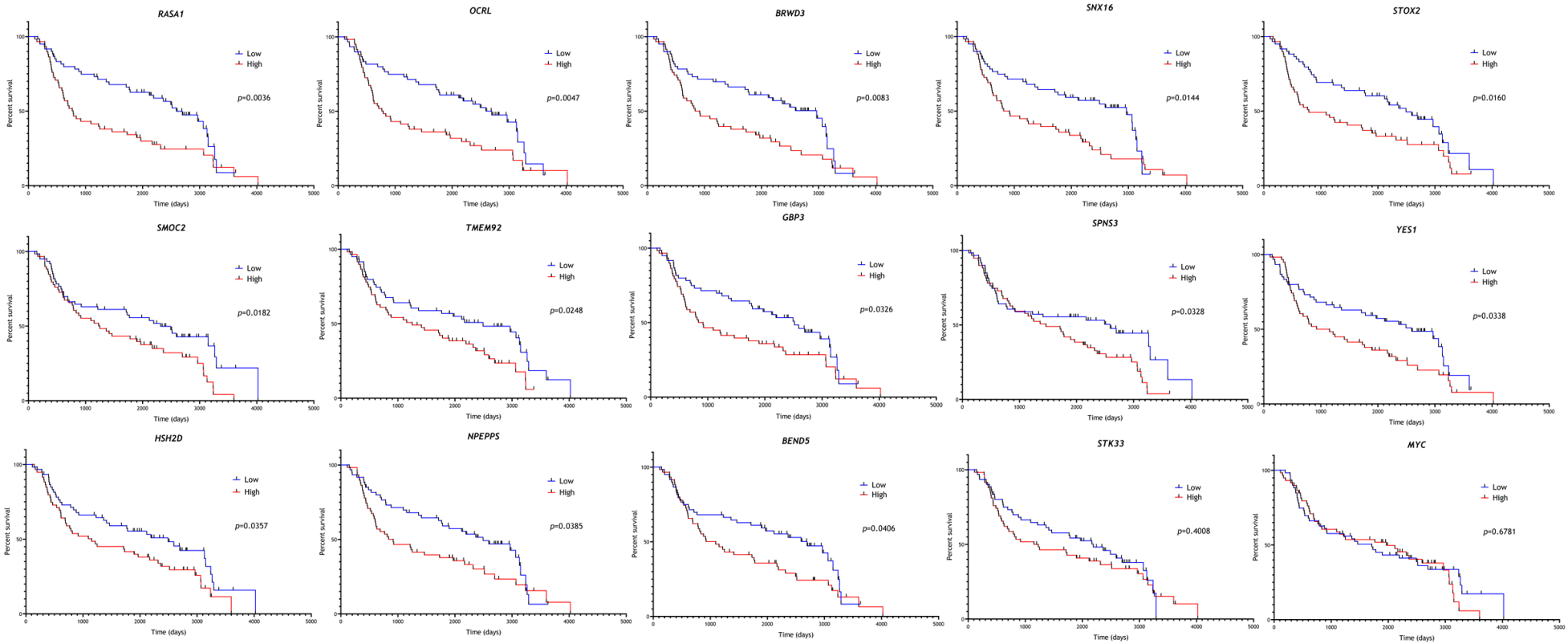

Figure 5-26. The expression of 13 putative *NFATC2*/NFATc2 target genes can individually stratify patients in the TARGET-AML trial cohort. Kaplan-Meier survival curves were generated from the TARGET-AML cohort for BM samples with associated RNA-Seq data (n=119; as shown in Chapter 3.2.1). Patients were divided into 2 cohorts by the expression of individual genes of interest, selected from the RNA-Seq and ChIP-Seq data analyses. The curves show the survival for the groups expressing each gene in the highest and lowest 50%. Curves included are those where the log-rank test *p* value was <0.05, and plots for *MYC* and *STK33*. The *p* value is shown on each plot, by which the plots are arranged in decreasing order of significance.

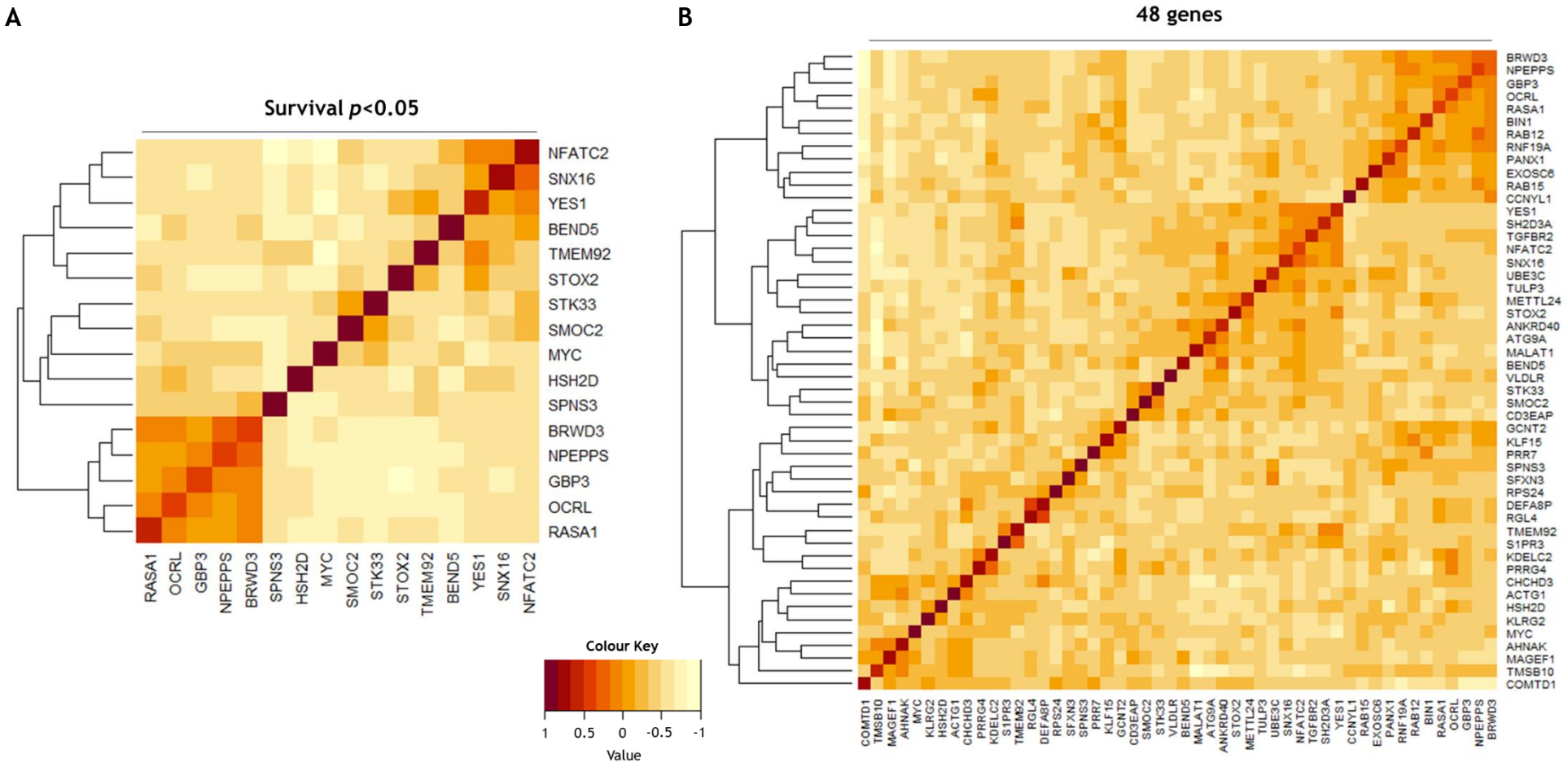

Figure 5-27. A subset of the genes which can be used to stratify patient survival in the TARGET-AML cohort are correlated.
Correlation heatmaps derived from the TARGET-AML RNA-Seq data for selected genes' expression in patient BM (n=119). The colours represent the correlation coefficient between pairs of genes and dendograms show clustering by (agglomerative hierarchical clustering). **A:** Selected genes for which their expression could stratify patient survival in the TARGET-AML cohort (log-rank test $p<0.05$); *NFATC2*, *MYC* and *STK33* were also included; total gene number 16. **B:** All 49 genes which were sub-selected from RNA-Seq and ChIP-Seq analyses for further analyses, in addition to *NFATC2*.

5.3.5 Discussion

5.3.5.1 RNA-Seq data: quality control

Sufficient KD of *NFATC2* was observed at 24 hr post-puromycin selection in THP-1 so this was chosen as the timepoint at which to harvest RNA for sequencing. However, the phenotype after *NFATC2* KD was characterised in these cells primarily at 72 hr post-selection and so the genes identified by this RNA-Seq may not necessarily capture the full transcriptomic changes contributing to this. Indeed, significant downregulation of *CCND1* was not observed until 144 hr post-selection (Chapter 4.2.3; Figure 4-10G) and so it is possible that key transcript changes were missed by the 24 hr post-selection timepoint. However, the higher proportion of cell death at later timepoints – partly due to increased apoptosis in the sh*NFATC2*-143 condition, and partly due to generalised cell death following shRNA transduction – might have risked poorer quality RNA harvest for sequencing. Ideally RNA would have been harvested at multiple timepoints for sequencing.

After filtering poorly expressed genes using the mean (within each condition) FPKM threshold of ≥1.0, a high concordance of co-expressed genes was observed amongst the 3 conditions (scrambled control, sh*NFATC2*-143 and sh*NFATC2*-146). However, PCA plots demonstrated differing patterns of variability between replicates and conditions, without the clustering that would be expected with experimental replicates. When viewed in 2- or 3-dimensions the principal components for replicate 1 were distinct from those for replicates 2-3, suggesting that some technical or biological factors might have contributed to divergent transcriptional changes.

The high quality of the sequencing and mapping processes make these unlikely contributing factors. The lower input RNA concentrations in replicate 1 may reflect some technical variation in the handling of cells, which could have contributed. The variation in level of *NFATC2* KD or transduction efficiency across replicates 1-3 does not reveal distinct experimental features of replicate 1 that would separate it from replicates 2-3, however there could have been multiple contributing factors to the PCA result. Additionally, even in replicates 2-3 there is not clear separation of experimental conditions by principal components. Together the PCA plots indicate that global changes between conditions after *NFATC2* KD are subtle and/or concentrated in a small subset of genes. In addition

to the small magnitude, significant changes between conditions may become lost in between-replicate variability, resulting in poorer sensitivity of this experiment to identify deregulated genes after *NFATC2* KD.

5.3.5.2 RNA-Seq data: differential expression after *NFATC2* KD

Transduction of THP-1 with either of two *NFATC2*-targeting shRNA led to the deregulation of two sets of genes, which overlapped to some extent between the 2 constructs. Firstly, both constructs led to the downregulation of *NFATC2* and no significant change in *NFATC1* or *NFATC3* expression, as expected from the predicted target specificity of the shRNA sequences. This also indicates that *NFATC2* does not regulate *NFATC1* or *NFATC3* transcription directly. Expression of *KDM4A* and *PAF1* was not affected, reinforcing the idea that these are upstream regulators of *NFATC2*.

NFATC2 KD led to significant upregulation and downregulation of 67 and 109 genes, respectively, across both constructs ($|\log_2$ fold change$| \geq 1$, adjusted $p<0.1$), which when the stringency of the criteria was relaxed to adjusted $p<0.1$ increased to 143 upregulated and 108 downregulated genes, respectively. The small number of genes may reflect the differences between replicates identified in the PCA plot, thus masking more significant changes, and/or that the changes induced by *NFATC2* KD at this timepoint are limited to few genes. The plots in Figure 5-7 demonstrated that a number of deregulated genes had a $\log_2$ mean FPKM between -5 and 0 (across all conditions), which is below the previously defined threshold of 0 (FPKM of 1) for 'expressed' genes. However, the DESeq2 differential expression package uses read counts as an input, without filtering out poorly expressed genes. This method uses a shrinkage estimator for fold changes and so is designed to improve the specificity of detection at low gene expression, while maintaining sensitivity (Love *et al.*, 2014). Caution should be applied when interpreting changes in these genes in subsequent validation qRT-PCR, which is inherently less sensitive for poorly expressed genes than RNA-Seq.

KD with sh*NFATC2*-143 led to the deregulation of more genes than with sh*NFATC2*-146, particularly with regard to downregulated genes. This could reflect some of the phenotypic changes *in vitro* which only occurred after sh*NFATC2*-143 transduction, such as the induction of apoptosis. Greater transcriptional deregulation would therefore be expected, though functional analyses were not

conducted on the subset of genes specific to -143 to correlate with the phenotype. Additionally, these changes might be secondary to off-target shRNA effects and so deregulated genes which were common to both constructs were prioritised.

STRING analyses of the top 35 significant genes did not reveal many known associations between their transcribed proteins, and those identified have immediate relevance to AML cells. For example, YES1 and RASA1 are described simultaneously in a number of publications, as key SH2-domain proteins with some lipid-binding properties (Park *et al.*, 2016). *HSH2D* and *SH2D3A*, also transcribe SH2-domain proteins. SH2-domain proteins are often characterised in tyrosine kinase signalling pathways and have wide-ranging cellular targets (Liu and Nash, 2012). The 25 upregulated genes also had a higher proportion annotated as 'membrane' or 'transport' genes, when compared to the background. Together these could suggest that *NFATC2* KD led to some regulatory changes relating to membrane-associated kinase signalling, but these are non-specific findings and further pathway analyses were required.

Genes involved in actin cytoskeleton were deregulated after *NFATC2* KD at several levels of the annotated pathway, showing primarily upregulated activity. Cytoskeletal assembly has been demonstrated as important to the activity of mechanosensitive cation channels, specifically in leukaemia cells (Staruschenko *et al.*, 2005). Actin polymerisation and specific cytoskeletal proteins have been shown to regulate calcium levels and transport within the cell, including with SOCE specifically, and also to regulate NFAT trafficking to the nucleus (Rivas *et al.*, 2004, Martin-Romero *et al.*, 2017). Additionally, NFAT activity acts downstream of SH2-domain kinase VAV and cytoskeletal reorganisation in T cells (Penninger and Crabtree, 1999). It is possible that *NFATC2* KD in THP-1 has triggered feedback signalling to upregulate calcium signalling and compensate for lost NFATc2 activity. However, this may be a biological response that would be observed in non-malignant cells, and it is not clear what the oncogenic significance of this is.

The cytoskeleton is well-characterised in cancer cell pathology, but its role is often linked to metastatic properties of cells (Aseervatham, 2020), which do not apply so readily to the pathology of AML cells. Changes in the actin cytoskeleton structure can be observed in apoptotic cells (Veselská *et al.*, 2003), but this seems an unlikely cause of the changes given that apoptosis was not observed after

transduction with both shRNA constructs. One study showed that cytoskeleton remodelling was involved in resistance of $FLT3^{ITD}$ AML to midostaurin, but this was likely mediated through interaction with stromal cells (Garitano-Trojaola *et al.*, 2021). Overall, it seems most likely that the involvement of the cytoskeleton after *NFATC2* KD is related to upregulated calcium/NFAT trafficking, or some other uncharacterised mechanism.

GSEA is a more global analysis of pathway perturbation as it focuses on patterns of small changes across the transcriptome, as opposed to relying on statistically significant changes in fewer genes (Subramanian *et al.*, 2005). GSEA identified 5 pathways relating to translation or ribosomal activity which followed *NFATC2* KD, albeit some of these pathways contained overlapping genes. This result may be secondary to deregulation of pathways upstream of ribosomal biogenesis or translation, such as PI3K/AKT/mTOR signalling, which is often constitutively active in AML (Khanna-Gupta, 2011). *NFATC2* may also directly bind genes which regulate any of the 250 components which are involved in ribosome synthesis (Awad *et al.*, 2019), but this has not been shown previously. Irrespective of the mechanism, it is not surprising that some cycle arrest is observed in THP-1 after *NFATC2* KD, given that translational processes are suppressed.

Upregulation of oxidative phosphorylation (OXPHOS) after *NFATC2* is an interesting finding, since THP-1 cells have been shown to be highly dependent on OXPHOS as means of energy production, as opposed to glycolysis (Suganuma *et al.*, 2010). Often cancer cells are thought to be more dependent on aerobic glycolysis, though the two processes can cooperate. Cancer cells are also known to utilise alternative sources of energy, including glutamine (Zheng, 2012). NFAT proteins directly upregulate genes involved in glycolysis in T cells (Vaeth *et al.*, 2017), though this may not be the case in OXPHOS-dependent THP-1.

Translation is highly energy-dependent and so intrinsically linked to cellular metabolic pathways. In fact, the cellular nutrient status can influence a number of RNA-led processes, from transcription through to translation and post-transcriptional modification (Lee and Tu, 2017). Additionally, some of the pathways which regulate translation also regulate metabolic activity (e.g. PI3K/AKT/mTOR) (Zheng, 2012). It may be the case that OXPHOS upregulation is a feedback mechanism, following reduced translational capacity with *NFATC2* KD,

or that deregulation occurs upstream of these processes. Numerous inhibitors of metabolic pathways have been trialled in leukaemias (Soltani *et al.*, 2021) and these would prove useful in investigating the role of NFAT further in these highly complex metabolic interactions.

Upregulation of DNA repair pathways following *NFATC2* KD is consistent with the cell cycle arrest observed in THP-1. Arrest at G1/S or G2/M exists to allow the recruitment of various pathways in DNA repair, including homologous recombination (HR) and non-homologous end joining (NHEJ) (Huang and Zhou, 2020). *TP53* normally has countless functions in these DNA repair processes (Williams and Schumacher, 2016), but these do not apply to in THP-1 cells, where *TP53* carries a 26 bp deletion, resulting in minimal functional expression of the gene (Sugimoto *et al.*, 1992). Increased transcription of DNA repair pathway genes following *NFATC2* KD could reinforce the suggestion discussed in Chapter 4; that *NFATC2* suppresses p53-independent mechanisms of DNA repair in proliferating THP-1 cells. Note also that pathways related to the G2/M cell cycle checkpoint and E2F, a regulator of the G1/S transition (Huang and Zhou, 2020), were upregulated after KD with 1 of 2 sh*NFATC2* constructs. Further exploration of other DNA damage proteins after *NFATC2* KD, such as ATM, ATR and the BRCA family, would expand the understanding of this picture further.

5.3.5.3 RNA-Seq data: *MYC* signalling and *NFATC2* in THP-1

Numerous targets of *MYC* from the MSigDB Hallmark datasets were downregulated following *NFATC2* KD. Additionally, NFATc2 ChIP-Seq found a c-Myc-binding DNA motif ('CACGTG') to be enriched, though narrowly missed statistical significance. *MYC* is a transcriptional regulator which acts downstream of myriad signalling pathways (Dang, 2012) and is well-characterised as an oncogene, which can arise through mutation, chromosome translocation or gene amplification (Meyer and Penn, 2008). *MYC* expression can be prognostic for survival in karyotype-normal AML (Ohanian *et al.*, 2014) and it has been shown to be involved in MLL-fusion/HOXA9-driven signalling in AML (Miyamoto *et al.*, 2021). Small molecule inhibition of c-Myc protein can also reverse the leukaemic phenotype in AML cells *in vitro* (Huang *et al.*, 2006).

Downregulation of *MYC* targets with *NFATC2* KD could suggest that they co-regulate, or function in a hierarchical axis. The evidence from this study suggests

that *MYC* expression is unlikely to be under the strict control of *NFATC2*, given that KD of *NFATC2* had minimal effect on *MYC*/c-Myc protein levels, and *NFATC2* overexpression raised c-Myc expression marginally. NFATc2 has been shown to bind the *MYC* promoter and differentially regulate its expression, although this was not in leukaemia cells (Mognol *et al.*, 2012). Interestingly, Singh *et al*. found enhanced cyclin D activity downstream of TGF-β in pancreatic cancer cells to be mediated by a NFATc1/c2-c-Myc axis (Singh *et al.*, 2010). Given that *TGFBR2* was significantly upregulated after *NFATC2* KD in THP-1 cells (in addition to *CCND1* downregulation), this may be a mechanism of interest for further investigation in this cell line.

It is possible that NFATc2 protein functions downstream of c-Myc, however the binding of NFATc2 to a known c-Myc binding motif suggests that they may in fact co-bind to particular transcriptional targets. It is known that c-Myc functions as part of a large 'interactome' in oncogenesis (Conacci-Sorrell *et al.*, 2014). Additionally, NFATs rely on transcriptional partners for transcriptional activity at the DNA level, although c-Myc was not identified as an NFAT partner in one large proteomic screen in T cells (Gabriel *et al.*, 2016). However, it is plausible that c-Myc and NFATc2 are transcriptional partners in THP-1 myeloid oncogenesis. Note also that c-Myc is a transcriptional regulator of glycolysis genes (Vaeth and Feske, 2018) and so this could be a common target shared with NFATc2 in THP-1 cells. The next stages of this investigation require a further look at NFATc2-c-Myc physical interaction, shared binding partners and transcriptional signatures in AML.

5.3.5.4 RNA-Seq data: deregulation of STK33 targets

The MSigDB pathway describing STK33 targets was generated from AML cell lines with *STK33* KD (Scholl *et al.*, 2009). STK33 is a kinase with structural similarity to the CAMK family (Mujica *et al.*, 2005) but is not well-characterised. Enrichment of putative STK33 target genes in the *NFATC2* KD data is supported by the fact that they were derived from AML cells, although not THP-1 cells. The study from Scholl *et al*. found THP-1 cells to not be sensitive to *STK33* KD, but other AML cell lines (e.g., NOMO-1) were, and it was hypothesised that only *KRAS*-dependent AML cells were *STK33*-dependent. A later study found numerous $KRAS^{mut}$ AML cell lines were not sensitive to STK33 kinase inhibitor BRD-8899, suggesting that it may have

non-kinase roles or that the original findings were non-specific shRNA effects (Luo *et al.*, 2012).

AML cell lines, including THP-1, were also found to be insensitive to a second STK33 kinase small molecule inhibitor, ML281 (Weïwer *et al.*, 2012). It is therefore not surprising that THP-1 cells were found to be insensitive to ML281 in this study. Furthermore, STK33 expression appeared to be poorly detected in these THP-1 cells, potentially due to a lack of experimental optimisation. Detailed information on the regulation of STK33 kinase activity has not been fully published, and the mechanism of action of ML281 on STK33 is not clear, although the ATP-binding loop is likely key to ST33 kinase activity. In addition, there is evidence that STK33 may self-regulate through autophosphorylation, like some other CAMKs (Brauksiepe *et al.*, 2008, Scholl *et al.*, 2009, Luo *et al.*, 2012). With the paucity of information around STK33 functional biochemistry and the data presented here, it is challenging to devise any hypotheses around its function (or lack thereof) in THP-1 cells.

Despite this, STK33 has been demonstrated to be important in oncogenic signalling of other cancer types. For example, in pancreatic cancer STK33 was found to drive oncogenesis downstream of HIF-1α, another regulator of glycolysis and OXPHOS (Kong *et al.*, 2017). STK33 protein may also drive hepatocellular carcinoma tumour growth by binding to c-Myc and upregulating its transcriptional activity (Yang *et al.*, 2016). Therefore, there are a number of biologically meaningful reasons to implicate STK33 and NFAT together in the context of the GSEA results.

CAMKs are not usually reported as regulators of NFAT activity, although they are activated downstream of calcium signalling in parallel to calcineurin (Hogan *et al.*, 2003). There is some evidence that CAMKs can regulate NFATs in cardiac tissue (MacDonnell *et al.*, 2009). It was observed here that ML281 inhibition of STK33 kinase activity marginally increased NFATc2 phosphorylation, and so it could be hypothesised that a calcium-STK33-NFATc2 axis exists in THP-1 cells. This requires further validation. In addition, further work into STK33 may require more sophisticated proteomics-based approaches, in order to fully understand its behaviour in the AML cell.

5.3.5.5 RNA-Seq data: *NFATC2* KD in other AML cells

A subset of genes was taken from THP-1 with either *NFATC2* KD or overexpression, to validate in other cell lines. The only statistically significant change observed was in the gene *SPNS3*, in HL-60 cells. It also appeared to be downregulated to varying extents in NOMO-1 and OCI-AML3. *SPNS3* is a sphingolipid transporter with some prognostic value in AML (Huang *et al.*, 2020). Sphingolipids are involved in calcium transport (Pulli *et al.*, 2018) and, therefore, could be involved in an *NFATC2*-driven mechanism.

All 5 cell lines, namely THP-1, NOMO-1, HL-60, Kasumi-1 and OCI-AML3, exhibited slightly differing phenotypes after *NFATC2* KD and carry distinct cytogenetic profiles, however they shared a common transcriptional profile with regard to these 6 genes, after *NFATC2* KD. Individual KD of these genes in a variety of AML cell lines would provide evidence as to the dependence of the cells' signalling on these, and possibly an understanding of the underlying mechanism(s).

In contrast, the murine MLL-AF9 BM did not show a similar trend (with regard to murine ortholog genes) after *Nfatc2* KD. The greatest change observed, *Vldlr* downregulation, was opposite to that observed in human cell lines. This difference may reflect distinctions in murine signalling networks, the artificial nature of the model, and/or that the *NFATC2*-driven regulation of these genes in human cells is not dependent on MLL-AF9 signalling.

5.3.5.6 NFATc2 ChIP-Seq in THP-1 cells

The quality metrics shown for the NFATc2 ChIP-Seq indicate that there is a lower signal-to-noise ratio than the guidance suggests is desirable (ENCODE, 2012). This may reflect inadequate formaldehyde fixation, low antibody binding to target and/or weak protein binding to DNA. NFATs are known to bind weakly to DNA in isolation (Mognol *et al.*, 2016) and so this could be a contributing factor. Replicate 2 appeared to show a higher proportion of reads in peaks, a larger fragment size and also a stronger peak near the TSS when observed in a metagene plot. Given the stronger enrichment observed, this was carried forward for analysis, however PCA revealed that the 3 replicates do not share similar variance across the data. As such, pooling of these replicates may have led to an increased statistical type II error rate in the data, leading to a more conservative estimate of the number of genes deregulated with statistical significance.

It is encouraging to observe almost 40% of ChIP-Seq peaks within 5 kb of the TSS – here, designated as promoter sites. NFATs are best characterised as binding to the IL-2 promoter, where they bind multiple different consensus sites which are not functionally redundant (Jain *et al.*, 1995, Rooney *et al.*, 1995b). NFAT also binds proximal promoter sites in the IL-4 gene (Rooney *et al.*, 1995a). The clustering of peaks around TSS is the expected binding pattern observed in other TFs (Koudritsky and Domany, 2008) and the data here indicate that NFATc2 binding is more often found distal to the promoter. The large proportion of sites in introns and distal intergenic regions could signal distal enhancer sites, which have also been characterised for NFAT in the control of GM-CSF, IL-3 and IL-4 transcription (Cockerill *et al.*, 1993, Agarwal *et al.*, 2000).

A high proportion of pseudogenes was identified in the NFATc2 binding targets. Pseudogenes are generally characterised as non-functional, although some studies have provided evidence for their contribution to transcriptional regulation of their parent genes. However, they often share close sequence homology with the parent but are incapable of transcription (Pink *et al.*, 2011). It is possible that NFATc2 can bind these genes, but the significance of this is unknown.

Functions of the NFATc2-bound protein coding genes appear to resemble closely some of the functional pathways identified in RNA-Seq analysis, such as: actin cytoskeleton regulation, ribosomal structure, calcium regulation and

mitochondrial function. It is disappointing that almost none of the identified RNA-Seq and ChIP-Seq targets overlapped in these analyses. This may reflect that pathways under the regulation of NFATc2 signalling are mediated by indirect effects, by NFATc2 binding to other genes. If this is the case, intermediate pathways and signalling should be defined in future work. Alternatively, NFATc2 may regulate some transcription through distal enhancers, or enhancer-promoter interactions, which are not immediately clear from individual binding site analysis. The occupancy of NFATc2 at specific histone modifications in murine dendritic cells (Yu *et al.*, 2014) suggests that it is also worth investigating the relationship with histone modification sites in THP-1 cells. Finally, the technical variation identified in these sequencing analyses may have led to a lower sensitivity of detection, so some binding or transcriptional targets have not been identified.

5.3.5.7 NFATc2 binding motifs

In addition to the c-Myc-binding motif a number of others were identified with statistical significance. Motif #2 was similar to a known NFATc1-binding motif, although statistical significance was poor for this association after correction for multiple testing. It also contains a portion of the 'GGAAA' motif that is described in some papers as a more general NFAT-binding site (Badran *et al.*, 2002, Simonett *et al.*, 2021). Additionally, the 'GGAAA' sequence can be observed in motif #4 identified in THP-1, and 'GAAA' in motif #5. Overall, these provide confidence that the observed binding sites are real.

The ZNF384 binding motif was a novel finding since little is published on this gene in AML. ZNF384 is more commonly associated with B-ALL as a fusion gene (Shinsuke *et al.*, 2017) and the significance of this here is not clear. As suggested for c-Myc, ZNF384 protein could be another binding partner of NFATc2 in THP-1 cells or AML more generally.

Ultimately, these binding motifs provide data for further analyses. These may be investigated in other ChIP-Seq datasets in AML to investigate DNA and histone methylation, in addition to the binding distribution of other TFs, such as c-Myc. Together these could provide further insight into the binding activity of NFATc2 and putative transcriptional partners in AML.

5.3.5.8 Translating the findings to patient datasets

Given the finding that *NFATC2* expression could stratify patients by survival outcome in the TARGET-AML dataset, it was important to review the effects of putative *NFATC2* targets' expression in these patients also. A number of identified genes were shown to impact survival outcomes in patients. This included targets identified by both RNA-Seq and ChIP-Seq analyses. Correlation analyses of these patients' data revealed some clusters which may indicate shared functional properties of some genes, including in genes which did not impact survival. These warrant further exploration in other AML datasets and functional analyses of specific clusters, which may provide clues to function and the role(s) of *NFATC2* in AML.

6 General discussion & future directions

This study aimed to test whether AML cells were dependent on *NFATC2* for survival and/or oncogenic function. The study characterised *NFATC2* in AML cell lines and its impact on patients' clinical outcomes, the effect on AML cells of *NFATC2* depletion, and its transcriptional/binding targets in these cells.

The suitability of the cell lines chosen for this study remains an outstanding question when interpreting the transferability of its findings to patients' AML biology. The open-source patient data analysis (Section 3.3.1) clearly demonstrated that *NFATC2* expression tends to be lower in AML subtypes with a more differentiated morphology, where FAB classification M5 tended to have the lowest. However, the cell lines studied do not reflect this pattern well. *NFATC2* expression was among the highest in THP-1 and NOMO-1 cells, which are both models of M5 AML, while expression was lower or undetectable in Kasumi-1, OCI-AML3 and HL-60, which are M2, M4 and M2, respectively.

As such, it is not clear if these models would truly reflect the oncogenic activity of NFATc2 that may be present in primary patients' AML cells. In generating cell lines, the very process of immortalisation and/or long-term culturing *in vitro* can contribute to the acquisition of substantial biological differences from the patient cells of origin (Kennedy and Barabé, 2008).

In spite of this, the number of differing mutations represented by the cell lines chosen covers a wide range of profiles that occur in AML, albeit lacking the heterogeneity that is present in an individual patient sample. All of these cell lines showed some degree of sensitivity to *NFATC2* KD and so while it may be challenging to infer any mechanistic relationship with individual mutations, there does appear to be a unifying dependence on *NFATC2* expression. Cells with increased apoptosis after *NFATC2* KD (HL-60 and OCI-AML3) share $NRAS^{mut}$, but also carry a number of other distinct aberrations. Cell lines with cell cycle arrest observed after *NFATC2* KD are molecularly heterogeneous, and in most cases the observed effects did not meet statistical significance at the timepoints used. Further exploration of cell cycle checkpoints and apoptosis at varying timepoints and using alternative methods could characterise these observations better.

It is possible that these AML cells with distinct driver mutations shared common oncogenic signalling through *NFATC2,* but this would be surprising given the molecular heterogeneity of AML, which is normally a major barrier to developing novel therapies. NFATs function by forming large complexes at DNA binding sites with downstream effectors of multiple signalling pathways (Crabtree and Olson, 2002) and they are known integrators of growth factor signalling in healthy myeloid tissue (Fric *et al.*, 2012a, Fric *et al.*, 2014). One possibility is that, in AML and healthy myeloid cells, NFATc2 is not dispensable for basic cellular function and therefore is non-selective for AML. Testing these inhibitors and potentially *NFATC2* depletion in non-AML tissue would be important to explore this. Additionally, the roles of the *NFAT* family are essential for T cells (Rao *et al.*, 1997a), meaning that NFAT inhibition might exceed desirable toxicity thresholds in patients, as has been observed for clinical drugs such as Tacrolimus and CsA previously.

It is unclear how the dependence of AML cells on *NFATC2* could be tested *in vivo* or in patients, given the lack of specific inhibitors, although steps towards this have been proposed (Kitamura and Kaminuma, 2021). This study showed that THP-1 cells are sensitive to calcium and calcineurin inhibition, which may be at least partially dependent on blockade of NFATc2 translocation (Section 4.3.1). However, Kasumi-1 cells were not sensitive to calcineurin-NFAT inhibition, despite being sensitive to *NFATC2* KD. Considerably lower *NFATC2* expression in Kasumi-1 cells might be the cause of lower drug sensitivity, but the kinetics of this were not investigated. Alternatively, NFATc2 may have some role(s) not dependent on calcineurin, through which KD – and not calcineurin/NFAT inhibition - would exert an observable functional effect. In summary, the phenotype observed after *NFATC2* KD do correlate closely with the phenotype following calcineurin-NFAT inhibition by CsA or VIVIT-11R, based on these data alone. This is not surprising, given the additional unknown contribution of NFATc1/NFATc3 inhibition by CsA/VIVIT-11R in these cells.

Better characterisation of calcium and NFATc2 biochemistry in AML cell lines would help to elucidate the nuances of its signalling network. The data in this study show that global phosphorylation changes in response to pathway inhibition/stimulation were often contrary to expectations. For example, an increase of highly-phosphorylated NFATc2 was observed in the nuclear protein

fraction after calcium chelation with EGTA. More sophisticated characterisation of phosphorylation sites and protein-protein interactions, as described in other cell types (Villar *et al.*, 2006, Sharma *et al.*, 2011, Gabriel *et al.*, 2016), would be beneficial to understand the dynamics of the calcium-NFATc2 axis in AML cells. Further optimisation of ionomycin treatment in AML cell lines, such as altering the concentrations of inhibitors or timepoints, is also necessary to robustly compare the response of NFATc2 with those observed in T cells. Additionally, characterising the effects of *NFATC1* KD and *NFATC3* KD in these cell lines would elucidate whether these genes/proteins are required for the AML cells' survival and/or growth. An understanding of the cells' dependencies on all of *NFATC1-3* would support further hypotheses on the mechanism of calcineurin-NFAT inhibition in these cells and clarify the value of this pathway as a therapeutic target.

However, other indirect means of targeting NFATc2 may be possible. Targeting of TFs has long been a challenging area of therapeutics development due to the non-kinase activity of many TFs and their subcellular location. For example, *MYC* is ubiquitous in normal physiology and a number of cancers, but is often described as 'undruggable'. Various indirect means of Myc inhibition are under investigation, which include targeting of Myc heterodimer partners, inhibition of Myc-stabilising proteins (such as PIM1 kinase) and blockade of epigenetic regulators which regulate MYC (such as BRD4) (Bushweller, 2019, Llombart and Mansour, 2022). Similar strategies have been described for NFAT, including the modification of nuclear import/export, increasing NFAT degradation, and prevention of NFAT-DNA binding (Qin *et al.*, 2014), but these are not well-developed.

The RNA-Seq and ChIP-Seq analyses together suggested that NFATc2 and c-Myc could be interaction partners, or that they co-regulate downstream targets, in the THP-1 model of MLL-AF9 AML. This offers a key insight into the possible mechanism(s) of NFATc2-led oncogenesis and opens therapeutic opportunities. The next step of this study would be to investigate compounds which indirectly target Myc and are known to be effective against AML *in vitro* and *in vivo* (Brondfield et al., 2015). Combination therapy of Myc and calcineurin-NFAT inhibition could potentially target transcriptional complexes which are selectively activated in AML cells. This could also circumvent the need for doses of an NFAT inhibitor at a level which is toxic to ordinary tissues.

Further information is needed to determine the exact relationship of Myc and NFATc2. ChIP-Seq of Myc in THP-1 cells would be useful to validate the finding that a subset of NFATc2-binding sites is common to Myc. Direct IP of Myc and NFATc2, separately, would also shed light on whether these two TFs are direct interaction partners. Together this information would inform the drug discovery process, if looking to target any NFATc2/Myc interaction.

The downstream mechanism(s) regulated by NFATc2 and Myc in THP-1 cells should also be elucidated. Tan *et al.* found that, in fibroblasts, cyclin D1 was a key suppressor of apoptotic responses in the context of Myc (Tan *et al.*, 2000). In fact, Myc is an established regulator of aberrant cyclin D1 activity in various cancers (Liao *et al.*, 2007). This thesis study found that *NFATC2* maintains *CCND1* (encoding cyclin D1) expression, either directly or indirectly, and so this could be a common feature of NFATc2/Myc activity. It is possible to target cyclin D activity therapeutically, but this is more commonly achieved through cyclin-dependent kinase (CDK) inhibition (Aleem and Arceci, 2015). A better understanding of the signalling between NFATc2 and cell cycle regulators is needed to highlight therapeutic vulnerabilities of the cells. The next stage of study would involve characterising the activity of cyclin D-related cell cycle proteins, including CDK4, CDK6, retinoblastoma protein (Rb) and E2F (Fu *et al.*, 2004).

Comparing the perturbations of cell cycle regulators across differing AML cell lines with *NFATC2* KD might provide some clarity on the relationship between cell phenotype and mutational status. For example, as hypothesised in Section 4.4.2, the deregulation of *CCND1* and the cell cycle after *NFATC2* KD in THP-1 cells may relate to the signalling downstream of $TP53^{mut}$ and/or $NRAS^{mut}$ within those cells. A comparison of *CCND1* transcription at late timepoints after *NFATC2* KD in $TP53^{wt}$ and $NRAS^{wt}$ cell lines could indicate whether these mutations were important to the *NFATC2*/*CCND1* relationship.

Comparison of THP-1 cells to MLL-AF9 murine BM with *Nfatc2* KD revealed that key genes, including *Ccnd1*, were deregulated in the opposite direction to the human orthologs when *NFATC2* was knocked down in THP-1 cells (Sections 4.3.2&4.3.4). This difference could be attributed to inter-species differences in orthologous signalling pathways, differing mutational profiles and/or that *NFATC2* signalling is unrelated to MLL-AF9 oncogenesis. Additionally, the MLL-AF9 BM

model did not develop from a process of leukaemogenesis, by which mutations accumulate sequentially (such as in CHIP or ARCH). As such, the artificial nature of these MLL-AF9 cells could be missing uncharacterised (epi)genetic features which arise from these more 'organic' processes, thus making it difficult to compare them to THP-1 cells which have been derived from patient tissue.

Additionally, the targets of *NFATC2* KD identified by RNA-Seq were not consistently deregulated after *NFATC2* KD in AML cell lines of differing cytogenetic backgrounds (Section 5.2.3.1). For example, THP-1 shared none of the putative *NFATC2* transcriptional targets with MOLM-13. In order to determine the most significant targets of *NFATC2*, a high-throughput shRNA/siRNA KD screen focusing on a common subset of the targets identified by RNA-Seq could be conducted in some of these cell lines. Genes which are deemed to be essential for survival may be taken forward as *NFATC2*-driven regulators of leukaemogenesis and could be investigated as therapeutic targets independently.

Of the targets identified by sequencing analyses, 13 were used to stratify patient survival in the TARGET-AML cohort (Section 5.3.5.8), indicating that they have some prognostic value in AML. The influence of these genes on these patients' clinical course is likely to be multi-dimensional. Major prognostic factors in paediatric AML include the cytogenetic profile and the kinetics of response to chemotherapy (Hoffman *et al.*, 2021). Cytogenetic subgroup analyses of the data may reveal greater prognostic importance for these *NFATC2* targets in specific groups of patients, yet small patient numbers per group makes this challenging.

The finding that *NFATC2* expression was higher at patient relapse, in another cohort (Section 3.3.1), suggests the emergence of therapy-resistant clones which are more *NFATC2*-dependent. It is worth noting that THP-1 cells, in addition to most of the other AML cell lines examined, were derived from patients at relapse, and so this study may be biased towards relapsed AML. Further study into the role of *NFATC2* in the development of relapse, resistance to chemotherapy, and resistance to other inhibitors would be valuable in determining whether *NFATC2* (and its putative gene targets) are related to a more specific mechanism in relapsed or *de novo* AML. AML cells, particularly LSCs, can be shielded from chemotherapy or targeted inhibition by the BM microenvironment and so the AML blast-niche interactions are of interest in the development of relapse (Tabe and

Konopleva, 2015). Such interactions are often mediated by secreted factors, which is particularly relevant to *NFAT*s, as regulators of cytokine transcription. As such, cytokine profiling and multi-dimensional *in vitro* modelling should be considered when assessing the contribution of *NFATC2* to AML oncogenesis and relapse, particularly in primary patient cells.

Exploring the prognostic value of this 13-gene list in other datasets could also prove useful. Firstly, to determine by univariate analysis if these genes' expression would be predictive of outcome in the TCGA and BEAT-AML datasets, since *NFATC2* expression itself was not found to be prognostic. Secondly, to develop a more robust gene signature predictive of patient outcomes and/or relapse using the sequencing data from *NFATC2* KD. Similar approaches have been taken for AML with a 17-gene stemness score (Ng *et al.*, 2016), a 29-gene/cytogenetic score (Tobias *et al.*, 2018) and a 9-gene score for targets of *KDM4A* (Massett et al., 2021).

Finally, given that *NFATC2* was found to be a target of *KDM4A* in MLL-AF9, it seems pertinent to return to the KDM4A-PAF1-NFATC2 axis. *NFATC2* KD did not result in deregulation of KDM4A enzymatic targets H3K9me3 or H3K27me3, diminishing the possibility that NFATc2 co-regulates *KDM4A* enzymatic activity. Comparison of histone methylation patterns in THP-1, for which data are available, with the ChIP-Seq binding sites of NFATc2, KDM4A and PAF1, may reveal more about the mechanics of the KDM4A-PAF1-NFATc2 axis. These epigenetic data in the context of KDM4A and PAF1 function in MLL-AF9 AML may further advance our understanding of the function of all three regulators in AML.

7 Conclusive remarks & future work summary

The findings of this study are valuable in the characterisation of *NFATC2* in AML cells and the pursuit of novel drug targets. It is now clearer that *NFATC2* is indispensable for AML function and/or survival. Novel downstream targets of *NFATC2* have been elucidated and, as such, any of these genes may be significant players in leukaemogenesis. *NFATC2* and some of its putative targets have prognostic value in the patient data examined, and so an initial connection between *NFATC2* function and clinical outcome has been established. The next stages should involve more thorough characterisation of the precise mechanisms of *NFATC2* function in AML cells, to determine how it interacts with other players within the cell. This includes the established onco-protein Myc, which this study

has demonstrated as a likely interactor of NFATc2. Specifically, data characterising the role of *NFATC2* in the cell cycle, cytokine release and resistance to chemotherapy should be sought. Open-source patient data should be maximally explored to determine the clinical applicability of a *NFATC2* target prognostic score, and these targets should be independently investigated *in vitro*. While awaiting the development of a specific NFATc2 inhibitor, this study has provided the grounds to explore further the therapeutic value of the NFATc2 signalling network, in the pursuit of a novel AML treatment strategy.

8 List of References

Agarwal, S., Avni, O. & Rao, A. 2000. Cell-Type-Restricted Binding of the Transcription Factor NFAT to a Distal IL-4 Enhancer In Vivo. *Immunity,* 12**,** 643-652.

Akashi, K., Traver, D., Miyamoto, T. & Weissman, I. L. 2000. A clonogenic common myeloid progenitor that gives rise to all myeloid lineages. *Nature,* 404**,** 193-197.

Alam, M. S., Gaida, M. M., Debnath, S., Tagad, H. D., Miller Jenkins, L. M., Appella, E., Rahman, M. J. & Ashwell, J. D. 2018. Unique properties of TCR-activated p38 are necessary for NFAT-dependent T-cell activation. *PLoS biology,* 16**,** e2004111-e2004111.

Aleem, E. & Arceci, R. J. 2015. Targeting cell cycle regulators in hematologic malignancies. *Frontiers in Cell and Developmental Biology,* 3.

Amadori, S., Venditti, A., Del Poeta, G., Stasi, R., Buccisano, F., Bruno, A., Tamburini, A., Cox, M. C., Maffei, L., Aronica, G., Simone, M. D., Adorno, G., Masi, M., Tribalto, M. & Papa, G. 1996. Minimally differentiated acute myeloid leukemia (AML-M0): a distinct clinico-biologic entity with poor prognosis. *Ann Hematol,* 72**,** 208-15.

Angelini, C. & Costa, V. 2014. Understanding gene regulatory mechanisms by integrating ChIP-seq and RNA-seq data: statistical solutions to biological problems. *Frontiers in Cell and Developmental Biology,* 2.

Aramburu, J., García-Cózar, F., Raghavan, A., Okamura, H., Rao, A. & Hogan, P. G. 1998. Selective Inhibition of NFAT Activation by a Peptide Spanning the Calcineurin Targeting Site of NFAT. *Molecular Cell,* 1**,** 627-637.

Aramburu, J., Yaffe, M. B., López-RodríGuez, C., Cantley, L. C., Hogan, P. G. & Rao, A. 1999. Affinity-Driven Peptide Selection of an NFAT Inhibitor More Selective Than Cyclosporin A. *Science,* 285**,** 2129.

Arber, D. A., Orazi, A., Hasserjian, R., Thiele, J., Borowitz, M. J., Le Beau, M. M., Bloomfield, C. D., Cazzola, M. & Vardiman, J. W. 2016. The 2016 revision to the World Health Organization classification of myeloid neoplasms and acute leukemia. *Blood,* 127**,** 2391.

Aseervatham, J. 2020. Cytoskeletal Remodeling in Cancer. *Biology (Basel),* 9.

Awad, D., Prattes, M., Kofler, L., Rössler, I., Loibl, M., Pertl, M., Zisser, G., Wolinski, H., Pertschy, B. & Bergler, H. 2019. Inhibiting eukaryotic ribosome biogenesis. *BMC Biology,* 17**,** 46.

Bacher, U., Haferlach, T., Schoch, C., Kern, W. & Schnittger, S. 2006. Implications of NRAS mutations in AML: a study of 2502 patients. *Blood,* 107**,** 3847-3853.

Badran, B. M., Wolinsky, S. M., Burny, A. & Willard-Gallo, K. E. 2002. Identification of Three NFAT Binding Motifs in the 5′-Upstream Region of the Human CD3 γ Gene That Differentially Bind NFATc1, NFATc2, and NF-κB p50. *Journal of Biological Chemistry,* 277**,** 47136-47148.

Baksh, S., Decaprio, J. A. & Burakoff, S. J. 2000. Calcineurin regulation of the mammalian G0/G1 checkpoint element, cyclin dependent kinase 4. *Oncogene,* 19**,** 2820-7.

Baksh, S., Widlund, H. R., Frazer-Abel, A. A., Du, J., Fosmire, S., Fisher, D. E., Decaprio, J. A., Modiano, J. F. & Burakoff, S. J. 2002. NFATc2-Mediated Repression of Cyclin-Dependent Kinase 4 Expression. *Molecular Cell,* 10**,** 1071-1081.

Balgobind, B. V., Zwaan, C. M., Pieters, R. & Van Den Heuvel-Eibrink, M. M. 2011. The heterogeneity of pediatric MLL-rearranged acute myeloid leukemia. *Leukemia,* 25**,** 1239-1248.

Ball, B. J., Hsu, M., Devlin, S. M., Arcila, M., Roshal, M., Zhang, Y., Famulare, C. A., Goldberg, A. D., Cai, S. F., Dunbar, A., Epstein-Peterson, Z., Menghrajani, K. N., Glass, J. L., Taylor, J., Viny, A. D., Giralt, S. S., Gyurkocza, B., Shaffer, B. C., Tamari, R., *et al*. 2021. The prognosis and durable clearance of RAS mutations in patients with acute myeloid leukemia receiving induction chemotherapy. *American Journal of Hematology,* 96**,** E171-E175.

Barbosa, C. M., Bincoletto, C., Barros, C. C., Ferreira, A. T. & Paredes-Gamero, E. J. 2014. PLCγ2 and PKC are important to myeloid lineage commitment triggered by M-SCF and G-CSF. *J Cell Biochem,* 115**,** 42-51.

Barbosa, K., Li, S., Adams, P. D. & Deshpande, A. J. 2019. The role of TP53 in acute myeloid leukemia: Challenges and opportunities. *Genes, Chromosomes and Cancer,* 58**,** 875-888.

Baumgart, S., Chen, N.-M., Zhang, J.-S., Billadeau, D. D., Gaisina, I. N., Kozikowski, A. P., Singh, S. K., Fink, D., Ströbel, P., Klindt, C., Zhang, L., Bamlet, W. R., Koenig, A., Hessmann, E., Gress, T. M., Ellenrieder, V. & Neesse, A. 2016. GSK-3ß Governs Inflammation-Induced NFATc2 Signaling Hubs to Promote Pancreatic Cancer Progression. *Molecular cancer therapeutics,* 15**,** 491-502.

Bécart, S., Charvet, C., Canonigo Balancio, A. J., De Trez, C., Tanaka, Y., Duan, W., Ware, C., Croft, M. & Altman, A. 2007. SLAT regulates Th1 and Th2 inflammatory responses by controlling Ca2+/NFAT signaling. *The Journal of clinical investigation,* 117**,** 2164-2175.

Behrens, K., Maul, K., Tekin, N., Kriebitzsch, N., Indenbirken, D., Prassolov, V., Müller, U., Serve, H., Cammenga, J. & Stocking, C. 2017. RUNX1 cooperates with FLT3-ITD to induce leukemia. *The Journal of experimental medicine,* 214**,** 737-752.

Bendickova, K., Tidu, F. & Fric, J. 2017. Calcineurin-NFAT signalling in myeloid leucocytes: new prospects and pitfalls in immunosuppressive therapy. *EMBO Mol Med,* 9**,** 990-999.

Benjamini, Y. & Hochberg, Y. 1995. Controlling the False Discovery Rate: A Practical and Powerful Approach to Multiple Testing. *Journal of the Royal Statistical Society. Series B (Methodological),* 57**,** 289-300.

Berry, W. L. & Janknecht, R. 2013. KDM4/JMJD2 histone demethylases: epigenetic regulators in cancer cells. *Cancer research,* 73**,** 2936-2942.

Bierer, B. E., Holländer, G., Fruman, D. & Burakoff, S. J. 1993. Cyclosporin A and FK506: molecular mechanisms of immunosuppression and probes for transplantation biology. *Curr Opin Immunol,* 5**,** 763-73.

Boila, L. D., Chatterjee, S. S., Banerjee, D. & Sengupta, A. 2018. KDM6 and KDM4 histone lysine demethylases emerge as molecular therapeutic targets in human acute myeloid leukemia. *Experimental Hematology,* 58**,** 44-51.e7.

Bolger, A. M., Lohse, M. & Usadel, B. 2014. Trimmomatic: a flexible trimmer for Illumina sequence data. *Bioinformatics (Oxford, England),* 30**,** 2114-2120.

Bonnet, D. & Dick, J. E. 1997. Human acute myeloid leukemia is organized as a hierarchy that originates from a primitive hematopoietic cell. *Nature Medicine,* 3**,** 730-737.

Borgne, A. & Golsteyn, R. M. 2003. The role of cyclin-dependent kinases in apoptosis. *Prog Cell Cycle Res,* 5**,** 453-9.

Borrow, J., Dyer, S. A., Akiki, S. & Griffiths, M. J. 2019. Terminal deoxynucleotidyl transferase promotes acute myeloid leukemia by priming FLT3-ITD replication slippage. *Blood,* 134**,** 2281-2290.

Bowen, D. T., Frew, M. E., Hills, R., Gale, R. E., Wheatley, K., Groves, M. J., Langabeer, S. E., Kottaridis, P. D., Moorman, A. V., Burnett, A. K. & Linch, D. C. 2005. RAS mutation in acute myeloid leukemia is associated with distinct cytogenetic subgroups but does not influence outcome in patients younger than 60 years. *Blood,* 106**,** 2113-2119.

Brauksiepe, B., Mujica, A. O., Herrmann, H. & Schmidt, E. R. 2008. The Serine/threonine kinase Stk33 exhibits autophosphorylation and phosphorylates the intermediate filament protein Vimentin. *BMC biochemistry,* 9**,** 25-25.

Bretz, C. A., Savage, S. R., Capozzi, M. E., Suarez, S. & Penn, J. S. 2015. NFAT isoforms play distinct roles in TNFα-induced retinal leukostasis. *Scientific Reports,* 5**,** 14963.

Brondfield, S., Umesh, S., Corella, A., Zuber, J., Rappaport, A. R., Gaillard, C., Lowe, S. W., Goga, A. & Kogan, S. C. 2015. Direct and indirect targeting of MYC to treat acute myeloid leukemia. *Cancer chemotherapy and pharmacology,* 76**,** 35-46.

Brown, G. & Ceredig, R. 2019. Modeling the Hematopoietic Landscape. *Frontiers in Cell and Developmental Biology,* 7.

Buggins, A. G. S., Milojkovic, D., Arno, M. J., Lea, N. C., Mufti, G. J., Thomas, N. S. B. & Hirst, W. J. R. 2001. Microenvironment Produced by Acute Myeloid Leukemia Cells Prevents T Cell Activation and Proliferation by Inhibition of NF-κB, c-Myc, and pRb Pathways. *The Journal of Immunology,* 167**,** 6021-6030.

Bushweller, J. H. 2019. Targeting transcription factors in cancer — from undruggable to reality. *Nature Reviews Cancer,* 19**,** 611-624.

Canaani, J., Beohou, E., Labopin, M., Socié, G., Huynh, A., Volin, L., Cornelissen, J., Milpied, N., Gedde-Dahl, T., Deconinck, E., Fegueux, N., Blaise, D., Mohty, M. & Nagler, A. 2017. Impact of FAB classification on predicting outcome in acute myeloid leukemia, not otherwise specified, patients undergoing allogeneic stem cell transplantation in CR1: An analysis of 1690 patients from the acute leukemia working party of EBMT. *American Journal of Hematology,* 92**,** 344-350.

Carvalho, L. D. S., Teixeira, L. K., Carrossini, N., Caldeira, A. T. N., Ansel, K. M., Rao, A. & Viola, J. P. B. 2007. The NFAT1 Transcription Factor is a Repressor of Cyclin A2 Gene Expression. *Cell Cycle,* 6**,** 1789-1795.

Chan, P. M. 2011. Differential signaling of Flt3 activating mutations in acute myeloid leukemia: a working model. *Protein & Cell,* 2**,** 108-115.

Chan, S. M., Thomas, D., Corces-Zimmerman, M. R., Xavy, S., Rastogi, S., Hong, W.-J., Zhao, F., Medeiros, B. C., Tyvoll, D. A. & Majeti, R. 2015. Isocitrate dehydrogenase 1 and 2 mutations induce BCL-2 dependence in acute myeloid leukemia. *Nature Medicine,* 21**,** 178-184.

Chaudhury, S., O'connor, C., Cañete, A., Bittencourt-Silvestre, J., Sarrou, E., Prendergast, Á., Choi, J., Johnston, P., Wells, C. A., Gibson, B. & Keeshan, K. 2018. Age-specific biological and molecular profiling distinguishes paediatric from adult acute myeloid leukaemias. *Nature Communications,* 9**,** 5280.

Chen, L., Glover, J. N. M., Hogan, P. G., Rao, A. & Harrison, S. C. 1998. Structure of the DNA-binding domains from NFAT, Fos and Jun bound specifically to DNA. *Nature,* 392, 42-48.

Chen, X., Bargonetti, J. & Prives, C. 1995. p53, through p21 (WAF1/CIP1), induces cyclin D1 synthesis. *Cancer Res,* 55, 4257-63.

Chen, X., Burkhardt, D. B., Hartman, A. A., Hu, X., Eastman, A. E., Sun, C., Wang, X., Zhong, M., Krishnaswamy, S. & Guo, S. 2019. MLL-AF9 initiates transformation from fast-proliferating myeloid progenitors. *Nature Communications,* 10, 5767.

Choudhary, C., Brandts, C., Schwable, J., Tickenbrock, L., Sargin, B., Ueker, A., Böhmer, F.-D., Berdel, W. E., Müller-Tidow, C. & Serve, H. 2007. Activation mechanisms of STAT5 by oncogenic Flt3-ITD. *Blood,* 110, 370.

Chuvpilo, S., Avots, A., Berberich-Siebelt, F., Glöckner, J., Fischer, C., Kerstan, A., Escher, C., Inashkina, I., Hlubek, F., Jankevics, E., Brabletz, T. & Serfling, E. 1999. Multiple NF-ATc Isoforms with Individual Transcriptional Properties Are Synthesized in T Lymphocytes. *The Journal of Immunology,* 162, 7294.

Chuvpilo, S., Jankevics, E., Tyrsin, D., Akimzhanov, A., Moroz, D., Jha, M. K., Schulze-Luehrmann, J., Santner-Nanan, B., Feoktistova, E., König, T., Avots, A., Schmitt, E., Berberich-Siebelt, F., Schimpl, A. & Serfling, E. 2002. Autoregulation of NFATc1/A Expression Facilitates Effector T Cells to Escape from Rapid Apoptosis. *Immunity,* 16, 881-895.

Cockerill, P. N., Shannon, M. F., Bert, A. G., Ryan, G. R. & Vadas, M. A. 1993. The granulocyte-macrophage colony-stimulating factor/interleukin 3 locus is regulated by an inducible cyclosporin A-sensitive enhancer. *Proceedings of the National Academy of Sciences of the United States of America,* 90, 2466-2470.

Conacci-Sorrell, M., Mcferrin, L. & Eisenman, R. N. 2014. An Overview of MYC and Its Interactome. *Cold Spring Harbor Perspectives in Medicine,* 4.

Corces-Zimmerman, M. R., Hong, W.-J., Weissman, I. L., Medeiros, B. C. & Majeti, R. 2014. Preleukemic mutations in human acute myeloid leukemia affect epigenetic regulators and persist in remission. *Proceedings of the National Academy of Sciences of the United States of America,* 111, 2548-2553.

Cozzio, A., Passegué, E., Ayton, P. M., Karsunky, H., Cleary, M. L. & Weissman, I. L. 2003. Similar MLL-associated leukemias arising from self-renewing stem cells and short-lived myeloid progenitors. *Genes & development,* 17, 3029-3035.

Crabtree, G. R. & Olson, E. N. 2002. NFAT Signaling: Choreographing the Social Lives of Cells. *Cell,* 109, S67-S79.

Csh. 2010. *Recipe: Sorensen's phosphate buffer (0.133 M, pH 7.2)* [Online]. Cold Spring Harb Protoc. Available: http://cshprotocols.cshlp.org/content/2010/10/pdb.rec12327.full [Accessed 2022].

Dai, Y., Jin, F., Wu, W. & Kumar, S. K. 2019. Cell cycle regulation and hematologic malignancies. *Blood Science,* 1.

Dang, C. V. 2012. MYC on the path to cancer. *Cell,* 149, 22-35.

Daver, N., Venugopal, S. & Ravandi, F. 2021. FLT3 mutated acute myeloid leukemia: 2021 treatment algorithm. *Blood Cancer Journal,* 11, 104.

De Kouchkovsky, I. & Abdul-Hay, M. 2016. 'Acute myeloid leukemia: a comprehensive review and 2016 update'. *Blood Cancer Journal,* 6, e441.

Didier, C., Cavelier, C., Quaranta, M., Galcera, M. O., Demur, C., Laurent, G., Manenti, S. & Ducommun, B. 2008. G2/M checkpoint stringency is a key parameter in the sensitivity of AML cells to genotoxic stress. *Oncogene,* 27**,** 3811-3820.

Ding, L. Ley, T.J., Larson, D.E., Miller, C.A., Koboldt, D.C., Welch, J.S., Ritchey, J.K., Young, M.A., Lamprecht, T., McLellan, M.D., McMichael, J.F., Wallis, J.W., Lu, C., Shen, D., Harris, C.C., Dooling, D.J., Fulton, R.S., Fulton, L.L., Chen, K., *et al*. 2012. Clonal evolution in relapsed acute myeloid leukemia revealed by whole genome sequencing. *Nature,* 481, 506-510.

Dinardo, C. D., Jonas, B. A., Pullarkat, V., Thirman, M. J., Garcia, J. S., Wei, A. H., Konopleva, M., Döhner, H., Letai, A., Fenaux, P., Koller, E., Havelange, V., Leber, B., Esteve, J., Wang, J., Pejsa, V., Hájek, R., Porkka, K., Illés, Á., *et al*. 2020. Azacitidine and Venetoclax in Previously Untreated Acute Myeloid Leukemia. *New England Journal of Medicine,* 383**,** 617-629.

Docking, T. R., Parker, J. D. K., Jädersten, M., Duns, G., Chang, L., Jiang, J., Pilsworth, J. A., Swanson, L. A., Chan, S. K., Chiu, R., Nip, K. M., Mar, S., Mo, A., Wang, X., Martinez-Høyer, S., Stubbins, R. J., Mungall, K. L., Mungall, A. J., Moore, R. A., *et al*. 2021. A clinical transcriptome approach to patient stratification and therapy selection in acute myeloid leukemia. *Nature Communications,* 12**,** 2474.

Döhner, H., Estey, E., Grimwade, D., Amadori, S., Appelbaum, F. R., Büchner, T., Dombret, H., Ebert, B. L., Fenaux, P., Larson, R. A., Levine, R. L., Lo-Coco, F., Naoe, T., Niederwieser, D., Ossenkoppele, G. J., Sanz, M., Sierra, J., Tallman, M. S., Tien, H.-F., *et al*. 2017. Diagnosis and management of AML in adults: 2017 ELN recommendations from an international expert panel. *Blood,* 129**,** 424-447.

Dutta, S., Pregartner, G., Rücker, F. G., Heitzer, E., Zebisch, A., Bullinger, L., Berghold, A., Döhner, K. & Sill, H. 2020. Functional Classification of TP53 Mutations in Acute Myeloid Leukemia. *Cancers,* 12**,** 637.

Elloumi, H. Z., Maharshak, N., Rao, K. N., Kobayashi, T., Ryu, H. S., Mühlbauer, M., Li, F., Jobin, C. & Plevy, S. E. 2012. A cell permeable peptide inhibitor of NFAT inhibits macrophage cytokine expression and ameliorates experimental colitis. *PLoS One,* 7**,** e34172.

Ema, H., Morita, Y. & Suda, T. 2014. Heterogeneity and hierarchy of hematopoietic stem cells. *Exp Hematol,* 42**,** 74-82.e2.

Encode. 2012. *Quality Metrics* [Online]. Available: https://genome.ucsc.edu/ENCODE/qualityMetrics.html [Accessed 09/12/2021 2021].

Estey, E., Karp, J. E., Emadi, A., Othus, M. & Gale, R. P. 2020. Recent drug approvals for newly diagnosed acute myeloid leukemia: gifts or a Trojan horse? *Leukemia,* 34**,** 671-681.

Falini, B., Sciabolacci, S., Falini, L., Brunetti, L. & Martelli, M. P. 2021. Diagnostic and therapeutic pitfalls in NPM1-mutated AML: notes from the field. *Leukemia,* 35**,** 3113-3126.

Fan, Y., Hu, Y., Yan, C., Chen, Q., Nguyen, C., Dunn, B. K., Ries, R. E., Bolouri, H., Smith, J. L., Kolb, E. A., Meshinchi, S. & Meerzaman, D. 2020. Altered Transcriptome in Pediatric AML Compared with Normal Hematopoiesis. *British Journal of Cancer Research,* 3.

Fathi, A. T. & Chabner, B. A. 2011. FLT3 inhibition as therapy in acute myeloid leukemia: a record of trials and tribulations. *The oncologist,* 16**,** 1162-1174.

Fathi, A. T. & Chen, Y.-B. 2011. Treatment of FLT3-ITD acute myeloid leukemia. *American journal of blood research,* 1**,** 175-189.

Feng, J., Liu, T., Qin, B., Zhang, Y. & Liu, X. S. 2012. Identifying ChIP-seq enrichment using MACS. *Nature protocols,* 7**,** 1728-1740.

Fric, J., Lim, C. X. F., Koh, E. G. L., Hofmann, B., Chen, J., Tay, H. S., Mohammad Isa, S. a. B., Mortellaro, A., Ruedl, C. & Ricciardi-Castagnoli, P. 2012a. Calcineurin/NFAT signalling inhibits myeloid haematopoiesis. *EMBO molecular medicine,* 4**,** 269-282.

Fric, J., Lim, C. X. F., Mertes, A., Lee, B. T. K., Viganò, E., Chen, J., Zolezzi, F., Poidinger, M., Larbi, A., Strobl, H., Zelante, T. & Ricciardi-Castagnoli, P. 2014. Calcium and calcineurin-NFAT signaling regulate granulocyte-monocyte progenitor cell cycle via Flt3-L. *Stem cells (Dayton, Ohio),* 32**,** 3232-3244.

Fric, J., Zelante, T., Wong, A. Y. W., Mertes, A., Yu, H.-B. & Ricciardi-Castagnoli, P. 2012b. NFAT control of innate immunity. *Blood,* 120**,** 1380.

Fu, M., Wang, C., Li, Z., Sakamaki, T. & Pestell, R. G. 2004. Minireview: Cyclin D1: Normal and Abnormal Functions. *Endocrinology,* 145**,** 5439-5447.

Gabriel, C. H., Gross, F., Karl, M., Stephanowitz, H., Hennig, A. F., Weber, M., Gryzik, S., Bachmann, I., Hecklau, K., Wienands, J., Schuchhardt, J., Herzel, H., Radbruch, A., Krause, E. & Baumgrass, R. 2016. Identification of Novel Nuclear Factor of Activated T Cell (NFAT)-associated Proteins in T Cells. *Journal of Biological Chemistry,* 291**,** 24172-24187.

García-Rodríguez, C. & Rao, A. 2000. Requirement for integration of phorbol 12-myristate 13-acetate and calcium pathways is preserved in the transactivation domain of NFAT1. *European Journal of Immunology,* 30**,** 2432-2436.

Garitano-Trojaola, A., Sancho, A., Götz, R., Eiring, P., Walz, S., Jetani, H., Gil-Pulido, J., Da Via, M. C., Teufel, E., Rhodes, N., Haertle, L., Arellano-Viera, E., Tibes, R., Rosenwald, A., Rasche, L., Hudecek, M., Sauer, M., Groll, J., Einsele, H., *et al.* 2021. Actin cytoskeleton deregulation confers midostaurin resistance in FLT3-mutant acute myeloid leukemia. *Communications Biology,* 4**,** 799.

Gelsi-Boyer, V., Brecqueville, M., Devillier, R., Murati, A., Mozziconacci, M.-J. & Birnbaum, D. 2012. Mutations in ASXL1 are associated with poor prognosis across the spectrum of malignant myeloid diseases. *Journal of Hematology & Oncology,* 5**,** 12.

Gilliland, D. G. & Griffin, J. D. 2002. The roles of FLT3 in hematopoiesis and leukemia. *Blood,* 100**,** 1532-1542.

Graef, I. A., Gastier, J. M., Francke, U. & Crabtree, G. R. 2001. Evolutionary relationships among Rel domains indicate functional diversification by recombination. *Proceedings of the National Academy of Sciences,* 98**,** 5740.

Green, M. R., Sambrook, J. 2012. *Molecular Cloning: A Laboratory Manual,* Cold Spring Harbor, New York, Cold Spring Harbor Laboratory Press.

Gregory, M. A., Phang, T. L., Neviani, P., Alvarez-Calderon, F., Eide, C. A., O'hare, T., Zaberezhnyy, V., Williams, R. T., Druker, B. J., Perrotti, D. & Degregori, J. 2010. Wnt/Ca(2+)/NFAT signaling maintains survival of Ph(+) leukemia cells upon inhibition of Bcr-Abl. *Cancer cell,* 18**,** 74-87.

Gwack, Y., Feske, S., Srikanth, S., Hogan, P. G. & Rao, A. 2007. Signalling to transcription: Store-operated Ca2+ entry and NFAT activation in lymphocytes. *New Developments in Ca2+ Influx Channels and their Regulation,* 42**,** 145-156.

Han, E. K. H., Ng, S. C., Arber, N., Begemann, M. & Weinstein, I. B. 1999. Roles of cyclin D1 and related genes in growth inhibition, senescence and apoptosis. *Apoptosis,* 4**,** 213-219.

Harris, William j., Huang, X., Lynch, James t., Spencer, Gary j., Hitchin, James r., Li, Y., Ciceri, F., Blaser, Julian g., Greystoke, Brigit f., Jordan, Allan m., Miller, Crispin j., Ogilvie, Donald j. & Somervaille, Tim c. P. 2012. The Histone Demethylase KDM1A Sustains the Oncogenic Potential of MLL-AF9 Leukemia Stem Cells. *Cancer Cell,* 21**,** 473-487.

Haubner, S., Perna, F., Köhnke, T., Schmidt, C., Berman, S., Augsberger, C., Schnorfeil, F. M., Krupka, C., Lichtenegger, F. S., Liu, X., Kerbs, P., Schneider, S., Metzeler, K. H., Spiekermann, K., Hiddemann, W., Greif, P. A., Herold, T., Sadelain, M. & Subklewe, M. 2019. Coexpression profile of leukemic stem cell markers for combinatorial targeted therapy in AML. *Leukemia,* 33**,** 64-74.

Healy, N. C. & O'connor, R. 2009. Sequestration of PDLIM2 in the cytoplasm of monocytic/macrophage cells is associated with adhesion and increased nuclear activity of NF-kappaB. *J Leukoc Biol,* 85**,** 481-90.

Hess, J. L. 2004. MLL: a histone methyltransferase disrupted in leukemia. *Trends in Molecular Medicine,* 10**,** 500-507.

Heuser, M., Thol, F. & Ganser, A. 2016. Clonal Hematopoiesis of Indeterminate Potential. *Deutsches Arzteblatt international,* 113**,** 317-322.

Hitomi, M. & Stacey, D. W. 1999. Cyclin D1 production in cycling cells depends on Ras in a cell-cycle-specific manner. *Current Biology,* 9**,** 1075-S2.

Hoffman, A. E., Schoonmade, L. J. & Kaspers, G. J. L. 2021. Pediatric relapsed acute myeloid leukemia: a systematic review. *Expert Review of Anticancer Therapy,* 21**,** 45-52.

Hogan, P. G., Chen, L., Nardone, J. & Rao, A. 2003. Transcriptional regulation by calcium, calcineurin, and NFAT. *Genes & Development,* 17**,** 2205-2232.

Hosen, N., Park, C. Y., Tatsumi, N., Oji, Y., Sugiyama, H., Gramatzki, M., Krensky, A. M. & Weissman, I. L. 2007. CD96 is a leukemic stem cell-specific marker in human acute myeloid leukemia. *Proc Natl Acad Sci U S A,* 104**,** 11008-13.

Huai, Q., Kim, H.-Y., Liu, Y., Zhao, Y., Mondragon, A., Liu, J. O. & Ke, H. 2002. Crystal structure of calcineurin-cyclophilin-cyclosporin shows common but distinct recognition of immunophilin-drug complexes. *Proceedings of the National Academy of Sciences of the United States of America,* 99**,** 12037-12042.

Huang, M.-J., Cheng, Y.-C., Liu, C.-R., Lin, S. & Liu, H. E. 2006. A small-molecule c-Myc inhibitor, 10058-F4, induces cell-cycle arrest, apoptosis, and myeloid differentiation of human acute myeloid leukemia. *Experimental Hematology,* 34**,** 1480-1489.

Huang, R.-X. & Zhou, P.-K. 2020. DNA damage response signaling pathways and targets for radiotherapy sensitization in cancer. *Signal Transduction and Targeted Therapy,* 5**,** 60.

Huang, W., Qian, T., Cheng, Z., Zeng, T., Si, C., Liu, C., Deng, C., Ye, X., Liu, Y., Cui, L. & Fu, L. 2020. Prognostic significance of Spinster homolog gene family in acute myeloid leukemia. *Journal of Cancer,* 11**,** 4581-4588.

Hwang, S. M. 2020. Classification of acute myeloid leukemia. *Blood research,* 55**,** S1-S4.

Iris, Z. U., Florian, B. & Veronika, S. 2017. p27 in FLT3-driven acute myeloid leukemia: many roads lead to ruin. *Haematologica,* 102**,** 1299-1301.

Ishikawa, F., Yoshida, S., Saito, Y., Hijikata, A., Kitamura, H., Tanaka, S., Nakamura, R., Tanaka, T., Tomiyama, H., Saito, N., Fukata, M., Miyamoto, T., Lyons, B., Ohshima, K., Uchida, N., Taniguchi, S., Ohara, O., Akashi, K., Harada, M., *et al*. 2007. Chemotherapy-resistant human AML stem cells home to and engraft within the bone-marrow endosteal region. *Nature Biotechnology,* 25**,** 1315-1321.

Iwasaki, H., Mizuno, S., Arinobu, Y., Ozawa, H., Mori, Y., Shigematsu, H., Takatsu, K., Tenen, D. G. & Akashi, K. 2006. The order of expression of transcription factors directs hierarchical specification of hematopoietic lineages. *Genes Dev,* 20**,** 3010-21.

Jain, J., Loh, C. & Rao, A. 1995. Transcriptional regulation of the IL-2 gene. *Current Opinion in Immunology,* 7**,** 333-342.

Jaiswal, S., Fontanillas, P., Flannick, J., Manning, A., Grauman, P. V., Mar, B. G., Lindsley, R. C., Mermel, C. H., Burtt, N., Chavez, A., Higgins, J. M., Moltchanov, V., Kuo, F. C., Kluk, M. J., Henderson, B., Kinnunen, L., Koistinen, H. A., Ladenvall, C., Getz, G., *et al*. 2014. Age-Related Clonal Hematopoiesis Associated with Adverse Outcomes. *New England Journal of Medicine,* 371**,** 2488-2498.

Jan, M., Snyder, T. M., Corces-Zimmerman, M. R., Vyas, P., Weissman, I. L., Quake, S. R. & Majeti, R. 2012. Clonal Evolution of Preleukemic Hematopoietic Stem Cells Precedes Human Acute Myeloid Leukemia. *Science Translational Medicine,* 4**,** 149ra118.

Jolma, A., Yan, J., Whitington, T., Toivonen, J., Nitta, K. R., Rastas, P., Morgunova, E., Enge, M., Taipale, M., Wei, G., Palin, K., Vaquerizas, J. M., Vincentelli, R., Luscombe, N. M., Hughes, T. R., Lemaire, P., Ukkonen, E., Kivioja, T. & Taipale, J. 2013. DNA-binding specificities of human transcription factors. *Cell,* 152**,** 327-39.

Jordan, C. T. 2007. The leukemic stem cell. *Best practice & research. Clinical haematology,* 20**,** 13-18.

Juárez-Salcedo, L. M., Desai, V. & Dalia, S. 2019. Venetoclax: evidence to date and clinical potential. *Drugs in context,* 8**,** 212574-212574.

Juliette, L., Cécile, P., Christine, T., Emmanuel, R., Pascal, T., Denis, C., Ollivier, L., Xavier, T., Claude, G., Karïn, G.-M., Stephen, D. R., Rebecca, J. B., Pierre, B., Claude, P., Sylvie, C., Herve, D. & Sylvie, C. 2019. Gemtuzumab ozogamicin for de novo acute myeloid leukemia: final efficacy and safety updates from the open-label, phase III ALFA-0701 trial. *Haematologica,* 104**,** 113-119.

Kantarjian, H., Kadia, T., Dinardo, C., Daver, N., Borthakur, G., Jabbour, E., Garcia-Manero, G., Konopleva, M. & Ravandi, F. 2021. Acute myeloid leukemia: current progress and future directions. *Blood Cancer Journal,* 11**,** 41.

Kar, P., Mirams, G. R., Christian, H. C. & Parekh, A. B. 2016. Control of NFAT Isoform Activation and NFAT-Dependent Gene Expression through Two Coincident and Spatially Segregated Intracellular Ca2+ Signals. *Molecular Cell,* 64**,** 746-759.

Kar, P., Nelson, C. & Parekh, A. B. 2011. Selective activation of the transcription factor NFAT1 by calcium microdomains near Ca2+ release-activated Ca2+ (CRAC) channels. *The Journal of biological chemistry,* 286**,** 14795-14803.

Karpurapu, M., Wang, D., Van Quyen, D., Kim, T. K., Kundumani-Sridharan, V., Pulusani, S. & Rao, G. N. 2010. Cyclin D1 is a bona fide target gene of

NFATc1 and is sufficient in the mediation of injury-induced vascular wall remodeling. *J Biol Chem,* 285**,** 3510-23.

Keating, S., Suciu, S., De Witte, T., Mandelli, F., Willemze, R., Resegotti, L., Broccia, G., Thaler, J., Labar, B., Damasio, E., Bizzi, B., Rotoli, B., Vekhoff, A., Muus, P., Petti, M. C., Dardenne, M., Solbu, G., Vegna, M. L. & Zittoun, R. A. 1996. Prognostic factors of patients with acute myeloid leukemia (AML) allografted in first complete remission: an analysis of the EORTC-GIMEMA AML 8A trial. The European Organization for Research and Treatment of Cancer (EORTC) and the Gruppo Italiano Malattie Ematologiche Maligne dell' Adulto (GIMEMA) Leukemia Cooperative Groups. *Bone Marrow Transplant,* 17**,** 993-1001.

Kelly, L. M., Liu, Q., Kutok, J. L., Williams, I. R., Boulton, C. L. & Gilliland, D. G. 2002. FLT3 internal tandem duplication mutations associated with human acute myeloid leukemias induce myeloproliferative disease in a murine bone marrow transplant model. *Blood,* 99**,** 310.

Kennedy, J. A. & Barabé, F. 2008. Investigating human leukemogenesis: from cell lines to in vivo models of human leukemia. *Leukemia,* 22**,** 2029-2040.

Kent, A., Vasu, S., Schatz, D., Monson, N., Devine, S., Smith, C., Gutman, J. A. & Pollyea, D. A. 2020. Glasdegib as maintenance therapy for patients with AML and MDS patients at high risk for postallogeneic stem cell transplant relapse. *Blood Advances,* 4**,** 3102-3108.

Khanna-Gupta, A. 2011. Regulation and deregulation of mRNA translation during myeloid maturation. *Experimental hematology,* 39**,** 133-141.

Kiani, A., Habermann, I., Haase, M., Feldmann, S., Boxberger, S., Sanchez-Fernandez, M. A., Thiede, C., Bornhäuser, M. & Ehninger, G. 2004. Expression and regulation of NFAT (nuclear factors of activated T cells) in human CD34+ cells: down-regulation upon myeloid differentiation. *Journal of Leukocyte Biology,* 76**,** 1057-1065.

Kiani, A., Kuithan, H., Kuithan, F., Kyttälä, S., Habermann, I., Temme, A., Bornhäuser, M. & Ehninger, G. 2007. Expression analysis of nuclear factor of activated T cells (NFAT) during myeloid differentiation of CD34+ cells: regulation of Fas ligand gene expression in megakaryocytes. *Experimental Hematology,* 35**,** 757-770.

Kikushige, Y., Shima, T., Takayanagi, S., Urata, S., Miyamoto, T., Iwasaki, H., Takenaka, K., Teshima, T., Tanaka, T., Inagaki, Y. & Akashi, K. 2010. TIM-3 is a promising target to selectively kill acute myeloid leukemia stem cells. *Cell Stem Cell,* 7**,** 708-17.

Kitamura, N. & Kaminuma, O. 2021. Isoform-Selective NFAT Inhibitor: Potential Usefulness and Development. *International journal of molecular sciences,* 22**,** 2725.

Klein, A. M. & Simons, B. D. 2011. Universal patterns of stem cell fate in cycling adult tissues. *Development,* 138**,** 3103-3111.

Klintmalm, G. 1994. A review of FK506: A new immunosuppressant agent for the prevention and rescue of graft rejection. *Transplantation Reviews,* 8**,** 53-63.

Kong, F., Kong, X., Du, Y., Chen, Y., Deng, X., Zhu, J., Du, J., Li, L., Jia, Z., Xie, D., Li, Z. & Xie, K. 2017. STK33 Promotes Growth and Progression of Pancreatic Cancer as a Critical Downstream Mediator of HIF1α. *Cancer Research,* 77**,** 6851-6862.

Koudritsky, M. & Domany, E. 2008. Positional distribution of human transcription factor binding sites. *Nucleic acids research,* 36**,** 6795-6805.

Krivtsov, A. V. & Armstrong, S. A. 2007. MLL translocations, histone modifications and leukaemia stem-cell development. *Nature Reviews Cancer,* 7**,** 823.

Krivtsov, A. V., Figueroa, M. E., Sinha, A. U., Stubbs, M. C., Feng, Z., Valk, P. J. M., Delwel, R., Döhner, K., Bullinger, L., Kung, A. L., Melnick, A. M. & Armstrong, S. A. 2013. Cell of origin determines clinically relevant subtypes of MLL-rearranged AML. *Leukemia,* 27**,** 852-860.

Krivtsov, A. V., Twomey, D., Feng, Z., Stubbs, M. C., Wang, Y., Faber, J., Levine, J. E., Wang, J., Hahn, W. C., Gilliland, D. G., Golub, T. R. & Armstrong, S. A. 2006. Transformation from committed progenitor to leukaemia stem cell initiated by MLL–AF9. *Nature,* 442**,** 818-822.

Kufe, D. W. & Major, P. P. 1982. Studies on the mechanism of action of cytosine arabinoside. *Med Pediatr Oncol,* 10 Suppl 1**,** 49-67.

Lagunas-Rangel, F. A. & Chávez-Valencia, V. 2017. FLT3–ITD and its current role in acute myeloid leukaemia. *Medical Oncology,* 34**,** 114.

Lapidot, T., Sirard, C., Vormoor, J., Murdoch, B., Hoang, T., Caceres-Cortes, J., Minden, M., Paterson, B., Caligiuri, M. A. & Dick, J. E. 1994. A cell initiating human acute myeloid leukaemia after transplantation into SCID mice. *Nature,* 367**,** 645-8.

Laurenti, E. & Göttgens, B. 2018. From haematopoietic stem cells to complex differentiation landscapes. *Nature,* 553**,** 418-426.

Lee, C.-D. & Tu, B. P. 2017. Metabolic influences on RNA biology and translation. *Critical reviews in biochemistry and molecular biology,* 52**,** 176-184.

Leung-Theung-Long, S., Mondor, I., Guiraud, M., Lamare, C., Nageleekar, V., Paulet, P.-E., Rincon, M. & Guerder, S. 2009. Impaired NFAT Transcriptional Activity in Antigen-Stimulated CD8 T Cells Linked to Defective Phosphorylation of NFAT Transactivation Domain. *The Journal of Immunology,* 182**,** 6807.

Levis, M., Murphy, K. M., Pham, R., Kim, K.-T., Stine, A., Li, L., Mcniece, I., Smith, B. D. & Small, D. 2005. Internal tandem duplications of the FLT3 gene are present in leukemia stem cells. *Blood,* 106**,** 673-680.

Levis, M. & Small, D. 2003. FLT3: ITDoes matter in leukemia. *Leukemia,* 17**,** 1738.

Ley, T. J., Miller, C., Ding, L., Raphael, B. J., Mungall, A. J., Robertson, A., Hoadley, K., Triche, T. J., Jr., Laird, P. W., Baty, J. D., Fulton, L. L., Fulton, R., Heath, S. E., Kalicki-Veizer, J., Kandoth, C., Klco, J. M., Koboldt, D. C., Kanchi, K. L., Kulkarni, S., *et al*. 2013. Genomic and epigenomic landscapes of adult de novo acute myeloid leukemia. *N Engl J Med,* 368**,** 2059-74.

Li, B. & Dewey, C. N. 2011. RSEM: accurate transcript quantification from RNA-Seq data with or without a reference genome. *BMC Bioinformatics,* 12**,** 323.

Li, H. 2013. Aligning sequence reads, clone sequences and assembly contigs with BWA-MEM. *arXiv preprint arXiv:1303.3997*.

Li, H., Rao, A. & Hogan, P. G. 2011a. Interaction of calcineurin with substrates and targeting proteins. *Trends Cell Biol,* 21**,** 91-103.

Li, L., Bailey, E., Greenblatt, S., Huso, D. & Small, D. 2011b. Loss of the wild-type allele contributes to myeloid expansion and disease aggressiveness in FLT3/ITD knockin mice. *Blood,* 118**,** 4935-4945.

Li, L., Piloto, O., Kim, K. T., Ye, Z., Nguyen, H. B., Yu, X., Levis, M., Cheng, L. & Small, D. 2007. FLT3/ITD expression increases expansion, survival and entry into cell cycle of human haematopoietic stem/progenitor cells. *Br J Haematol,* 137**,** 64-75.

Li, S., Garrett-Bakelman, F. E., Chung, S. S., Sanders, M. A., Hricik, T., Rapaport, F., Patel, J., Dillon, R., Vijay, P., Brown, A. L., Perl, A. E., Cannon, J.,

Bullinger, L., Luger, S., Becker, M., Lewis, I. D., To, L. B., Delwel, R., Löwenberg, B., *et al*. 2016. Distinct evolution and dynamics of epigenetic and genetic heterogeneity in acute myeloid leukemia. *Nature Medicine,* 22**,** 792-799.

Liao, D. J., Thakur, A., Wu, J., Biliran, H. & Sarkar, F. H. 2007. Perspectives on c-Myc, Cyclin D1, and their interaction in cancer formation, progression, and response to chemotherapy. *Crit Rev Oncog,* 13**,** 93-158.

List, A. F., Kopecky, K. J., Willman, C. L., Head, D. R., Persons, D. L., Slovak, M. L., Dorr, R., Karanes, C., Hynes, H. E., Doroshow, J. H., Shurafa, M. & Appelbaum, F. R. 2001. Benefit of cyclosporine modulation of drug resistance in patients with poor-risk acute myeloid leukemia: a Southwest Oncology Group study. *Blood,* 98**,** 3212-3220.

Liu, B. A. & Nash, P. D. 2012. Evolution of SH2 domains and phosphotyrosine signalling networks. *Philosophical transactions of the Royal Society of London. Series B, Biological sciences,* 367**,** 2556-2573.

Livak, K. J. & Schmittgen, T. D. 2001. Analysis of Relative Gene Expression Data Using Real-Time Quantitative PCR and the 2−ΔΔCT Method. *Methods,* 25**,** 402-408.

Llombart, V. & Mansour, M. R. 2022. Therapeutic targeting of “undruggable” MYC. *eBioMedicine,* 75.

Lo, Y. H., Wu, C. C., Shih, H. M. & Lai, M. Z. 2008. Selective activation of NFAT by promyelocytic leukemia protein. *Oncogene,* 27**,** 3821.

Love, M. I., Huber, W. & Anders, S. 2014. Moderated estimation of fold change and dispersion for RNA-seq data with DESeq2. *Genome Biology,* 15**,** 550.

Luo, C., Burgeon, E., Carew, J. A., Mccaffrey, P. G., Badalian, T. M., Lane, W. S., Hogan, P. G. & Rao, A. 1996a. Recombinant NFAT1 (NFATp) is regulated by calcineurin in T cells and mediates transcription of several cytokine genes. *Molecular and cellular biology,* 16**,** 3955-3966.

Luo, C., Burgeon, E. & Rao, A. 1996b. Mechanisms of transactivation by nuclear factor of activated T cells-1. *Journal of Experimental Medicine,* 184**,** 141-147.

Luo, T., Masson, K., Jaffe, J. D., Silkworth, W., Ross, N. T., Scherer, C. A., Scholl, C., Fröhling, S., Carr, S. A., Stern, A. M., Schreiber, S. L. & Golub, T. R. 2012. STK33 kinase inhibitor BRD-8899 has no effect on KRAS-dependent cancer cell viability. *Proceedings of the National Academy of Sciences,* 109**,** 2860.

Ma, W., Mishra, S., Gee, K., Mishra, J. P., Nandan, D., Reiner, N. E., Angel, J. B. & Kumar, A. 2007. Cyclosporin A and FK506 Inhibit IL-12p40 Production through the Calmodulin/Calmodulin-dependent Protein Kinase-activated Phosphoinositide 3-Kinase in Lipopolysaccharide-stimulated Human Monocytic Cells*. *Journal of Biological Chemistry,* 282**,** 13351-13362.

Macdonnell, S. M., Weisser-Thomas, J., Kubo, H., Hanscome, M., Liu, Q., Jaleel, N., Berretta, R., Chen, X., Brown, J. H., Sabri, A.-K., Molkentin, J. D. & Houser, S. R. 2009. CaMKII negatively regulates calcineurin-NFAT signaling in cardiac myocytes. *Circulation research,* 105**,** 316-325.

Machanick, P. & Bailey, T. L. 2011. MEME-ChIP: motif analysis of large DNA datasets. *Bioinformatics,* 27**,** 1696-1697.

Macian, F. 2005. NFAT proteins: key regulators of T-cell development and function. *Nat. Rev. Immunol.,* 5**,** 472.

Macián, F., López-Rodríguez, C. & Rao, A. 2001. Partners in transcription: NFAT and AP-1. *Oncogene,* 20**,** 2476-2489.

Mancini, M. & Toker, A. 2009. NFAT Proteins: Emerging Roles in Cancer Progression. *Nature reviews. Cancer,* 9, 810-820.

Marofi, F., Rahman, H. S., Al-Obaidi, Z. M. J., Jalil, A. T., Abdelbasset, W. K., Suksatan, W., Dorofeev, A. E., Shomali, N., Chartrand, M. S., Pathak, Y., Hassanzadeh, A., Baradaran, B., Ahmadi, M., Saeedi, H., Tahmasebi, S. & Jarahian, M. 2021. Novel CAR T therapy is a ray of hope in the treatment of seriously ill AML patients. *Stem Cell Research & Therapy,* 12, 465.

Martin-Romero, F. J., Lopez-Guerrero, A. M., Carlospascual-Caro & Pozo-Guisado, E. The Interplay between Cytoskeleton and Calcium Dynamics. 2017.

Massett, M. E., Monaghan, L., Patterson, S., Mannion, N., Bunschoten, R. P., Hoose, A., Marmiroli, S., Liskamp, R. M. J., Jørgensen, H. G., Vetrie, D., Michie, A. M. & Huang, X. 2021. A KDM4A-PAF1-mediated epigenomic network is essential for acute myeloid leukemia cell self-renewal and survival. *Cell Death & Disease,* 12, 573.

Masuda, T., Kubota, H., Sakuramoto, N., Hada, A., Horiuchi, A., Sasaki, A., Takeda, K., Takeda, M., Matsuo, H., Sugiyama, H., Adachi, S. & Kamikubo, Y. 2020. RUNX-NFAT Axis As a Novel Therapeutic Target for AML and T Cell Immunity. *Blood,* 136, 25-26.

Metzelder, S. K., Michel, C., Von Bonin, M., Rehberger, M., Hessmann, E., Inselmann, S., Solovey, M., Wang, Y., Sohlbach, K., Brendel, C., Stiewe, T., Charles, J., Ten Haaf, A., Ellenrieder, V., Neubauer, A., Gattenlöhner, S., Bornhäuser, M. & Burchert, A. 2015. NFATc1 as a therapeutic target in FLT3-ITD-positive AML. *Leukemia,* 29, 1470.

Meyer, N. & Penn, L. Z. 2008. Reflecting on 25 years with MYC. *Nature Reviews Cancer,* 8, 976-990.

Mitchell, C. A., Beall, J. A., Wells, J. R. & Gray, P. P. 1991. Growth and protein production kinetics of a murine myeloma cell line transfected with the human growth hormone gene. *Cytotechnology,* 5, 223-31.

Miyamoto, R., Kanai, A., Okuda, H., Komata, Y., Takahashi, S., Matsui, H., Inaba, T. & Yokoyama, A. 2021. HOXA9 promotes MYC-mediated leukemogenesis by maintaining gene expression for multiple anti-apoptotic pathways. *eLife,* 10, e64148.

Mognol, G. P., Carneiro, F. R. G., Robbs, B. K., Faget, D. V. & Viola, J. P. B. 2016. Cell cycle and apoptosis regulation by NFAT transcription factors: new roles for an old player. *Cell Death & Disease,* 7, e2199.

Mognol, G. P., De Araujo-Souza, P. S., Robbs, B. K., Teixeira, L. K. & Viola, J. P. 2012. Transcriptional regulation of the c-Myc promoter by NFAT1 involves negative and positive NFAT-responsive elements. *Cell Cycle,* 11, 1014-28.

Monlish, D. A., Bhatt, S. T. & Schuettpelz, L. G. 2016. The Role of Toll-Like Receptors in Hematopoietic Malignancies. *Frontiers in Immunology,* 7, 390.

Monticelli, S. & Rao, A. 2002. NFAT1 and NFAT2 are positive regulators of IL-4 gene transcription. *European Journal of Immunology,* 32, 2971-2978.

Mopin, A., Driss, V. & Brinster, C. 2016. A Detailed Protocol for Characterizing the Murine C1498 Cell Line and its Associated Leukemia Mouse Model. *J Vis Exp*.

Morita, K., Wang, F., Jahn, K., Hu, T., Tanaka, T., Sasaki, Y., Kuipers, J., Loghavi, S., Wang, S. A., Yan, Y., Furudate, K., Matthews, J., Little, L., Gumbs, C., Zhang, J., Song, X., Thompson, E., Patel, K. P., Bueso-Ramos, C. E., *et al*. 2020. Clonal evolution of acute myeloid leukemia revealed by high-throughput single-cell genomics. *Nature Communications,* 11, 5327.

Mu, Z. M., Chin, K. V., Liu, J. H., Lozano, G. & Chang, K. S. 1994. PML, a growth suppressor disrupted in acute promyelocytic leukemia. *Mol Cell Biol,* 14**,** 6858-67.

Mujica, A. O., Brauksiepe, B., Saaler-Reinhardt, S., Reuss, S. & Schmidt, E. R. 2005. Differential expression pattern of the novel serine/threonine kinase, STK33, in mice and men. *Febs j,* 272**,** 4884-98.

Mullen, P. 2004. PARP Cleavage as a Means of Assessing Apoptosis. *In:* LANGDON, S. P. (ed.) *Cancer Cell Culture: Methods and Protocols*. Totowa, NJ: Humana Press.

Murtagh, F. 1983. A Survey of Recent Advances in Hierarchical Clustering Algorithms. *The Computer Journal,* 26**,** 354-359.

Nair, R., Salinas-Illarena, A. & Baldauf, H.-M. 2021. New strategies to treat AML: novel insights into AML survival pathways and combination therapies. *Leukemia,* 35**,** 299-311.

Needleman, S. B. & Wunsch, C. D. 1970. A general method applicable to the search for similarities in the amino acid sequence of two proteins. *Journal of Molecular Biology,* 48**,** 443-453.

Haematological Malignancy Research Network. 2016. *Survival: Acute Myeloid Leukaemia* [Online]. Available: https://www.hmrn.org/statistics/survival [Accessed 2019].

Ng, S. W. K., Mitchell, A., Kennedy, J. A., Chen, W. C., Mcleod, J., Ibrahimova, N., Arruda, A., Popescu, A., Gupta, V., Schimmer, A. D., Schuh, A. C., Yee, K. W., Bullinger, L., Herold, T., Görlich, D., Büchner, T., Hiddemann, W., Berdel, W. E., Wörmann, B., *et al*. 2016. A 17-gene stemness score for rapid determination of risk in acute leukaemia. *Nature,* 540**,** 433-437.

Noguchi, H., Matsushita, M., Okitsu, T., Moriwaki, A., Tomizawa, K., Kang, S., Li, S.-T., Kobayashi, N., Matsumoto, S., Tanaka, K., Tanaka, N. & Matsui, H. 2004. A new cell-permeable peptide allows successful allogeneic islet transplantation in mice. *Nature Medicine,* 10**,** 305-309.

Notta, F., Zandi, S., Takayama, N., Dobson, S., Gan, O. I., Wilson, G., Kaufmann, K. B., Mcleod, J., Laurenti, E., Dunant, C. F., Mcpherson, J. D., Stein, L. D., Dror, Y. & Dick, J. E. 2016. Distinct routes of lineage development reshape the human blood hierarchy across ontogeny. *Science (New York, N.Y.),* 351**,** aab2116-aab2116.

Nowell Peter, C. 1976. The Clonal Evolution of Tumor Cell Populations. *Science,* 194**,** 23-28.

Ohanian, M., Kantarjian, H. M., Rozovski, U., Loghavi, S., Huh, Y., Abruzzo, L., Garcia-Manero, G., Ravandi, F., Borthakur, G., Stingo, F., Hu, P., Nguyen, M. H., Fox, P. S., Medeiros, L. J., Estrov, Z., Bueso-Ramos, C. E. & Cortes, J. E. 2014. Clinical significance of MYC expression in acute myeloid leukemia. *Journal of Clinical Oncology,* 32**,** 7094-7094.

Okamura, H., Aramburu, J., García-Rodríguez, C., Viola, J. P. B., Raghavan, A., Tahiliani, M., Zhang, X., Qin, J., Hogan, P. G. & Rao, A. 2000. Concerted Dephosphorylation of the Transcription Factor NFAT1 Induces a Conformational Switch that Regulates Transcriptional Activity. *Molecular Cell,* 6**,** 539-550.

Olsson, I., Bergh, G., Ehinger, M. & Gullberg, U. 1996. Cell differentiation in acute myeloid leukemia. *Eur J Haematol,* 57**,** 1-16.

Ono, R., Nakajima, H., Ozaki, K., Kumagai, H., Kawashima, T., Taki, T., Kitamura, T., Hayashi, Y. & Nosaka, T. 2005. Dimerization of MLL fusion proteins and

FLT3 activation synergize to induce multiple-lineage leukemogenesis. *The Journal of Clinical Investigation,* 115**,** 919-929.

Park, D. J., Kwon, A., Cho, B.-S., Kim, H.-J., Hwang, K.-A., Kim, M. & Kim, Y. 2020. Characteristics of DNMT3A mutations in acute myeloid leukemia. *Blood research,* 55**,** 17-26.

Park, M.-J., Sheng, R., Silkov, A., Jung, D.-J., Wang, Z.-G., Xin, Y., Kim, H., Thiagarajan-Rosenkranz, P., Song, S., Yoon, Y., Nam, W., Kim, I., Kim, E., Lee, D.-G., Chen, Y., Singaram, I., Wang, L., Jang, M. H., Hwang, C.-S., *et al.* 2016. SH2 Domains Serve as Lipid-Binding Modules for pTyr-Signaling Proteins. *Molecular cell,* 62**,** 7-20.

Paz-Priel, I. & Friedman, A. 2011. C/EBPα dysregulation in AML and ALL. *Critical reviews in oncogenesis,* 16**,** 93-102.

Pear, W. S., Nolan, G. P., Scott, M. L. & Baltimore, D. 1993. Production of high-titer helper-free retroviruses by transient transfection. *Proc Natl Acad Sci U S A,* 90**,** 8392-6.

Pellin, D., Loperfido, M., Baricordi, C., Wolock, S. L., Montepeloso, A., Weinberg, O. K., Biffi, A., Klein, A. M. & Biasco, L. 2019. A comprehensive single cell transcriptional landscape of human hematopoietic progenitors. *Nature Communications,* 10**,** 2395.

Penninger, J. M. & Crabtree, G. R. 1999. The Actin Cytoskeleton and Lymphocyte Activation. *Cell,* 96**,** 9-12.

Perl, A. E., Martinelli, G., Cortes, J. E., Neubauer, A., Berman, E., Paolini, S., Montesinos, P., Baer, M. R., Larson, R. A., Ustun, C., Fabbiano, F., Erba, H. P., Di Stasi, A., Stuart, R., Olin, R., Kasner, M., Ciceri, F., Chou, W.-C., Podoltsev, N., *et al.* 2019. Gilteritinib or Chemotherapy for Relapsed or Refractory FLT3-Mutated AML. *New England Journal of Medicine,* 381**,** 1728-1740.

Pink, R. C., Wicks, K., Caley, D. P., Punch, E. K., Jacobs, L. & Carter, D. R. F. 2011. Pseudogenes: pseudo-functional or key regulators in health and disease? *RNA (New York, N.Y.),* 17**,** 792-798.

Placke, T., Faber, K., Nonami, A., Putwain, S. L., Salih, H. R., Heidel, F. H., Krämer, A., Root, D. E., Barbie, D. A., Krivtsov, A. V., Armstrong, S. A., Hahn, W. C., Huntly, B. J., Sykes, S. M., Milsom, M. D., Scholl, C. & Fröhling, S. 2014. Requirement for CDK6 in MLL-rearranged acute myeloid leukemia. *Blood,* 124**,** 13-23.

Pollyea, D. A. & Jordan, C. T. 2017. Therapeutic targeting of acute myeloid leukemia stem cells. *Blood,* 129**,** 1627.

Prange, K. H. M., Mandoli, A., Kuznetsova, T., Wang, S. Y., Sotoca, A. M., Marneth, A. E., Van Der Reijden, B. A., Stunnenberg, H. G. & Martens, J. H. A. 2017. MLL-AF9 and MLL-AF4 oncofusion proteins bind a distinct enhancer repertoire and target the RUNX1 program in 11q23 acute myeloid leukemia. *Oncogene,* 36**,** 3346-3356.

Ptasinska, A., Pickin, A., Assi, S. A., Chin, P. S., Ames, L., Avellino, R., Gröschel, S., Delwel, R., Cockerill, P. N., Osborne, C. S. & Bonifer, C. 2019. RUNX1-ETO Depletion in t(8;21) AML Leads to C/EBPα- and AP-1-Mediated Alterations in Enhancer-Promoter Interaction. *Cell Rep,* 28**,** 3022-3031.e7.

Puck, T. T. & Marcus, P. I. 1956. Action of x-rays on mammalian cells. *J Exp Med,* 103**,** 653-66.

Pulli, I., Asghar, M. Y., Kemppainen, K. & Törnquist, K. 2018. Sphingolipid-mediated calcium signaling and its pathological effects. *Biochimica et Biophysica Acta (BBA) - Molecular Cell Research,* 1865**,** 1668-1677.

Puri, S., Magenheimer, B. S., Maser, R. L., Ryan, E. M., Zien, C. A., Walker, D. D., Wallace, D. P., Hempson, S. J. & Calvet, J. P. 2004. Polycystin-1 activates the calcineurin/NFAT (nuclear factor of activated T-cells) signaling pathway. *J Biol Chem,* 279**,** 55455-64.

Qin, J.-J., Nag, S., Wang, W., Zhou, J., Zhang, W.-D., Wang, H. & Zhang, R. 2014. NFAT as cancer target: Mission possible? *Biochimica et biophysica acta,* 1846**,** 297-311.

Quintás-Cardama, A., Hu, C., Qutub, A., Qiu, Y. H., Zhang, X., Post, S. M., Zhang, N., Coombes, K. & Kornblau, S. M. 2017. p53 pathway dysfunction is highly prevalent in acute myeloid leukemia independent of TP53 mutational status. *Leukemia,* 31**,** 1296-1305.

Ramadass, V., Vaiyapuri, T. & Tergaonkar, V. 2020. Small Molecule NF-κB Pathway Inhibitors in Clinic. *International journal of molecular sciences,* 21**,** 5164.

Rampersad, S. N. 2012. Multiple applications of Alamar Blue as an indicator of metabolic function and cellular health in cell viability bioassays. *Sensors (Basel, Switzerland),* 12**,** 12347-12360.

Ranger, A. M., Oukka, M., Rengarajan, J. & Glimcher, L. H. 1998. Inhibitory Function of Two NFAT Family Members in Lymphoid Homeostasis and Th2 Development. *Immunity,* 9**,** 627-635.

Rao, A., Luo, C. & Hogan, P. G. 1997a. Transcription factors of the NFAT family: regulation and function. *Annu Rev Immunol,* 15**,** 707-47.

Rao, A., Luo, C. & Hogan, P. G. 1997b. TRANSCRIPTION FACTORS OF THE NFAT FAMILY:Regulation and Function. *Annual Review of Immunology,* 15**,** 707-747.

Rao, D. D., Senzer, N., Cleary, M. A. & Nemunaitis, J. 2009. Comparative assessment of siRNA and shRNA off target effects: what is slowing clinical development. *Cancer Gene Therapy,* 16**,** 807-809.

Ren, Y. R., Pan, F., Parvez, S., Fleig, A., Chong, C. R., Xu, J., Dang, Y., Zhang, J., Jiang, H., Penner, R. & Liu, J. O. 2008. Clofazimine inhibits human Kv1.3 potassium channel by perturbing calcium oscillation in T lymphocytes. *PloS one,* 3**,** e4009-e4009.

Reya, T., Morrison, S. J., Clarke, M. F. & Weissman, I. L. 2001. Stem cells, cancer, and cancer stem cells. *Nature,* 414**,** 105-111.

Rivas, F. V., O'keefe, J. P., Alegre, M.-L. & Gajewski, T. F. 2004. Actin cytoskeleton regulates calcium dynamics and NFAT nuclear duration. *Molecular and cellular biology,* 24**,** 1628-1639.

Robbs, B. K., Cruz, A. L. S., Werneck, M. B. F., Mognol, G. P. & Viola, J. P. B. 2008. Dual Roles for NFAT Transcription Factor Genes as Oncogenes and Tumor Suppressors. *Molecular and Cellular Biology,* 28**,** 7168.

Robinson, M. D. & Oshlack, A. 2010. A scaling normalization method for differential expression analysis of RNA-seq data. *Genome Biology,* 11**,** R25.

Rocnik, J. L., Okabe, R., Yu, J.-C., Lee, B. H., Giese, N., Schenkein, D. P. & Gilliland, D. G. 2006. Roles of tyrosine 589 and 591 in STAT5 activation and transformation mediated by FLT3-ITD. *Blood,* 108**,** 1339-1345.

Roehrl, M. H. A., Kang, S., Aramburu, J., Wagner, G., Rao, A. & Hogan, P. G. 2004. Selective inhibition of calcineurin-NFAT signaling by blocking protein–protein interaction with small organic molecules. *Proceedings of the National Academy of Sciences of the United States of America,* 101**,** 7554.

Román, J., De Arriba, A. F., Barrón, S., Michelena, P., Giral, M., Merlos, M., Bailón, E., Comalada, M., Gálvez, J., Zarzuelo, A. & Ramis, I. 2007. UR-1505, a

new salicylate, blocks T cell activation through nuclear factor of activated T cells. *Mol Pharmacol,* 72**,** 269-79.

Rooney, J. W., Hoey, T. & Glimcher, L. H. 1995a. Coordinate and cooperative roles for NF-AT and AP-1 in the regulation of the murine IL-4 gene. *Immunity,* 2**,** 473-483.

Rooney, J. W., Sun, Y. L., Glimcher, L. H. & Hoey, T. 1995b. Novel NFAT sites that mediate activation of the interleukin-2 promoter in response to T-cell receptor stimulation. *Molecular and cellular biology,* 15**,** 6299-6310.

Rybka, J., Butrym, A., Wróbel, T., Jaźwiec, B., Stefanko, E., Dobrzyńska, O., Poręba, R. & Kuliczkowski, K. 2015. The expression of Toll-like receptors in patients with acute myeloid leukemia treated with induction chemotherapy. *Leukemia Research,* 39**,** 318-322.

Sandoval, J. E., Huang, Y.-H., Muise, A., Goodell, M. A. & Reich, N. O. 2019. Mutations in the DNMT3A DNA methyltransferase in acute myeloid leukemia patients cause both loss and gain of function and differential regulation by protein partners. *Journal of Biological Chemistry,* 294**,** 4898-4910.

Sasaki, K., Ravandi, F., Kadia, T. M., Dinardo, C. D., Short, N. J., Borthakur, G., Jabbour, E. & Kantarjian, H. M. 2021. De novo acute myeloid leukemia: A population-based study of outcome in the United States based on the Surveillance, Epidemiology, and End Results (SEER) database, 1980 to 2017. *Cancer,* 127**,** 2049-2061.

Savage, S. R., Bretz, C. A. & Penn, J. S. 2015. RNA-Seq Reveals a Role for NFAT-Signaling in Human Retinal Microvascular Endothelial Cells Treated with TNFα. *PLOS ONE,* 10**,** e0116941.

Schiffer, C., Stone, Rm. 2003. Morphologic Classification and Clinical and Laboratory Correlates. *In:* KUFE, D. W., POLLOCK, P.E., WEICHSELBAUM, R.R., BAST, R.C. JR., GANSLER, T.S., HOLLAND, J.F., FREI, E., III (ed.) *Holland-Frei Cancer Medicine*. 6th edition ed. Hamilton, ON, USA: BC Decker.

Schnerch, D., Yalcintepe, J., Schmidts, A., Becker, H., Follo, M., Engelhardt, M. & Wäsch, R. 2012. Cell cycle control in acute myeloid leukemia. *Am J Cancer Res,* 2**,** 508-28.

Schoch, C., Schnittger, S., Klaus, M., Kern, W., Hiddemann, W. & Haferlach, T. 2003. AML with 11q23/MLL abnormalities as defined by the WHO classification: incidence, partner chromosomes, FAB subtype, age distribution, and prognostic impact in an unselected series of 1897 cytogenetically analyzed AML cases. *Blood,* 102**,** 2395-2402.

Scholl, C., Fröhling, S., Dunn, I. F., Schinzel, A. C., Barbie, D. A., Kim, S. Y., Silver, S. J., Tamayo, P., Wadlow, R. C., Ramaswamy, S., Döhner, K., Bullinger, L., Sandy, P., Boehm, J. S., Root, D. E., Jacks, T., Hahn, W. C. & Gilliland, D. G. 2009. Synthetic lethal interaction between oncogenic KRAS dependency and STK33 suppression in human cancer cells. *Cell,* 137**,** 821-34.

Schroeder, A., Mueller, O., Stocker, S., Salowsky, R., Leiber, M., Gassmann, M., Lightfoot, S., Menzel, W., Granzow, M. & Ragg, T. 2006. The RIN: an RNA integrity number for assigning integrity values to RNA measurements. *BMC Molecular Biology,* 7**,** 3.

Seita, J. & Weissman, I. L. 2010. Hematopoietic stem cell: self-renewal versus differentiation. *Wiley interdisciplinary reviews. Systems biology and medicine,* 2**,** 640-653.

Serfling, E., Chuvpilo, S., Liu, J., Höfer, T. & Palmetshofer, A. 2006. NFATc1 autoregulation: a crucial step for cell-fate determination. *Trends in Immunology,* 27**,** 461-469.

Sharma, S., Findlay, G. M., Bandukwala, H. S., Oberdoerffer, S., Baust, B., Li, Z., Schmidt, V., Hogan, P. G., Sacks, D. B. & Rao, A. 2011. Dephosphorylation of the nuclear factor of activated T cells (NFAT) transcription factor is regulated by an RNA-protein scaffold complex. *Proceedings of the National Academy of Sciences of the United States of America,* 108**,** 11381-11386.

Shi, J., Wang, E., Zuber, J., Rappaport, A., Taylor, M., Johns, C., Lowe, S. W. & Vakoc, C. R. 2013. The Polycomb complex PRC2 supports aberrant self-renewal in a mouse model of MLL-AF9;NrasG12D acute myeloid leukemia. *Oncogene,* 32**,** 930-938.

Shih, A. H., Jiang, Y., Meydan, C., Shank, K., Pandey, S., Barreyro, L., Antony-Debre, I., Viale, A., Socci, N., Sun, Y., Robertson, A., Cavatore, M., De Stanchina, E., Hricik, T., Rapaport, F., Woods, B., Wei, C., Hatlen, M., Baljevic, M., *et al*. 2015. Mutational cooperativity linked to combinatorial epigenetic gain of function in acute myeloid leukemia. *Cancer cell,* 27**,** 502-515.

Shin, S.-Y., Kim, M.-W., Cho, K.-H. & Nguyen, L. K. 2019. Coupled feedback regulation of nuclear factor of activated T-cells (NFAT) modulates activation-induced cell death of T cells. *Scientific Reports,* 9**,** 10637.

Shinsuke, H., Kentaro, O., Kazuhiko, N., Hitoshi, I., Yukihide, M., Kohji, O., Akinori, Y., Kazuki, T., Yuya, S., Ai, Y., Hiroko, O.-K., Hiromi, S., Motohiro, K., Junya, F., Moeko, H., Akitoshi, K., Harumi, K., Hidemitsu, K., Keisuke, K., *et al*. 2017. ZNF384-related fusion genes define a subgroup of childhood B-cell precursor acute lymphoblastic leukemia with a characteristic immunotype. *Haematologica,* 102**,** 118-129.

Shlush, L. I. 2018. Age-related clonal hematopoiesis. *Blood,* 131**,** 496-504.

Sieber, M., Karanik, M., Brandt, C., Blex, C., Podtschaske, M., Erdmann, F., Rost, R., Serfling, E., Liebscher, J., Pätzel, M., Radbruch, A., Fischer, G. & Baumgrass, R. 2007. Inhibition of calcineurin-NFAT signaling by the pyrazolopyrimidine compound NCI3. *European Journal of Immunology,* 37**,** 2617-2626.

Simonett, S. P., Shin, S., Herring, J. A., Bacher, R., Smith, L. A., Dong, C., Rabaglia, M. E., Stapleton, D. S., Schueler, K. L., Choi, J., Bernstein, M. N., Turkewitz, D. R., Perez-Cervantes, C., Spaeth, J., Stein, R., Tessem, J. S., Kendziorski, C., Keleş, S., Moskowitz, I. P., *et al*. 2021. Identification of direct transcriptional targets of NFATC2 that promote ß cell proliferation. *The Journal of Clinical Investigation,* 131.

Singh, G., Singh, S. K., König, A., Reutlinger, K., Nye, M. D., Adhikary, T., Eilers, M., Gress, T. M., Fernandez-Zapico, M. E. & Ellenrieder, V. 2010. Sequential Activation of NFAT and c-Myc Transcription Factors Mediates the TGF-β Switch from a Suppressor to a Promoter of Cancer Cell Proliferation *. *Journal of Biological Chemistry,* 285**,** 27241-27250.

Solovey, M., Wang, Y., Michel, C., Metzeler, K. H., Herold, T., Göthert, J. R., Ellenrieder, V., Hessmann, E., Gattenlöhner, S., Neubauer, A., Pavlinic, D., Benes, V., Rupp, O. & Burchert, A. 2019. Nuclear factor of activated T-cells, NFATC1, governs FLT3(ITD)-driven hematopoietic stem cell transformation and a poor prognosis in AML. *Journal of hematology & oncology,* 12**,** 72-72.

Solovey, M. A., Wang, Y., Gattenloehner, S., Hessmann, E., Metzelder, S., Michel, C., Ellenrieder, V., Goethert, J. R., Neubauer, A. & Burchert, A. 2016. Nuclear NFATc1 Causes Development of Fms-like Receptor Tyrosine Kinase 3 Receptor (FLT3) Internal Tandem Duplication Mutation-Positive (FLT3-ITD) Acute Myeloid Leukemia (AML) and Mediates Drug Resistance. *Blood,* 128**,** 1722.

Soltani, M., Zhao, Y., Xia, Z., Ganjalikhani Hakemi, M. & Bazhin, A. V. 2021. The Importance of Cellular Metabolic Pathways in Pathogenesis and Selective Treatments of Hematological Malignancies. *Frontiers in Oncology,* 11.

Somervaille, T. C. P. & Cleary, M. L. 2006. Identification and characterization of leukemia stem cells in murine MLL-AF9 acute myeloid leukemia. *Cancer Cell,* 10**,** 257-268.

Sood, R., Kamikubo, Y. & Liu, P. 2017. Role of RUNX1 in hematological malignancies. *Blood,* 129**,** 2070-2082.

Spiekerkoetter, E., Sung, Y. K., Sudheendra, D., Scott, V., Del Rosario, P., Bill, M., Haddad, F., Long-Boyle, J., Hedlin, H. & Zamanian, R. T. 2017. Randomised placebo-controlled safety and tolerability trial of FK506 (tacrolimus) for pulmonary arterial hypertension. *European Respiratory Journal,* 50**,** 1602449.

Stark, R., Grzelak, M. & Hadfield, J. 2019. RNA sequencing: the teenage years. *Nature Reviews Genetics,* 20**,** 631-656.

Starr, T., Bauler, T. J., Malik-Kale, P. & Steele-Mortimer, O. 2018. The phorbol 12-myristate-13-acetate differentiation protocol is critical to the interaction of THP-1 macrophages with Salmonella Typhimurium. *PLOS ONE,* 13**,** e0193601.

Staruschenko, A., Negulyaev, Y. & Morachevskaya, E. 2005. Actin cytoskeleton disassembly affects conductive properties of stretch-activated cation channels in leukaemia cells. *Biochimica et biophysica acta,* 1669**,** 53-60.

Steensma, D. P. 2018. Clinical consequences of clonal hematopoiesis of indeterminate potential. *Blood advances,* 2**,** 3404-3410.

Stein, E. M., Garcia-Manero, G., Rizzieri, D. A., Tibes, R., Berdeja, J. G., Savona, M. R., Jongen-Lavrenic, M., Altman, J. K., Thomson, B., Blakemore, S. J., Daigle, S. R., Waters, N. J., Suttle, A. B., Clawson, A., Pollock, R., Krivtsov, A., Armstrong, S. A., Dimartino, J., Hedrick, E., *et al.* 2018. The DOT1L inhibitor pinometostat reduces H3K79 methylation and has modest clinical activity in adult acute leukemia. *Blood,* 131**,** 2661.

Steudel, C., Wermke, M., Schaich, M., Schäkel, U., Illmer, T., Ehninger, G. & Thiede, C. 2003. Comparative analysis of MLL partial tandem duplication and FLT3 internal tandem duplication mutations in 956 adult patients with acute myeloid leukemia. *Genes, Chromosomes and Cancer,* 37**,** 237-251.

Stubbs, M. C., Kim, Y. M., Krivtsov, A. V., Wright, R. D., Feng, Z., Agarwal, J., Kung, A. L. & Armstrong, S. A. 2008. MLL-AF9 and FLT3 cooperation in acute myelogenous leukemia: development of a model for rapid therapeutic assessment. *Leukemia,* 22**,** 66-77.

Subramanian, A., Tamayo, P., Mootha, V. K., Mukherjee, S., Ebert, B. L., Gillette, M. A., Paulovich, A., Pomeroy, S. L., Golub, T. R., Lander, E. S. & Mesirov, J. P. 2005. Gene set enrichment analysis: a knowledge-based approach for interpreting genome-wide expression profiles. *Proceedings of the National Academy of Sciences of the United States of America,* 102**,** 15545-15550.

Suganuma, K., Miwa, H., Imai, N., Shikami, M., Gotou, M., Goto, M., Mizuno, S., Takahashi, M., Yamamoto, H., Hiramatsu, A., Wakabayashi, M., Watarai,

M., Hanamura, I., Imamura, A., Mihara, H. & Nitta, M. 2010. Energy metabolism of leukemia cells: glycolysis versus oxidative phosphorylation. *Leukemia & Lymphoma,* 51**,** 2112-2119.

Sugimoto, K., Toyoshima, H., Sakai, R., Miyagawa, K., Hagiwara, K., Ishikawa, F., Takaku, F., Yazaki, Y. & Hirai, H. 1992. Frequent mutations in the p53 gene in human myeloid leukemia cell lines. *Blood,* 79**,** 2378-83.

Sung, P. J., Sugita, M., Koblish, H., Perl, A. E. & Carroll, M. 2019. Hematopoietic cytokines mediate resistance to targeted therapy in FLT3-ITD acute myeloid leukemia. *Blood Advances,* 3**,** 1061-1072.

Szklarczyk, D., Gable, A. L., Nastou, K. C., Lyon, D., Kirsch, R., Pyysalo, S., Doncheva, N. T., Legeay, M., Fang, T., Bork, P., Jensen, L. J. & Von mering, C. 2021. The STRING database in 2021: customizable protein–protein networks, and functional characterization of user-uploaded gene/measurement sets. *Nucleic Acids Research,* 49**,** D605-D612.

Tabe, Y. & Konopleva, M. 2015. Role of Microenvironment in Resistance to Therapy in AML. *Curr Hematol Malig Rep,* 10**,** 96-103.

Takahashi, S. 2006. Identification of Flt3 internal tandem duplications downstream targets by high-throughput immunoblotting protein array system. *American Journal of Hematology,* 81**,** 717-719.

Takei, H. & Kobayashi, S. S. 2019. Targeting transcription factors in acute myeloid leukemia. *International Journal of Hematology,* 109**,** 28-34.

Tallman, M. S., Kim, H. T., Paietta, E., Bennett, J. M., Dewald, G., Cassileth, P. A., Wiernik, P. H. & Rowe, J. M. 2004. Acute monocytic leukemia (French-American-British classification M5) does not have a worse prognosis than other subtypes of acute myeloid leukemia: a report from the Eastern Cooperative Oncology Group. *J Clin Oncol,* 22**,** 1276-86.

Tan, A., Bitterman, P., Sonenberg, N., Peterson, M. & Polunovsky, V. 2000. Inhibition of Myc-dependent apoptosis by eukaryotic translation initiation factor 4E requires cyclin D1. *Oncogene,* 19**,** 1437-1447.

Taylor, W. R. & Stark, G. R. 2001. Regulation of the G2/M transition by p53. *Oncogene,* 20**,** 1803-1815.

Tedesco, D. & Haragsim, L. 2012. Cyclosporine: a review. *Journal of transplantation,* 2012**,** 230386-230386.

Thiede, C., Koch, S., Creutzig, E., Steudel, C., Illmer, T., Schaich, M., Ehninger, G. & For the Deutsche Studieninitiative, L. M. 2006. Prevalence and prognostic impact of NPM1 mutations in 1485 adult patients with acute myeloid leukemia (AML). *Blood,* 107**,** 4011-4020.

Tobias, H., Vindi, J., Aarif, M. N. B., Stefanos, A. B., Maja, R.-T., Bianka, K., Luise, H., Philipp, A. G., Julia, P.-M., Stefan, K., Helmut, B., Susanne, A., Stephanie, S., Nikola, K., Maria Cristina, S., Dennis, G., Wolfgang, E. B., Bernhard, J. W., Johanna, T.*, et al.* 2018. A 29-gene and cytogenetic score for the prediction of resistance to induction treatment in acute myeloid leukemia. *Haematologica,* 103**,** 456-465.

Tyner, J. W., Tognon, C. E., Bottomly, D., Wilmot, B., Kurtz, S. E., Savage, S. L., Long, N., Schultz, A. R., Traer, E., Abel, M., Agarwal, A., Blucher, A., Borate, U., Bryant, J., Burke, R., Carlos, A., Carpenter, R., Carroll, J., Chang, B. H., *et al.* 2018. Functional genomic landscape of acute myeloid leukaemia. *Nature,* 562**,** 526-531.

Uckelmann, H. J., Kim, S. M., Wong, E. M., Hatton, C., Giovinazzo, H., Gadrey, J. Y., Krivtsov, A. V., Rücker, F. G., Döhner, K., Mcgeehan, G. M., Levine, R. L., Bullinger, L., Vassiliou, G. S. & Armstrong, S. A. 2020. Therapeutic

targeting of preleukemia cells in a mouse model of NPM1 mutant acute myeloid leukemia. *Science (New York, N.Y.),* 367**,** 586-590.

Vaeth, M. & Feske, S. 2018. NFAT control of immune function: New Frontiers for an Abiding Trooper [version 1; peer review: 2 approved]. *F1000Research,* 7.

Vaeth, M., Maus, M., Klein-Hessling, S., Freinkman, E., Yang, J., Eckstein, M., Cameron, S., Turvey, S. E., Serfling, E., Berberich-Siebelt, F., Possemato, R. & Feske, S. 2017. Store-Operated Ca2+ Entry Controls Clonal Expansion of T Cells through Metabolic Reprogramming. *Immunity,* 47**,** 664-679.e6.

Vago, L. & Gojo, I. 2020. Immune escape and immunotherapy of acute myeloid leukemia. *The Journal of clinical investigation,* 130**,** 1552-1564.

Vainchenker, W. & Plo, I. 2017. P53 deletion and NrasG12D cooperate for AML. *Blood,* 129**,** 271-273.

Valent, P. 2007. Imatinib-resistant chronic myeloid leukemia (CML): Current concepts on pathogenesis and new emerging pharmacologic approaches. *Biologics : targets & therapy,* 1**,** 433-448.

Van Galen, P., Hovestadt, V., Wadsworth Ii, M. H., Hughes, T. K., Griffin, G. K., Battaglia, S., Verga, J. A., Stephansky, J., Pastika, T. J., Lombardi Story, J., Pinkus, G. S., Pozdnyakova, O., Galinsky, I., Stone, R. M., Graubert, T. A., Shalek, A. K., Aster, J. C., Lane, A. A. & Bernstein, B. E. 2019. Single-Cell RNA-Seq Reveals AML Hierarchies Relevant to Disease Progression and Immunity. *Cell,* 176**,** 1265-1281.e24.

Van Gils, N., Denkers, F. & Smit, L. 2021. Escape From Treatment; the Different Faces of Leukemic Stem Cells and Therapy Resistance in Acute Myeloid Leukemia. *Frontiers in Oncology,* 11**,** 1454.

Vardiman, J. W., Harris, N. L. & Brunning, R. D. 2002. The World Health Organization (WHO) classification of the myeloid neoplasms. *Blood,* 100**,** 2292-2302.

Vassiliou, G. S., Cooper, J. L., Rad, R., Li, J., Rice, S., Uren, A., Rad, L., Ellis, P., Andrews, R., Banerjee, R., Grove, C., Wang, W., Liu, P., Wright, P., Arends, M. & Bradley, A. 2011. Mutant nucleophosmin and cooperating pathways drive leukemia initiation and progression in mice. *Nat Genet,* 43**,** 470-5.

Veselská, R., Zitterbart, K., Jelínková, S., Neradil, J. & Svoboda, A. 2003. Specific cytoskeleton changes during apoptosis accompanying induced differentiation of HL-60 myeloid leukemia cells. *Oncol Rep,* 10**,** 1049-1058.

Vetrie, D., Helgason, G. V. & Copland, M. 2020. The leukaemia stem cell: similarities, differences and clinical prospects in CML and AML. *Nature Reviews Cancer,* 20**,** 158-173.

Vihma, H., Pruunsild, P. & Timmusk, T. 2008. Alternative splicing and expression of human and mouse NFAT genes. *Genomics,* 92**,** 279-291.

Villar, M., Ortega-Pérez, I., Were, F., Cano, E., Redondo, J. M. & Vázquez, J. 2006. Systematic characterization of phosphorylation sites in NFATc2 by linear ion trap mass spectrometry. *Proteomics,* 6 Suppl 1**,** S16-27.

Vives, R., Pontes, C., Sarasa, M. & Millier, A. 2015. Safety and Activity of UR-1505 in Atopic Dermatitis: A Randomized, Double-blind Phase II Exploratory Trial. *Clinical Therapeutics,* 37**,** 1955-1965.

Von Mering, C., Jensen, L. J., Snel, B., Hooper, S. D., Krupp, M., Foglierini, M., Jouffre, N., Huynen, M. A. & Bork, P. 2005. STRING: known and predicted protein-protein associations, integrated and transferred across organisms. *Nucleic acids research,* 33**,** D433-D437.

Walter, R. B., Othus, M., Burnett, A. K., Löwenberg, B., Kantarjian, H. M., Ossenkoppele, G. J., Hills, R. K., Van Montfort, K. G., Ravandi, F., Evans,

A., Pierce, S. R., Appelbaum, F. R. & Estey, E. H. 2013. Significance of FAB subclassification of "acute myeloid leukemia, NOS" in the 2008 WHO classification: analysis of 5848 newly diagnosed patients. *Blood,* 121, 2424-31.

Wang, C., Li, J.-F., Zhao, L., Liu, J., Wan, J., Xiu Wang, Y., Wang, J. & Wang, C. 2009a. Inhibition of SOC/Ca2+/NFAT pathway is involved in the anti-proliferative effect of sildenafil on pulmonary artery smooth muscle cells. *Respiratory Research,* 10, 123.

Wang, Y. X. R. & Huang, H. 2014. Review on statistical methods for gene network reconstruction using expression data. *Journal of Theoretical Biology,* 362, 53-61.

Wang, Z., Gerstein, M. & Snyder, M. 2009b. RNA-Seq: a revolutionary tool for transcriptomics. *Nature Reviews Genetics,* 10, 57-63.

Webb, D. K. H., Wheatley, K., Harrison, G., Stevens, R. F., Hann, I. M. & For The, M. R. C. C. L. W. P. 1999. Outcome for children with relapsed acute myeloid leukaemia following initial therapy in the Medical Research Council (MRC) AML 10 trial. *Leukemia,* 13, 25-31.

Weïwer, M., Spoonamore, J., Wei, J., Guichard, B., Ross, N. T., Masson, K., Silkworth, W., Dandapani, S., Palmer, M., Scherer, C. A., Stern, A. M., Schreiber, S. L. & Munoz, B. 2012. A Potent and Selective Quinoxalinone-Based STK33 Inhibitor Does Not Show Synthetic Lethality in KRAS-Dependent Cells. *ACS Medicinal Chemistry Letters,* 3, 1034-1038.

Welch, J. S., Ley, T. J., Link, D. C., Miller, C. A., Larson, D. E., Koboldt, D. C., Wartman, L. D., Lamprecht, T. L., Liu, F., Xia, J., Kandoth, C., Fulton, R. S., Mclellan, M. D., Dooling, D. J., Wallis, J. W., Chen, K., Harris, C. C., Schmidt, H. K., Kalicki-Veizer, J. M., *et al*. 2012. The origin and evolution of mutations in acute myeloid leukemia. *Cell,* 150, 264-278.

Williams, A. B. & Schumacher, B. 2016. p53 in the DNA-Damage-Repair Process. *Cold Spring Harbor perspectives in medicine,* 6, a026070.

Winters, A. C. & Bernt, K. M. 2017. MLL-Rearranged Leukemias-An Update on Science and Clinical Approaches. *Frontiers in pediatrics,* 5, 4-4.

Wong, K. K., Lawrie, C. H. & Green, T. M. 2019. Oncogenic Roles and Inhibitors of DNMT1, DNMT3A, and DNMT3B in Acute Myeloid Leukaemia. *Biomarker Insights,* 14, 1177271919846454.

Yang, K., Hitomi, M. & Stacey, D. W. 2006. Variations in cyclin D1 levels through the cell cycle determine the proliferative fate of a cell. *Cell Division,* 1, 32.

Yang, T., Song, B., Zhang, J., Yang, G.-S., Zhang, H., Yu, W.-F., Wu, M.-C., Lu, J.-H. & Shen, F. 2016. STK33 promotes hepatocellular carcinoma through binding to c-Myc. *Gut,* 65, 124-133.

Yeung, C. C. S. & Radich, J. 2017. Predicting Chemotherapy Resistance in AML. *Current Hematologic Malignancy Reports,* 12, 530-536.

Young, B., Lowe, J.S., Stevens, A., Heath, J.W. 2006. *Wheater's Functional Histology: A Text and Colour Atlas*, Elsevier Limited.

Yu, G., Wang, L.-G. & He, Q.-Y. 2015. ChIPseeker: an R/Bioconductor package for ChIP peak annotation, comparison and visualization. *Bioinformatics,* 31, 2382-2383.

Yu, H.-B., Yurieva, M., Balachander, A., Foo, I., Leong, X., Zelante, T., Zolezzi, F., Poidinger, M. & Ricciardi-Castagnoli, P. 2014. NFATc2 mediates epigenetic modification of dendritic cell cytokine and chemokine responses to dectin-1 stimulation. *Nucleic Acids Research,* 43, 836-847.

Yu, H., Van Berkel, T. J. C. & Biessen, E. a. L. 2007. Therapeutic Potential of VIVIT, a Selective Peptide Inhibitor of Nuclear Factor of Activated T cells, in Cardiovascular Disorders. *Cardiovascular Drug Reviews,* 25**,** 175-187.

Zarka, J., Short, N. J., Kanagal-Shamanna, R. & Issa, G. C. 2020. Nucleophosmin 1 Mutations in Acute Myeloid Leukemia. *Genes,* 11**,** 649.

Zhang, Y., Gao, S., Xia, J. & Liu, F. 2018. Hematopoietic Hierarchy – An Updated Roadmap. *Trends in Cell Biology,* 28**,** 976-986.

Zheng, J. 2012. Energy metabolism of cancer: Glycolysis versus oxidative phosphorylation (Review). *Oncology letters,* 4**,** 1151-1157.

Zhu, J. & Emerson, S. G. 2002. Hematopoietic cytokines, transcription factors and lineage commitment. *Oncogene,* 21**,** 3295-3313.

Zhu, N., Chen, M., Eng, R., Dejong, J., Sinha, A. U., Rahnamay, N. F., Koche, R., Al-Shahrour, F., Minehart, J. C., Chen, C.-W., Deshpande, A. J., Xu, H., Chu, S. H., Ebert, B. L., Roeder, R. G. & Armstrong, S. A. 2016. MLL-AF9- and HOXA9-mediated acute myeloid leukemia stem cell self-renewal requires JMJD1C. *The Journal of Clinical Investigation,* 126**,** 997-1011.

Zink, F., Stacey, S. N., Norddahl, G. L., Frigge, M. L., Magnusson, O. T., Jonsdottir, I., Thorgeirsson, T. E., Sigurdsson, A., Gudjonsson, S. A., Gudmundsson, J., Jonasson, J. G., Tryggvadottir, L., Jonsson, T., Helgason, A., Gylfason, A., Sulem, P., Rafnar, T., Thorsteinsdottir, U., Gudbjartsson, D. F., *et al*. 2017. Clonal hematopoiesis, with and without candidate driver mutations, is common in the elderly. *Blood,* 130**,** 742-752.

Zuber, J., Radtke, I., Pardee, T. S., Zhao, Z., Rappaport, A. R., Luo, W., Mccurrach, M. E., Yang, M. M., Dolan, M. E., Kogan, S. C., Downing, J. R. & Lowe, S. W. 2009. Mouse models of human AML accurately predict chemotherapy response. *Genes Dev,* 23**,** 877-89.

Zuryn, A., Grzanka, A., Stepien, A., Grzanka, D., Debski, R. & Smolinski, D. 2007. Expression of cyclin A in human leukemia cell line HL-60 following treatment with doxorubicin and etoposide: The potential involvement of cyclin A in apoptosis. *Oncol Rep,* 17**,** 1013-1019.

9 Appendices

9.1 Patient characteristics from open-source datasets

A TARGET-AML

Characteristic		Data
Age at diagnosis, in years - median (range)		9.3 (0.4-22.6)
Sex - n (% total)	Male	60 (50.4)
	Female	59 (49.6)
Ethnic background - n (% total)	White	90 (75.6)
	Black or African American	13 (10.9)
	All other	11 (9.2)
	Unknown	5 (4.2)
FAB Classification - n (% total)	M0	2 (1.7)
	M1	15 (12.6)
	M2	27 (22.7)
	M4	29 (24.4)
	M5	26 (21.8)
	M6	2 (1.7)
	M7	7 (5.9)
	No Classification	7 (5.9)
	Unknown	4 (3.4)
Primary cytogenetic classification (% total)	Karyotype normal	26 (21.8)
	MLL fusion	24 (20.2)
	Inversion 16	20 (16.8)
	RUNX1-RUNX1T1	17 (14.3)
	Other	26 (21.8)
	Unknown	6 (5.0)
Other gene fusions (% known)	CBFB-MYH11	20 (17.7)
	DEK-NUP214	1 (0.9)
	NUP98 fusions	10 (8.8)
Mutations - (% known)	NPM1	4 (3.5)
	CEBPA	7 (5.9)
	RUNX1	17 (9.8)
$FLT3^{ITD}$ - n (% total)		7 (5.9)

B BEAT-AML

Characteristic		Data
Age at diagnosis, in years - median (range)		58 (18-88)
Sex - n (% total)	Male	92 (53.2)
	Female	81 (46.8)
Ethnic background - n (% total)	White	127 (74.7)
	Black	8 (4.7)
	All other	38 (22.4)
FAB Classification - n (% known)	M0	16 (9.2)
	M1	44 (25.4)
	M2	38 (22.0)
	M3	16 (9.2)
	M4	34 (19.7)
	M5	18 (10.4)
	M6	2 (1.2)
	M7	3 (1.7)
	No Classification	2 (1.2)
Molecular classification - n (% total)	Karyotype normal	75 (43.4)
	Poor or intermediate cytogenetic risk	26 (15.0)
	Complex cytogenetics	22 (12.7)
	PML-RARA	16 (9.2)
	CBFB-MYH11	10 (5.8)
	MLL Fusion	8 (4.6)
	RUNX-RUNX1T1	7 (4.0)
	BCR-ABL1	3 (1.7)
	NUP98-NSD1	3 (1.7)
	Unknown	3 (1.7)
Mutations - (% known)	NPM1	48 (27.7)
	CEBPA	13 (7.5)
	RUNX1	17 (9.8)
$FLT3^{ITD}$ - n (% known)		37 (27.2)

C TCGA

Characteristic		Data
Age at diagnosis, in years - median (range)		61 (2-87)
Sex - n (% total)	Male	93 (56.4)
	Female	72 (43.6)
Ethnic background – n (% total)	White/mixed white	139 (84.2)
	Hispanic	17 (10.3)
	Asian	5 (0.3)
	Black	4 (2.4)
Primary diagnosis – n (% total)	AML NOS	20 (12.1)
	AML with NPM1 mutation	48 (29.1)
	AML with MDS-related changed	31 (18.8)
	AML (other)	28 (17.0)
	AML with biallelic CEBPA mutation	12 (7.3)
	APL with PML-RARA	11 (6.7)
	AML with CBFB-MYH11	10 (6.1)
	AML with RUNX-RUNX1T1	5 (3.0)
$FLT3^{ITD}$ – n (% total)		39 (23.6)
Gene Fusions – n (% total)	MLLT3-KMT2A	5 (3.0)
	GATA2-MECOM	2 (1.2)
	Unknown	4 (2.4)

Figure A-1. Detailed patient characteristics from three open-source datasets. Data were extracted from **A:** TARGET-AML; **B:** BEAT-AML; **C:** TCGA AML datasets, for BM-derived tumour expression of *NFATC1*, *NFATC2* and *NFATC3*, as measured by RNA-Seq. Survival data were also extracted. The patient characteristics shown are selected demographic attributes and known mutational features, based around the FAB classification of AML, the WHO classification of myeloid neoplasms, and other well-characterised mutations (such as $FLT3^{ITD}$).

9.2 RNA-Seq QC

9.2.1 Determining timepoints

In order to generate RNA samples for RNA-Seq the optimal timepoint for cell harvest was determined by comparing the level of *NFATC2* KD at 24hr and 48hr post-puromycin selection, by qRT-PCR. Due to the increased cell death observed with construct -143 transduction at 72hr post-selection this was deemed too late, to avoid dead cell RNA contamination. Figure A-2 shows that KD was stronger at 24hr post-selection and so this was chosen as a suitable timepoint for harvest.

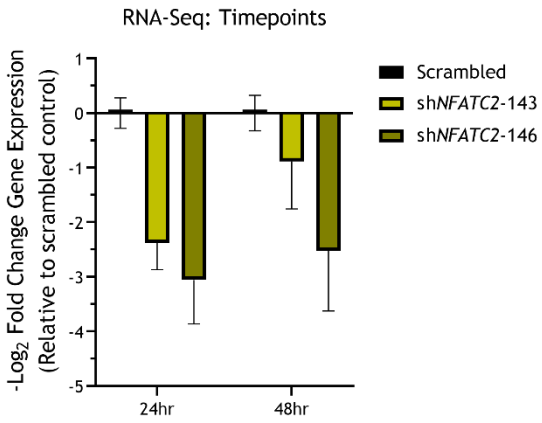

Figure A-2. *NFATC2* KD in bulk THP-1 cells was strongest at 24hr post-selection. qRT-PCR was used to measure *NFATC2* expression in THP-1 cells 24hr and 48hr post-puromycin selection. Shown are the mean ± SD $-\log_2$ fold changes relative to the scrambled control, using the ΔΔCt method (n=3, technical replicates).

9.2.2 Experimental quality

5 replicate experiments' RNA samples were extracted and quantified as described previously. These were compared for *NFATC2* expression after shRNA KD (Figure A-3A). *NFATC2* is downregulated the least in replicate 5 and this was excluded. Replicates 1-4 were compared for transduction efficiency, which was estimated by cell counts at 0hr and 24hr post-puromycin selection (Figure A-3B). Replicates 1-2 showed the highest proportion of cells remaining after selection.

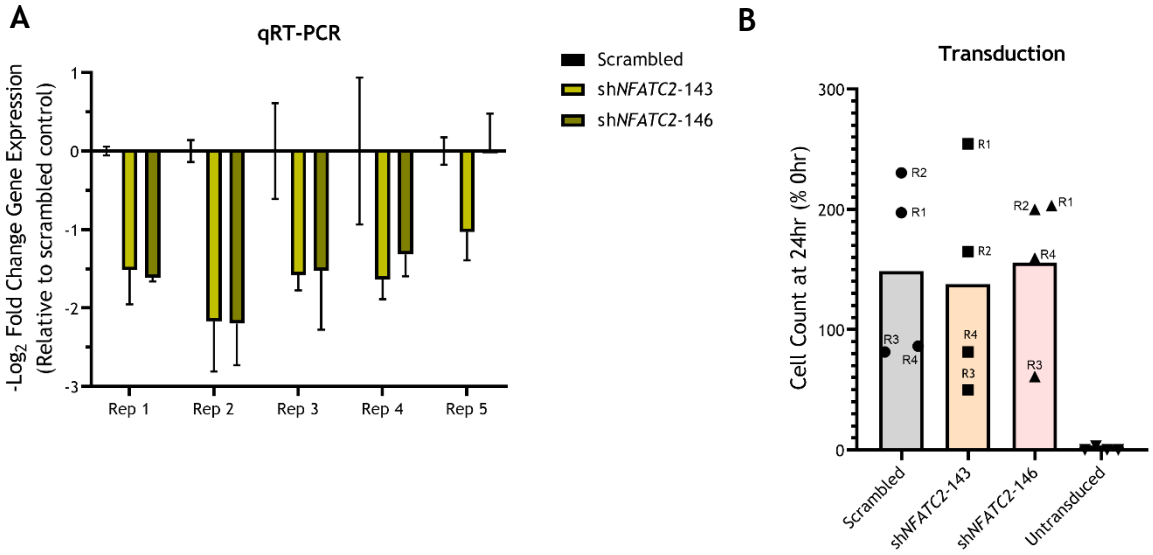

Figure A-3. Experimental replicate 5 was initially excluded from RNA-Seq submission. 5 experimental replicates of *NFATC2* KD in THP-1 cells were conducted. 'Rep' = replicate. **A.** Replicates 1-5. qRT-PCR was used to measure *NFATC2* expression in THP-1 cells 24 hr post-puromycin selection. Shown are the mean ± SD -$\log_2$ fold changes relative to the scrambled control, using the ΔΔCt method (n=3, technical replicates). **B.** Replicates 1-4. Cell counts taken in liquid culture at 24hr are expressed as a % of counts at 0hr, as a measure of transduction efficiency.

9.2.3 Sample preparation and QC

The samples were also analysed for quality using a 2100 Bioanalyzer system, with an RNA 6000 Nano Kit (both Agilent). The 2100 Expert Software (Agilent) was used for data visualisation. The kit was applied as per protocol. Briefly, RNA samples were loaded onto a chip, before they were passed through chip micro-channels and separated by electrophoresis. The Bioanalyzer system can measure sample quantity and quality by comparing each sample's electropherogram with that of a known reference. An example electropherogram is shown in Figure A-4.

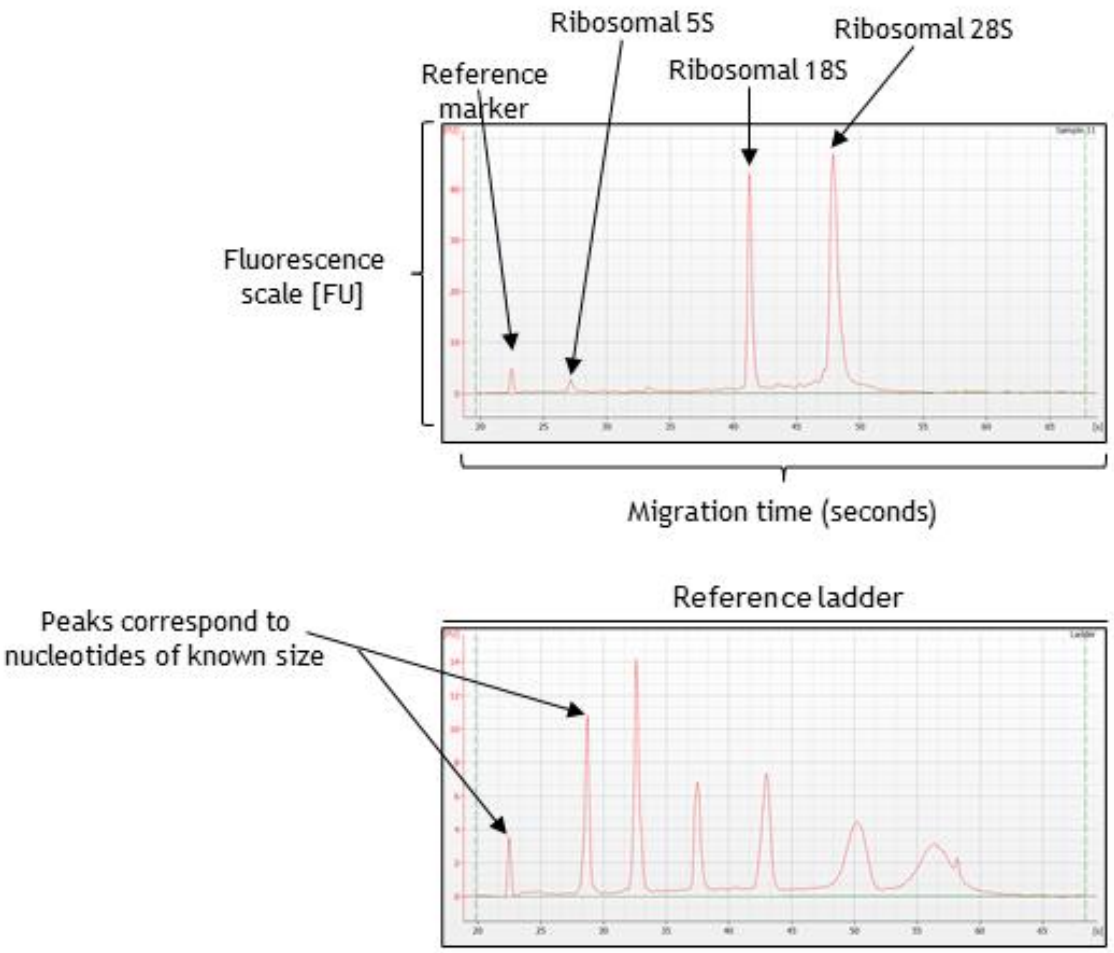

Figure A-4. Agilent electropherogram shows RNA quality.
A: The diagram shows the electropherogram measured by the 2100 Bioanalyzer on an RNA sample. The expected peaks are those for ribosomal RNA and a reference marker, as indicated. **B:** The electropherogram for the reference ladder.

Two quantitative values can be derived from these sample plots to represent sample quality. The dominant peaks represent 28S and 18S ribosomal RNA and are expected to have a 28S:18S ratio of ≥2.0 in good quality RNA. Alternatively, the RNA integrity number (RIN) is calculated by an algorithm which takes account of the whole electropherogram plot, to estimate RNA integrity. It is generally considered to be a superior and more reproducible measure of quality than the 28S:18S ratio. RIN ranges from 1-10, where 10 is the best possible quality (Schroeder *et al.*, 2006). Example plots are shown from 4 experimental replicates in Figure A-5. Using RNA quality assessment in the Bioanalyzer it was deemed that replicates 1-3 were of the best quality and concentration to be submitted for sequencing.

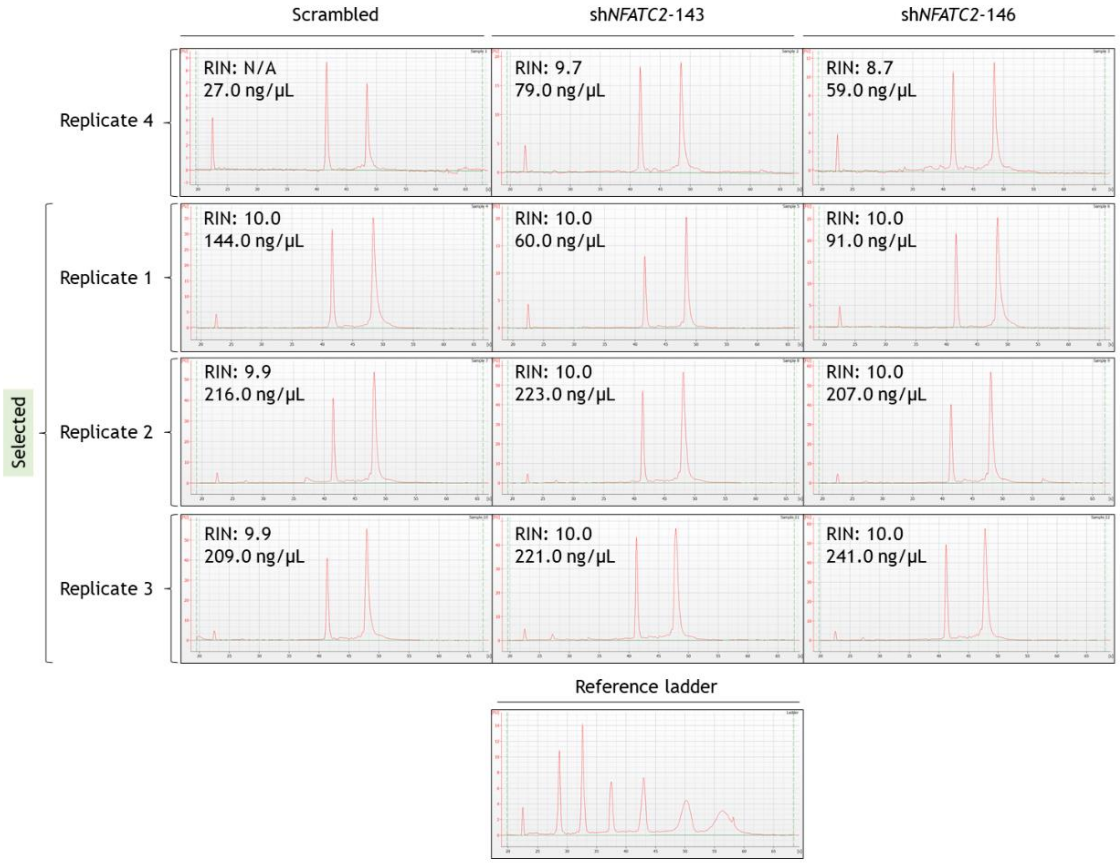

Figure A-5. Experimental replicates 1-3 were the best quality for RNA-Seq submission. Replicates 1-4 of samples examined in Figure 2-X. RNA harvested at 24hr was analysed using automated electrophoresis in an Agilent 2100 Bioanalyzer system. Shown are the electropherograms for each, and a reference ladder. Below this is the measured RNA concentration.

9.2.4 Library preparation and sequencing

The cDNA libraries were prepared from RNA samples by Novogene, using a Next® Ultra™ RNA Library Preparation Kit (NEB). They also sequenced these libraries, after which read and mapping quality statistics were provided (see Table A-1).

Sample details		Read quality			Mapping quality	
Replicate	**Condition**	**Clean reads (% total)**	**Base error rate (%)**	**GC content (%)**	**Mapping rate (% reads)**	**Multiple mapping (%)**
1	Scrambled	96.51	0.03	49.84	96.85	4.16
	-143	96.65	0.02	50.08	97.54	3.50
	-146	95.98	0.02	47.34	95.66	3.22
2	Scrambled	96.29	0.02	50.20	97.27	3.48
	-143	97.12	0.02	50.44	97.23	3.61
	-146	97.16	0.03	50.49	96.67	3.39
3	Scrambled	96.44	0.03	50.17	96.31	4.20
	-143	96.86	0.02	50.36	96.93	3.60
	-146	97.64	0.03	50.73	96.05	3.53

Table A-1. Read and mapping quality measures of RNA-Seq data were found to be >95%. The table shows selected statistics derived from the sequencing process, containing metrics of read quality or quality of mapping reads to the genome.

95.98-97.64% of reads were determined to be clean across all samples, with a base error rate of ≤0.03% across the whole sequencing. After alignment to the human genome (build hg38) the analysis of mapping found that 3.22-4.20% of reads were mapped to multiple loci, and 96.87-98.02% of total reads mapped to exon regions.

9.3 ChIP-Seq QC

9.3.1 DNA QC

DNA libraries were quality-assessed using an Agilent DNA 1000 Kit, which works in a manner similar to that described for RNA. The electropherograms for 3 replicates are shown in Figure A-6. Electrophoresis using the Bioanalyzer revealed that size-selected library preparations of input DNA peaked at size ~300 bp. This is approximately expected based on the gel in Figure 5-23 and with the addition of adapters. The NFATc2 IP DNA showed smaller peaks, as expected, with similar sizes for replicates 1 and 3. However, replicate 2 showed an unexpectedly large peak at >1500 bp. The region from 170-750 bp was measured for concentration, which was also lower than replicates 1 and 2.

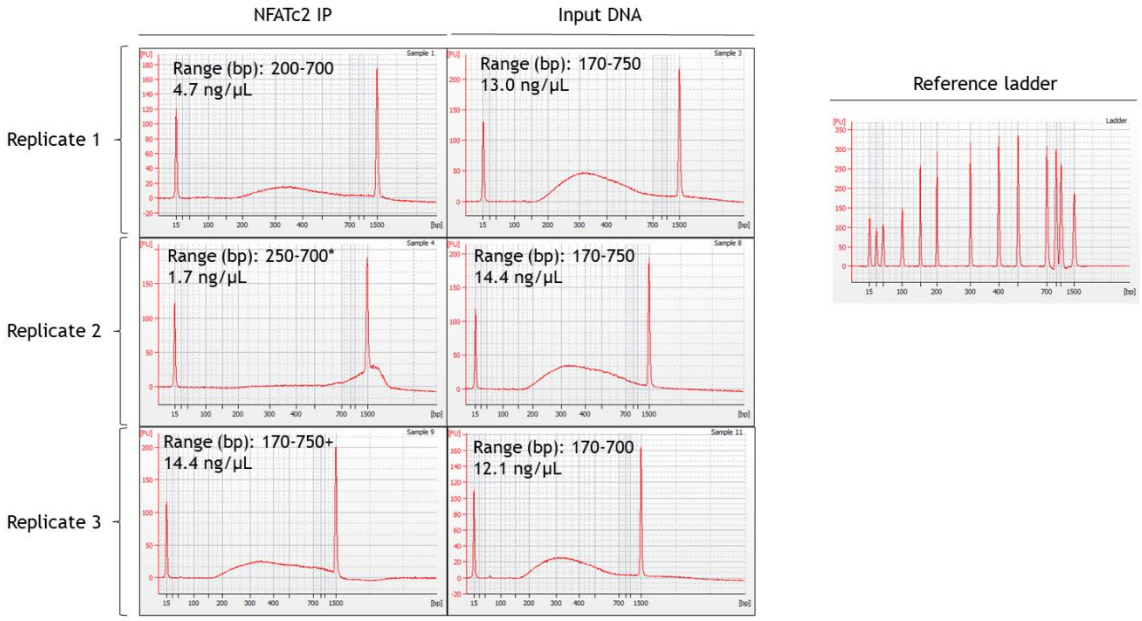

Figure A-6. Bioanalyzer electrophoresis shows an unexpected, larger DNA peak in the DNA library preparation for replicate 2. Electropherograms from the Bioanalyzer were generated by electrophoresis of the DNA libraries generated from each of the 3 ChIP-Seq replicates. Given on each plot is the range of the central peak and the concentration measured in this peak. *The range for NFATc2 IP in replicate 2 is where the DNA concentration was measured, although the main peak observed is larger. The reference ladder plot is also shown.

9.3.2 Shearing analyses

DNA samples taken immediately after sonication were reverse-crosslinked and purified as follows. They were diluted in elution buffer from the IPure V2 Kit, before the addition of NaCl to 365 mM and RNase A to 152 µg/mL. These were incubated at 60°C with shaking for 2 hr. Proteinase K was then added to 300 µg/mL and incubated overnight at 60°C with shaking. The eluted DNA were then purified using a QIAquick PCR Purification Kit (QIAGEN), as per protocol. The DNA product (~500 µg) was loaded into a 1.5% agarose gel with SYBR™ Safe DNA Gel Stain (TFS) and run at 100 V for 30-60 min, with visualisation using a LI-COR Odyssey instrument.

Library samples were also visualised on an agarose gel in this way, to assess fragment size. This is illustrated most clearly in Figure A-7.

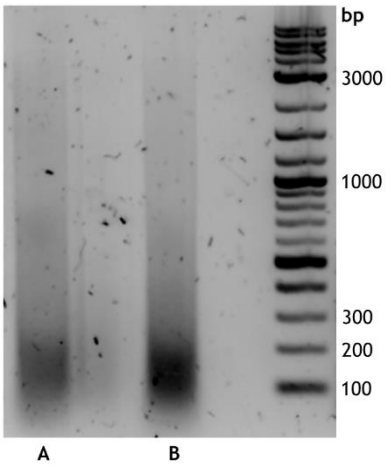

Figure A-7. DNA library samples were in the size range of 100-200bp. Samples of size-selected library DNA was electrophoresed on a 1.5% agarose gel and visualised to determine the efficiency of chromatin shearing. DNA sizes for the ladder are shown in bp.

9.3.3 Sequencing and read QC

The DNA library was sequenced using a NovaSeq 6000 platform (Illumina) by the external service provider Novogene. Paired-end sequencing was carried out with a read length of 150 bp and a minimum sequencing depth of 20 million read pairs per sample. The service provider reported sequencing quality metrics, including the base error rate, Q-Phred scores and % GC content per sample.

Sequencing reads were generated for 3 NFATc2 IP and 3 input DNA samples. The quality metrics provided from the sequencing are shown in Table A-2.

Sample	Replicate	Number of raw reads	Clean reads (% raw)	Base error rate (%)	GC content (%)
NFATc2	1	49,102,414	99.99	0.03	40.07
Input	1	51,508,504	99.99	0.03	41.35
NFATc2	2	58,169,000	99.99	0.03	42.88
Input	2	70,420,838	99.99	0.03	40.19
NFATc2	3	56,377,884	99.99	0.03	40.95
Input	3	51,727,124	99.99	0.03	40.87

Table A-2. Read quality of ChIP-Seq data was found to be 99.99% clean.
The table shows selected statistics derived from the sequencing process, containing metrics of read quality or quality of mapping reads to the genome.

The quality of reads was found to be very high at 99.99% and a low base error rate at 0.03% for all samples. The GC content ranged from 40.07-42.88%. Reads were mapped to the human genome (build hg19), followed by PCR duplicate removal and filtering of low-quality or multiply mapped reads. Subsequently, 17.93-64.68% of the originating clean reads remained and were taken forward for peak calling. By pooling the 3 replicates MACS2 called 240 peaks with a *q*-value<0.1. After excluding regions with ≥1 base overlap with hg19 blacklisted regions and gene annotation, 131 peak regions were defined as enriched with NFATc2 IP, compared to input DNA.

9.3.4 Data QC

QC metrics were obtained from the filtered bam files and MACS2 peak regions using the *ChIPQC* package in RStudio. This provided data on duplication, read length and various measures of peak strength and distribution. Some of these are described in Table A-3.

Sample	Replicate	Number of filtered/mapped reads	Filtered/mapped reads as % of clean/raw	Duplicates (% of filtered/mapped reads)	Read length (bases)	Fragment length (bases)	RelCC	SSD	RiP (%)
NFATc2	1	22,343,408	45.50	0.0	138	277	0.41	1.20	1.50
Input	1	33,315,902	64.68	0.0	140	281	0.33	1.30	-
NFATc2	2	10,429,492	17.93	0.0	130	267	0.55	1.50	2.60
Input	2	34,463,759	48.94	0.0	139	279	0.4	1.40	-
NFATc2	3	23,896,823	42.39	0.0	140	282	0.42	1.30	1.60
Input	3	30,859,184	59.66	0.0	137	276	0.34	1.30	-

Table A-3. Less than 3.0% of reads were found in ChIP-Seq peaks after NFATc2 IP.

The table describes quality metrics provided by analyses in the ChIPQC R package. The mapped reads which passed filtering are shown and also expressed as a % of the clean raw reads shown in Table A-2. The proportion of duplicate reads was also measured as a quality control for the earlier duplicate filtering step. The read length and fragment length were estimated per sample and input by calculating the cross-correlation scores between on opposite strands, with shifting of these. Plotting these values can provide an estimate of the actual read and fragment length. The relative cross-correlation score (RelCC) is shown as a measure of signal-to-noise. Also shown are SSD, a measure of enrichment, and RiP, which gives the % of reads found in peaks called for NFATc2 IP. Individual replicates are shown.

This package automatically produced boxplots to present frequency of reads in peaks (FRIP) and read counts in peaks. The RelCC (described as 'RSC' by Encode) was ≤0.55 for all conditions, however the value was higher for each NFATc2 IP than their paired input DNA in each case. In contrast the SSD score, which is used to compare coverage and enrichment between samples, does not show a clear pattern of higher enrichment in the NFATc2 IP samples, relative to the input controls; values range from 1.20-1.50. Finally, the RiP ranged from 1.50-2.60% across the 3 replicates, which is illustrated in Figure A-8.

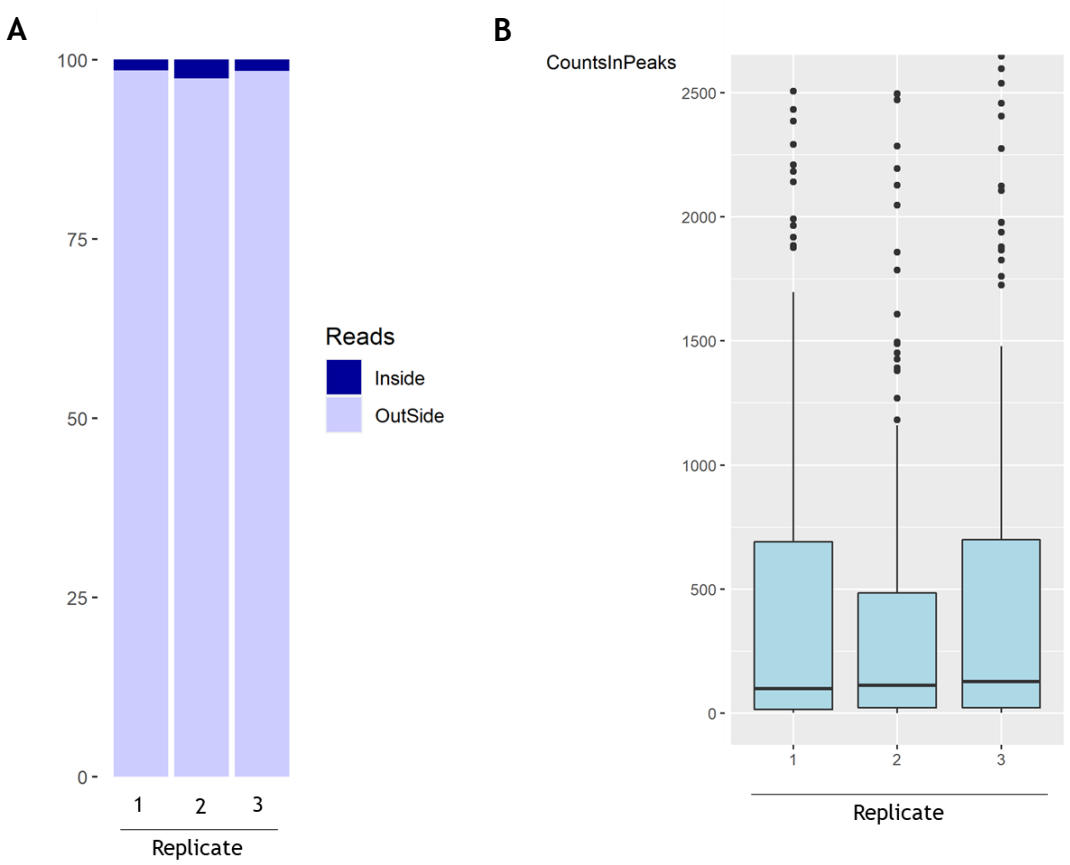

Figure A-8. Replicate 2 has a higher fraction of reads overlapping with peaks called from NFATc2 IP. A: The fraction of RiP (FRIP) is shown per replicate for NFATc2 IP in THP-1, respective to peaks called by MACS2 and filtered/mapped reads. The proportion of reads overlapping with any peaks is shown; the colour scale is given. **B:** The boxplot shows the absolute number of reads counted in each peak, per sample replicate of NFATc2 IP, compared to the peaks used in **A**. Shown are the median, upper and lower quartiles. Whiskers extend to the data point within 1.5x the inter-quartile range (IQR) beyond the upper quartile limit, while everything beyond this is presented as an outlier dot. The y-axis is clipped at y=2750 for size.

While a higher proportion of the filtered and mapped reads from replicate 2 intersected peaks (Figure A-8A), the median absolute number of reads intersecting each peak was approximately similar (Figure A-8B). There were a number of outlying read counts in all conditions, with some extending beyond the selected axis limits for replicate 3 data, showing that some peak calls were based on a high number of intersecting reads (>1500 in some cases).

9.4 *KDM4A* KD data compared to *NFATC2* KD key genes

These data were generated by Dr. Matthew Massett in a previous study.

A Upregulated after *NFATC2* KD

Gene Symbol	sh*KDM4A*-1111		sh*KDM4A*-1115	
	Log_2 fold change	Adjusted *p* value	Log_2 fold change	Adjusted *p* value
YES1	-1.28	$7.45x10^{-54}$	-0.45	$1.71x10^{-7}$
VLDLR	0.25	$5.00x10^{-5}$	0.49	$1.02x10^{-17}$
UBE3C	0.54	$1.81x10^{-13}$	-0.14	0.123
TULP3	0.98	$3.60x10^{-19}$	1.15	$1.48x10^{-26}$
TGFBR2	0.89	$1.87x10^{-24}$	0.23	0.026
SNX16	0.56	0.001	0.30	0.140
SFXN3	-0.33	$7.73x10^{-7}$	0.04	0.764
S1PR3	1.06	$2.90x10^{-26}$	0.58	$3.61x10^{-8}$
RNF19A	0.72	$3.78x10^{-22}$	0.75	$6.83x10^{-24}$
RASA1	0.28	0.003	-0.14	0.246
RAB15	0.63	$8.67x10^{-14}$	0.61	$3.95x10^{-13}$
RAB12	1.36	$3.79x10^{-40}$	0.40	0.001
PRRG4	0.36	0.006	0.83	$3.83x10^{-14}$
PANX1	0.46	0.001	-0.46	0.001
OCRL	0.93	$7.82x10^{-37}$	0.85	$8.98x10^{-31}$
NPEPPS	0.88	$5.48x10^{-50}$	0.61	$3.42x10^{-24}$
KDELC2	-0.07	N/A	0.30	0.002
GCNT2	0.49	0.084	0.23	0.558
GBP3	0.08	0.713	1.45	$1.60x10^{-31}$
CCNYL1	0.66	$1.05x10^{-16}$	0.46	$1.33x10^{-8}$
BRWD3	-0.12	0.294	-0.21	0.048
BIN1	0.71	$2.62x10^{-7}$	-0.77	$1.98x10^{-7}$
ATG9A	0.49	$3.46x10^{-12}$	0.25	0.001
ANKRD40	0.24	0.012	-0.30	0.001
AHNAK	-1.11	$1.66x10^{-62}$	0.50	$2.13x10^{-13}$

B Downregulated after *NFATC2* KD

Gene Symbol	sh*KDM4A*-1111		sh*KDM4A*-1115	
	Log_2 fold change	Adjusted *p* value	Log_2 fold change	Adjusted *p* value
TMEM92	-0.70	0.093	-0.07	0.93
SPNS3	-0.96	$7.52x10^{-19}$	1.00	$2.97x10^{-21}$
SH2D3A	0.22	0.452	-0.05	0.913
RGL4	-0.48	0.110	0.14	0.762
PRR7	-0.12	0.734	-0.15	0.704
KLF15	-0.47	0.081	-0.41	0.162
HSH2D	-1.24	$1.30x10^{-10}$	2.28	$1.67x10^{-44}$
EXOSC6	-0.12	0.395	-0.34	0.005
DEFA8P	-0.45	0.256	0.63	0.092
COMTD1	-1.22	$1.90x10^{-10}$	-0.45	0.036

Table A-4. Genes upregulated after *NFATC2* KD are predominantly upregulated after *KDM4A* KD also. THP-1 cells were transduced with two shRNA constructs for *KDM4A* KD: (-1111 and -1115) and selected using puromycin at 24 hr post-transduction. RNA was harvested 48 hr post-puromycin selection for RNA-Seq. Shown are the log_2 fold changes and adjusted *p* values from the RNA-Seq analyses, per each sh*KDM4A* construct. The genes selected are those **A:** upregulated or **B:** downregulated after *NFATC2* KD with adjusted $p<0.1$, as described from the RNA-Seq data previously in Chapter 5. Highlighted in green are those which were deregulated after *KDM4A* KD with both adjusted $p<0.1$ and in the same direction of change as was observed for *NFATC2* KD.